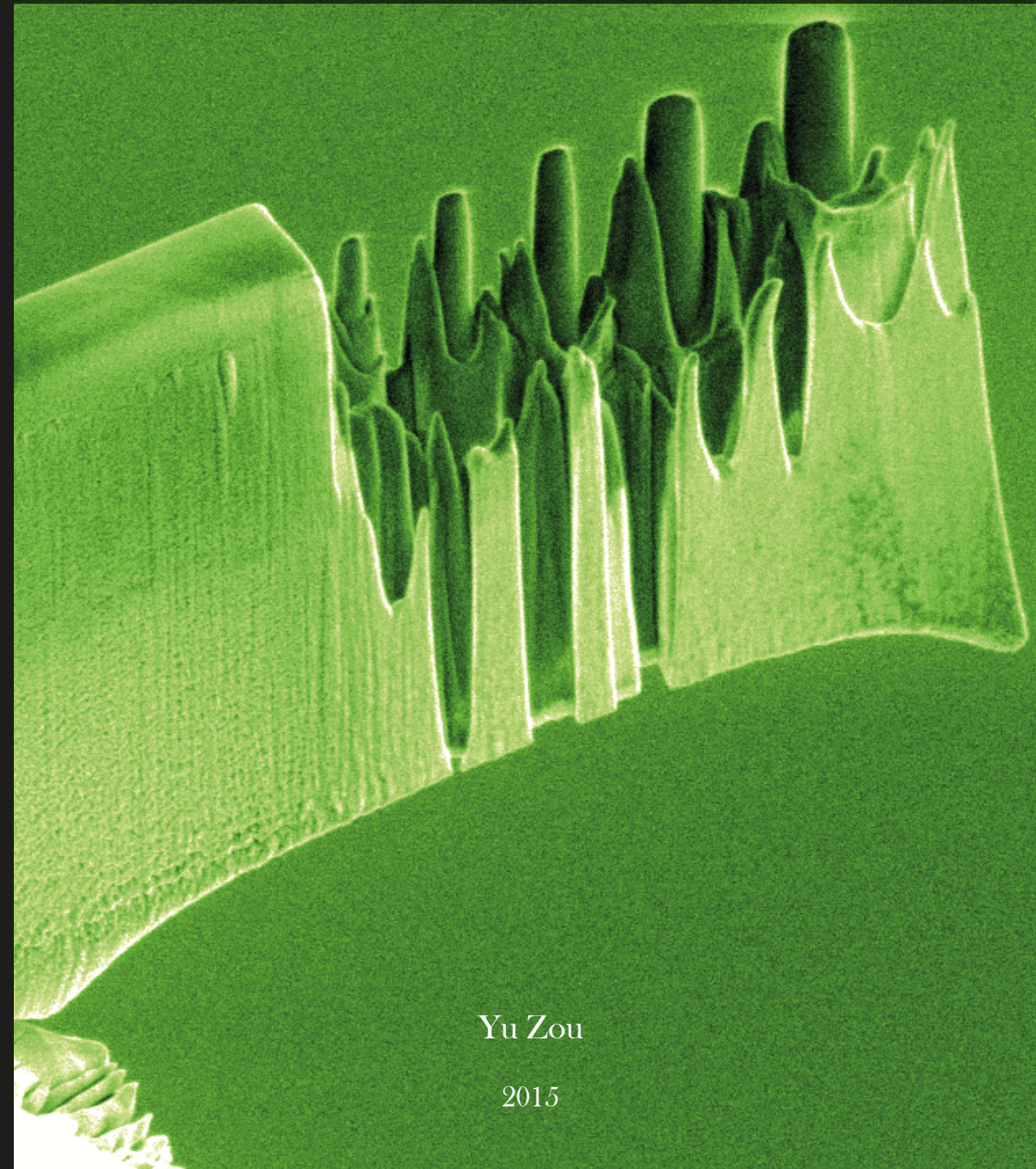


Probing Small-scale Plasticity: from Simple Ionic Crystals to Complex Intermetallic Phases



Yu Zou

2015

Yu Zou Probing Small-scale Plasticity: from Simple Ionic Crystals to Complex Intermetallic Phases 2015



DISS. ETH NO. 23118

**Probing Small-scale Plasticity: from Simple Ionic Crystals
to Complex Intermetallic Phases**

A thesis submitted to attain the degree of
DOCTOR OF SCIENCES of ETH ZURICH

(Dr. sc. ETH Zurich)

presented by

Yu Zou

M.Eng., McGill University

born on 18.03.1983

citizen of China

accepted on the recommendation of

Prof. Dr. Ralph Spolenak, examiner

Prof. Dr. Walter Steurer, co-examiner

Prof. Dr. Oliver Kraft, co-examiner

2015

Perfect love casts out fear.

Acknowledgements

I can still reminisce the image of me boarding the flight from Montreal to Zurich four and half years ago. In the farewell letter to my friends in Montreal I wrote “...*two passions, mainly and simply, have led me make this choice: the desire for doing good work and the longing for new experience.*” Now, it is time to summarize what I have done at ETH Zurich and also a good chance to say “*thank you*” to the people who have helped me during the past couple of years.

I would like to thank Prof. Dr. Spolenak for offering me the PhD position when I was frustrated in looking for a new opportunity after finishing my Master’s degree. It was my best of luck to meet him in San Diego in the spring of 2011. I appreciated all of his encouragement, support and given freedom in research. It is my great pleasure to grow towards a qualified researcher under his guide. *Thank you*, Ralph! My sincere thanks to Prof. Dr. Oliver Kraft, Prof. Dr. Walter Steurer and Prof. Dr. Manfred Fiebig, who served in my PhD thesis committee, spent their time in reading my thesis and provided valuable comments.

I appreciated the collaborations both within the group and with several other research groups, in particular to Huan Ma for sputtering superior high-entropy alloy films, Dr. Alla Sologubenko for a big amount of TEM works, Dr. Jeffrey Wheeler and Dr. Johann Michler (Empa Thun) for their elegant high-temperature micro-pillar compression, Prof. Dr. Walter Steurer, Dr. Pawel Kuczera and Soumyadipta Maiti (Laboratory of Crystallography) for introducing fascinating quasicrystals and high-entropy alloys to me, Prof. Takayuki Kitamura, Prof. Takashi Sumigawa and Dr. Hongjun Yu (Kyoto University) for being enthusiastic hosts and teaching me fracture mechanics in Japan, and Philippe Gasser, Dr. Karsten Kunze and Dr. Stephan Gerstl (ScopeM) for their technical supports.

Of course, to you, my colleagues in LNM, past and present, I say “*thank you*” for being such an important part of my PhD life. In addition to the people mentioned above, I would like to express many thanks to Dr. Claudia Müller and Dr. Anna

Evans for proofreading my thesis, and Dr. Diana Courty and Philipp Okle for helping with the translation of the summary into German as well as indentation and atom probe experiments. I should not forget the joy of working with any of you: Dr. Markus Diener and Beatrice Wegmann for your support in the Praktikum, Dr. Christian Solenthaler for your helpful discussions on TEM, Dr. Galinski Henning, Dr. Matteo Seita, Dr. Martin J. Süess and Dr. Matthias Schamel for your sincere discussions, Dr. Franz Vüllers, Dr. Christina Pecnik and André Röthlisberger for being nice office mates, Franziska Schlich for setting up the conductive indenter, Alain Reiser for sharing and talking in the lab in late evenings, Andi Wyss for sharing your biking experiences, Ayse Özkaraca for sharing your Turkish delights, Carola Herren for organizing administrative stuff for me, Xiao Yuan for all your delicious dishes and interesting discussions, and so on. I am so proud to have been among all of you! I would also like to thank my Bachelor and Master students Dong Hao, Fabian Gygax and Micha Calvo for their work. In addition, I acknowledge the financial support through the Swiss National Science Foundation (200021_143633), ETH Zurich and the JSPS program (GR14103).

With equal vision I have explored in research, I have experienced new cultures in Switzerland, from which my vision and values are tested, verified and modified. I really want to thank Dorothee Rübél for being such a nice flat mate and sincere friend to help me experience and adapt to the Swiss life. Great thanks to the Chinese community in Switzerland for building a warm home far away from our motherland. Special thanks to Yingnan Zhao who once shared joy and sorrow with me and always stimulated me to be the best.

Last but not least, I give more gratitude than I can express to my parents who are always there to support me. Their love has been the driving force for me to move forward, forever.

Summary

Plasticity is the ability of a solid to flow or to change its shape permanently without rupture when subjected to external stresses. More than a century has passed since the initial scientific study on plastic deformation of solids. Still today, research on plasticity plays an essential role in materials science, especially in metallurgy. As stated by Alan H. Cottrell at the beginning of this century, a complete understanding of plasticity is one of the most difficult remaining problems in classical physics. Nowadays, the rapid development of microelectronics and nanotechnology poses an urgent challenge to the fundamental understanding of mechanical properties of materials at the micrometer and nanometer dimensions. At such length scales, the plastic behavior of materials is not well described by the classic theory of plasticity. Hence, a good understanding of the plasticity at small scales is critical to the overall functionality and reliability of micro- or nano-devices.

This thesis studies the plastic behavior of three types of materials— ionic crystals, high-entropy alloys and quasicrystals, at the length scales from about 100 nanometers to a few microns, which have scarcely, or never, been reported before. Together with the literature data on metals, metallic glasses and covalent crystals to date, the thesis aims to present a big picture of size-dependent plasticity in various classes of inorganic solids. Throughout the thesis, I mainly seek to answer two fundamental questions: what size and internal structure lead to the strongest materials? And what mechanism controls the size effect? Here, I show a general trend for the maximum strengths in these materials at sub-micrometer scales, regardless of chemical composition, lattice structure, atomic order and periodicity, that they all fall in the strength range between $G/30$ and $G/100$, where G corresponds to the shear modulus. Furthermore, their size dependence (log-log exponent m) of strength generally decreases with increasing resistance (τ_p) for the propagation of plasticity mediums— dislocations or shear bands: when τ_p is smaller than about 0.1 GPa, m is in the range between 0.6 and 0.8, nearly constant

size effect; when τ_p increases from 0.1 GPa to 1 GPa, m decreases accordingly from about 0.6-0.8 to almost zero; when τ_p is larger than about 1 GPa, m is zero, no size effect.

In addition to answering these two questions, a couple of interesting and extraordinary properties were found in these materials at such length scales. The most important findings of my thesis studies are: (i) an external electric field can reduce the flow stress and enhance the plasticity in small-scale ionic crystals, which may represent a new class of smart materials or nanoscale actuators; (ii) the micro-compression of high-entropy alloys was reported for the first time, and by optimizing the grain size and sample dimension, nanocrystalline high-entropy alloy pillars achieve a new record in strength among all metallic micro- or nano-pillars as well as exhibits excellent thermal stability; (iii) the thesis also includes the first report on micro-compression/bending of quasicrystals, which probes an unknown size and temperature regime for quasicrystal plasticity, showing that these quasicrystal micro-pillars have the highest specific strengths among the metallic pillars reported to date.

This thesis, using emerging nano-mechanical testing techniques, demonstrates new opportunities for a fundamental understanding of plastic behavior in ionic crystals and complex intermetallic phases at small scales. The related approaches can be applied for a broad range of materials. Much work, however, is still required to further optimize the material properties. The superior and useful plasticity properties of the small-scale materials presented in this thesis may permit their implementation in critical applications as well as offer a strong motivation for their further development.

Zusammenfassung

Plastizität ist die Fähigkeit eines Festkörpers zu fließen oder seine Form irreversibel zu ändern ohne dabei zu brechen, wenn externe Kräfte aufgebracht werden. Mehr als ein Jahrhundert ist seit der ersten wissenschaftlichen Abhandlung über die plastische Verformung von Festkörpern vergangen. Auch heute spielt die Erforschung der Plastizität eine wichtige Rolle in der Materialwissenschaft, besonders in der Metallurgie. Wie von Alan H. Cottrell zu Beginn des Jahrhunderts gesagt, bleibt das vollständige Verständnis der Plastizität eines der schwierigsten offenen Fragen der klassischen Physik.

Aufgrund der rapiden Entwicklung der Mikro- und Nanotechnologie wird das grundsätzliche Verständnis der mechanischen Eigenschaften im Mikro- und Nanometerbereich immer wichtiger. In dieser Grössenordnung ist das plastische Verhalten der Materialien nicht gut durch die klassische Plastizitätstheorie beschrieben. Deshalb ist ein besseres Verständnis der Plastizität auf niedriger Grössenskala wichtig um die Funktionsweise und die Zuverlässigkeit von Mikro- und Nanokomponenten sicherzustellen.

Diese Doktorarbeit untersucht das plastische Verhalten von ionischen Kristallen, Hoch-Entropie-Legierungen und Quasikristallen in einem Grössenbereich von ca. 100 Nanometern bis zu wenigen Mikrometern, welches bis dato von diesen Materialtypen selten oder nie berichtet wurde. Zusammen mit bisherigen Literaturdaten über Metalle, metallische Gläser und kovalente Kristalle, soll diese Arbeit eine umfassende Darstellung grössenabhängiger Plastizität in unterschiedlichen anorganischen Feststoffen liefern. In dieser Dissertation sollen in erster Linie zwei grundsätzliche Fragen beantwortet werden: Welche Grösse und interne Struktur führen zu den grössten Materialfestigkeiten? Und welcher Mechanismus kontrolliert den Grösseneffekt? Hierzu wird der allgemeine Trend gezeigt, dass die Festigkeiten dieser Materialien im Submikrometerbereich alle zwischen $1/30$ und $1/100$ des Schermoduls liegen. Dieser Trend gilt unabhängig von der chemischen Zusammensetzung, der Gitterstruktur sowie der Ordnung

und Periodizität der Atome. Die Grössenabhängigkeit (log-log Exponent m) der Festigkeit nimmt gewöhnlich mit wachsendem Widerstand (τ_p) gegen das Ausbreiten von Versetzungen oder Scherbänder ab: Wenn τ_p kleiner als ca. 0.1 GPa ist, liegt m im Bereich von 0.6 und 0.8 bei einem nahezu konstanten Grösseneffekt. Wenn τ_p zwischen 0.1 GPa und 1 GPa liegt, nimmt m von Werten zwischen 0.6 und 0.8 zu Werten nahe 0 mit wachsendem τ_p ab. Wenn τ_p grösser als 1 GPa ist, ist m nahezu 0 und es gibt keinen Grösseneffekt.

Zusätzlich zur Beantwortung der beiden Fragen wurden einige interessante und aussergewöhnliche Eigenschaften der untersuchten Materialien entdeckt. Die wichtigsten Ergebnisse der vorliegenden Arbeit sind: (i) Ein externes elektrisches Feld kann die Fliessspannung senken und die Plastizität in kleinskaligen ionischen Kristallen erhöhen. Dies könnte für eine neue intelligente Materialklasse oder Aktuatoren auf der Nanoskala verwendet werden. (ii) Mikrodruckversuche an Säulen aus Hoch-Entropie-Legierungen wurden zum ersten Mal vorgestellt. Durch Optimieren der Korngrösse und der Probendimensionen erreichen die nanokristallinen Säulen einen neuen Festigkeitsrekord aller metallischen Mikro- und Nanosäulen. Zudem zeichnet sich das Material durch eine hervorragende Thermostabilität aus. (iii) Diese Dissertation enthält auch erstmalig einen Bericht zur Plastizität von Quasikristallen bei Mikrodruck- und Biegeversuchen in einem bislang unerforschten Grössen- und Temperaturbereich. Die getesteten quasikristallinen Mikrosäulen haben die höchste spezifische Festigkeit die bisher je in Mikrosäulendruckexperimenten berichtet wurde.

Diese Arbeit verwendet fortschrittliche Testmethoden um neue Wege zu einem grundsätzlichen Verständnis der plastischen Verformungsmechanismen in ionischen Kristallen und komplexen intermetallischen Phasen in kleinen Dimensionen aufzuzeigen. Die Herangehensweise lässt sich auf eine grosse Bandbreite an Materialien übertragen. Nichtsdestotrotz bleibt es ein arbeitsintensiver Entwicklungsprozess die Materialeigenschaften weiter zu

optimieren. Die herausragenden und nützlichen Verformungseigenschaften der kleinskaligen Materialien, welche in dieser Arbeit dargelegt sind, könnten zu einem Einsatz in kritischen Anwendungen führen und machen deren Weiterentwicklung interessant.

Contents

Acknowledgements	i
Summary	iii
Zusammenfassung	v
Contents	viii
Abbreviations	xii
Chapter 1. Introduction	1
1.1. A brief history of plasticity.....	2
1.2. Classical plasticity theory: a few important concepts	5
1.3. Size effect in plasticity.....	10
1.4. Experimental methods: focused ion beam and micro-compression techniques	13
1.5. Micro-compression: metals and metallic glasses	16
Metals	16
Metallic glasses	18
1.6. Macroscopic plasticity in ionic crystals, high-entropy alloys and quasicrystals.....	19
Ionic crystals.....	19
High-entropy alloys.....	23
Quasicrystals	25
1.7. Aim and scope of the thesis.....	28
References.....	31
Chapter 2. Size Effect in Ionic Crystals	35
2.1. Single crystalline NaCl, KCl, LiF and MgO	35

Introduction.....	35
Experimental methods	37
Results	37
Discussion	41
Conclusions.....	44
2.2. The influence of orientation, temperature, pre-straining and doping: a case study in KCl and LiF	45
Introduction.....	45
Experimental	48
Results	49
Discussion	58
Summary and conclusions	67
2.3. Electro-plasticity of sodium chloride at small scales.....	69
Introduction.....	69
Materials and methods	71
Results	72
Discussion	73
Outlook.....	77
References	79
Chapter 3. Size Effect in High-entropy Alloys.....	82
3.1. Single crystalline micro-pillars made of a Nb ₂₅ Mo ₂₅ Ta ₂₅ W ₂₅ high-entropy alloy	82
Introduction.....	83
Materials and methods	85
Results	87

Discussion	93
Summary	104
3.2. Fracture properties of the high-entropy alloy: single crystals vs. bi-crystals	106
3.3. Thin films and fine-scale pillars made of nanocrystalline high-entropy alloys	115
Introduction	115
Results	117
Discussion	121
Methods	127
References.....	132
Chapter 4. Size Effect in Quasicrystals.....	136
4.1. Icosahedral Al-Pd-Mn at room temperature.....	136
4.2. Decagonal Al-Ni-Co at room temperature	149
Introduction	149
Materials and methods	151
Results	152
Discussion	155
4.3. Decagonal Al-Ni-Co from room temperature to high temperatures	160
Introduction and background	161
Materials and experimental procedure.....	164
Nano-thermomechanical testing.....	166
STEM characterization.....	169
Discussion	170
Conclusion and outlook.....	186

References	188
Chapter 5. Discussion, Conclusions and Outlook.....	193
5.1. Discussion.....	193
5.2. Conclusions	197
5.3. Outlook	199
References	201
Declaration.....	202
Curriculum Vitae	204

Abbreviations

3D	Three-dimensional
AFM	Atomic force microscopy
BCC	Body centered cubic
CRSS	Critical resolved shear stress
DQC	Decagonal quasicrystal
EBSD	Electron backscatter diffraction
EDX	Energy dispersive X-ray spectroscopy
FCC	Face centered cubic
FEM	Finite element method
FIB	Focused ion beam
GB	Grain boundary
HEA	High-entropy alloys
IBAD	Ion beam assisted deposition
IQC	Icosahedral quasicrystal
QC	Quasicrystal
SC	Single crystalline
SEM	Scanning electron microscope
STEM	Scanning transmission electron microscopy
TEM	Transmission electron microcopy
XRD	X-ray powder diffraction

Chapter 1. Introduction

In materials science, plasticity describes the deformation of a solid undergoing a non-reversible change in shape or size when subjected to a stress. Plastic deformation is commonly observed in both natural and man-made materials such as metals, soils, rocks, concrete, foams, skins and bones. Among them, for the most widely used structural materials in the world—metals, plasticity plays an essential role in their mechanical performance by determining two most important properties—yield strength and ductility. The former one limits the stress at which a material begins to deform permanently and the latter one governs the ability of the material to change shape non-reversibly without breaking. A proper use of the knowledge of materials' plastic properties will greatly contribute to the progress of the society, while a lacking of the relevant knowledge may cause serious economic losses and even loss of life. For example, the Eiffel Tower, which was completed in 1889, is made of 7300 tons of puddled iron (wrought iron) (Fig. 1a), and nowadays, much less of that weight would be needed using high-strength and low-density materials [1]. The tragedy of Titanic in 1912 had been thought to be caused by the failure of its steel plates, now it is known that it was primarily because of the poor quality and low strength of the rivets securing the hull sections (Fig. 1b) [2]. Therefore, a complete understanding of plastic properties of materials is highly desired. Arrived in the 21st century, materials researchers are facing many new challenges in this classical field, wherein a critical one is “size effect”. As small-sized devices are ubiquitous in modern technological applications, a fundamental understanding of the size effect on materials' performance is critical to the overall reliability of emerging nanotechnology and also to paving the way in the design for novel functionality.

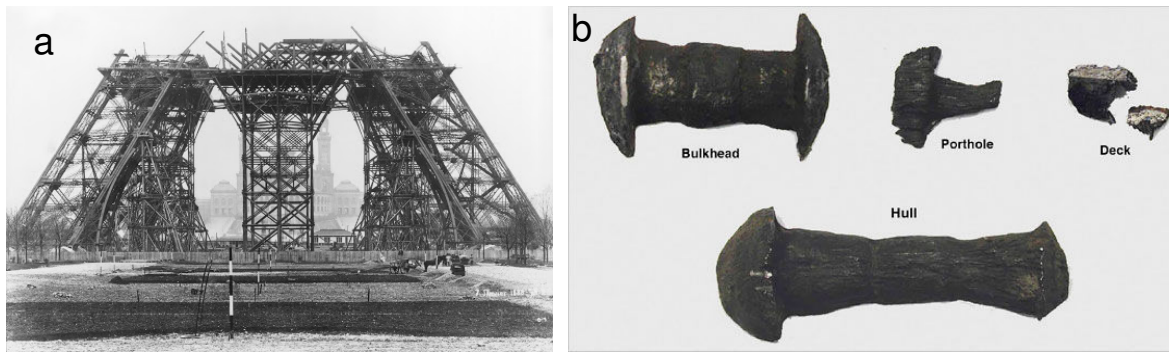


Fig. 1. (a) Construction of the Eiffel Tower using puddled iron - the first floor of the tower in the background Trocadero in January 1888 (Image from ref. [3] © Collection tour Eiffel | Eiffel Tower). (b) Samples of four different types of rivets recovered from the Titanic. While some ships of that time were built entirely with steel rivets, the Titanic used a mix of steel and iron rivets. In the bow, where the Titanic hit the iceberg, weaker iron rivets were used [4] © 2008 The New York Times Company.

1.1. A brief history of plasticity

The first record of metalworking by human traces back to over 5000 years ago [5], but metallurgy as a science only dates from about a century and a half ago, when Sorby used an optical microscope to observe the structure of polished and etched ferrous specimens in Sheffield in 1863 [6]. As early as in the end of the 19th century, Mügge [7] as well as Ewing and Rosenhai [8, 9] detected slip lines on rock salts and various metals, and they suggested that the plastic yielding was due to slip on certain crystallographic planes along certain directions. However, intensive research into the plasticity of crystals only began around 1920 after the developments of the X-ray diffraction technique [10]. In 1924, Schmid [11] formulated an empirical law describing quantitatively the slip planes and directions related to crystallographic orientation in a uniaxial deformation of a single crystals (see example of single slip in Fig. 2).

The understanding of the crystalline structure made it possible to calculate the shear strength of a crystal. However, there was still a question that puzzled the metallurgists: the theoretical strength of a metal calculated from their atomic properties is 100-1000 times higher than the measured stress required to produce plastic deformation. In 1934, the puzzle had successfully been solved by introducing the concept of dislocations—linear defects in crystals (Fig. 3a), which

was introduced almost simultaneously by Orowan [13], Polanyi [14] and Taylor [15]. After that, the dislocation theory played a central role throughout the development of plasticity theory, but it was still challenging to prove the existence of dislocations. The existence of dislocations were first demonstrated by etching pit formation and by doping with impurity atoms in alkali halides and semiconductors such as the etch pit formation in LiF [16]. Only in 1956, the first direct observation of dislocations was reported by Menter [17] using transmission electron microscopy (TEM) to see edge dislocations in platinum phthalocyanine with the lattice planes spaced 1.2 nm apart (Fig. 3b) and also by Hirsch and Whelan [18] in the same year revealing dislocations by diffraction contrast in aluminum.

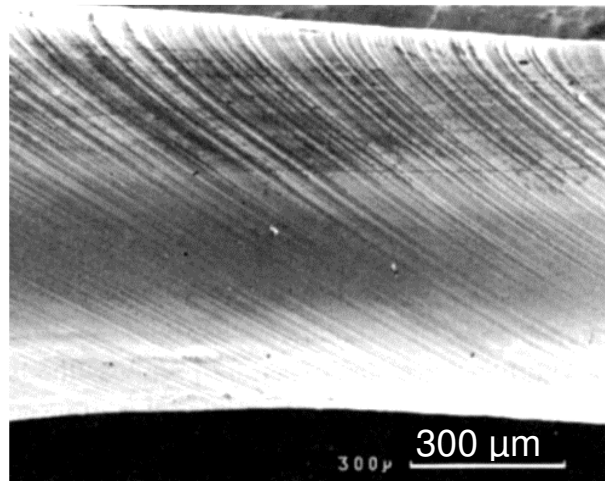


Fig. 2. A scanning electron micrograph of a single crystalline cadmium after deformation (image from ref. [12] © DoITPoMS standard terms of use, University of Cambridge).

The dislocation theory was further developed by theoretical physicists such as Mott [19] and metallurgists such as Cottrell [20] and Read [21]. Since then, modern physical metallurgy or mechanical metallurgy opened up a broad field of plasticity. A large number of classes of materials were studied for their plastic behaviors, including pure metals, metallic alloys, intermetallic alloys, ionic crystals, semiconductors, ceramics, quasicrystals and metallic glasses [22]. It was known that the deformation mechanisms were not limited to dislocation activities [23], and many other mechanisms could also play essential roles in plastic

deformation, such as deformation twinning [24], grain-boundary sliding [25], crack formation and propagation [26], shear banding [27], phase transformation [28] and diffusion [29]. The deformation-mechanism maps developed by Ashby [30], as an example of sodium chloride (Fig. 4a), revealed the dominate mechanism of plastic flow under certain stress, temperature and strain rate for various materials. Together with Ashby plots for material selection [31], as an example of the modulus-density relation (Fig. 4b), the deformation-mechanism maps provided a qualitative guide for choosing a material for engineering applications and also for predicting the deformation mechanism. With the maturation of the theory of plasticity, especially dislocation theory, many mechanical behaviors were successfully explained, and the new materials and structures were designed and used according to the fundamental principles of plasticity. The success of the theory of plasticity made metallic materials the major workhorse of our modern industries, such as automobile, aerospace, marine, oil, nuclear industries and so on.

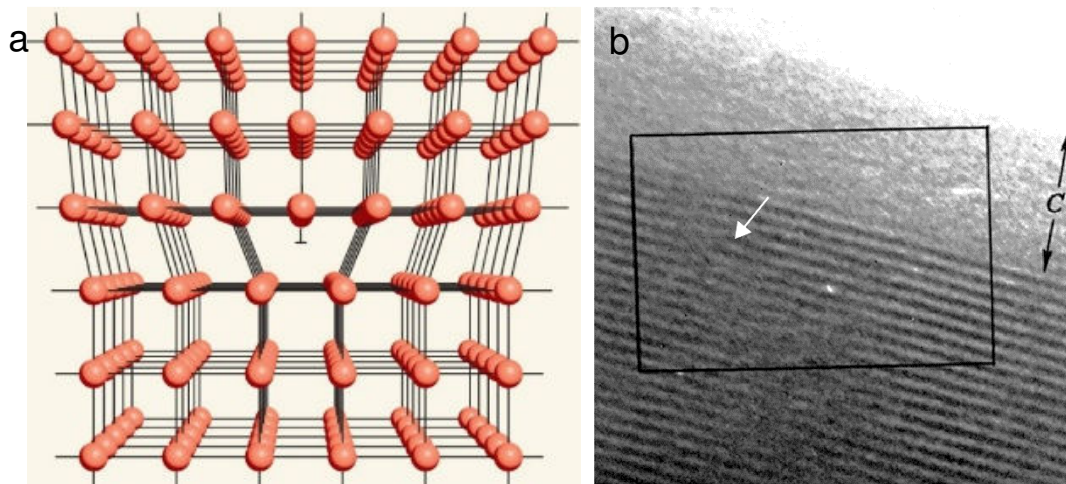


Fig. 3. (a) Edge dislocation in a cubic crystal. (b) The first observation of dislocation using TEM: single edge dislocation in platinum phthalocyanine crystal and the row indicate the exact position of the edge dislocation [17]. ((a) reproduced with permission from [32], © 2013, Nature Publishing Group; (b) reproduced from [17], reprinted with permission from The Royal Society).

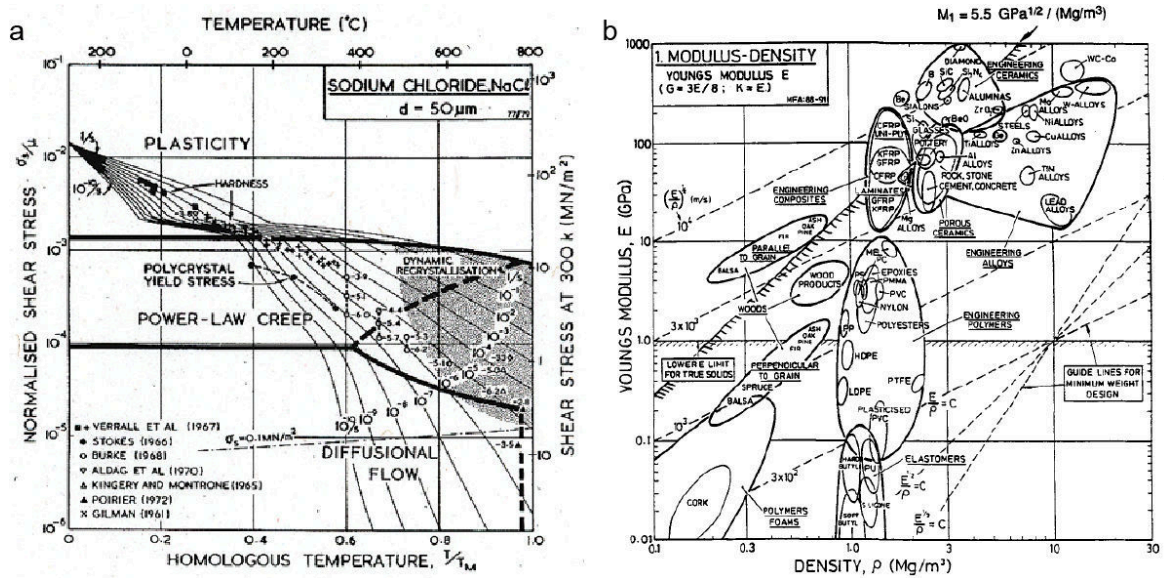


Fig. 4. (a) A stress-temperature map for NaCl of grain size 50 μm with data labelled in log10 [33] (with permission from John Wiley & Sons, Inc.). (b) An example of an Ashby plot (density vs. Young's modulus) for materials selection in mechanical design [31] (with permission from EDP Sciences 1993).

1.2. Classical plasticity theory: a few important concepts

Schmid's law [34, 35]

Dislocation glide (i.e. a dislocation moves in a plane containing both a dislocation line and Burgers vector) is the most common manifestation of plastic deformation in crystals—slip. The slip planes and slip directions are not random but are along specific crystallographic orientations. Normally, the slip planes have the highest density of atoms, i.e. the most closely packed planes, and the slip direction has one of the shortest lattice translation vectors, i.e. the most closely packed direction. Slip results in the formation of steps on the surface of a material, most often in a single crystal. The shear stress, τ , resolved on the slip plane in the slip direction can be calculated using measured tensile or compressive stress, σ , the angle, λ , between applied force and the slip direction, and the angle, Φ , between applied force and the normal to the slip plane (Fig. 5), as:

$$\tau = \sigma \cos \lambda \cos \Phi \quad (1)$$

The quantity of $\cos \lambda \cos \Phi$ is called *Schmid factor*, m_s , which depends on the loading direction and the activated slip system of a crystalline solid. The required shear stress to start slip process is *critical resolved shear stress* (CRSS) or τ_c .

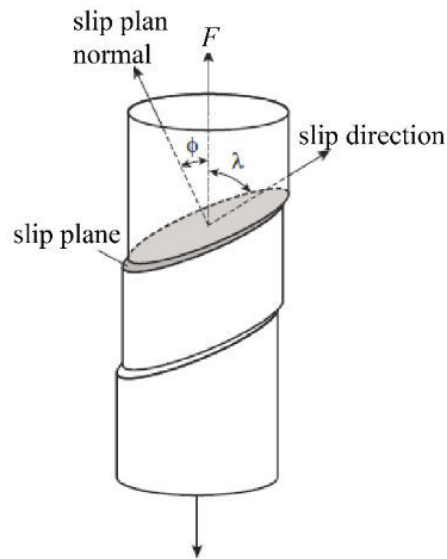


Fig. 5. Illustration of the geometry of a slip in a cylindrical crystal under tensile stress. (Schematic is from [34], reprinted with the permission from 2011 Elsevier Ltd.)

Thermal activation process [34, 36]

The “topography” for the motion of dislocations is not flat, which could be associated with interatomic bonding in a lattice (i.e. Peierls barrier), solute atoms or precipitates. In order to overcome the barriers they encounter during slip, dislocations can either be “pushed” over the barrier by force or “jump” over the barrier by thermal activation, or both (See Fig. 6). In the extreme scenario, at 0 K, the applied resolved shear stress required to make a dislocation glide in a perfect crystal without any thermal activation is called Peierls (or Peierls-Nabarro) stress, τ_p . In another extreme case, if thermal energy is in the level of a significantly part of the energy barriers, a very tiny force is needed for the dislocation motion with the assistant of thermal vibrations.

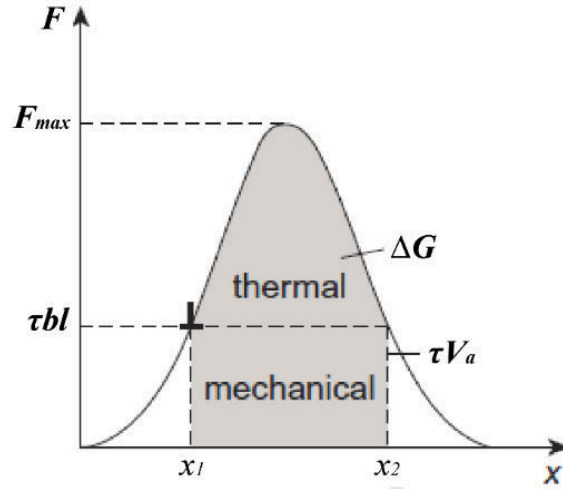


Fig. 6. The profile of lattice force barrier opposing dislocation motion. (Schematic is adapted from [34], reprinted with the permission from 2011 Elsevier Ltd.)

In general, both thermal activation and applied force are provided for dislocations to overcome the barriers, ΔG_0 , from position x_1 to position x_2 . The mechanical work under the applied shear stress, τ , is $\tau bl(x_1 - x_2)$, where b is the Burgers vector, l is the spacing between the obstacles and the value of $bl(x_1 - x_2)$ is called activation volume, V_a . The other part of energy has to be supplied by thermal activation, as

$$\Delta G = \Delta G_0 - \tau V_a \quad (2)$$

where ΔG is the Gibbs free energy of activation. The probability for this dislocation segment to jump over the energy barrier can thus be expressed using the Boltzmann factor as $\exp(-\Delta G/k_B T)$, where k_B is the Boltzmann constant and T is the absolute temperature. If the vibration frequency of dislocation is ν , the dislocation segment can jump over the energy barrier at a rate of $\nu \exp(-\Delta G/k_B T)$ and, therefore, the dislocation velocity, v_{dis} , can be expressed as:

$$v_{dis} = d \nu \exp\left(-\frac{\Delta G}{k_B T}\right) \quad (3)$$

where d is the distance moved for each obstacle overcome. Because the strain rate, $\dot{\epsilon}$, can be calculated by the Orowan-Taylor law as:

$$\dot{\epsilon} = b \rho_m v_{dis} \quad (4)$$

where ρ_m is the mobile dislocation density and $A = bdv$. The following formula can be obtained:

$$\dot{\epsilon} = \rho_m A \exp\left(-\frac{\Delta G}{k_B T}\right) \quad (5)$$

Under such conditions, an increase in temperature, or a reduction in applied strain rate, will reduce the flow stress. The flow stress overcome the energy barrier at the testing temperature T_t can be simplified as:

$$\tau = \left(1 - \frac{T_t}{T_c}\right) \tau_p \quad (6)$$

where T_c is the critical temperature above that the flow stress is not temperature sensitive.

The τ_p can be calculated using the following equation:

$$\tau_p = \frac{2\pi}{b^2} E_p \quad (7)$$

where E_p is known as Peierls energy (Peierls energy barrier) and can be estimated using the relation:

$$E_p = \frac{Gb^2}{\pi(1-\nu)} \exp\left(\frac{-2\pi\omega}{b}\right) \quad (8)$$

where ν is Poisson's ratio and ω is the width of the dislocation core.

In experiment, the measurement of V_a is important, because V_a is related to the area swept by the dislocation during the thermally activated event. In general, it is believed that a very small V_a ($\sim 0.1-1 b^3$) corresponds to a diffusion-controlled deformation; a small one ($\sim 10-100 b^3$) can be related to Peierls mechanism; a large one ($100-1000 b^3$) can be associated with dislocation solute interactions, and a very large one ($\sim 1000 b^3$) is the forest mechanism. Strain-rate jump experiments can be used to measure the strain-rate sensitivity of the stress, S , which is related to the apparent activation volume, as:

$$V_a = \sqrt{3} \frac{k_B T}{S \sigma} \quad (9)$$

where S can be measured by the relation of flow stress, σ , as a function of strain rate, $\dot{\epsilon}$, by:

$$S = \frac{\partial \ln \sigma}{\partial \ln \dot{\epsilon}} \quad (10)$$

Dislocation multiplication [34, 35]

In order to accommodate plastic strain, generation of new dislocations, or multiplication, is necessary. A well-known mechanism is the Frank-Read source developed in the early 1950s. As shown in Fig. 7a, a dislocation segment AB has its Burgers vector lying in a plane but held by two pin points at both ends, which can be point defects, dislocation intersections, composite jogs, precipitates, etc. A maximum applied resolved shear stress, τ_{max} , should be reached to active the motion of the dislocation segment, as:

$$\tau_{max} = Gb/L \quad (11)$$

Where L is the length of the segment AB . It is known that, to act as Frank-Read sources at applied stresses close to the yield strength, dislocation should have the length of segments $L \sim 10^4 b$. Assuming b is in the order of 0.1 nm, the critical value of L should be in the order of 100 nm, which is in the sub-micrometer regime. Another model that can account for dislocation multiplication is single-end source, or single-arm source, wherein only one end of dislocation segment is fixed or pinned and the other end can move freely, generating new dislocations (Fig.7b).

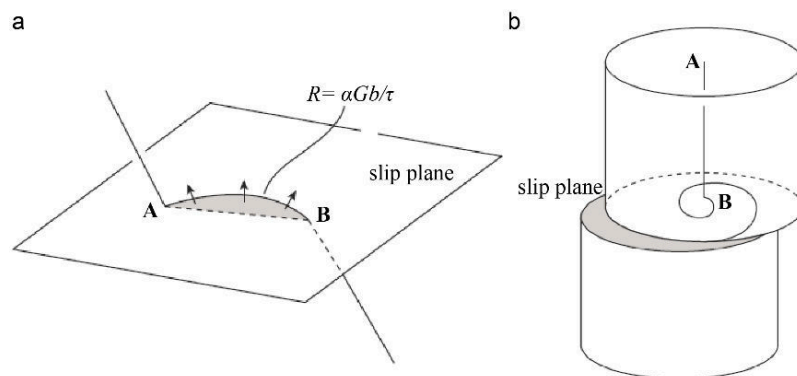


Fig.7. Schematics of (a) the Frank-Read source and (b) single-end source. (Schematics are from [34], reprinted with the permission from 2011 Elsevier Ltd.)

Strengthening mechanisms: [35, 37]

Classical methods for strengthening materials, especially metals, rely on strategies in preventing dislocation motion by introducing various defects. The most commonly used methods are summarized in Fig. 8 [37]: (1) solid solution hardening by introducing atomic vacancies and interstitials (point defects); (2) work hardening by enhancing dislocations interactions (line defects); (3) grain-boundary strengthening (Hall-Petch effect) by grain refinement (planar defects); (4) precipitate strengthening by introducing dispersed reinforcement particles (volume defects) of a different phase or material than the surrounding matrix.

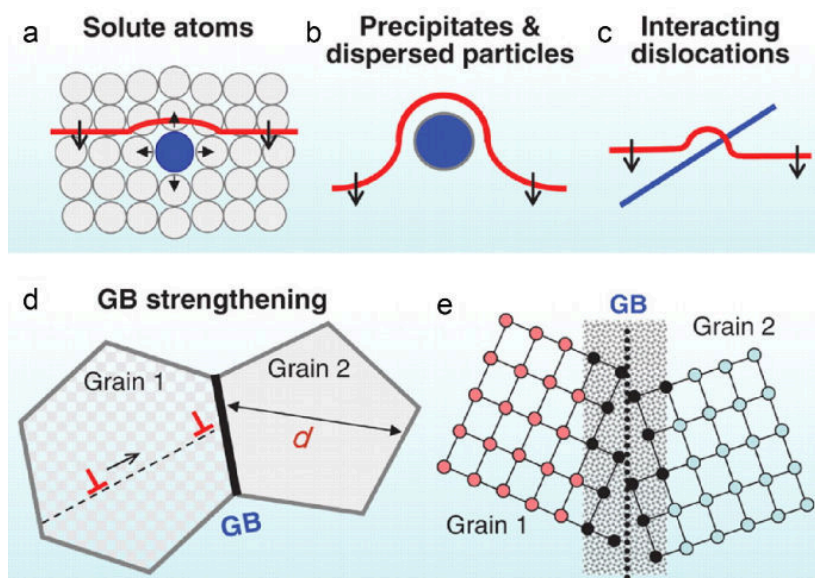


Fig. 8. Schematic illustrations of examples of structural modifications for strengthening metals and alloys: (a) solid solution hardening, (b) precipitate strengthening, (c) work hardening, (d) grain-boundary strengthening, and (e) structure of incoherent grain boundary (GB). (Schematics taken from [37]. Reprinted with permission from AAAS.)

1.3. Size effect in plasticity

In fact, ‘size effect’ is not new. As early as in the 1930s, it was reported that “*one of the commonest methods of increasing strength of a metal or alloy is to diminish its crystal size and increase its boundary area by suitable thermal and mechanical treatment*” (here crystal size refers to grain size) [38]. Gough, Hanson and Wright (1927) [39] studied the polycrystalline aluminum and concluded that “*it is clear, therefore, that the well-defined elastic limit found in the polycrystalline bar is not*

a property of the metal crystal, but the crystal aggregate in the case of aluminium.” Later, this grain-size dependence of strength was known as grain-boundary strengthening or the Hall-Petch effect [40, 41]. Rather than the size effect associated with microstructural constraints, those due to dimensional constraints have also been reported. The tensile strengths of dislocation-free whiskers in the size of a few microns approach their theoretical values [42], the strength of metallic thin films inversely scales with the film thickness [43] and the hardness of materials increases with decreasing indentation size [44].

With the development of emerging nanotechnology such as micro- or nano-electro-mechanical-systems (MEMS or NEMS) (Fig. 9), some new challenges are posed to the classical theory of plasticity. MEMS are usually made up of components between 1 to 100 micrometers and NEMS consist of parts in the size from a few nanometers to about 100 nanometers. At such small length scales, the components are always associated with large surface-to-volume ratios, limited numbers of defect sources, and short breeding distances of defect and so on, and the standard constructs of classical theory of plasticity may not be always useful.

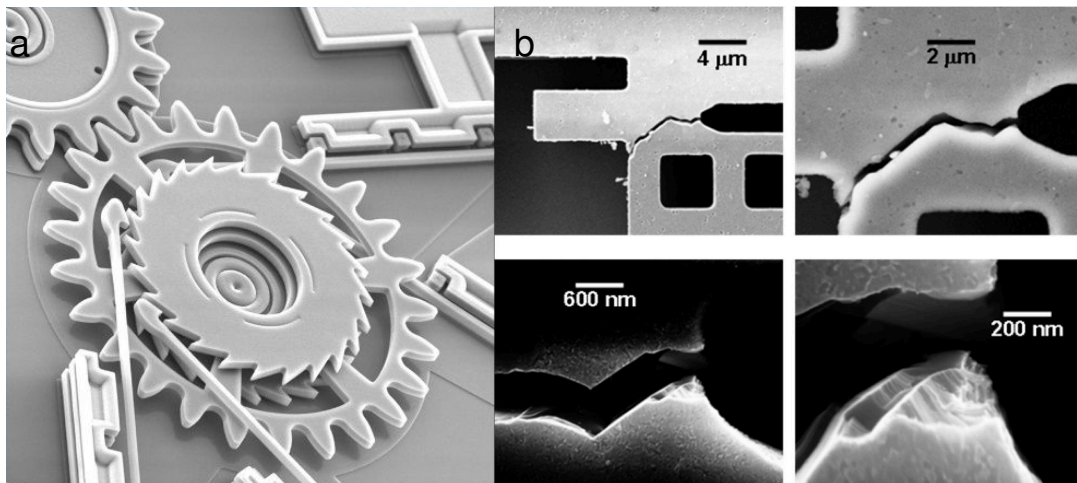


Fig. 9. (a) SEM image of a spider mite on a polysilicon MEMS gear-train (Sandia national laboratories, USA, image from [45], copyright ©Sandia Corporation). (b) SEM images of the failure of MEMS devices (images from [46]).

Till the end of last century, the study of deformation behavior of materials at the length scale between a few nanometers to a few micrometers was still scarce. Due to the development of emerging focused ion beam (FIB) system, lithography,

atomic force microscopy (AFM) and nanoindentation techniques, great advances have been made in understanding the plastic behavior at small scales in many materials since the last decade. So far, over a thousand related studies have been reported for a large variety of materials, including regular metals [47], ordered intermetallics [48], semiconductors [49], ceramics [50], metallic glasses [51] and even polymers [52].

It is now well accepted that the plasticity theory presents multiscale complexity [53], which extends from the atomistic size to the macroscopic scale of characteristic lengths, as illustrated in Fig. 10. At the atomistic scale, the interactions between individual atoms, atomic defects (vacancies or interstitials) or dislocation cores may govern the deformation; at the nanometer scale (<100 nm), the number of dislocations is usually very small, so that individual dislocation activity may play an essential role as well as a high surface-to-volume ratio; at sub-micrometer scales (~100 nm-1 μm), this length scale is usually in the mean dislocation spacing, $\rho^{-1/2}$, and the dislocation segment may play an important role in plasticity; at micrometer scales (~1 μm -100 μm), there would be a transition between small-scale plasticity to macroscopic plasticity. However, fundamental mechanisms of plasticity covering the whole length scales are still not fully understood. The deformation-mechanism and material-selection maps that were developed to describe conventional coarse-grain or single-crystal bulk materials are known to break down at these reduced length scales. Thus, the new maps of the size dependence of material properties should be created.

Up to date, the studies of the size effect on plasticity have been intensively focusing on two types of materials—pure metals and metallic glasses, which have been well reviewed [58-60]. Regular metals and metallic glasses present two extreme classes of materials in terms of chemical and structural complexity—the number of constituted elements, structure order and periodicity. There are still several intermediate states of materials between single-element regular metals and multi-element disordered metallic glasses, such as such as ionic crystals,

high-entropy alloys and quasicrystals, as illustrated (Fig. 11). One may ask what the plastic behavior of such materials at small scales looks like and whether there is a general scaling law controlling the size effect for all the inorganic solids. This is the main motivation of this thesis.

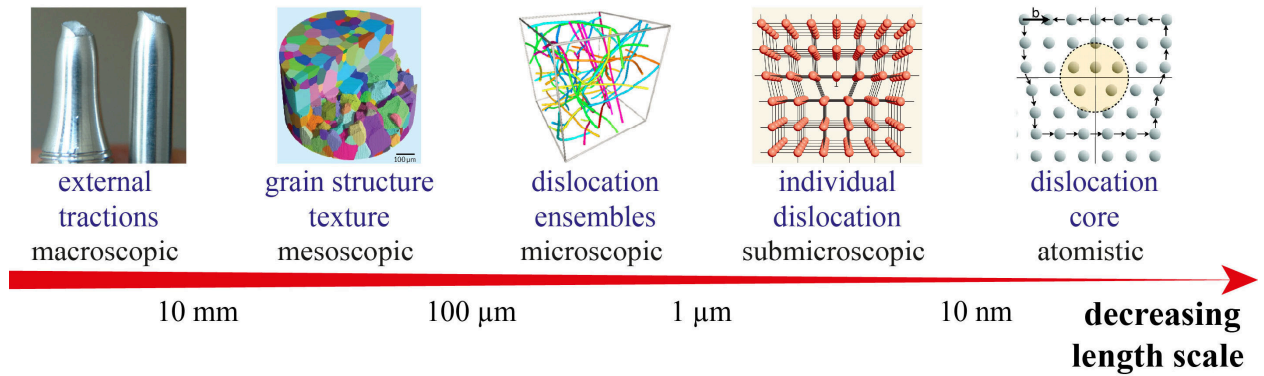


Fig. 10. Length scales associated with structure defects and dislocation systems from nanometer scale to macroscopic scale (the concept is adapted from Zaiser and Seeger [53], and the schematic illustrations are from [54], [32], [55], [56] and [57].)

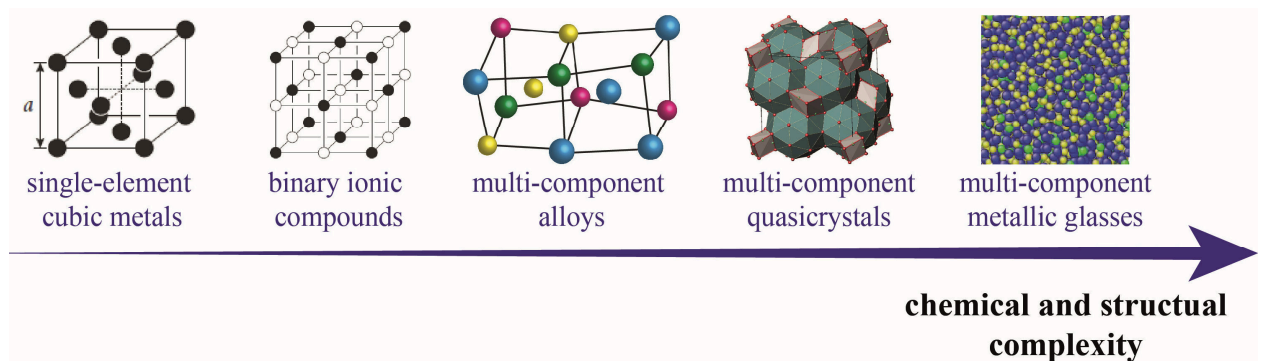


Fig. 11. The increasing chemical and structure complexity from single-element fcc metals to multi-component metallic glasses, a couple of intermediate states such as ionic compounds, high-entropy alloys and quasicrystals. The periodicity and structural order of materials decreases from left to right (the schematic illustrations taken from [34], [61] and [62]).

1.4. Experimental methods: focused ion beam and micro-compression techniques

In the last decade, there has been a significant advance in applying FIB technique and micro-compression methodology to study mechanical behaviors of materials at small scales, usually between several microns down to 100 nanometers, as illustrated in Fig. 12. In 2004, Uchic and his co-workers [48] first reported the

plastic behavior of micrometer-scale cylinder metal pillars under uniaxial compression. The micro-pillars were produced by FIB milling and the compression was employed in a nanoindentation system with a flat-punch tip. Since the initial report, over a thousand related studies have been reported, covering a broad range of materials. It is widely found that the strengths of metals usually inversely scale with sample dimensions, exhibiting a “smaller is stronger” phenomenon and the yield strength can attain a significant fraction of the material’s theoretical strength.

The majority (over 90%) of reported micro-compression samples are fabricated using FIB milling, because it allows a precise control over the location and size of the samples and also there are almost no restrictions of material type. However, a few well-known issues are found to be associated with the FIB-prepared samples. The biggest concern is about FIB-induced irradiation damage. In most commercially available systems, Ga ions are employed. The bombardment and collision of the Ga ions with the sample atoms can remove or mill off the sample materials, but also implant Ga ions and cause damage within the interacted volume [63]. Quantitative analysis of FIB effects on materials is very complicated and depends on a large number of parameters, such as angle of incident beam, ion energy, material type, crystal orientation and so on [58, 63]. Systematic investigation of FIB damage is still lacking. But it is well known that ion beam can induce amorphization in semiconductors such as Si, Ge, GaAs and C, generally in the thickness range of a few nanometers [63]. Point defects and dislocation loops can also be created in metals during FIB processing. Some comparisons have been made in FIB-prepared and non-FIB-prepared Au [65, 66] and LiF [67], they show that irradiation damage layers (~3-4 nm) do not have remarkable effect on their mechanical properties, although some materials such as Cu and Al are prone to Ga ion damage [58].

The second issue is associated with the sample shape. The micro-pillars fabricated using the annular milling method always show some degree of taper—the diameter

of the top part is smaller than that of the bottom part, generally $\sim 2\text{-}5^\circ$, which may result in stress concentration at the pillar top and, consequently, inhomogeneous deformation [58]. Another FIB milling method called “lathe milling” as introduced by Uchic and his co-workers [48] provides an opportunity to avoid taper, but it requires significantly longer time and more effort in pillar preparation and, consequently, leads to more ion irradiation damage [68].

Nevertheless, the FIB technique has so far been the most important and widely used technique to prepare micro-compression samples. The artificial effects mentioned above can be significantly reduced by a careful use of FIB, such as selecting proper materials and refining the milling procedures. The micro-compression samples studied in this thesis were prepared by annular FIB milling where a few milling steps with the fine milling current and voltage were used.

The micro-compression experiment mimics the macroscopic compression for bulk samples. The main difference is that the fabricated sample is not free-standing but attached to the bulk substrate. There are also a few technical issues associated with the micro-compression experiment. First, the elastic deflection of the substrate may influence the obtained modulus values. Second, the misalignment between the flat-punch tip and the top of the pillar may lead to stress concentration, pillar bending or pillar buckling [58]. In order to avoid buckling, the aspect ratio of the sample is suggested to be about 1: 2.5. Third, the friction between the flat-punch tip and pillar top may affect the stress state within the sample. Fourth, the testing modes—load control or displacement control, and even the testing system can result in some differences in the results, especially for displacement burst behavior [58].

In order to minimize the above influences in the micro-compression tests carried out in this thesis, the indenter system was well calibrated, and the sample shape and the flat-punch tip were checked prior to the experiments. Furthermore, a number of pillars were used to repeat the experiment under the same conditions, and compressed pillars were re-checked in the electron microscope.

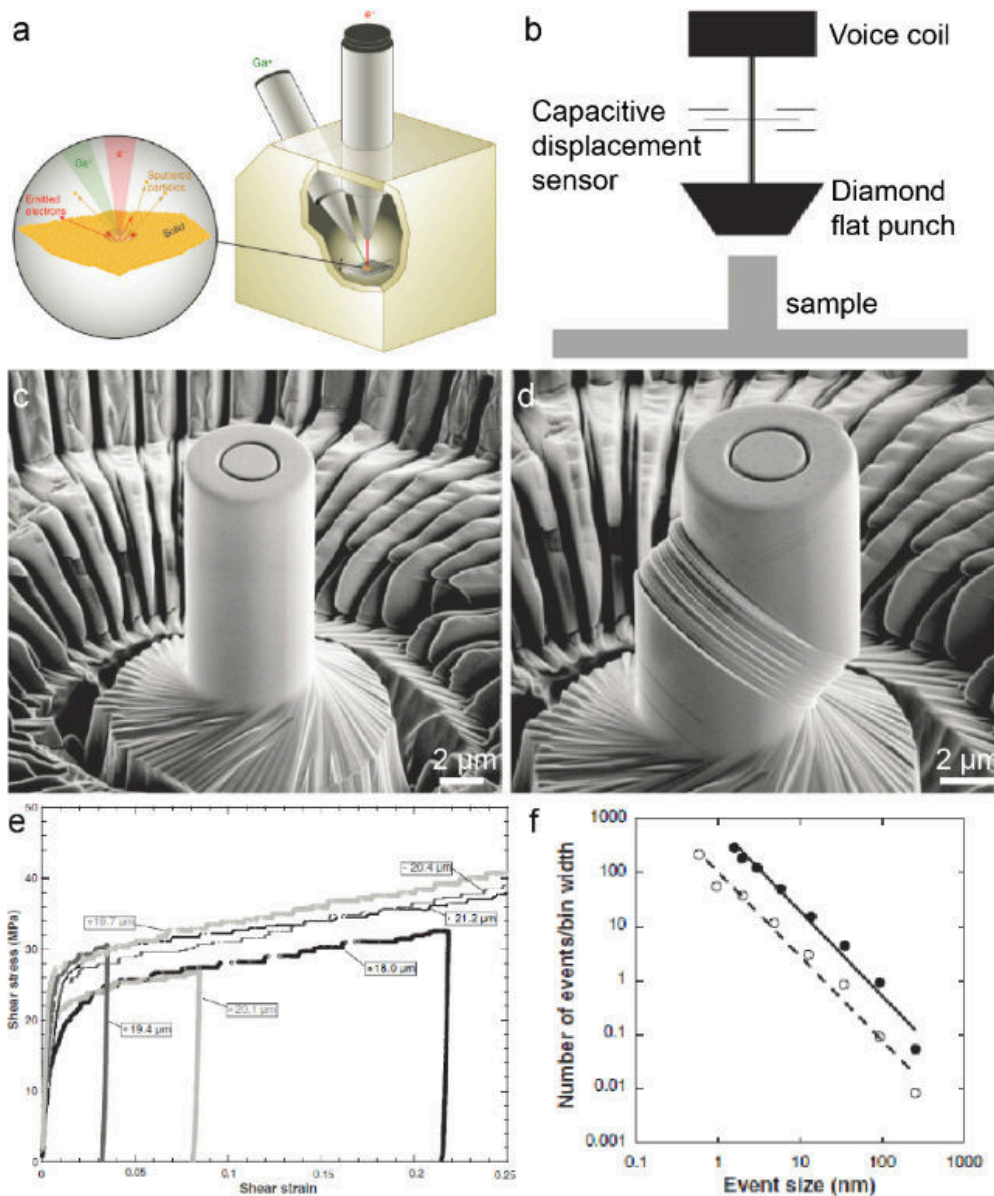


Fig. 12. (a) Schematic illustration of a dual-beam FIB–SEM instrument. Expanded view shows the electron and ion beam sample interaction [63]. (Reprinted with permission from MRS) (b) Schematic of micro-compression experimental setup [58]. SEM images of a 5- μm -diameter microcrystal sample of pure Ni oriented for single slip (c) before compression and (d) after compression [47]. (b-d reprinted with permission from © 2009, Annual Reviews) (e) Displacement burst during compression and (f) scale-free burst phenomenon [64]. Reprinted with permission from AAAS).

1.5. Micro-compression: metals and metallic glasses

Metals

A vast majority of reported size-dependent plasticity is focused on pure metals: face centered cubic (fcc) Ni [69], Au [65], Cu [70] and Al [71], body centered

cubic (bcc) Nb, Ta, Mo, W [72-74] and V [75], and hexagonal closest packed (hcp) Ti [76] and Mg [77]. Most of these results reveal a strong size dependence of yield strength or flow stress when the sample dimension is in submicron- and micrometer scales. Dou and Derby [78] quantified the micro-compression data of single crystalline pillars using a power-law fit:

$$\frac{\sigma}{G} = A \left(\frac{D}{b} \right)^{-m} \quad (12)$$

where σ is yield strength or flow stress, G is shear modulus of corresponding slip system, A constant, D the pillar diameter, b the Burgers vector and m named size-effect exponent. Interestingly, the measured values of m for fcc metals all fall in the range between ~ 0.6 to 0.7 . This exponent is nearly identical to all FIB-milled fcc pillar compression studies (Fig. 13a). However, later investigations reveal that bcc metal pillars (Nb, Mo, Ta, W [72-74] and V [75]) have a large range of size effect exponents ($m \sim 0.2$ to 0.9) (Fig. 13b), while hcp metal pillars exhibit an exponent depending on slip systems: $m \approx 0.4$ for prismatic slip and $m \approx 0.6$ for basal slip [60].

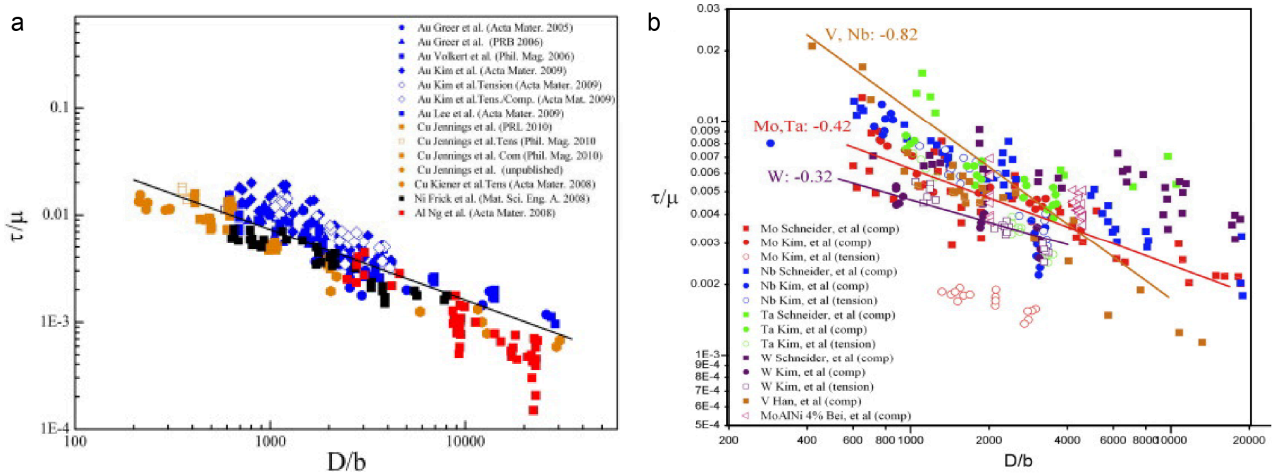


Fig. 13. (a) Resolved shear flow stress normalized by shear modulus on appropriate slip system for fcc metallic micro- and nano-pillars tested in compression and tension. (b) Resolved shear flow stress normalized by shear modulus on $\{110\}/\langle 111 \rangle$ slip system vs. diameter normalized by the Burgers vector for all five tested bcc metals [60] (reprinted with the permission from 2011 Elsevier Ltd.).

One may ask what mechanism controls the size dependence of strength in these materials. So far two prominent mechanisms have been proposed to explain these

size-related phenomena: single-arm source (SAS) or source-dominated model developed by Rao *et al.* [69, 79] and dislocation starvation theory proposed by Greer and Nix [65, 66]. In the former, dislocations are created by the operation of “partial Frank-Read sources” or single-end source, a random distribution of dislocation sources either initially present in the pillars or generated by the interactions of initially present dislocations. In the latter, the dislocation starvation model is followed by surface nucleation theory, the surface nucleation of dislocations starts all the pre-existing mobile dislocations that have annihilated at the free pillar surface. Rather than high strengths observed in metal pillar samples, intermittent flow in crystal plasticity showing discrete slip events, an earthquake-like (shock-and-aftershock) behavior, as shown in Fig. 12e, is commonly found for micro- and nano-sized pillars and the events reveals power-law scaling between the number of events and their magnitude [64] (Fig. 12f).

Metallic glasses

In addition to the micro-compression of metals, the study on small-scale plasticity of metallic glasses has attracted great attention. Metallic glass is a class of metallic system showing disordered atomic structure. Hence, metallic glasses do not process dislocation which is presented in regular metals. Nevertheless, plastic deformation in metallic glasses can be carried by the formation and propagation of a shear band, an extremely thin (~10 nm) sheet-like volume. The micro-compression results demonstrate that there is no obvious, if any, size dependence of strength for metallic glasses (Fig. 14). The yield strength of the Cu- and Zr-based ones are both around 1.8 GPa. However, similar to metal pillars, the metallic glass pillars also exhibit displacement-burst behavior, which is believed to be associated with initiation and propagation of shear bands. It is also interesting to note that a graduate transition from highly inhomogeneous deformation to homogeneous deformation was observed by decreasing the sample size to ~100 nm or decreasing the strain rate [51, 80].

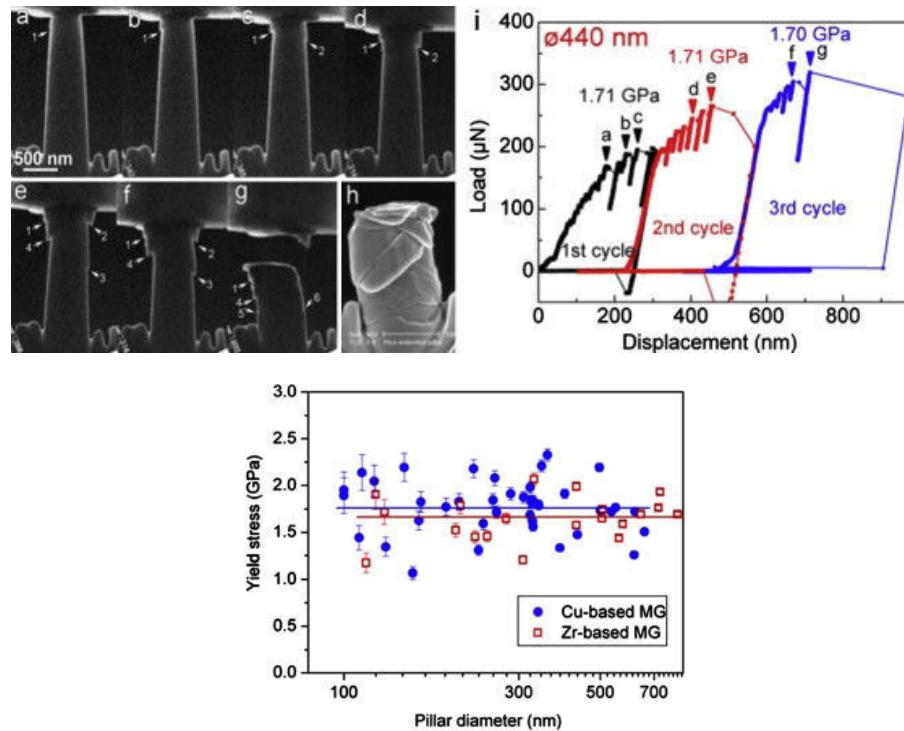


Fig. 14. (a–g) Video frames recording the deformation of a 440-nm Cu-based metallic glass pillar compressed under displacement control and subjected to three loading–unloading cycles. (h) Post-mortem SEM micrograph of the deformed pillar. (i) The yield stresses measured in each loading cycle are also indicated. (g) Yield stress versus pillar diameter for both metallic glasses with trend lines [81] (Reprinted with the permission from 2011 Elsevier Ltd.).

1.6. Macroscopic plasticity in ionic crystals, high-entropy alloys and quasicrystals

Ionic crystals

Ionic crystals consist of positive and negative ions, i.e. cations and anions, which are bonded ionically by electrostatic attraction. The simplest form is rock salt (NaCl) structure, as shown in Fig. 15a, such as NaCl, KCl, LiF, and MgO. In the NaCl structure, each anion is surrounded by six cations and *vice versa*. It has a face-centered cubic Bravais lattice with an anion-cation pair for each lattice point, one ion at 0, 0, 0 and the other at $\frac{1}{2}$, 0, 0. Ever since research on crystalline plasticity began in the 1930s, ionic crystals have been used as a testing ground for new ideas and experimental methods [82]. The very simple and fundamental

studies on ionic crystals have led to great insights in the whole dislocation theory of plasticity.

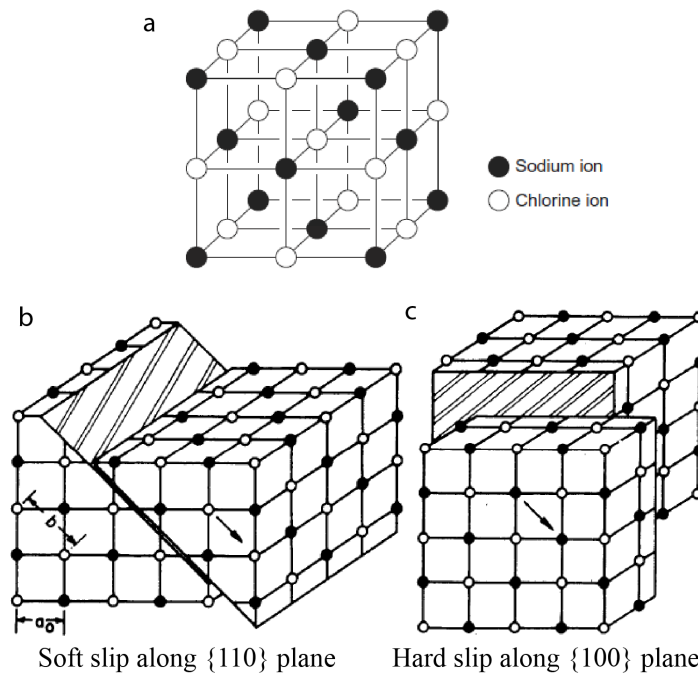


Fig. 15. (a) Sodium chloride structure which consists of two interpenetrating face-centred cubic lattices of the two types of atom, with the corner of one located at the point $1/2, 0, 0$ of the other (image from [34]. (Reprinted with the permission from 2011 Elsevier Ltd.) (b) The primary slip planes $\{110\}$ and (c) the secondary slip planes $\{100\}$ (images from [82]. Reprinted with the permission from W. S. Maney & Son Ltd).

In the NaCl structure, the shortest lattice vector is $\frac{1}{2}\langle 110 \rangle$ (close-packed direction), and this is the Burgers vector of the dislocations responsible for slip. The principal slip planes are $\{110\}$ (Fig. 15b). Slip steps are also observed on $\{100\}$ (Fig. 15c) and (occasionally) on $\{111\}$ and $\{112\}$ planes after high stresses [34]. The latter cases are observed in particular at high temperatures and in crystals of high polarizability when the ionic nature of the bonding decreases. The reason underlying the choice of $\{110\}$ as the principal slip plane rather than $\{111\}$ (the most densely packed slip plane) is unclear. It has long been considered that the glide system is determined by the strengths of the electrostatic interactions within the dislocation core [34]. The plasticity of ionic crystals is temperature dependent and anisotropic. Critical resolved shear stress (CRSS) on for $\{110\}$ and $\{100\}$ slip planes of alkali halides typically depend on temperature, with the

critical temperature of about 80 K and 250-300 K, respectively [82]. For alkali halides, the deformation on the $\{110\}$ planes has lower CRSS than that on the $\{001\}$ planes at the same temperature, because the electrostatic interaction is expected to dominate the Peierls potential, which is correlated to the critical shear stress [82].

Dislocations in ionic crystals can carry charges. Charged dislocations can either interact with an electric field and influence plasticity or they can cause an electric current upon plastic deformation. These two phenomena are called electroplasticity and plasto-electricity, respectively [83, 84]. The simplest type of charged defect is a vacancy, which represents a missing ion. Cation vacancies are charged negatively, while anion vacancies are charged positively. Interaction with these vacancies can make a dislocation charged as well. The related phenomenon was first discovered by Stepanov [85], who observed that deformation produced potential difference for NaCl in 1933, and later explained using the concepts of charged dislocations by Fischbach and Nowick in 1955 [86, 87]. Fig. 16 shows a jog in a dislocation consisting of a step one atomic row higher perpendicular to the glide plane [34]. Here, it shows a negative jog, which has a charge of $-q$. Charged defects on a dislocation core can be classified as jogs, kinks or bound point defects.

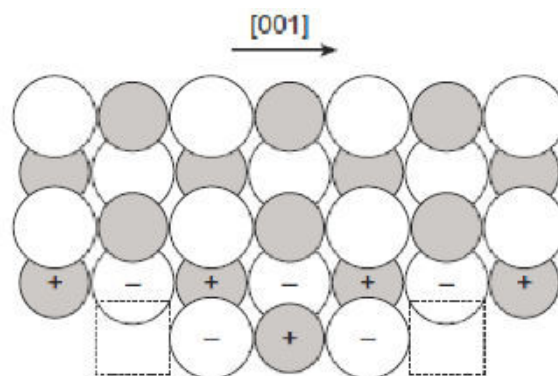


Fig. 16. Extra half-planes of the edge dislocation with a jog at each end denoted by the squares (schematic is from [34], Reprinted with the permission from 2011 Elsevier Ltd.).

Ever since the 1950s, many sophisticated experiments and theories have been developed on this topic. Machlin (1959) [88] found that a field of 2 MVm^{-1} considerably reduced the flow stress and increased the ductility of NaCl deformed in bending. So far, it has been well known that in ionic crystals applied electric fields could reducing the strength and increasing ductility. For example, Figs. 17a and b show that applying an electric field can obviously reduce the flow stresses for both “pure” and Ca^{2+} doped KCl [89].

Whenever a crystal is deformed plastically, the motion of charged dislocations can produce some redistribution of charge within the sample. The motion of charges may be detected as an electrical signal on suitably placed electrodes. In order to develop the plasto-electric effect some non-uniform deformation is usually involved, This effect is called plasto-electricity, which was first discovered in 1933 [85] and intensively studied from the 1950s to 1970s. The most used experimental setup to detect electric signal is bending tests. Kataoka and Li [90, 91] measured the potential difference developed between the side surfaces while a Ca^{2+} -doped KCl single crystal specimen was being compressed between tilted plates [90, 91], as shown in Figs. 17c and d. The dislocation charge was found to be negative, and its magnitude increased with Ca^{2+} concentration as well as with temperature.

For the small-scale plasticity in ionic crystals, the following questions are to be answered:

- Is there a universal size-effect exponent for the ionic crystals deformed on the same slip systems?
- What is the influence of crystal orientation, testing temperature, pre-straining and doping levels in the size dependence?
- How does an electric field influence the plastic behavior of pure and doped ionic crystals and can any current be generated during micro-compression?

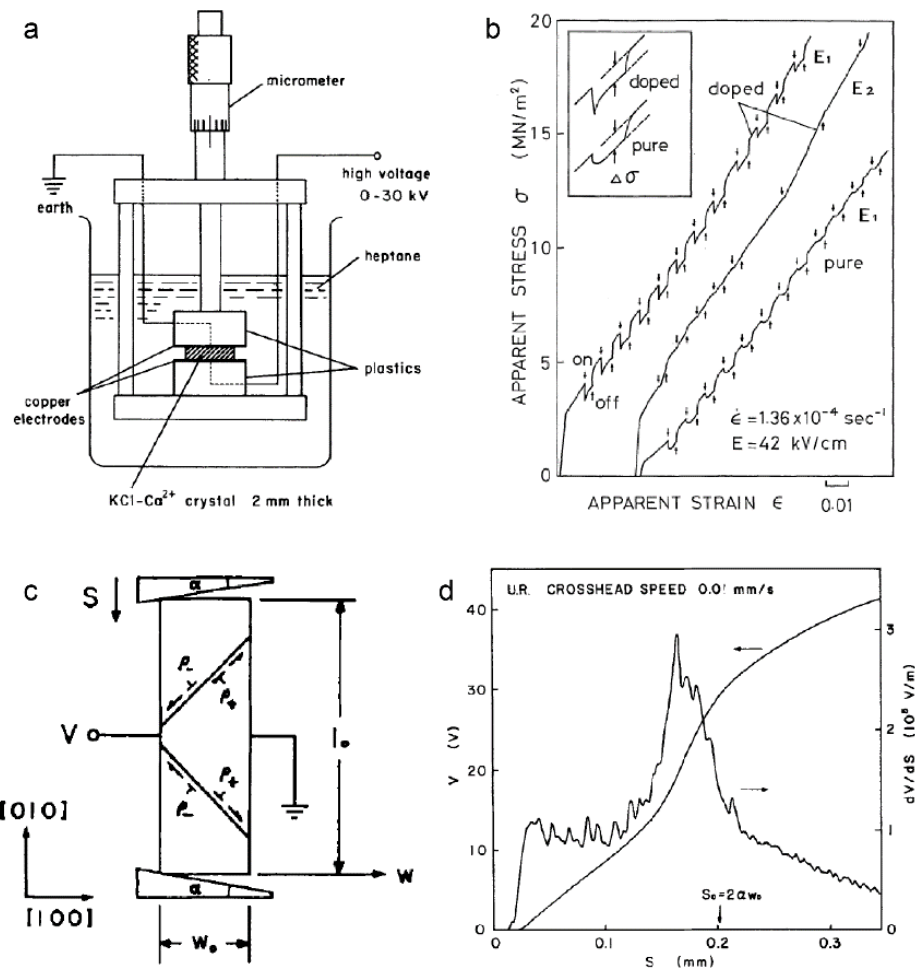


Fig. 17. (a) The schematic of experiment for KCl compression under high voltage [90]. (b) Typical stress-strain curves for the “pure” and the “doped” crystals. Arrows show the application and the cut off of the electric field [89]. (c) A rectangular specimen compressed between two plates tilted through angles $\pm\alpha$. The potential difference across the two side surfaces is V and (d) the relative displacement of the top and bottom plates is S , the variation of voltage and load with displacement of time during compression at a crosshead speed of 0.01 mms^{-1} [90, 91] (Images reprinted with permissions from The Japan Society of Applied Physics and Taylor & Francis Group).

High-entropy alloys

High-entropy alloys (HEAs) are evolving multi-component intermetallic systems, wherein multiple principal elements tend to form single solid-solution-like phases with a strong tendency to solid solution strengthening, as illustrated in Fig. 18a. The concept of HEAs, introduced by Yeh *et al.* in 2004 [92], is loosely defined as solid-solution alloys that made of five or more metallic elements with equimolar or near-equimolar ratios. Conventional alloys generally have one or two principal components and their composition are mostly restricted to the

corners and edges of a multi-component phase diagram. In HEAs, it is difficult to distinguish which component is the principal one, i.e. solvent, and their composition is at the center of the phase diagrams. In such HEAs, their configurational entropy, S_{mix} , increases with the number of elements n , as $\Delta S_{mix} = R \ln(n)$, with R the universal gas constant. Consequently, the larger number of elements, the higher entropy. According to Gibbs law, $\Delta G_{mix} = \Delta H_{mix} - T\Delta S_{mix}$, the high levels of entropy may stabilize solid-solution phases at elevated temperatures and prevents the formation of possible intermetallics in these compositions [92-94]. Another manifested character of HEAs is their severely distorted lattice. Because the atomic size and modulus for each constituted elements can be very different, the lattice of HEAs can be highly distorted, as confirmed by X-ray diffraction [95] and leading enormous solid-solution strengthening effect. HEAs may have interesting applications due to their simple average structures (fcc, bcc and hcp), their distorted lattice and low diffusion rate in a multi-component system. The main potential applications of HEAs are in the development of high-strength and high-temperature sustaining alloys, wear-resistant materials and diffusion barriers. The conventional HEAs based on Al, Co, Cr, Cu, Fe and Ni have reached the strengths and workability comparable to those of steels. In order to achieve higher strengths in the high-temperature regime above 1100°C, the use of refractory metals in HEAs was implemented by Senkov *et al.* [96, 97], showing even better high-temperature strength than conventional Ni based superalloys (Fig. 18b). However, their low room-temperature ductility might be a limitation for further processing steps (Fig. 18c) [97].

For the small-scale plasticity in HEAs, the following questions are to be answered:

- What mechanisms control the size dependence of strength in the NbTaMoW HEA and pure bcc metals?

- Why is bulk NbTaMoW HEA so brittle and what is the role of the grain boundaries?
- What are the strength, ductility and thermal stability of nanocrystalline HEAs?

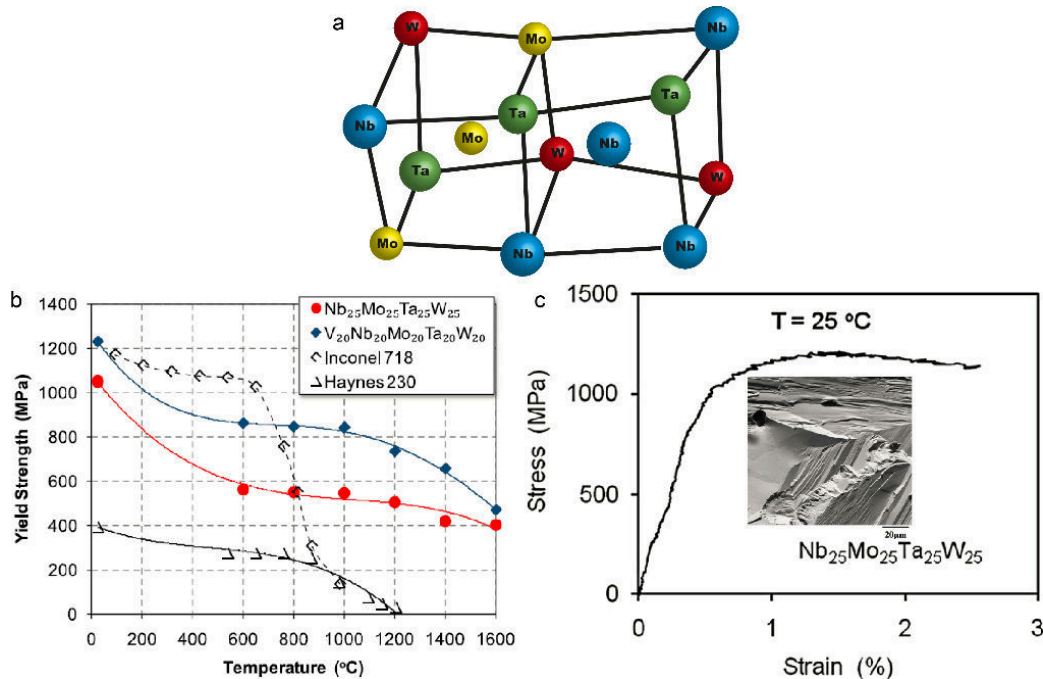


Fig. 18. (a) Ideal lattice structure for an NbTaMoW HEA, (b) The temperature dependence of the yield stress of Nb₂₅Mo₂₅Ta₂₅W₂₅ and V₂₀Nb₂₀Mo₂₀Ta₂₀W₂₀ HEAs and two superalloys, Inconel 718 and Haynes 230. (c) Compressive engineering stress-strain curve for the Nb₂₅Mo₂₅Ta₂₅W₂₅ alloy. The insert SEM image shows the fracture surface [97] (Reprinted with the permission from 2011 Elsevier Ltd.).

Quasicrystals

Quasiperiodic crystals, or quasicrystals (QCs), are a class of materials that exhibit long-range order in atomic arrangement yet lack translational symmetry, in addition to crystalline and amorphous states of solids [98-100]. The first experimental observation of QCs by Shechtman in the 1980s [98] demonstrated that a rapidly quenched Al-Mn alloy showed a five-fold symmetry, which was significantly forbidden according to the classical theorems of crystallography: two-, three-, four- and six-fold symmetries are allowed, but five-, seven- and all higher rotations are impossible. Owing to their special atomic arrangement, quasicrystals possess many unusual and useful properties, such as low thermal

and electronic transport [101], mechanical reinforcement particles [102], light absorption [103], hydrogen storage [104], very low surface energies, and corrosion- and oxidation, wear-resistance with low friction coefficients [105]. For the last three decades, hundreds of new quasicrystals have been synthesized in the laboratory [106], predicted by simulations [107] and even have been reported to be discovered in nature [108]. However, despite their interesting structures and useful properties, only few quasicrystals have been converted into practical products. A well-known drawback that hinders their applications is that they are extremely brittle: plastic deformation is only possible at high temperatures (above $\sim 75\%$ of their melting temperatures, T_m) [109, 110] or under confining hydrostatic pressures (indentation [111] or gas/solid hydrostatic pressures [112]). Deformation at low and intermediate temperatures generally result in a catastrophic failure [113], rendering them very difficult to further process and often unsuitable for usage.

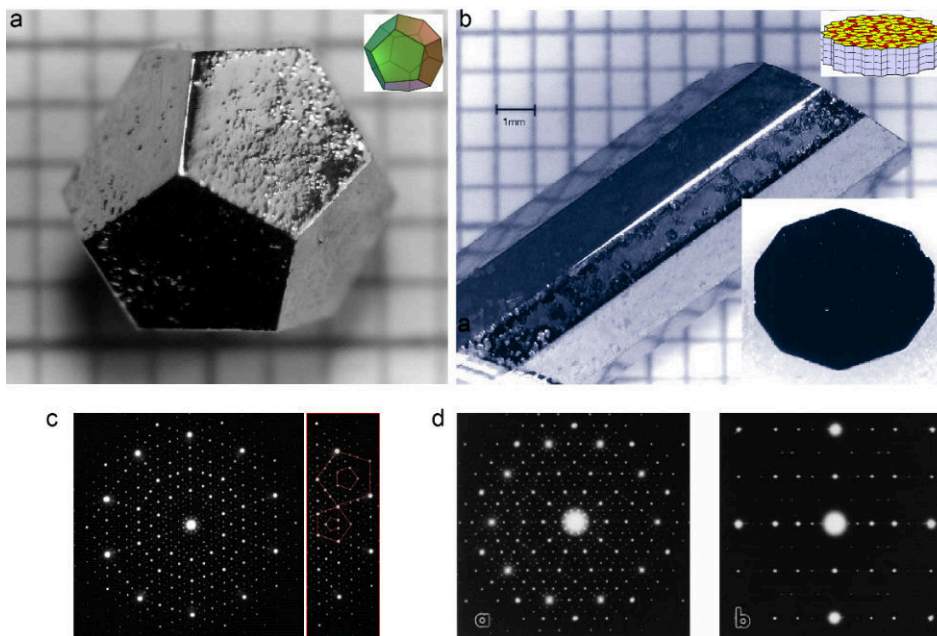


Fig. 19. (a) Photograph of a single-grain icosahedral Ho-Mg-Zn quasicrystal grown from the ternary melt and formed as a pentagonal dodecahedron [116]. (b) Photograph of a decagonal Al-Ni-Co quasicrystal grown from the ternary melt [117]. (c) Electron diffraction pattern from a typical icosahedral quasicrystal along tenfold axis. Note the presence of perfect pentagons highlighted in the diagram to the right. The linear scale between pentagons is τ , and the scale between a pentagon inscribed in another pentagon is τ^2 . [118] (d) Diffraction patterns of a typical decagonal quasicrystal, along ten-fold axis and two fold axis [119] (images reprinted with the permission from ©1999 The American Physical Society and ©1999 Taylor & Francis Ltd.).

Two well-known types of QCs are icosahedral QCs (IQCs) and decagonal QCs (DQCs), as shown in Fig. 19. Icosahedral QCs are quasiperiodic in three dimensions (e.g. i-Al-Pd-Mn [114]) and decagonal quasicrystals consist of quasiperiodic atomic planes with tenfold symmetry but stacked in a periodic order (e.g. d-Al-Ni-Co [115]). The distinct atomic arrangements along tenfold axis (periodic) and twofold axis (aperiodic) in decagonal quasicrystals.

Similar to regular crystals, quasicrystals can also be deformed via dislocation activities, but their dislocations include specific components—phasons [120, 121], in addition to phonons, the components in the dislocation of regular crystals. The phasons are introduced by the violations of the matching rules due to the missing periodicity in quasicrystals. As shown in Fig. 20, if a part of quasicrystal is shifted with respect to the rest, because of missing periodicity, a three-dimensional displacement vector cannot lead to a perfect match without lattice distortion. The motion of their dislocations have to overcome this mismatch by the rearrangement of phasons, called phason flip [122]. As a consequence, the Burgers vector, B , of the dislocation for quasicrystals contains both phonon components, b_{\perp} , and phason components, b_{\parallel} , as: $B = b_{\perp} + b_{\parallel}$. In IQCs, their Burgers vector has six components, and in DQCs, their Burgers vector has five components. Because of their brittleness, their plastic deformation at low and intermediate temperatures is rarely studied and the underlying mechanism is still poorly understood.

For the small-scale plasticity in QCs, the following questions are to be answered:

- Is there any brittle-to-ductile transition in QCs at room temperature? If so, what is the critical size?
- What is the plastic anisotropy of DQC Al-Ni-Co at small scales and room temperature?
- What is the plastic behavior of QCs in the temperature range of 25-500°C, which is an unknown regime for QC plasticity?

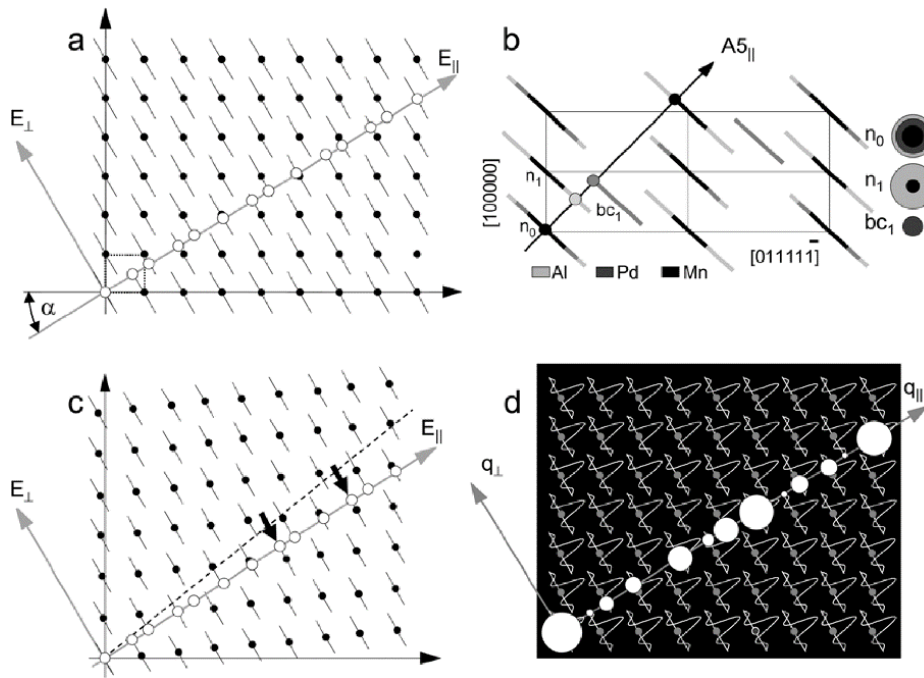


Fig. 20. (a) Construction of an ideal one-dimensional quasicrystals QC by the intersection procedure, and (b) hyperlattice unit cell employed in the structure model of icosahedral Al–Pd–Mn. (c) Construction of a 1-dimensional quasicrystals QC in the presence of linear phason strain and construction of the diffraction pattern (d) corresponding to the ideal quasicrystals QC in (a) [121] (images reprinted with permission from © 2012, Royal Society of Chemistry).

1.7. Aim and scope of the thesis

This thesis focuses on the plastic deformation properties of three types of materials: ionic crystals, high-entropy alloys and quasicrystals at the micron- and sub-micron scales. So far, these materials have rarely, or never, been studied for their plasticity at such small length scales. The general aim of this thesis is to unveil, or attempt to find, a general scaling law of plasticity for all inorganic solids and ultimately to create material-property maps for the materials selection in small-scale device design.

Here, I seek to answer the following fundamental questions throughout the thesis:

- What size (intrinsic and extrinsic) and internal structure lead to the strongest materials?
- What mechanism governs the size dependence of strength in all the micro- and nano-pillars tested to date?

This entire thesis is organized in five chapters. Except for Chapter 1 (Introduction) and Chapter 5 (Discussion, Conclusion and Outlook), each chapter is focused on one type of material and consists of three first-author publications or manuscripts to be submitted. My thesis starts with ionic crystals which contribute significantly to the classical theory of plasticity (Chapter 2), followed by a class of novel multi-component alloys—high-entropy alloys (Chapter 3), and finally studies on the complex ordered yet aperiodic intermetallics—quasicrystals (Chapter 4).

Chapter 1 introduces the general concepts and brief history of plasticity, reviews experimental methods, surveys the literature on the plasticity of different types of materials, and finally states the scope and aims of the whole thesis. The theory and data presented here are based on textbooks and selected literature to give a general review and background of this thesis.

Chapter 2 focuses on the size-dependent plasticity of several typical ionic crystals (NaCl, KCl, LiF and MgO):

- The size-effect exponents for the four ionic crystals deformed on the soft slip systems $\langle 110 \rangle \{1\bar{1}0\}$ are compared (published in *Philosophical Magazine Letters* 2013).
- Two ionic crystals, KCl and LiF, are chosen for studying the influence of crystal orientation, testing temperature, pre-straining and doping levels in the size effect (published in *Philosophical Magazine* 2015).
- This section presents some results on the coupling between a mechanical load and an electric field on the plastic behavior of doped NaCl (*manuscript in preparation*).

Chapter 3 is concentrated on both sample (extrinsic) and microstructural (intrinsic) size effects on the mechanical properties of an NbTaMoW high-entropy alloy as well as its fracture behavior and thermal stability:

- This section investigates what mechanisms control the size dependence of strength in a single crystalline NbTaMoW HEA micro-pillars (published in *Acta Materialia* 2014).
- The second section compares the fracture properties of a single crystalline HEA and a bi-crystal one (manuscript to be submitted *Scripta Materialia*).
- This section reports a novel ultra-strong, ductile and high temperature stable nanocrystalline HEA film prepared using magnetron co-sputtering (published in *Nature Communications*, 2015).

Chapter 4 is dedicated to exploring room- and intermediate-temperature plasticity of quasicrystals by utilizing a scaling effect:

- This section reports a size-induced brittle-to-ductile transition in an icosahedral Al-Pd-Mn quasicrystal at room temperature (submitted to *Nature Communications*).
- This second section studies the plastic anisotropy of a decagonal Al-Ni-Co quasicrystal at small scales and room temperature (submitted to *Extreme Mechanics Letters*).
- In the last section, *in situ* high-temperature compression is employed to study the decagonal Al-Ni-Co micro-pillars at elevated temperatures (25-500°C) (submitted to *Acta Materialia*).

Chapter 5 makes further discussions on the strength and size-effect exponent for the materials studied in this thesis and tested to date, concludes the main contributions of the thesis work and suggests open questions interesting for future studies.

References

- [1] McQueen H. Successful transition from wrought iron to steel in hot work processing with mechanism differences. *Materials Science Forum*, vol. 638: Trans Tech Publ, 2010. p.3380.
- [2] Foecke T. *Mater Today* 2008;11:48.
- [3] <https://www.google.com/culturalinstitute/asset-viewer/travaux-de-la-tour-eiffel-premier-%C3%A9tage-de-la-tour-en-arri%C3%A8re-plan-le-trocad%C3%A9ro-janvier-1888/3gEdXyFaqQyg5A>. 2015, 1988. (25.10.2015)
- [4] Broad WJ. In *Weak Rivets, a Possible Key to Titanic's Doom*, http://www.nytimes.com/slideshow/2008/04/14/science/041308Titanic_index-9.html. 2015: The New York Times Company, 2008. (25.10.2015)
- [5] Photos E. *World Archaeology* 1989;20:403.
- [6] Edyvean RG, Hammond C. *Historical metallurgy* 1997;31:54.
- [7] Mügge O. *Neues Fahr. F. Miner* 1898;7:71.
- [8] Ewing JA, Rosenhain W. *Proceedings of the Royal Society of London* 1899;65:85.
- [9] Ewing J, Rosenhain W. *Philosophical Transactions of the Royal Society of London. Series A, Containing Papers of a Mathematical or Physical Character* 1900:353.
- [10] Friedrich W, Knipping P, Laue M. *Annalen der Physik* 1913;346:971.
- [11] Schmid E. *Proc. internat. Congr. appl. mech. Delft* 1924:342.
- [12] http://www.doitpoms.ac.uk/tlplib/miller_indices/uses.php?printable=1. (25.10.2015)
- [13] Orowan E. The crystal plasticity. III: about the mechanism of the sliding. *Phys*, 1934.
- [14] Polanyi M. *Z. Phys* 1934;89:660.
- [15] Taylor GI. *Proceedings of the Royal Society of London. Series A, Containing Papers of a Mathematical and Physical Character* 1934:362.
- [16] Gilman JJ, Johnston WG, Sears GW. *J Appl Phys* 1958;29:747.
- [17] Menter J. The direct study by electron microscopy of crystal lattices and their imperfections. *Proceedings of the Royal Society of London A: Mathematical, Physical and Engineering Sciences*, vol. 236: The Royal Society, 1956. p.119.
- [18] Hirsch PB, Horne RW, Whelan MJ. *Philos Mag* 1956;1:677.
- [19] Mott N. *The London, Edinburgh, and Dublin Philosophical Magazine and Journal of Science* 1952;43:1151.
- [20] Cottrell AH. *Dislocations and plastic flow in crystals*: Clarendon Press, 1965.
- [21] Read WT. *Dislocations in crystals*: McGraw-Hill, 1953.
- [22] Messerschmidt U. *Dislocation Dynamics During Plastic Deformation.*, Springer Series in Materials Science, Volume 129. ISBN 978-3-642-03176-2. Springer-Verlag Berlin Heidelberg, 2010 2010;1.
- [23] Hirth JP, Lothe J. *Theory of dislocations*, 1982.
- [24] Christian JW, Mahajan S. *Progress in materials science* 1995;39:1.
- [25] Raj R, Ashby M. *MT* 1971;2:1113.
- [26] Lawn BR. *Fracture of brittle solids*: Cambridge university press, 1993.

- [27] Greer AL, Cheng YQ, Ma E. *Materials Science and Engineering: R: Reports* 2013;74:71.
- [28] Christian JW. *The theory of transformations in metals and alloys*: Newnes, 2002.
- [29] Herring C. *J Appl Phys* 1950;21:437.
- [30] Ashby MF. *Acta Metallurgica* 1972;20:887.
- [31] Ashby MF, Cebon D. *Le Journal de Physique IV* 1993;3:C7.
- [32] McNally PJ. *Nature* 2013;496:37.
- [33] Verrall RA, Fields RJ, Ashby MF. *J Am Ceram Soc* 1977;60:211.
- [34] Hull D, Bacon DJ. *Introduction to dislocations*: Elsevier, 2011.
- [35] Courtney TH. *Mechanical behavior of materials*: Waveland Press, 2005.
- [36] Caillard D, Martin J-L. *Thermally activated mechanisms in crystal plasticity*: Elsevier, 2003.
- [37] Lu K, Lu L, Suresh S. *Science* 2009;324:349.
- [38] Carpenter H. *Nature* 1930;126:17.
- [39] Gough H, Hanson D, Wright S. *Philosophical Transactions of the Royal Society of London. Series A, Containing Papers of a Mathematical or Physical Character* 1927:1.
- [40] Hall E. *Proceedings of the Physical Society. Section B* 1951;64:747.
- [41] Petch N. J. *Iron Steel Inst.* 1953;174:25.
- [42] Brenner SS. *J Appl Phys* 1956;27:1484.
- [43] Nix WD. *Metall Trans A* 1989;20:2217.
- [44] Stelmashenko N, Walls M, Brown L, Milman YV. *Acta Metall Mater* 1993;41:2855.
- [45] <http://www.sandia.gov/mstc/mems/>. 2015. (25.10.2015)
- [46] <http://risorse.dei.polimi.it/sensorlab/Research.php>. (25.10.2015)
- [47] Dimiduk DM, Uchic MD, Parthasarathy TA. *Acta Mater* 2005;53:4065.
- [48] Uchic MD, Dimiduk DM, Florando JN, Nix WD. *Science* 2004;305:986.
- [49] Michler J, Wasmer K, Meier S, Ostlund F, Leifer K. *Appl Phys Lett* 2007;90.
- [50] Korte S, Clegg WJ. *Scripta Materialia* 2009;60:807.
- [51] Volkert C, Donohue A, Spaepen F. *J Appl Phys* 2008;103:083539.
- [52] Wang S, Yang Y, Zhou L, Mai Y-W. *J Mater Sci* 2012;47:6047.
- [53] Zaiser M, Seeger A. Chapter 56 Long-range internal stresses, dislocation patterning and work-hardening in crystal plasticity. In: Nabarro FRN, Duesbery MS, editors. *Dislocations in Solids*, vol. Volume 11. Elsevier, 2002. p.1.
- [54] Walker A, Carrez P, Cordier P. *Mineral Mag* 2010;74:381.
- [55] <http://www.for1650.kit.edu/57.php>. (25.10.2015)
- [56] <http://www.esrf.eu/UsersAndScience/Experiments/StructMaterials/news/data-explosion>. (25.10.2015)
- [57] https://commons.wikimedia.org/wiki/File%3AAAl_tensile_test.jpg.
- [58] Uchic MD, Shade PA, Dimiduk DM. *Annu Rev Mater Res* 2009;39:361.
- [59] Kraft O, Gruber PA, Monig R, Weygand D. *Annual Review of Materials Research*, Vol 40 2010;40:293.
- [60] Greer JR, De Hosson JTM. *Progress in Materials Science* 2011;56:654.

- [61] Lin Q, Corbett JD. Proceedings of the National Academy of Sciences 2006;103:13589.
- [62] <https://research.wpi-aimr.tohoku.ac.jp/eng/research/584>.
- [63] Volkert C, Minor A. Mrs Bull 2007;32:389.
- [64] Dimiduk DM, Woodward C, LeSar R, Uchic MD. Science 2006;312:1188.
- [65] Greer JR, Oliver WC, Nix WD. Acta Mater 2005;53:1821.
- [66] Greer JR, Nix WD. Phys Rev B 2006;73.
- [67] Soler R, Molina-Aldareguia JM, Segurado J, Llorca J, Merino RI, Orera VM. Int J Plasticity 2012;36:50.
- [68] Hütsch J, Lilleodden ET. Scripta Materialia 2014;77:49.
- [69] Norfleet DM, Dimiduk DM, Polasik SJ, Uchic MD, Mills MJ. Acta Mater 2008;56:2988.
- [70] Kiener D, Motz C, Dehm G. Materials Science and Engineering: A 2009;505:79.
- [71] Ng KS, Ngan AHW. Acta Mater 2008;56:1712.
- [72] Schneider AS, Kaufmann D, Clark BG, Frick CP, Gruber PA, Monig R, Kraft O, Arzt E. Phys Rev Lett 2009;103.
- [73] Kim J-Y, Jang D, Greer JR. Acta Mater 2010;58:2355.
- [74] Han SM, Bozorg-Grayeli T, Groves JR, Nix WD. Scripta Materialia 2010;63:1153.
- [75] D. Kaufmann RM, C.A. Volkert, O. Kraft,. Int J Plasticity 2011;27:470.
- [76] Sun J, Yu Q, Shan ZW, Li J, Huang XX, Xiao L, Ma E. Nature 2010;463:335.
- [77] Lilleodden E. Scripta Materialia 2010;62:532.
- [78] Dou R, Derby B. Scripta Materialia 2009;61:524.
- [79] Rao SI, Dimiduk DM, Tang M, Parthasarathy TA, Uchic MD, Woodward C. Philos Mag 2007;87:4777.
- [80] Tönnies D, Maaß R, Volkert CA. Adv Mater 2014;26:5715.
- [81] Chen CQ, Pei YT, De Hosson JTM. Acta Mater 2010;58:189.
- [82] Haasen P. Mater Sci Tech-Lond 1985;1:1013.
- [83] Conrad H. Materials Research Innovations 1998;2:1.
- [84] Li JCM. Materials Science and Engineering A 2000;287:265.
- [85] Stepanov AV. Phys.Z. Sowj. 1933.
- [86] Fischbach DB, Nowick AS. Phys Rev 1955;99:1333.
- [87] Fischbach DB, Nowick AS. Phys Rev 1955;98:1543.
- [88] Machlin ES. J Appl Phys 1959;30:1109.
- [89] Kataoka T, Sakamoto M, Yamada T. Jpn J Appl Phys 1975;14:1609.
- [90] Kataoka T, Colombo L, Li JCM. Philos Mag A 1984;49:395.
- [91] Kataoka T, Li JCM. Philosophical Magazine a-Physics of Condensed Matter Structure Defects and Mechanical Properties 1985;51:1.
- [92] Yeh JW, Chen SK, Lin SJ, Gan JY, Chin TS, Shun TT, Tsau CH, Chang SY. Advanced Engineering Materials 2004;6:299.
- [93] Huang PK, Yeh JW, Shun TT, Chen SK. Advanced Engineering Materials 2004;6:74.
- [94] Yeh JW, Chen YL, Lin SJ, Chen SK. Materials Science Forum 2007;560:1.

- [95] Yeh J-W, Chang S-Y, Hong Y-D, Chen S-K, Lin S-J. *Mater Chem Phys* 2007;103:41.
- [96] Senkov ON, Wilks GB, Miracle DB, Chuang CP, Liaw PK. *Intermetallics* 2010;18:1758.
- [97] Senkov ON, Wilks GB, Scott JM, Miracle DB. *Intermetallics* 2011;19:698.
- [98] Shechtman D, Blech I, Gratias D, Cahn JW. *Phys Rev Lett* 1984;53:1951.
- [99] Levine D, Steinhardt PJ. *Phys Rev Lett* 1984;53:2477.
- [100] Steurer W. *Chemical Society Reviews* 2012;41:6717.
- [101] Dubois J-M. *Chemical Society Reviews* 2012;41:6760.
- [102] Dubois J, Kang S, Stebut JV. *Journal of Materials Science Letters* 1991;10:537.
- [103] Demange V, Milandri A, De Weerd M, Machizaud F, Jeandel G, Dubois J. *Phys Rev B* 2002;65:144205.
- [104] Stroud RM, Viano AM, Gibbons PC, Kelton KF, Misture ST. *Appl Phys Lett* 1996;69:2998.
- [105] Dubois JM, Kang SS, Massiani Y. *J Non-Cryst Solids* 1993;153-154:443.
- [106] Takakura H, Gomez CP, Yamamoto A, De Boissieu M, Tsai AP. *Nat Mater* 2007;6:58.
- [107] Engel M, Damasceno PF, Phillips CL, Glotzer SC. *Nat Mater* 2015;14:109.
- [108] Bindi L, Steinhardt PJ, Yao N, Lu PJ. *Science* 2009;324:1306.
- [109] Feuerbacher M, Schall P. *Scripta Materialia* 2003;49:25.
- [110] Edagawa K, Ohta S, Takeuchi S, Kabutoya E, Guo J, Tsai A-P. *Materials Science and Engineering: A* 2000;294:748.
- [111] Wollgarten M, Saka H, Inoue A. *Philosophical Magazine A* 1999;79:2195.
- [112] Momprou F, Caillard D. *Acta Mater* 2004;52:3613.
- [113] Yokoyama Y, Inoue A, Masumoto T. *Materials Transactions, JIM* 1993;34:135.
- [114] Tsai A, Inoue A, Yokoyama Y, Masumoto T. *Materials Transactions, JIM* 1990;31:98.
- [115] Tsai AP, Inoue A, Masumoto T. *Mater T Jim* 1989;30:150.
- [116] Fisher I, Cheon K, Panchula A, Canfield P, Chernikov M, Ott H, Dennis K. *Phys Rev B* 1999;59:308.
- [117] Fisher I, Kramer M, Islam Z, Ross A, Kracher A, Wiener T, Sailer M, Goldman A, Canfield P. *Philosophical Magazine B* 1999;79:425.
- [118] The Nobel Prize in Chemistry 2011 - Advanced Information". http://www.nobelprize.org/nobel_prizes/chemistry/laureates/2011/advanced.html: Nobelprize.org., 2011. (25.10.2015)
- [119] Schall P, Feuerbacher M, Urban K. *Philos Mag* 2004;84:705.
- [120] Socolar JES, Lubensky TC, Steinhardt PJ. *Phys Rev B* 1986;34:3345.
- [121] Feuerbacher M. *Chemical Society Reviews* 2012;41:6745.
- [122] Edagawa K. *Materials Science and Engineering: A* 2001;309–310:528.

Chapter 2. Size Effect in Ionic Crystals

2.1. Single crystalline NaCl, KCl, LiF and MgO¹

Abstract

Uniaxial micro-compression methodology is applied to study mechanical behavior of <100>-oriented NaCl, KCl, LiF and MgO single-crystal pillars ranging from 250 nm to 4 μm in diameter. As in metallic materials a strong size effect with regard to compressive strength is observed, NaCl, KCl, LiF and MgO pillars exhibit scaling exponents of -0.64 ± 0.02 , -0.72 ± 0.02 , -0.68 ± 0.02 and -0.8 ± 0.03 , respectively. These compare well to face centered cubic (fcc) metals, but the normalized stress levels of LiF and MgO are higher than those of NaCl, KCl and fcc metals. The differences in strength levels are interpreted in terms of the susceptibility to ion induced damage, which is intrinsic to the fabrication process. In addition, the strong size-dependent plasticity of <100>-oriented ionic crystals can be correlated with their lower critical temperatures.

Introduction

Significant advances have been made in applying uniaxial micro-compression methodology [1] to study mechanical behavior of small-sized materials (i.e. from a few microns to about 100 nm). It is well established that yield stress (σ_y) scales inversely with sample dimension (d) in metals, by a relationship of $\sigma_y \propto d^m$ [2-5], where m is the size-effect exponent. Fcc metals (e.g. Ni [1], Au [6], Al [7], Cu [8]) show strong and relatively constant size dependence with m of -0.6 to -0.7

¹ Y. Zou, R. Spolenak, "Size-dependent plasticity in micron- and submicron-sized ionic crystals". Philosophical Magazine Letters, 93 (2013) 431-438.

[2, 5, 9], but in bcc metals less pronounced and inconstant size-effect exponents of -0.20 to -0.5 and of -0.4 to -0.9 were found in Nb, Ta, Mo and W by Schneider et al. [10, 11] and Kim et al. [12, 13], respectively. To date the studies on size-dependent plasticity have mostly been performed on metallic systems.

Ionic crystals (e.g. NaCl, KCl, LiF and MgO) in single-crystal forms are normally highly pure and with low dislocation densities (less than 10^9 m^{-2}) [14]. One of the simplest forms among ionic crystals is the rocksalt (NaCl) structure. Normally ionic crystals have two types of slip systems: soft slip systems with $\{110\}$ slip planes and Burgers vectors of $\frac{1}{2} \langle 110 \rangle$ and hard slip systems with $\{100\}$ slip planes and Burgers vectors of $\frac{1}{2} \langle 110 \rangle$. For example, at room temperature, the soft slip systems ($\{110\} \langle 110 \rangle$) of NaCl and KCl have critical resolved shear stresses (CRSS) of approximately 1 MPa and 0.5 MPa, respectively, while their hard systems ($\{100\} \langle 110 \rangle$) have CRSS of approximately 7 MPa and 2 MPa, respectively [15]. Ionic crystal has been used as a testing ground for dislocations and plasticity since the 1930s and has been thoroughly investigated [15, 16]. This is the starting point of the current study on size-related phenomena.

The first study of size-related phenomena in ionic crystals was reported by Nadgorny et al. [14], who observed similar plastic flows and size-effect exponents in both as-grown and γ -irradiated LiF micropillars. Recently, Korte and Clegg [17] and Soler et al. [18] found that, in MgO and LiF respectively, the size-related plasticity was also dependent on crystal orientations: The micropillars deformed on soft slip systems exhibited a stronger size effect than the ones deformed on hard slip systems. However, understanding of the size effect in ionic crystals is far from mature, and systematic experimental studies on small-sized ionic crystals are scarce. To the authors' knowledge, micro-compression tests of NaCl and KCl, which have been serving as good examples of ionic crystals, have not been reported so far. In addition, the lower limit of pillar diameter in previous studies on ionic crystals was 0.5 μm . This paper constitutes

a study on the mechanical behavior of <100>-orientated NaCl, KCl, LiF and MgO pillars in the diameter ranging from a few microns to about 200 nm.

Experimental methods

Micron- and submicron-sized pillars were prepared from bulk pure NaCl, KCl, LiF and MgO single crystals (CrysTec GmbH, Germany) with <100> direction normal to surface planes using focused ion beam (FIB) technique (Helios Nanolab 600i, FEI). To avoid the charging problem, a 5 nm thick gold layer was deposited before FIB milling. A two-step milling method using different beam currents was applied to produce cylindrical pillars: 2.5 nA for coarse milling and 40-80 pA for fine milling. The pillars produced were in the diameters of approximately 4 μm , 2 μm , 1 μm , 500 nm and 250 nm, and an aspect ratio of 2.5-4. A taper of 2-3° was generally observed for these pillars, and the top diameters were chosen to calculate stresses. At least 4 pillars of each size were compressed using a nanoindenter (Triboindenter, Hysitron Inc., USA) with a flat diamond punch tip (5 μm in diameter, Synton, Switzerland) under displacement control mode by feedback mechanism. The displacement and loading time were changed according to the pillar height in order to keep a constant strain rate. A strain rate of $2.2 \times 10^{-3} \text{ s}^{-1}$ was used for all compression tests. The morphologies of the pillars were characterized using scanning electron microscopy (SEM) before and after compression. It should be noted that NaCl and KCl are hygroscopic, so all the samples had to be stored in an exsiccator before and after tests.

Results

Engineering stress-strain curves for the compressed NaCl, KCl, LiF and MgO pillars with different diameters ranging from 4 μm to 250 nm are shown in Figure 1 (a), (c), (e) and (g), respectively. It is observed that the smaller pillars have higher yield and flow stresses than the bigger pillars. For example, 250-nm NaCl

pillars have yield stress (measured as offset flow stress at 0.2% of strain) of ~0.25-0.35 GPa, which is ~ $\times 5-7$ of that of 4- μm NaCl pillar (~0.05 GPa) and ~ $\times 250-350$ of that of bulk NaCl single crystal (~1 MPa) [15, 19]. Moreover, displacement bursts generally occurred in both big and small pillars, showing a similar phenomenon to what has been found in fcc and bcc metals [20, 21]. Due to displacement bursts, both the stress of the pillars and the lateral friction can be released, which may affect the strain hardening rate. Some of the stress-strain curves exhibit nonlinear part at the initial stage of compression, as shown in the curve for MgO in Figure 1 (g), which could be due to the misalignment between the flat punch and the top surface of the sample [2]. To reduce the influence of the displacement bursts on analysis, the highest stress value measured below 5% strain is defined as flow stress $\sigma_{0.05}$. The relationships between $\sigma_{0.05}$ and the pillar diameter for NaCl, KCl, LiF and MgO are plotted in Figure 1 (b), (d), (f) and (h), respectively.

As shown in the compressed pillars in Figure 2, discrete slip bands are observed along the gage length of the samples, showing either one or two localized slip bands on the deformed pillars. Both single and multiple slip is observed in the pillar samples. Those slip bands traverse the entire cross sections of each sample, and multiple slips are always observed for the samples that experienced large strains, as shown in the 4- μm NaCl pillar. Multiple slip is expected to contribute to strain hardening. No wavy morphologies as those observed in W and Mo pillars [10, 11] are found in the ionic crystals. The slip bands are oriented at approximately 45° from the loading axis ($\langle 100 \rangle$ direction), indicating that all pillars were deformed by crystallographic slip on $\{110\}$ -type planes along $\langle 110 \rangle$ -type directions, which are the same as the soft slip systems in their bulk forms.

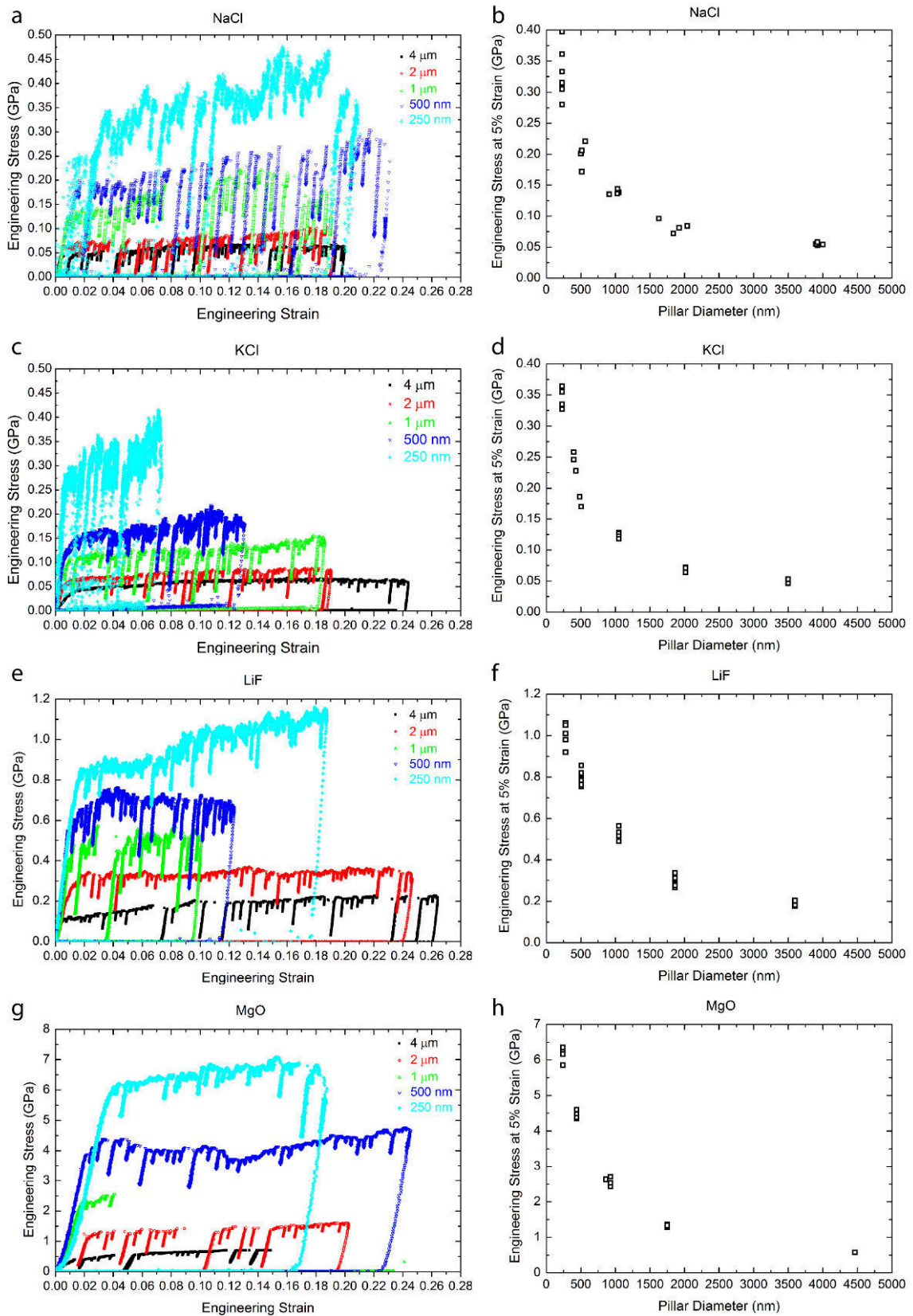


Figure 1. Representative engineering stress-strain curves for $\langle 100 \rangle$ -oriented single crystals: (a) NaCl, (c) KCl, (e) LiF and (g) MgO pillars with the diameters ranging from 4 μm to 250 nm; the corresponding engineering stress at 5% strain ($\sigma_{0.05}$) as a function of the pillar diameter: (b) NaCl, (d) KCl, (f) LiF and (h) MgO.

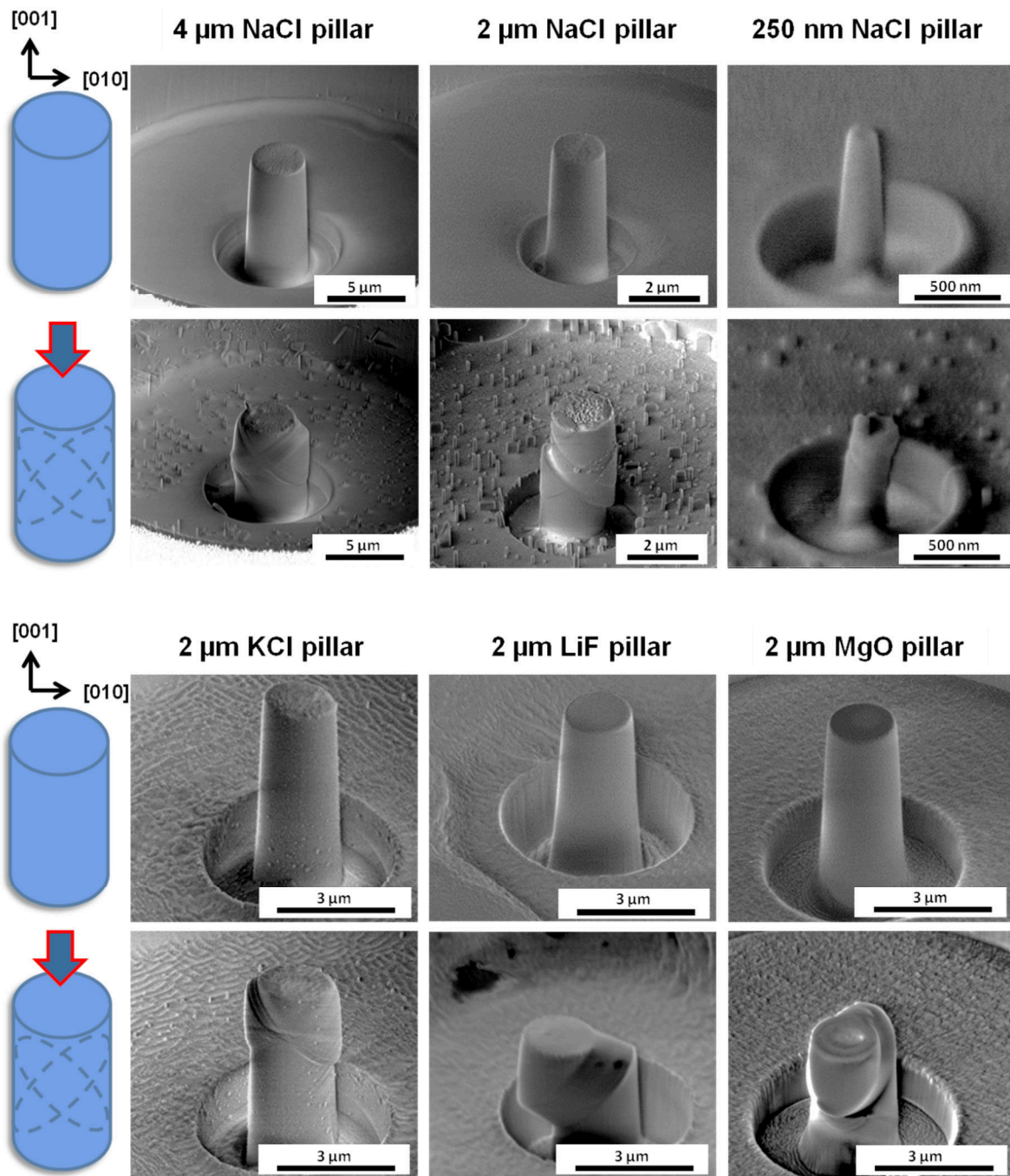


Figure 2. SEM images of representative NaCl, KCl, LiF and MgO pillars: as FIB-milled (the top row) and compressed (the bottom row). The loading direction is along the surface normal axis of $\langle 100 \rangle$, the slip bands caused by $\{110\} \langle 110 \rangle$ slip systems are schematically illustrated.

As shown in Figure 2, a bigger taper and some degrees of bending are observed in the smallest pillars, although not always. This bigger tapering could lead to localized plastic deformation on the top area of the pillar and also higher effective stress values. The bending of the pillars could be introduced by misalignment between the pillar and punch, leading to a reduction in the measured modulus and stress [22-24]. It should be also noted that in the FIB-milled NaCl and KCl

trenches a large number of small crystals grew around the FIB-milled pillars. They might be caused by the FIB-milled NaCl and KCl surfaces absorbing water in air, but they were too small to be contacted by the flat punch during compression and did not influence the results of measurement.

Discussion

By compression along $\langle 100 \rangle$ direction, four equivalent slip systems with a Schmid factor of 0.5 can be activated. Because it is difficult to judge yield strength here, $\sigma_{0.05}$ is used to give a quantitative analysis. The highest $\sigma_{0.05}$ of NaCl observed in this study is 0.4 GPa (as shown in Figure 1(b)), so its resolved shear strength is 0.2 GPa, which corresponds to a normalized shear strength of $G_{NaCl\{110\}}/90$ ($G_{\{110\}\langle 1-10 \rangle} = 1/2(C_{11} - C_{12}) = 18$ GPa). Using the same method, the highest $\sigma_{0.05}$ for KCl, LiF and MgO are $G_{KCl\{110\}}/90$, $G_{LiF\{110\}}/60$ and $G_{MgO\{110\}}/32$, respectively, where the shear modulus can be calculated using elastic constants from reference [25]. As the theoretical strength is in the range of $G/30$ - $G/2\pi$ [26], the plastic deformation in NaCl and KCl pillars is expected to be controlled by both dislocation nucleation and propagation. The values for LiF and MgO, however, approach their theoretical strengths.

The difference of the normalized stresses between these ionic crystals could be caused by various defect densities induced by irradiation damage during the FIB milling process. Although LiF, NaCl and KCl are all alkali halides, the defect formation energy of LiF is ~3-5 times higher than those of NaCl and KCl [27, 28]. Thus, LiF pillars may have lower defect densities than NaCl and KCl pillars after FIB milling. Similarly, despite having the identical crystal structure, MgO is much less susceptible to radiation damage than alkali halides [29]. Consequently, the lower defect densities in FIB-milled LiF and MgO could lead to higher strengths, even close to the theoretical values.

Dou and Derby [9] analyzed the micro-compression data of single crystal Au, Al, Ni and Cu pillars by a power-law fit in the form of $\sigma/G=A(D/b)^m$, where σ is the resolved shear stress on the appropriate slip system, G is the shear modulus of corresponding slip system, A is a constant, D is the pillar diameter, b is the Burgers vector and m is the size-effect exponent. We applied this power law to fit the data of <100>-orientated NaCl, KCl, LiF and MgO pillars in this study, LiF [14, 18] and MgO [17] as reported, fcc metals (Au [6, 30], Ni [31], Al and Cu [32]) and bcc metals (Nb, Ta, Mo and W [10, 11]), as shown in Figure 3. In order to make a comparison, the curves published in the literature were re-evaluated, and resolved shear stresses at 5% strain are used for both the samples in this study and the data from literature. Figure 3 (a) indicates that <100>-orientated NaCl, KCl, LiF and MgO exhibit size-effect exponents of -0.64 ± 0.02 , -0.72 ± 0.02 , -0.68 ± 0.02 and -0.8 ± 0.03 , respectively, and the exponents for LiF and MgO in this study are close to those reported in literatures [14, 17]. Moreover, the absolute normalized strength levels for NaCl and KCl are similar, but the ones for LiF and MgO are significantly higher. This difference in normalized stresses might be due to the lower FIB-induced defect densities in LiF and MgO pillars, as indicated above. Interestingly, the hard slip systems ($\{100\}$ <110>) of MgO measured by Korte and Clegg [17] and LiF measured by Soler et al. [18] show much weaker size effects than the ones deformed on the soft slip systems in this study. It is observed that the normalized strengths of MgO and LiF deformed on the soft slip systems in this study can even surpass those deformed on the hard slip systems in the studies of [17] and [18]. However, as both hard and soft systems are expected to converge to the theoretical values in the same magnitude, we attribute this effect to a lower initial or FIB-induced dislocation densities in MgO and LiF in this study compared to [17] and [18].

Figure 3 (b) pinpoints the similarities in normalized strength levels between fcc metals and ionic crystals. It seems that the difference in slip systems does not play an essential role in the size-effect exponents between fcc metals and ionic crystals. Figure 3 (c) compares ionic crystals to bcc metals (i.e. W, Mo, Ta and

Nb) as reported by Schneider et al. [10]. Unlike ionic crystals and fcc metals, they exhibit various size-effect exponents ranging from -0.43 to -0.93 [10].

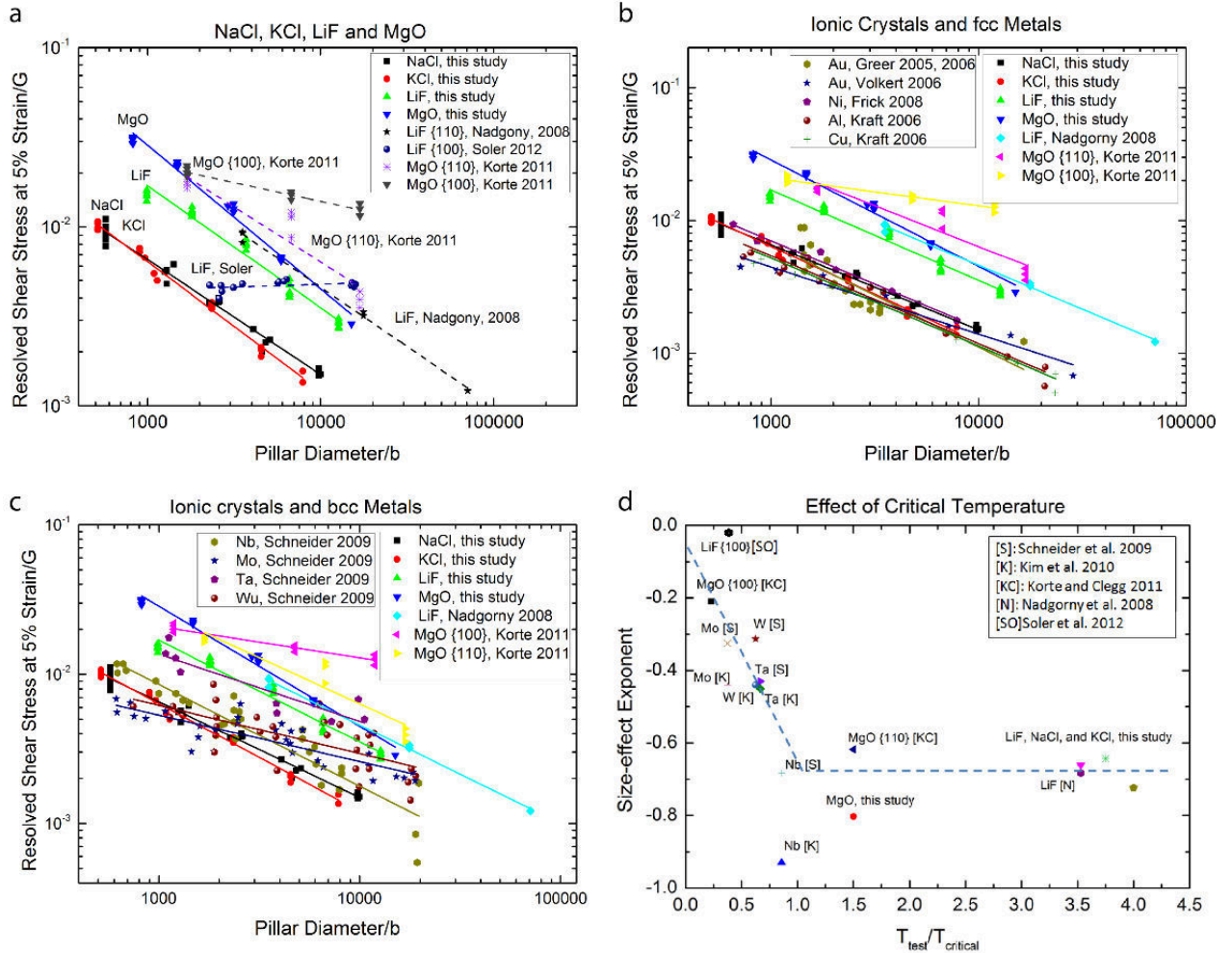


Figure 3. Resolved shear stress at 5% strain normalized by the shear modulus G on corresponding slip system versus the diameters normalized by the Burgers vector b for FIB-milled (a) ionic crystals, i.e. NaCl, KCl, LiF, and MgO in this study and ref [14, 17, 18]. (b) with fcc metals (i.e. Au, Ni, Al and Cu [6, 30-32]) and (c) bcc metals (i.e. Nb, Mo, Ta, W [10]) and (d) the relationship between the size-effect exponents and the test temperature normalized by the critical temperatures.

Schneider et al. [10] correlated the size dependence of several bcc metals to their critical temperatures and found that the size-effect exponent scales inversely with the critical temperature. Here, the critical temperature is defined as the temperature above which the flow stress becomes insensitive to the test temperature. When the test temperature is close to the critical temperature, the mobility of screw dislocations is close to that of edge dislocations, and the size-effect exponents of bcc metals approach those of fcc metals. Here, we plot the

power-law exponents of ionic crystals and bcc metals as a function of test temperature over the critical temperature [10, 15], as shown in Figure 3 (d). The critical temperatures of ionic crystals in this study are obtained from stress-temperature curves measured in [15]. It shows the ionic crystals follow this pattern well. Those deformed on $\{110\} \langle 110 \rangle$ slip systems have low critical temperatures (generally below 100 K [15]). Thus, they exhibit almost uniform size-effect exponent around -0.7. Those deformed on $\{100\} \langle 110 \rangle$ systems have higher critical temperatures (~ 1200 K for MgO [15] and ~ 500 K for LiF [33]) and they have much smaller, and even no, size dependence of plasticity.

Conclusions

The micro-compression technique was applied to study the mechanical behavior of FIB-milled $\langle 100 \rangle$ -orientated NaCl, KCl, LiF and MgO single crystals at micron- and submicron scales. The results show that the size-effect exponents of these $\langle 100 \rangle$ -orientated ionic crystals are similar to fcc metals. A variation in normalized strengths for these ionic crystals might be attributed to different defect densities induced by FIB milling. The size dependence correlated with critical temperature can be used to compare ionic crystals to fcc and bcc metals.

Acknowledgements

The authors would like to thank Dr. A. Sologubenko (LNM, ETH Zurich), Mr. P. Gasser and Dr. K. Kunze (EMEZ, ETH Zurich) for their help in the sample preparation using FIB; Dr. D. Courty (LNM, ETH Zurich) for her help in the micro-compression testing and manuscript preparation. The authors also gratefully acknowledge financial support of this project through a SNF grant (200021_143633).

2.2. The influence of orientation, temperature, pre-straining and doping: a case study in KCl and LiF²

Abstract

Size effects in plasticity are mostly studied in metallic systems, but they are rarely investigated in ionic crystals. In this study, single-crystalline KCl and LiF pillars were fabricated by focused ion beam technique and compressed using a flat-punch tip in a nanoindenter. The materials were investigated with regards to crystal orientation, test temperature, pre-straining and doping. The results show: (1) [111] LiF pillars do exhibit size effect with an exponent of -0.38, in contrary to no size effect in [111] LiF reported in literature; (2) [001] LiF and [001]- and [111] KCl have similar size-effect exponents of -0.68, -0.71 and -0.65, respectively; (3) the size effect of [111] LiF pillars is more sensitive to the temperature change than that of [001] LiF pillars; (4) pre-straining of [111] LiF pillars results in a reduced size effect; (5) the 0.05 mol% CaCl₂ doping in [001] KCl slightly increases strength levels and does not change the size effect much. The magnitude of the size effects in ionic crystals can be attributed to the bulk stress level, but not the slip systems. In addition, a correlation between critical temperatures and size-effect slopes is illustrated, and the additivity of strengthening mechanisms is critically discussed.

Introduction

The mechanism controlling size dependence of strengths in micron- and submicron-sized pillars has been under debate since micro-compression

² Y. Zou, R. Spolenak, "Size-dependent plasticity in KCl and LiF single crystals: influence of orientation, temperature, pre-straining and doping". *Philosophical Magazine* 95 (2015), 1795-1813.

methodology [1] was introduced in 2004 (see reviews [2, 5, 34]). The yield or flow strength (σ) of a pillar sample scales inversely with the pillar dimension (D), commonly and empirically expressed as $\sigma \propto D^m$, with m size-effect exponent. Initial studies focus on face-centered-cubic (fcc) metal pillars (e.g. Au [4], Ni [35], Cu [32] and Al [36]), in which pronounced and relatively constant size effects ($m \sim -0.7$) have been discovered. Later investigations reveal that body-centered-cubic (bcc) metal pillars (e.g. Nb, V, Mo, Ta and W [10, 13, 37, 38]) exhibit a large range of size-effect exponents ($m \sim -0.2$ to -0.9). In some covalent solids (e.g. Si [39-41], GaAs [42], InSb [43]), the size effects are not obvious or significantly reduced compared with fcc metals. The increased strength in the metal pillars could be attributed to decreased dislocation-source lengths, especially in micron and submicron regimes. This theory, so-called single-arm source model, was first proposed by Parthasarathy, Rao and their co-workers [44, 45] using discrete dislocation dynamics (DDD) simulations, and later it was evidenced by Oh *et al.* [46] by in-situ TEM observation. However, very recently, a few experimental reports implied that the size-effect phenomena could be more complicated. Kim *et al.* [47] observed that the size effect in Mo pillars was orientation-sensitive; Schneider *et al.* [48] found that Mo pillars exhibited a similar size effect to fcc metal pillars at 500 K; both Schneider *et al.* [49] and El-Awady *et al.* [50] reported that the size effect in Ni pillars was decreased after pre-straining. Therefore, how different factors, such as orientation, temperature, dislocation density and alloying, influence the size dependence of strengths in small-sized pillars is still not well understood.

So far, the investigation of micro-pillar compression has been mostly focused on metallic systems. However, there are many reasons to choose ionic crystals to improve our understanding of this currently popular topic of the size effect [15, 16, 51]: (1) ionic crystals, especially rock-salt structures, have been used as a testing ground for the theories of dislocation and plasticity since the 1930s, so their lattice mechanics have been thoroughly studied; (2) compared with metals, ionic crystals have much lower and more constant dislocation densities ($\sim 10^9 \text{ m}^{-2}$

in ionic crystals vs. $\sim 10^{12} \text{ m}^{-2}$ in metals); (3) the two types of slip systems in the rock-salt structure (soft slips $\langle 110 \rangle \{1\bar{1}0\}$ and hard slips $\langle 110 \rangle \{001\}$) have different intrinsic resistance to dislocation motion and also different temperature dependence of critical resolved shear stress (CRSS), so they are ideal systems to study the effects of orientation and temperature on the size effect; (4) solid-solution (doping) effect on flow stress has also been well studied in various bulk ionic crystals, which supplies a good database to investigate the doping effect at small scales.

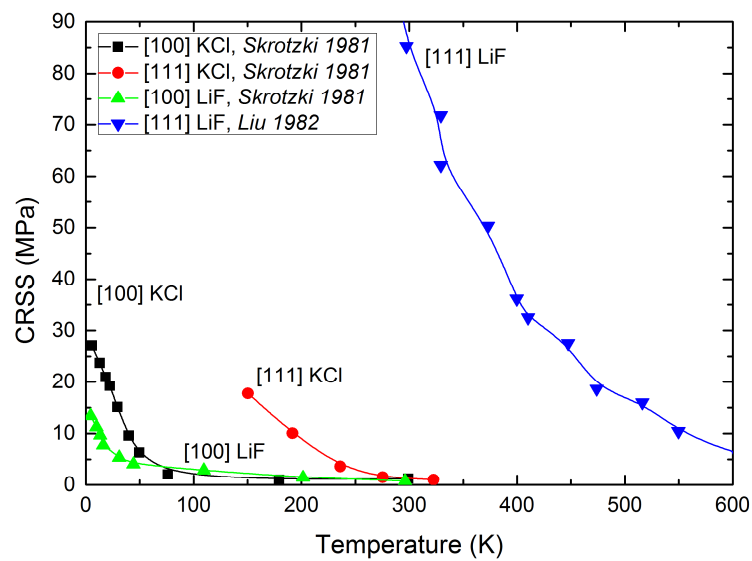


Fig. 1. Temperature dependence of the CRSS for bulk KCl and LiF single crystals: the primary slip systems for [001] and [111] loading axes are $\langle 110 \rangle \{1\bar{1}0\}$ and $\langle 110 \rangle \{001\}$, respectively (summarized from Refs. [26] and [37]).

The first study on the size effect in ionic crystals was reported in 2008 by Nadgorny *et al.* [14], who observed similar plastic flows in as-grown and γ -irradiated [001] LiF micro-pillars. Later, Korte and Clegg [17] and Soler *et al.* [18] found that [111] MgO and LiF pillars, respectively, had much smaller size effects than those in [001] orientation. Very recently, the authors of this paper expanded their research to NaCl and KCl micro- and submicro-pillars [52]. They reported all of [001] NaCl, KCl, LiF and MgO showed a similar size effect to fcc metal pillars, with m between -0.65 and -0.80. Still, the experimental data for ionic-crystal pillars are scarce and understanding the controlling mechanisms of

size-dependent plasticity requires more study. In this paper, we chose two typical ionic crystals with low and high plastic anisotropy (i.e., the difference of CRSS between hard and soft slips): KCl and LiF, respectively (see Fig. 1). By activating hard and soft slips separately, testing at elevated temperature, pre-straining and doping, we aim to understand the mechanisms which influence the size-dependent plasticity.

Experimental

One-side polished [001] and [111]-oriented pure KCl and LiF single crystals and 0.05 mol% CaCl₂ doped [001]-oriented KCl wafers (10 mm × 10 mm × 1 mm) were supplied by CrysTec GmbH (Germany). Cylindrical pillars were produced from the wafers using focused ion beam (FIB) technique (Helios Nanolab 600i, FEI). To avoid charging during FIB milling, a 5-nm thick gold layer was deposited using a plasma sputter coater. A two-step milling method was applied: 2.5 nA for coarse milling, and 10-40 pA for fine milling. The diameters of the milled pillars are approximately 4 μm, 2 μm, 1 μm, 500 nm and 250 nm, and the aspect ratios are about 3.0-4.5. A taper of 2-3° was generally observed, and the top diameter was chosen to calculate stress. The nanoindenter (Hysitron Inc., USA) with a diamond flat-punch tip (5 μm in diameter, Synton-MDP, Switzerland) was employed to compress the pillars in a displacement control mode by feedback mechanism. In order to keep the strain rate constant ($2 \times 10^{-3} \text{ s}^{-1}$), the displacement and loading time was adjusted according to the pillar heights. At least four pillars for each size were compressed. The pillars were imaged using a scanning electron microscopy (SEM) before and after compression. As KCl is hygroscopic, all the samples were stored in an exsiccator before and after measurement.

LiF wafers, in both [001] and [111] orientations, were chosen to investigate the size-dependent strengths at an elevated temperature. The wafers with FIB-milled pillars were placed on a heating stage which was fitted in the nanoindenter. In

order to stabilize the machine and sample, the whole wafers were heated up to 470 K and kept for about one hour before measurement. The actual temperature of the sample surface was measured using an infrared thermometer and a thermal couple. It was approximately 450 K. To protect the tip and transducer, the flat punch tip was brazed to a low thermal expansion coefficient shaft, which was attached directly to a load transducer behind a heat shield. To reduce the temperature gradient between the flat-punch tip and the top surface of the tested pillar, the tip was in contact with the pillar top with a tiny force of 2 μN for 15 seconds before further compression in a displacement control mode. The thermal drift was monitored during preloading and unloading process over a 15 s hold segment (similar experimental set-up is described in [53]). The load control mode was also used to verify the strength values. To study the effect of pre-straining, [111] LiF pillars were selected to be first compressed to $\sim 15\%$ strain, re-milled using FIB and finally re-compressed (a method developed by Schneider *et al.* [54]).

Results

Effect of crystal orientation

For the pillar compression along [001] axis, the Schmid factors of the hard slip systems $\langle 110 \rangle \{001\}$ are zero, while four Schmid factors of the soft slip systems $\langle 110 \rangle \{1\bar{1}0\}$ (on two pairs of orthogonal planes) are 0.5. So, in this scenario the $\{110\}$ slip systems are activated but the slips on the $\{001\}$ planes do not occur. Contrarily, the compression along [111] axis activates three of $\langle 110 \rangle \{001\}$ slip systems with the Schmid factors of 0.47 and inhibits slips on $\langle 110 \rangle \{1\bar{1}0\}$ with the Schmid factor of zero. Fig. 2 shows the [001]- and [111]-oriented KCl and LiF pillars after compression to $\sim 15\text{-}25\%$ strain. Both [001] KCl and LiF pillars (Figs. 2a and 2c) show one or two discrete slip bands traversing along the gage length of the specimens, at approximately 45° from the loading axis. The slip

bands are sharp without wavy morphology. Some pillars show a single-slip-like morphology, such as Fig. 2c. This could be due to either a slight misalignment between the flat punch and the pillar top or one plane having more initial mobile dislocations than the others. For [111]-oriented pillars, KCl and LiF exhibit distinct post-deformed morphologies: obvious slip bands are observed in [111] KCl pillars (Fig. 2b), although they are not as sharp as those in [001] KCl pillars; it is difficult to find slip bands in the compressed [111] LiF pillars (Fig. 2d). Some of the [111] LiF pillars were slightly bent, which was also observed by Soler *et al.* [18]. This could be attributed to the high anisotropy in [111] LiF pillar, which was proved by the finite element simulation [55].

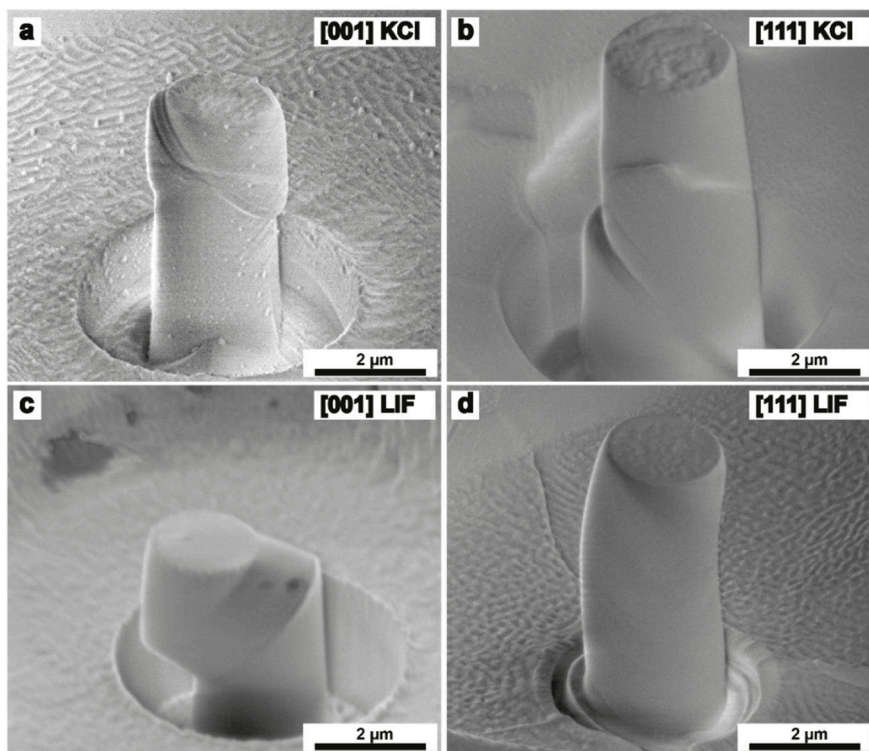


Fig. 2. Typical SEM images of [100]- and [111]-oriented KCl and LiF pillars after compression. The pillars were imaged with 52° tilting angle. (a) and (c) are adapted from the authors' previous publication [31] [copyright Taylor & Francis]

Fig. 3 shows engineering stress-strain curves for [001]- and [111] KCl and LiF pillars with the diameters ranging from approximately 4 μm to 200 nm. Displacement bursts are generally observed during the loading process. It is interesting to note that although experimental parameters are the same for all the

pillars, generally [111]-oriented pillars show smaller burst levels than [100]-oriented pillars. Specifically, [111] LiF exhibits the smallest amplitude of displacement-bursts and highest hardening rate among all the pillars.

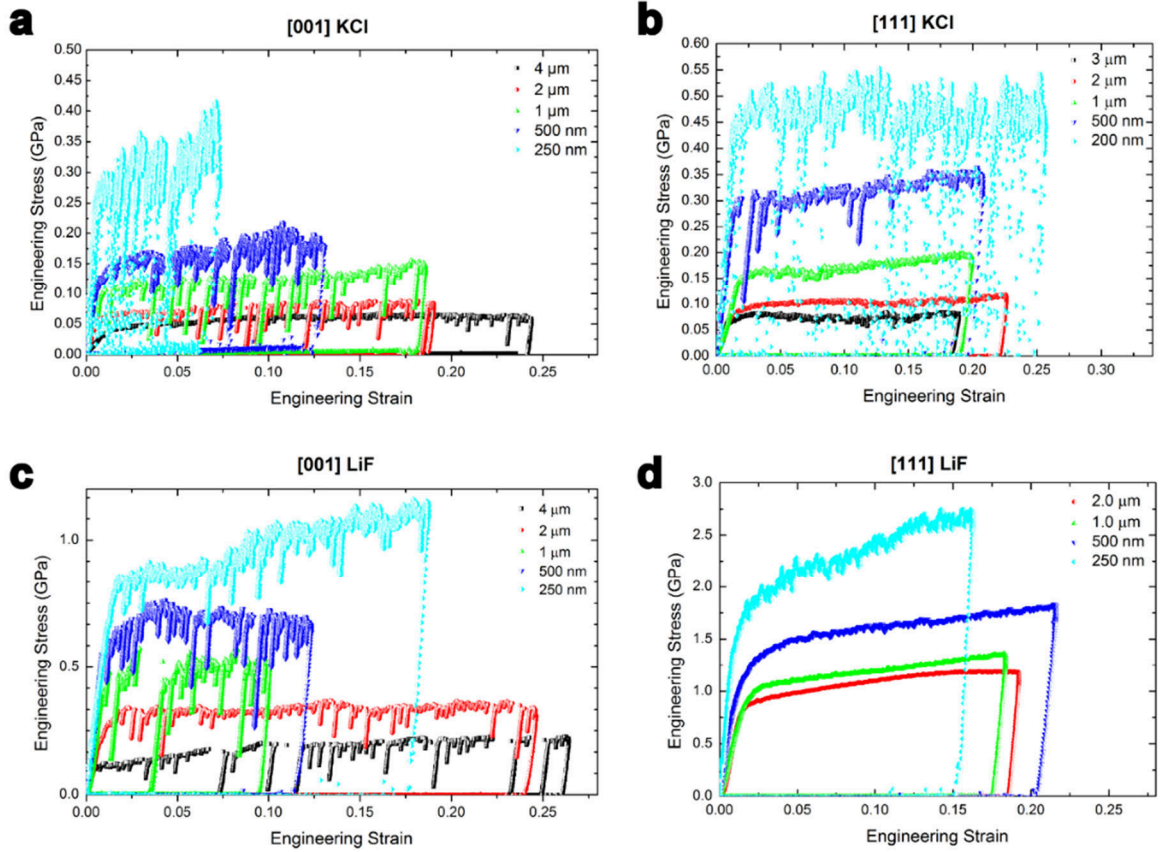


Fig. 3. Representative engineering stress-strain curves for [001]- and [111]-oriented KCl and LiF pillars with diameters ranging approximately from 4 μm to 200 nm. (a) and (c) are adapted from the authors' previous publication [31] [copyright Taylor & Francis]

In order to compare the magnitude of size dependence, the measurement results of the compressed pillars have been collected in log-log plots (Fig. 4) as $\sigma/G=A(D/b)^m$, where $\sigma_{0.05}$ is the highest stress value measured below 5% strain, G the corresponding shear modulus, D the pillar diameter and b the Burgers vector. The reason to use $\sigma_{0.05}$ instead of yield strength is to reduce the influence of the displacement bursts on analysis and make a good comparison with literature values. For KCl, [111] pillars have slightly higher stress levels than [001] pillars. In terms of size-effect exponents, [111] KCl has m of -0.65 ± 0.03 , and [001] KCl has m of -0.71 ± 0.05 . So, the orientation change has a minor influence

in the size effect of the KCl pillars. By contrast, [111] LiF shows a much smaller size dependence ($m = -0.38 \pm 0.02$) than [001] LiF ($m = -0.68 \pm 0.02$). Although KCl and LiF have the same NaCl-type structure, they exhibit different responses to the change of orientation, equivalently the change of slip systems.

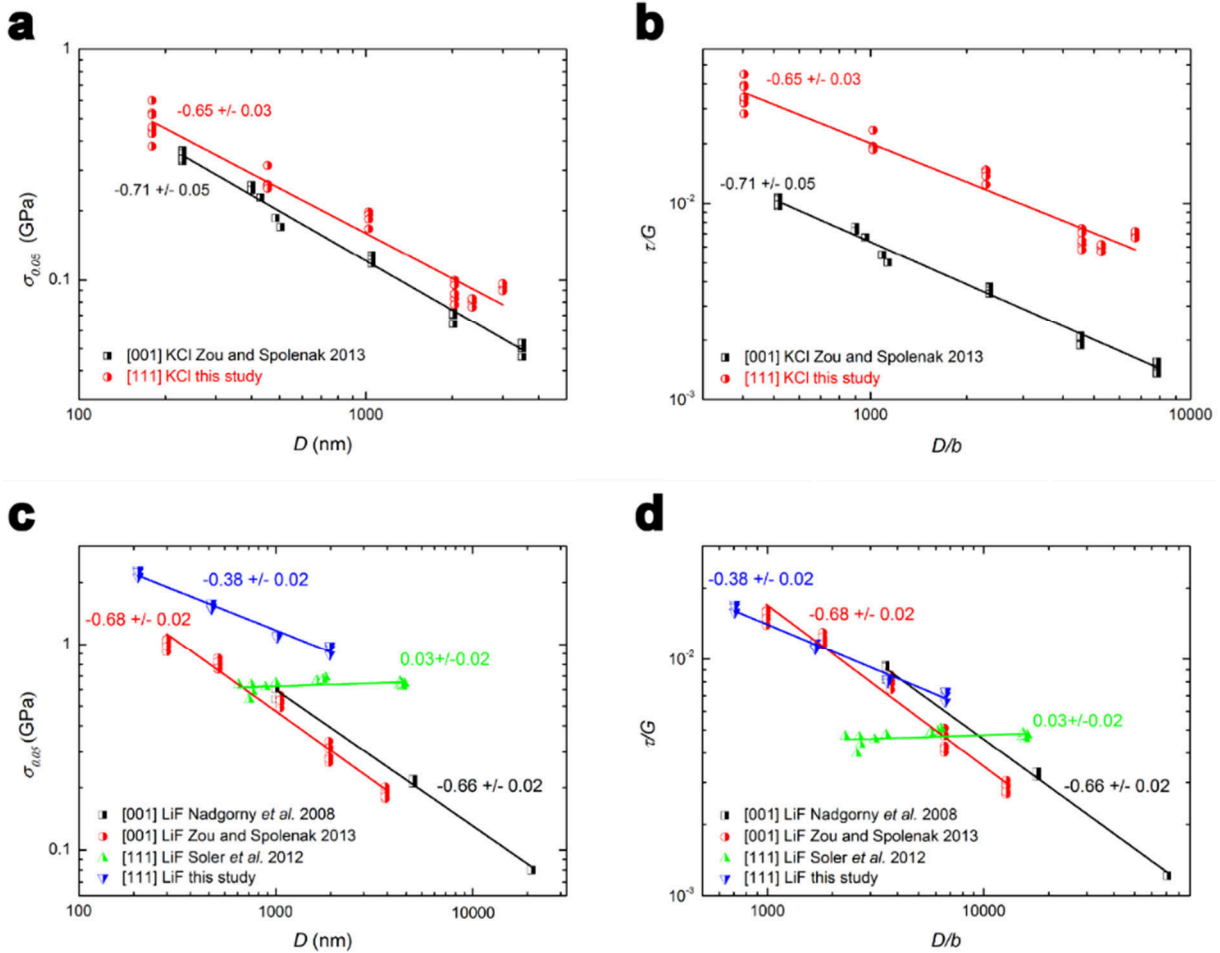


Fig. 4. (a) and (c): $\sigma_{0.05}$ versus D for KCl and LiF pillars, respectively. (b) and (d): $\sigma_{0.05}$ normalized by G versus D normalized by b for KCl and LiF pillars, respectively. The values of size-exponents are indicated, accordingly.

Effect of temperature

As shown in Fig. 1, below 520 K the CRSS of [111] LiF is strongly temperature-dependent, while the CRSS of [001] LiF is less temperature-sensitive above 100 K. Fig. 5 shows the representative SEM images and stress-strain curves for [001]- and [111] LiF pillars measured at high temperature (HT). At this temperature, the CRSS of [111] LiF is temperature-sensitive, but that of [001] LiF is not. For [001] LiF pillars, an obvious feature of multiple slips is revealed. Comparing Fig. 5a to

Fig. 2c implies that more slip systems could be activated at HT. In terms of stress levels and displacement bursts, the corresponding stress-strain curves of [001] LiF at HT (Fig. 5c) are similar to those measured at room temperature (Fig. 3c). To make a direct comparison in the log-log plot, Fig. 5e shows that the strength levels of [001] LiF at HT are decreased by ~ 0.2 - 0.4 GPa compared with those measured at room temperature.

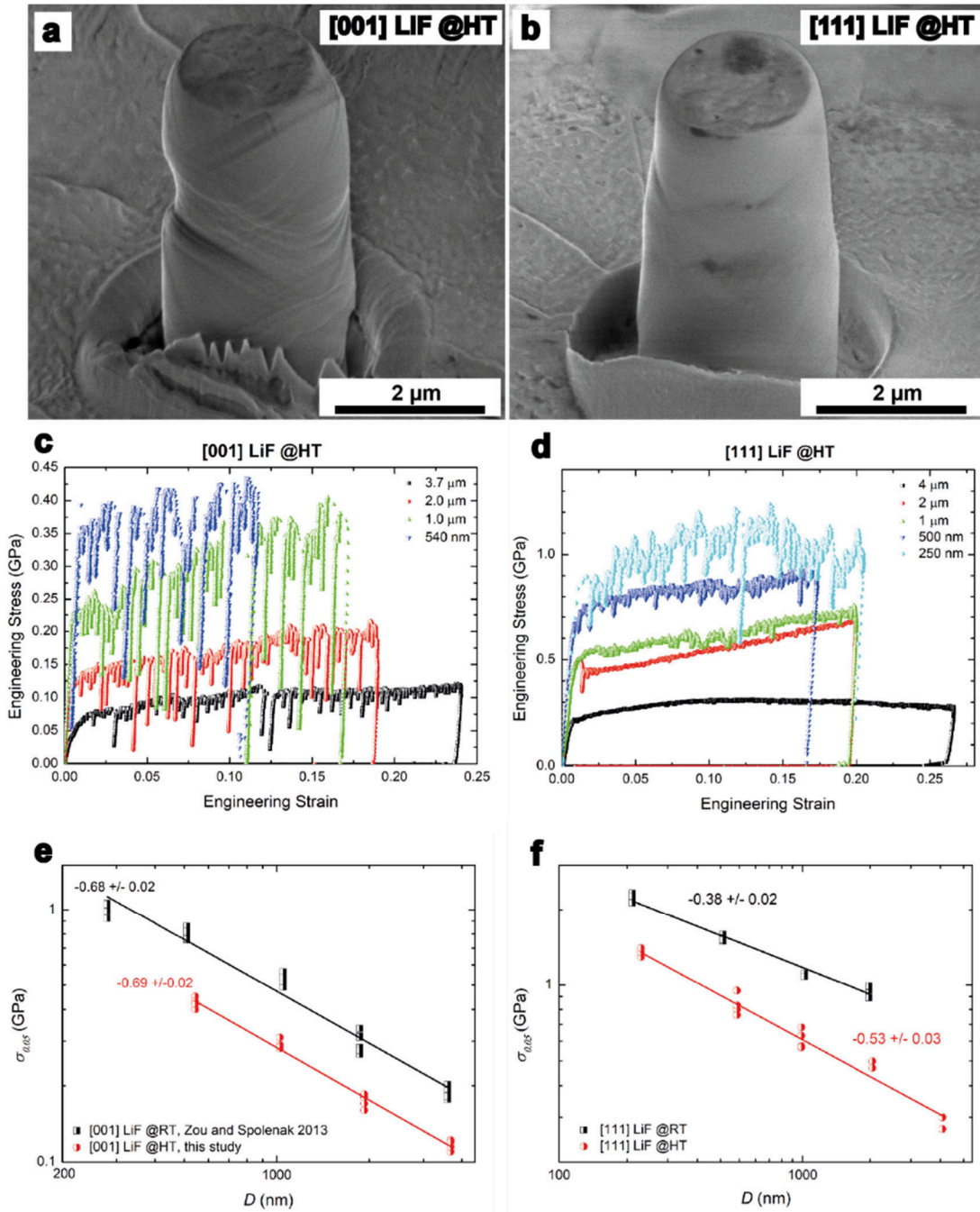


Fig. 5. Micro-compression of [001]- and [111]-oriented LiF pillars at high temperature: (a) and (b) are typical SEM images of the compressed pillars; (c) and (d) are the representative engineering stress-strain curves; (e) and (f) compare the size effects of the pillars tested at room temperature (RT) and high temperature (HT).

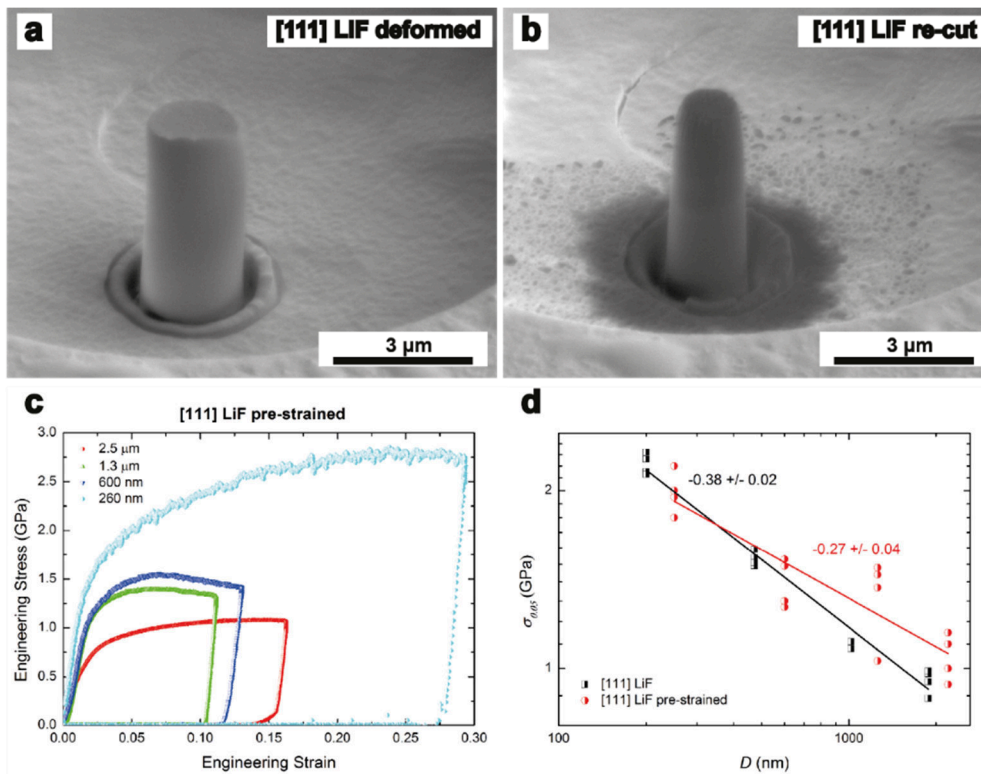


Fig. 6. Micro-compression of $\sim 15\%$ pre-strained $[111]$ LiF at room temperature: (a) and (b) are the SEM images of a pillar after the first compression and the same pillar after re-cutting by FIB, respectively; (c) representative engineering stress-strain curves; (d) the stress-size relationships for non-deformed and pre-strained $[111]$ LiF.

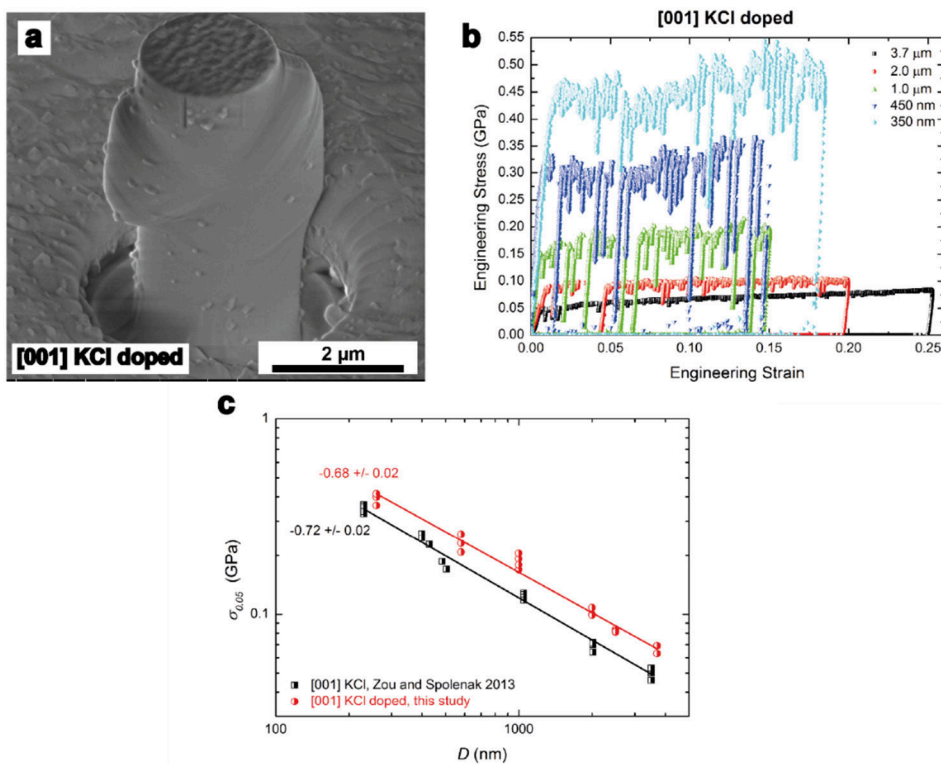


Fig. 7. Micro-compression of 0.05 mol% CaCl_2 doped $[001]$ KCl pillars at room temperature: (a) a typical SEM image of a 2- μm pillar; (b) representative engineering stress-strain curves; (c) a comparison of the stress-size relationships between pure and doped $[001]$ KCl pillars.

For [111] LiF, the pillars measured at HT (Fig. 5b) exhibit some features of slip bands. This implies that the slips on {001} planes become easier at HT. From the stress-strain curves (Fig. 5d), it is interesting to note that displacement bursts become more obvious, especially for the small pillars. This also suggests an increased mobility of dislocations at HT. Compared to those tested at room temperature, the stress levels of [111] LiF pillars measured at HT are reduced by ~0.6-1.0 GPa. As shown in Fig. 5f, the size dependence of [111] LiF at HT is increased with m of -0.52 ± 0.03 . The size dependence of strength in [111] LiF is therefore more sensitive to the temperature change than that in [001] LiF. It should be noted that thermal drift may occur during the pre-loading and loading processes due to the thermal gradient between the tip and the pillar top. In our experiment, the drift values were monitored, showing a drift depth of ~5-10 nm during the pre-loading process. For the pillar height of ~1-6 μm , an error of ~0.1-1% may be added in the strain measurement. Considering no obvious work hardening in the range of 4-6% strain at the high-temperature condition (as seen in Fig. 5c and 5d), we keep using the 5% flow stress as to compare size effects.

Effect of pre-straining

The effect of pre-straining were studied on [111] LiF pillars. The pillars had been compressed to ~15% strain (Fig. 6a), re-milled by FIB (Fig. 6b), and re-compressed to ~10%-25% strain. The average dislocation density in a bulk ionic crystal increases linearly with the plastic strain (ϵ) [56], as $\rho \approx 10^{13} \epsilon / \text{m}^2$. Compare with bulk specimens, the dislocations in pillars could move to the surface more easily [57], so the increased dislocation density in the pre-strained pillar samples might be lower than $\sim 10^{12} \text{ m}^{-2}$. Fig. 6c shows the stress-strain curves of the pre-strained [111] LiF pillars, which qualitatively exhibit no significant differences. In the log-log plot (Fig. 6d), the pre-strained pillars show obvious higher strengths in the size range above 1 μm , but they converge to the same, or even lower, strength levels as the non-prestrained ones in the size regime

below 1 μm . Thus, the size effect in the pre-strained pillars is smaller than for non-deformed pillars, whereas the scattering level is higher.

Effect of doping

To study the influence of doping on the size effect, micro-compression was carried out on 0.05 mol% CaCl_2 doped [001] KCl. Fig. 7a is a SEM image of a doped [001] KCl pillar after compression, and Fig. 7b shows the representative stress-strain curves. We found that the doped [001] KCl exhibits a very similar post-deformed morphology and stress-strain curves to the pure [001] KCl. In the strength-diameter relationship (Fig. 7c), doped [001] KCl pillars have slightly higher stress levels than pure [001] KCl pillars, and nearly the same size effect within the experimental error.

Table 1. Summary of physical values for KCl and LiF.

Materials	loading axis	primary slip systems	Schimid factor	b (Å)	τ_p (MPa)	τ_{bulk0} (MPa)	τ_{bulk} (MPa)	G (GPa)	T_{c0} (K)	T_c (K)	γ (mJ m ⁻²)	$2H_k$ (eV)	E_L/Gb^2	m
KCl	[001]	<110>{1 $\bar{1}$ 0}	0.5	4.45	35	1.2	1.2	16.8	60	68	239	0.16	~1.0	-0.71±0.05
	[111]	<110>{001}	0.47	4.45	80	1.3	1.3	6.3	250	280	276	0.43	1.2	-0.65±0.03
LiF	[001]	<110>{1 $\bar{1}$ 0}	0.5	2.85	20	0.8	0.8	33	40	49	538	0.09	0.7	-0.68±0.02
	[111]	<110>{001}	0.47	2.85	380±30	85.3	138	64.9	520±10	620±11	849	1.1	2.2	-0.38±0.02

Schmid factor is calculated for the primary slip systems according to the Schmid law; the Burgers vector, b , is along <110> directions; Peierls stress, τ_p , is collected from Refs. [15] and [33]; shear modulus, G , is calculated from $G\{110\}\langle 110\rangle = \frac{1}{2}(C_{11}-C_{12})$ and $G\{100\}\langle 110\rangle = C_{44}$, where C_{ij} are obtained from Ref. [25]; the bulk stress, τ_{bulk0} , was measured from stress-strain curve at a strain rate of $\sim 5 \times 10^{-5} \text{ s}^{-1} - 1 \times 10^{-4} \text{ s}^{-1}$ in Refs. [23][31]; τ_{bulk} is the stress calculated for the pillar compression at the strain rate of $\sim 2 \times 10^{-3} \text{ s}^{-1}$; the critical temperatures for bulk compression, T_{c0} , in the strain rate $5 \times 10^{-5} \text{ s}^{-1} - 1 \times 10^{-4} \text{ s}^{-1}$ are collected from Refs. [15, 33, 60], and the values of T_c for the pillar compression at the strain rate of $\sim 2 \times 10^{-3} \text{ s}^{-1}$ are calculated, as described in the text; the stacking fault energy, γ , are atomistic calculated values for corresponding slip planes [61]; kink pair formation energy, $2H_k$, are collected from [16], E_L is the line energy per unit length of a dislocation and the values of E_L/Gb^2 are from Refs. [16, 33, 60]; size-effect exponents, m , are obtained from this study.

Discussion

Displacement bursts

The phenomenon of plastic bursts was first reported in Zn single crystals in 1973 [58]. Nowadays, the displacement-burst behavior has been widely observed during micro-pillar compression, either in the load control mode or in the displacement control mode [2]. Bursts occur when the feedback loop of a nanoindenter is not fast enough to follow the discontinuous movement of a pillar. Dimiduk *et al.* [59] associated this type of phenomenon with an avalanche-like, or earthquake-like, movement of the dislocations those are triggered within unstable dislocation networks or dislocation sources. In this study, we found that [111] LiF pillars showed much less pronounced bursts, i.e., low levels of force drops, than the other types of pillars. As shown in Fig. 8, representative depth-time and load-time curves were chosen from 500-nm pillars. Because of high stacking fault energies for both hard and soft slips (Table 1), the dissociation of a perfect dislocation into two partials is unlikely and the samples are plastically deformed by dislocation glide. The magnitude of the bursts could be correlated to the dislocation mobility on the activated slip systems. Critical temperature, T_c , can be used as an indicator of dislocation mobility. Here, T_c is defined as the temperature above which the flow stress becomes insensitive to the test temperature. In ionic crystals, below T_c , screw dislocations have lower mobility than edge dislocations, and the former ones control plastic deformation; above T_c , screw dislocations have nearly the same mobility as edge dislocations.

As shown in Fig. 1 and Table 1, [111]-oriented LiF with $\langle 110 \rangle \{001\}$ slips has a T_c higher than room temperature, while the others have the T_c lower than room temperature. This suggests at room temperature the plastic flow of [111] LiF is mainly controlled by screw dislocations, which is similar to the case of bcc Mo at room temperature. Based on molecular dynamics (MD) and dislocation dynamics (DD) simulations, Weinberger and Cai [62] demonstrates that in bcc Mo pillars screw dislocations interact with each other, self-replicate and form

hard junctions. In this scenario, the initial and newly generated dislocations cannot move out of the pillar easily, leading to a relatively continuous flow. Meanwhile, the increased dislocation density in the pillar results in hardening. The opposite case can be observed on [001] LiF with T_c lower than room temperature. During deformation, dislocations can move out of a pillar quickly without multiplication and forming hard junctions, causing a relatively discontinuous flow. This phenomenon is similar as that observed in fcc Au pillars. In terms of displacement-burst behavior, the [111] and [001] LiF pillars in this study could be comparable with Mo and Au in Ref. [62], respectively. Although [111] KCl also has the same slip systems as [111] LiF, due to a lower T_c and Peierls barriers, the dislocations in [111] KCl can move out of the pillars easily, resulting in a higher magnitude of displacement bursts. Thus, it is not the crystal orientation but the lattice resistance of a given slip system that controls the displacement bursts during pillar compression.

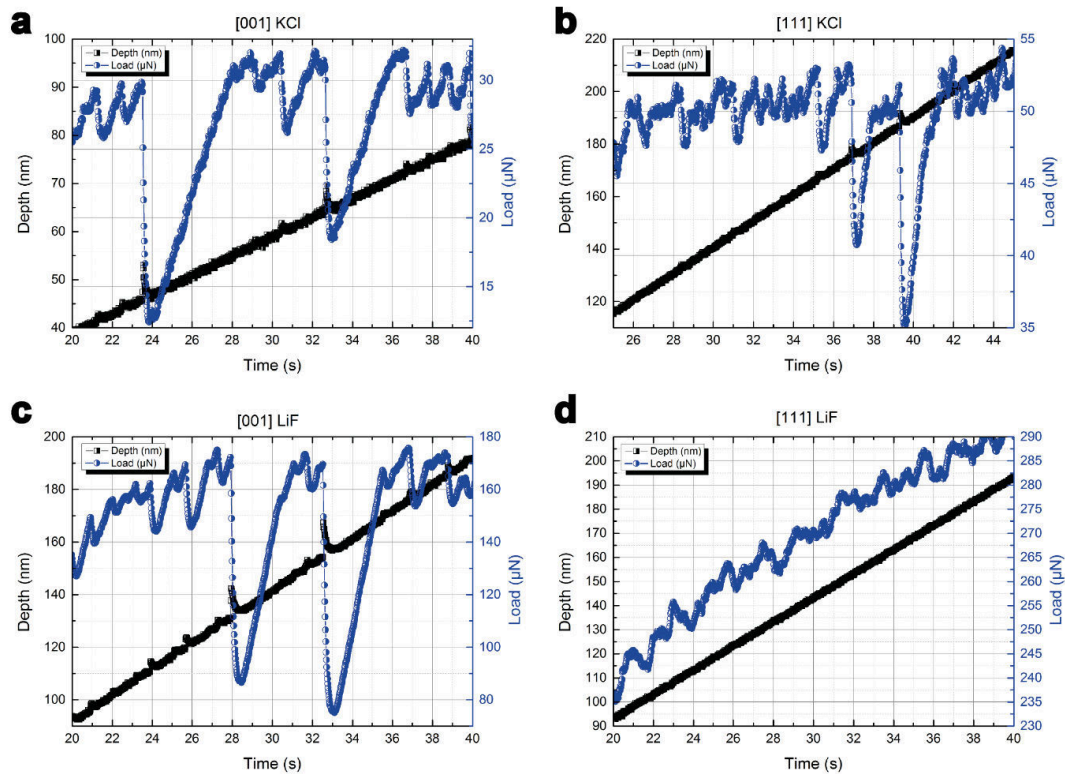


Fig.8. Displacement (depth) and force (load) signals as a function of time during displacement bursts in the displacement control mode for (a) [001] KCl, (b) [111] KCl, (c) [001] LiF and (d) [111] LiF (500-nm pillars in all the cases). The [111] LiF pillar exhibits smaller burst levels and higher hardening rate than the other types of pillars. (The feedback rate is up to 30 kHz)

Size effect and critical temperature

The magnitude of m was first correlated to T_c by Schneider *et al.* [10] in 2009. They found that m scaled inversely with T_c for several bcc metals. Here, we adapt this method to correlate m and T_t/T_c for pure FIB-milled metal and ionic-crystal pillars in the literature and this study. However, the critical temperature is not an intrinsic property of a material but can be affected by material and experimental parameters, particularly by dislocation density and strain rate [63]. Therefore, the critical temperature for the conditions of the pillar compression (T_c) has to be estimated and used here, rather than the critical temperatures in bulk forms (T_{c0}) reported in the literature [15, 33, 60]. To measure the dislocation densities in the FIB-milled KCl and LiF, the method of chemical etching [56] was applied to the specimens after FIB milling. The measured dislocation densities for KCl and LiF specimens are between 10^8 - 10^9 m^{-2} , which is in the same order of magnitude as those reported in the literature [15, 33, 60]. The strain rate for pillar compression in this study is 2×10^{-3} s^{-1} , which are about one order higher than those for bulk compression ($\sim 5 \times 10^{-5}$ s^{-1} - 1×10^{-4} s^{-1}) [15, 33, 60]. Thus, we need to consider the influence of strain rate in the critical temperatures and bulk stresses.

For thermally activated processes, the shear strain rate, $\dot{\alpha}$, is usually described by an Arrhenius equation of:

$$\dot{\alpha} = a_0 \exp\left(-\frac{\Delta G(\tau)}{kT}\right) \quad (1)$$

where a_0 is a frequency factor, which is related to mobile dislocation density and the Burger's vector, $\Delta G(\tau)$ the barrier activation energy at the shear stress τ , and k the Boltzmann constant. At a certain strain rate $\dot{\alpha}$, the critical temperature can be calculated using the following relation [63]:

$$T_c = \Delta G_0 / \left(k \ln \frac{a_0}{\dot{\alpha}}\right) \quad (2)$$

with ΔG_0 the barrier activation energy at zero stress. If the dislocation density and purity of the pillar specimens are comparable to the bulk specimens in literature, the following equation can be obtained:

$$T_c/T_{c0} = \ln \frac{\dot{a}_0}{\dot{a}_b} / \ln \frac{\dot{a}_0}{\dot{a}_p} \quad (3)$$

where \dot{a}_b and \dot{a}_p are strain rates for the bulk compression and pillar compression, respectively. Using the values of \dot{a}_0 and T_{c0} [15, 33, 60], T_c for the pillar compression are obtained, as list in Table 1. Compared to the values of T_{c0} , the value T_c for [111] LiF is significantly increased by 100 K, while the others are slightly increased.

As shown in Fig. 9, [001]-oriented NaCl, KCl, LiF and MgO and [111]-oriented KCl with $T_t > T_c$, have a strong and relatively constant size dependence, falling in the same region as fcc metals, with the m values of $\sim -0.6-0.8$. LiF and MgO in the [111] orientation has $T_t < T_c$, and they have different size dependence with the m values between -0.5 to -0.2 , following the trend of bcc metals. In the latter cases, the plastic deformation is controlled by screw dislocations. For the [111] LiF pillars measured at HT, the size dependence is increased accordingly, fitting the pattern well. It seems that FIB-produced pillars can follow this pattern well, but not the [111] LiF prepared using chemical etching [18]. This difference might be due to the processing method. The pillars in this work were produced by FIB milling, whereas the pillars in [18] were prepared from etching NaCl–LiF and KCl–LiF eutectic compounds, which could contain NaCl or KCl in its solid solution, although it could be a tiny amount. In addition, defects could be induced by either solidification, polishing or etching processes. However, it is difficult to make a meaningful comparison unless the purity and initial defect density of LiF specimens in both studies are known.

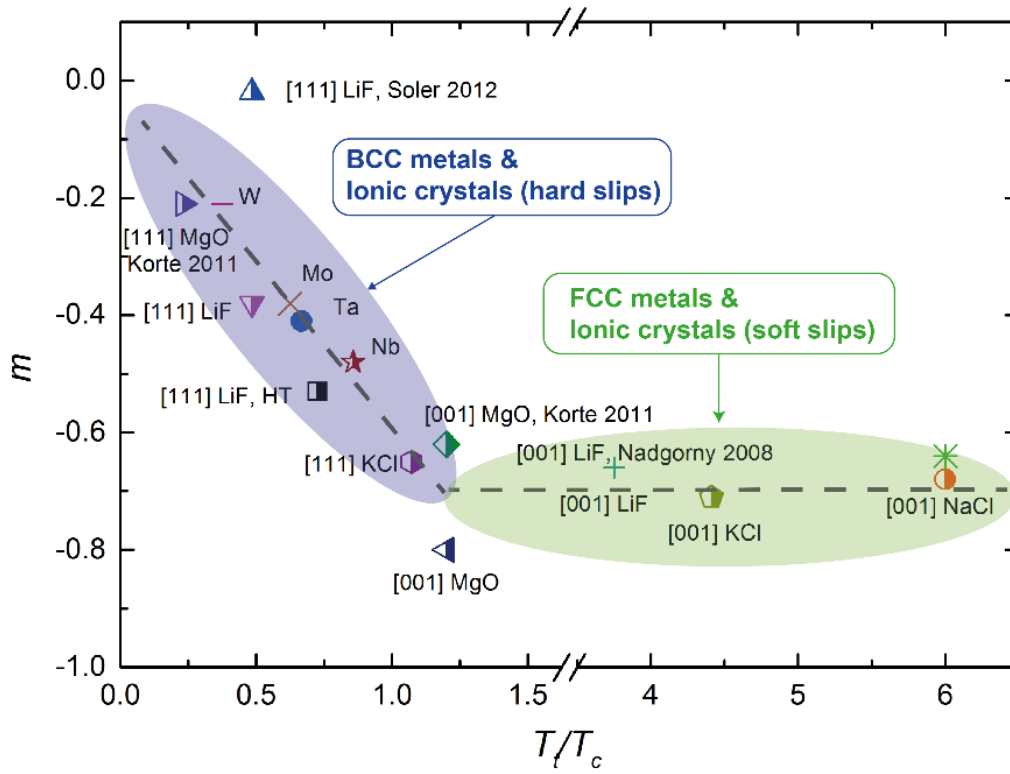


Fig. 9. The relationship between size-effect exponent (m) and normalized temperature (T/T_c) for metals and ionic crystals: ionic crystals with hard slip systems have similar trend to the bcc metals [9], while those with soft slips are similar as fcc metals.

Size-effect slopes in large scale and temperature ranges

As the local slope m could also significantly depend on experimental size range and other size-independent strengthening mechanisms, it needs to be discussed, how relevant such a parameter is, even if it is widely used. In a small-sized pillar specimen, it is generally believed that the applied resolved shear stress, τ , can be calculated as a sum of lattice friction, τ^* , Taylor hardening, τ_G , and dislocation-source strength, τ_s . Here, we adapt a simple analysis on how different strengthening mechanisms influence the strength of a pillar [44, 64, 65], expressed as:

$$\tau = \tau^* + \tau_G + \tau_s \quad (4)$$

In NaCl-structured ionic crystals, Suzuki *et al.* [60] and Liu *et al.* [33] suggest that double-kink formation controls dislocation activity below T_c , and the relation between lattice friction and test temperature can be estimated as [33, 66]:

$$\tau^* = \left[1 - \left(\frac{T_t}{T_c} \right)^{1/2} \right] \tau_p \quad \text{with } T_t < T_c \quad (5)$$

where τ_p is the Peierls stress. If T_t is higher than T_c , there is sufficient thermal energy to overcome the Peierls barriers by thermal activation, so

$$\tau^* \approx 0 \quad \text{with } T_t \geq T_c \quad (6)$$

The Taylor hardening in Eq. (4) is attributed to the dislocation interactions, which is typically expressed as:

$$\tau_G = \alpha b G \sqrt{\rho_0 + \rho_\Delta} \quad (7)$$

where α is a constant, falling in the range 0.1 to 1.0, ρ_0 the initial dislocation density, and ρ_Δ increased dislocation density due to deformation. For a small amount of strain, the dislocation density is in the order of 10^{12} - 10^{13} m⁻² for most metals and 10^9 - 10^{10} m⁻² for most ionic crystals. For the strength due to dislocation-source lengths can be estimated by the following equation [44, 64, 65]:

$$\tau_s = KG \frac{\ln(\bar{\lambda}_{max}/b)}{\bar{\lambda}_{max}/b} \quad (8)$$

where K is a source-strengthening constant in the order of 0.1; $\bar{\lambda}_{max}$ is the statistical average length of the longest dislocation source, i.e., the weakest source. For the source strengthening, we further assume $\bar{\lambda}_{max}$ is proportional to the pillar diameter as:

$$\bar{\lambda}_{max} = D/n \quad \text{with } n \text{ natural number} \quad (9)$$

It should be noted that the source length is not only limited by the pillar dimension, but also influenced by defect densities, their distribution inside the pillar and at the surface. These defects can act as pin points of dislocation sources. By chemical etching, an average dislocation density of 5×10^9 m⁻², which is in the same order of the bulk LiF in Liu et al. [33], was obtained in both FIB-milled region and the region without FIB irradiation. Although FIB may not change

dislocation density much, it could introduce other defects, such as point defects, amorphous layers and other or other unusual effects [67]. These defects would change average source length inside a pillar. The number of pins, P , is related to the sample dimensions and defect density in a FIB-milled pillar, expressed by a model in Parthasarathy *et al.* [44]:

$$P = \text{Integer} \left[\rho_0 \frac{\pi D^2 h}{4L_{seg}} \right] \quad (10)$$

with h the pillar height, L_{seg} is the average length of dislocation segments.

For big pillars ($> \sim 20 \mu\text{m}$ in diameter) and bulk samples, Frank-Read source acts as dislocation source instead of the single-end source; for even smaller pillars ($< \sim 100 \text{ nm}$ in diameter), surface image forces could play an important role in the pillar strength [45]. The single-end source model applies to the micron- and sub-micron range discussed in this study. According to Eqs. (4)-(10), we obtain a more precise model for ionic crystals, as:

$$\frac{\tau}{G} = \left[1 - \left(\frac{T_t}{T_c} \right)^{1/2} \right] \frac{\tau_p}{G} + \alpha b \sqrt{\rho_0 + \rho_\Delta} + K \frac{\ln(D/nb)}{D/nb} \quad \text{with } T_t < T_c \quad (11)$$

$$\frac{\tau}{G} \approx \alpha b \sqrt{\rho_0 + \rho_\Delta} + K \frac{\ln(D/nb)}{D/nb} \quad \text{with } T_t \geq T_c \quad (12)$$

For the samples tested at room temperature, the bulk stress, τ_{bulk} , can be used to present the sum of τ^* and τ_G [17], thus both Eqs. (11) and (12) can be simply expressed as:

$$\frac{\tau}{G} \approx \frac{\tau_{bulk}}{G} + K \frac{\ln(D/nb)}{D/nb} \quad (13)$$

In order to compare the experimental data with calculation using the Eq. (13), the bulk stress and shear modulus for different slip systems are used (Table 1), α and K are chosen as 0.5, and n is chosen as various integers to give the best fit to the experiment. As shown in Fig. 10, [001] and [111] KCl can fit the experimental data well, using the $\bar{\lambda}_{max} = D/n$ ($n=2$ and $n=8$, respectively). For [111] LiF, which is strain-rate sensitive in strengths at room temperature, it is not appropriate

to use the bulk stress obtained at $5 \times 10^{-5} \text{ s}^{-1}$ in Liu *et al.* [33] to calculate the strengths of the pillars those were deformed at a strain rate of $2 \times 10^{-3} \text{ s}^{-1}$. Considering the strain-rate dependence of bulk shear stress, the equation for thermally activated flow is used to calculate the bulk stress in the strain rate of $2 \times 10^{-3} \text{ s}^{-1}$, as [63]:

$$\tau = - \left(\ln \frac{a_0}{\dot{a}} \right) kT/V + \Delta G_0/V \quad (14)$$

Where V is the activation volume ($25b^3$ for [111] LiF deformed at room temperature [33]). Calculated from Eq (14), a bulk stress of 138 MPa was obtained. For [001] LiF and [001]- and [111] KCl, their bulk stresses are not strain-rate sensitive at room temperature. Eq. (11) can fit [001] and [111] LiF best with $n = 7$ and $n = 4$, respectively. The difference of $\bar{\lambda}_{max}$ value might be due to localized dislocation densities and also different lengths of kink pairs.

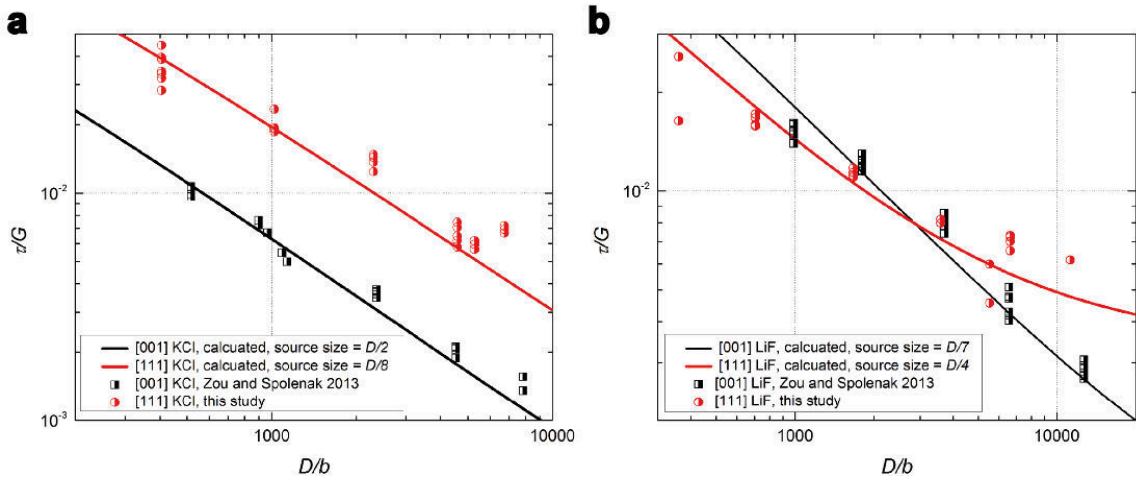


Fig. 10. The calculated curves of normalized strength vs. normalized length for KCl (a) and LiF (b) pillars according to Eq. (11). The bulk stress and shear modulus for different slip systems are used (Table 1), α and K are chosen as 0.5, and n is chosen as various integers to give the best fit to the experiment data.

To illustrate how the various strengthening mechanisms in Eq. (11) influence the size-dependent strengths in the KCl and LiF pillars in different size and temperature ranges, Fig. 11 shows 3D graphs of normalized strength (τ/G) vs. normalized length (D/b) and normalized temperature (T/T_c). For simplification, it is assumed that $(\rho_0 + \rho_\Delta) \approx 10^{10} \text{ m}^{-2}$. $\bar{\lambda}_{max}$ is set to the best-fit values in Fig.

10. As show in Fig. 11, the surfaces with contour lines represent a sum of strengthening mechanisms: [001] in green and [111] in blue.

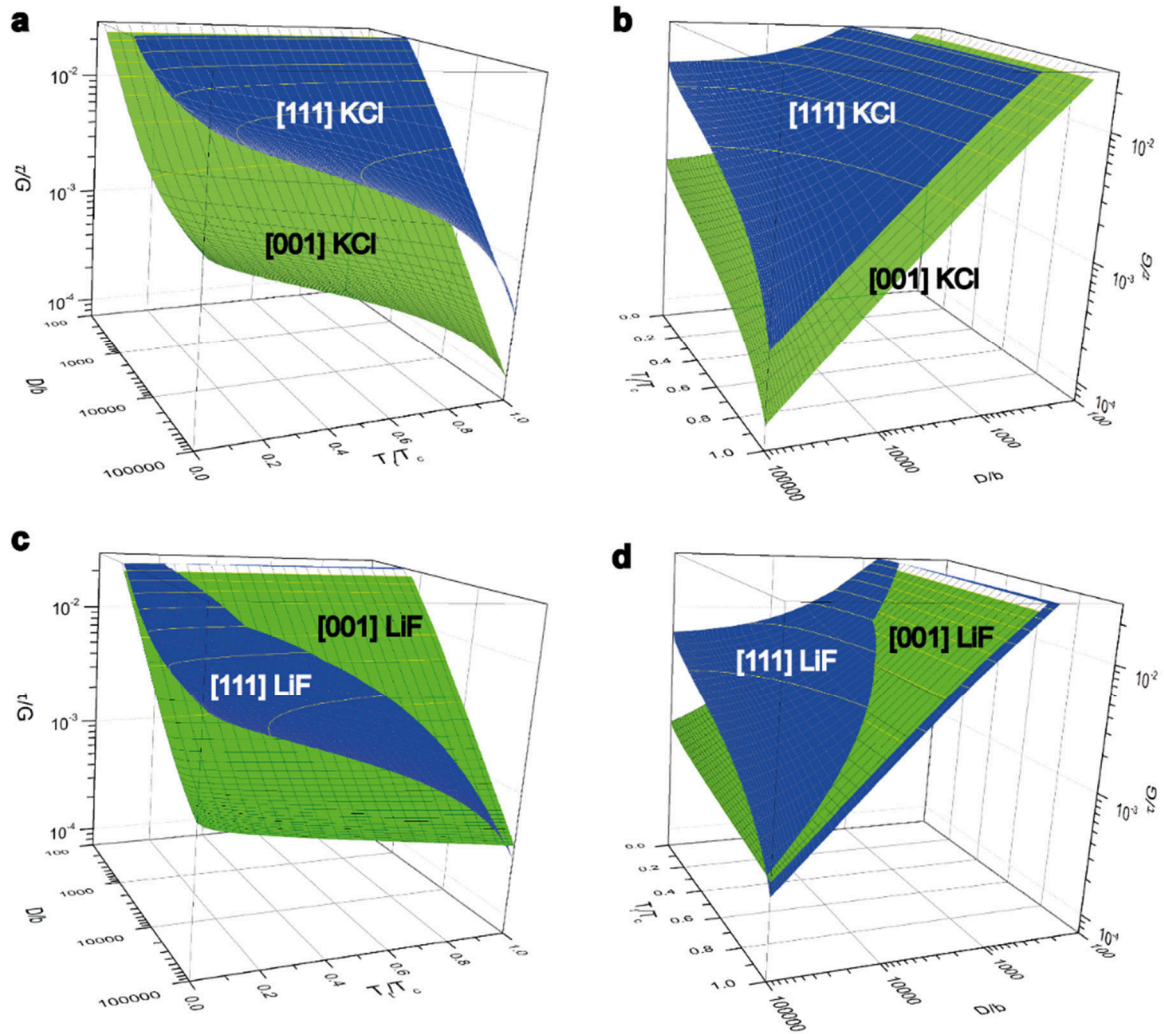


Fig.11. A 3D illustration for the size and temperature dependence of the strengths in KCl ((a) and (b)) and LiF ((c) and (d)) pillars according to Eq. (9): normalized strength (τ/G) vs. (normalized length scale (D/b) and normalized temperature (T/T_c)) in the size range of 10^2 - $10^5 b$ and the temperature range of $0-T_c$. (b) and (d) are different views of (a) and (c), respectively.

According to these graphs, we can observe the following phenomena: (1) in a large range of the log-log plot, the size dependence is not linear any more. For a relatively small pillar, the strength has a stronger size dependence, which is controlled by the size-dependent source strength; when the dimension of the pillar is increased, the size effect is decreased accordingly, because size-independent mechanisms, i.e., Peierls potentials and dislocation interactions, play important roles. When the dimension of the pillar reaches the bulk size, the strength shows no size-dependent behavior, the same as bulk stress. (2) The size dependence is

strongly influenced by the normalized temperature. In the low temperature range, the pillars have a relatively low size effect, showing a bcc-like feature, while in the high temperature range, the pillars have a relatively high size effect, similar as fcc metals. (3) Generally, [111]-oriented LiF and KCl have higher normalized strength levels than [001]-oriented ones. However, in a certain length and temperature range, [001]-oriented ones can be higher. For the current treatment identical defect densities were assumed for all samples and orientations, which is not necessarily true in the experiments. The defect density is a further factor that needs careful consideration in evaluating and comparing experimental data.

Although the empirical relation, $\sigma/G=A(D/b)^m$, has been commonly used to describe the phenomena of size-dependent plasticity, the above treatment illustrates that it is a simplification of a more complex relationship of the size effect. This simplification is only suitable for a small range of sample size and at a certain temperature.

Summary and conclusions

In this work, we have studied how the crystal orientation, test temperature, pre-straining and doping influence the size-dependent plasticity in KCl and LiF single crystals. The following phenomena have been observed: (1) the smaller size effect in [111] LiF, compared with [001] LiF and [001]- and [111] KCl, is attributed to its higher residual Peierls stress at room temperature; (2) below critical temperature, increasing the test temperature can reduce Peierls barriers and, therefore, increase the size effect; (3) increasing the dislocation densities strengthens the pillars and reduces the size effect; (4) the doping under a certain level may slightly increase strength levels and does not change the size effect much. Generally, in terms of size-dependent behavior, [111] LiF is similar to bcc metals, while [001] LiF and [001]- and [111] KCl are comparable to fcc metals.

The flow strength of a small-scaled pillar is determined by lattice friction, Taylor hardening, and source strength. If the lattice friction or Taylor hardening is in the same order of source strength, in a large size range the log-log plot is not linear anymore. Although the line fitting with the size-effect slope, m , has been commonly used to compare the size dependence in different materials, it might be not appropriate to describe size effects in a large range of experimental size and temperature.

Acknowledgements

The authors would like to thank P. Gasser (EMEZ, ETH Zurich) for their help in FIB milling, H. Ma, and M. Schamel (LNM, ETH Zurich) for their help in SEM and indentation, respectively, Dr. W. W. Gerberich (University of Minnesota) for his helpful discussion; C. Müller (LNM ETH Zurich) for proof reading the manuscript. The authors also gratefully acknowledge financial support through SNF grant (200021_143633).

2.3. Electro-plasticity of sodium chloride at small scales³

Abstract

Dislocations in rock salt, the mineral form of sodium chloride (NaCl), can carry charges. Interacting with the charged dislocations, an electric field may control the plasticity—flow strength and ductility of the rock salt. Although this unusual phenomenon has been known since the early 1930s, it has not been converted into any useful applications, which is significantly impeded by the brittleness of the material and the extremely high magnitude of electric voltage required. Here, we show that external electric potentials of a few volts can govern the flow stresses of single crystalline NaCl micro-pillars in a large strain range to over 50%. At the micrometer scale, the electric field might not only enhance dislocation propagation but also their nucleation. Rock-salt structured ionic crystals with controllable strength and ductility represent a new class of actuators or smart materials for design of small-dimensional devices.

Introduction

Actuators and sensors are ubiquitous in our society ranging from applications in automotive industry over microelectronics to biomedical actuation and monitoring. Most strain actuators and sensors take advantage of sophisticated materials properties such as piezoelectricity [68], ferroelectricity [69] and shape memory effects [70], and are targeted towards very small strains (< 0.1%). Alternatively, one applies a clever design in combination with a materials property i.e. piezoresistivity and targets towards large strain applications (<10%), for example, PbTiO₃ with a strain of 6% [71]. However, actuators and sensors

³ Y. Zou and R. Spolenak “Nanoscale sensor and actuator based on NaCl nanopillars” (in preparation)

made of a material that functions in a large strain range are highly desirable for critical applications.

Rock-salt structure ionic crystals (e.g. NaCl, KCl, LiF and MgO) can be regarded as natural smart materials, able to convert electric potential to plastic deformation and *vice versa*. They exhibit two unusual properties: electro-plasticity, which is the ability to enhance plastic deformation by the external stimulus of an electric potential [72, 73], and plasto-electricity, which is the ability to convert mechanical plasticity to electric potential [74]. The underlying mechanism in rock salt is that their lattice consists of cations and anions and, consequently, their defects such as vacancies and dislocation jogs carry net charges [75, 76]. An external electric field that exerts a force on the charged dislocations can increase their mobility (electro-plasticity) or plastic deformation that induces redistribute of the charge dislocations may result in electricity (plasto-electricity). In an absolutely pure ionic crystal the concentration of positively and negatively charged defects is balanced. A small amount of cation impurities is needed to tip that balance [77]. The transition property between electricity and plasticity renders rock-salt ionic crystals potentially useful in a wide variety of applications in actuation, switching and sensing.

To be of practical use, the material must be able to accommodate the large plastic strains without failure and a large critical electric field, which is in the order of 1 MVm^{-1} . However, macroscopic ionic crystals are generally very brittle, comparable to ceramics, failing by cracking at low strains, and more crucially, an extremely high magnitude of voltage, usually above $\sim 10 \text{ kV}$, is necessary to be applied. To avoid the breakdown of air (a breakdown strength of $\sim 3 \text{ MVm}^{-1}$ in a general environment), electrodes have to be immersed in a liquid medium, such as heptanes (a breakdown field of 166 MVm^{-1}), rendering them difficult to be built up for device and often unsuitable for usage.

So far, a large number of sophisticated experiments have been developed to study the electro-plasticity, yet all the studies are limited to using macroscopic samples.

Our strategy is to suppress fracture as well as to decrease the applied voltage by scaling sample dimensions down to the micrometer regime. First, a smaller sample may have higher fracture strength than yield strength, leading to a brittle-to-ductile transition [39, 78]. Second, the magnitude of electric voltage applied is decreased accordingly. For instance, if the critical field is 1 MV m^{-1} , for a micrometer-size sample only 1 V is needed.

Materials and methods

Our experiments used cylinder micro-pillars prepared from 0.05 mol% CaCl_2 doped [001]-oriented NaCl single crystals by focused ion beam (FIB) milling. The bottom part of the pillar was covered using thin gold layers of $\sim 10 \text{ nm}$. The micro-pillars are compressed using conductive nanoindenter with an external electric field switched either “on” or “off”, as shown in Fig. 1.

One-side polished [001]-oriented NaCl single crystals (0.05 mol% CaCl_2 doped, $10 \text{ mm} \times 10 \text{ mm} \times 1 \text{ mm}$) were supplied by CrysTec GmbH (Germany). Cylindrical pillars were produced from the single crystal using FIB technique (Helios Nanolab 600i, FEI). To avoid charging during FIB milling, a gold layer of $\sim 5 \text{ nm}$ was deposited using a plasma sputter coater. A coarse milling step was first applied using 2.5 nA beam current (Fig.S1a). The coarsely prepared pillars were subsequently coated with another gold layer of $\sim 5 \text{ nm}$ thick to ensure that the entire sample surface was conductive (Fig. S1b and S1c). The final milling step with 10-40 pA for fine milling was used to remove the gold layer on the top and side of the pillar, but the gold layer at the bottom part was retained (Fig. S1d). The diameters of the milled pillars are approximately $6 \mu\text{m}$, $4 \mu\text{m}$ and $2 \mu\text{m}$, and the aspect ratios are about 2.5-3.0. A taper of $2\text{-}3^\circ$ was generally observed, and the top diameter was chosen to calculate stress. As NaCl is hygroscopic, all the samples had to be stored in a desiccator before and after measurement.

The nanoindenter (CSM, Switzerland) with a conductive diamond flat-punch tip ($8 \mu\text{m}$ in diameter, Synton-MDP, Switzerland) was employed to compress the

pillars in a load-controlled or displacement-controlled mode by feedback mechanism. In the load-controlled mode, a loading rate of $\sim 5\text{-}100 \mu\text{Ns}^{-1}$ was applied. In the displacement controlled mode, a constant strain rate of $2 \times 10^{-3} \text{ s}^{-1}$ was used for all the pillars. During the compression process, a controllable external power supply was used to apply an electric potential to the pillar and was switched either “on” or “off” in the voltage range of 1-10 V. The current in the circuit was measured with an amperemeter with a resolution of 1 nA.

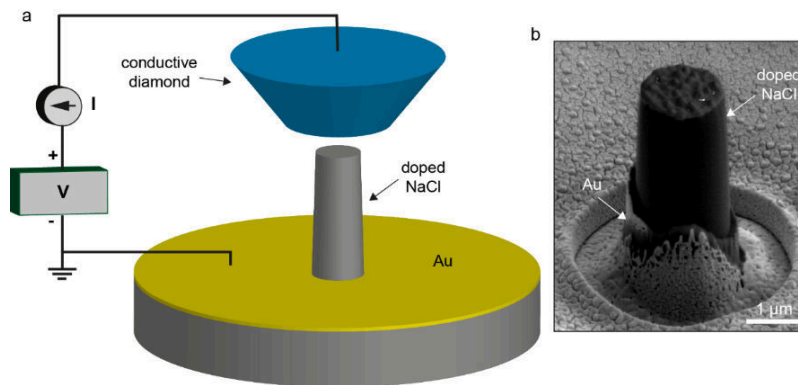


Fig. 1. (a) Schematic illustration of micro-compression of a doped NaCl pillar using a conductive diamond flat punch with electric voltage control. (b) SEM image of a FIB-prepared pillar sample, showing the bottom part is covered with gold, which works as an electrode.

Results

We started out by compressing micro-pillars without an electric potential. Fig. 2 shows the typical stress-strain curves of a 2- μm pillar in both force-controlled (load-controlled) mode and depth-controlled (displacement-controlled) mode. The yield strength is about 0.13 GPa and the flow stress is about 0.15 GPa with typical displacement bursts in the magnitudes of $\sim 0.01\text{-}0.02$ GPa.

The effect of an external electric field on the plasticity of NaCl micro-pillars can be verified by implementing cyclic potential jumps during compression tests. Fig. 3 shows typical strain/stress-time and stress-strain curves recorded upon potential jumps (3 V). We found that when the potential is suddenly increased (to 3 V), the flow stress decreased rapidly to almost zero. Upon removing the potential, there

is a linear elastic response in stress back to original stress levels, leading to a full recovery. In the plastic regime of the micro-pillars, their flow stress can thus be tunable by applying an external electric potential.

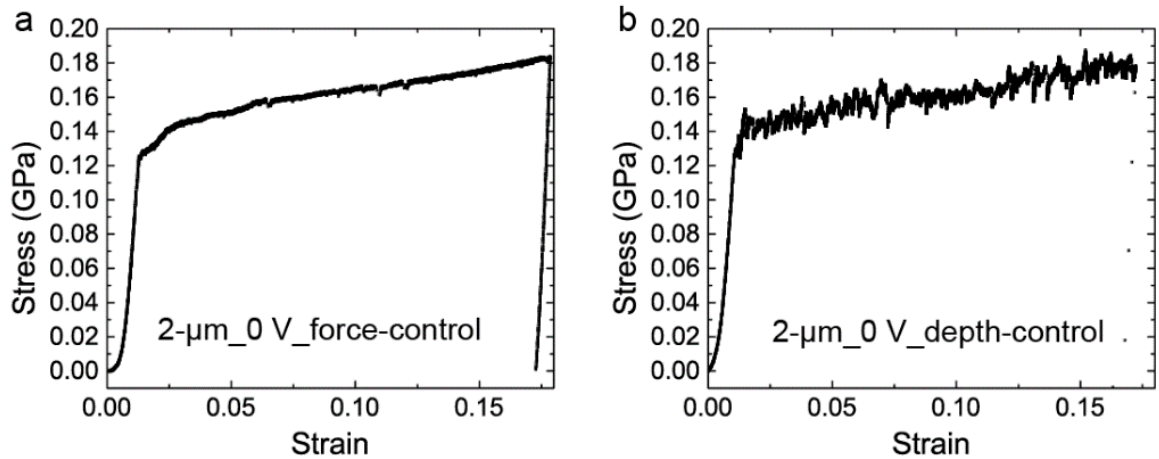


Fig. 2. Typical stress-strain curves for a 2- μm diameter pillar without electric field applied in (a) the force-controlled mode and (b) the depth-controlled mode.

The effect of the electric potential can be also examined in the original elastic regime of the micro-pillars. Under a constant stress that is much lower than the yield strength of the pillars in a force-controlled mode, we applied potential jumps during load holding, and meanwhile examine the change of displacement, as shown in Fig. 4. With 5 V “on” and “off”, non-reversible strains can be detected, suggesting that the dislocations are activated and move under the electric potential, although the externally applied stress is still far below yield strength. This effect can be repeated for many times. A higher magnitude of potential (e.g. 10 V) can also result in plastic strains, until the air is breakdown of air at ~ 15 V, as shown in Fig. S2.

Discussion

To confirm the electro-plasticity in micro-pillar compression, two possibilities have to be ruled out: electrostatic force and Joule heating. Assuming a simple scenario as plate electrodes during micro-compression, the 8- μm flat punch is an electrode and the gold layer at the pillar bottom is the other one. The electrostatic force, F_c , applied on the pillar can be estimated as:

$$F_c = \frac{\varepsilon_r \varepsilon_0 A U^2}{2d^2} \quad (1)$$

where ε_r is the relative permittivity, $\sim 5-6$ for NaCl, ε_0 is the vacuum permittivity, 8.854×10^{-12} F/m, A is the area of the parallel electrode plate, $\pi \times (4 \mu\text{m})^2$, U is the electric potential of 5 V and d is the distance of $\sim 5 \mu\text{m}$ between the two electrodes. We obtained that F_c is between 1-10 nN and electrostatic stress, σ_c is between 100-1000 Pa. Thus, the electrostatic stress calculated for the potential of 5 V and the pillar diameter of 2 μm is less than 0.001 MPa, which is too small to cause any plastic deformation. For Joule heating, the slightly doped NaCl is still an insulator and the electric current was not detected during the whole experimental procedure except when arcing occurred, with the resolution of 1 nA of the amperemeter. Thus, the Joule heating may not influence the detected change in plasticity.

The results shown in Figs. 3 and 4, as well as the above analysis, confirm that the rock salts are capable of electro-plasticity at the micrometer scale. According to the classical theory of electro-plasticity, the shear stress, τ , exerting on a charged dislocation along the slip direction can be simply calculated as [79] [80]:

$$\tau = qE \cos \theta / b \quad (2)$$

where q is the charge per unit length on a dislocation which depends on the impurity content, E is the magnitude of electric field, θ is the angle between the Burgers vector and the electric field and b is the Burgers vector. Considering deformation on the slip systems of $\langle 110 \rangle \{1\bar{1}0\}$ with θ of 45° , b of 0.4 nm, E of $\sim 1 \text{ MVm}^{-1}$ and q of $\sim 2 \times 10^{-10} \text{ Cm}^{-1}$ for a doped halide [81], we can obtain that τ is about 1 MPa, which is in the same order of the critical resolved shear stress (CRSS) for single-crystalline NaCl (~ 1 MPa) [15], suggesting that the external electric field may drive or assist the dislocation motion.

However, the micro-pillar NaCl specimen has a much higher CRSS ($\sim 20-80$ MPa) than the bulk single-crystalline one due to nucleation-controlled dislocation source strengthening. It is surprising to observe that the stress drop is much larger

than the calculated stress on charged dislocations. A different question to ask is whether an electric field only influences the motion of dislocations or also their nucleation. If the applied electric field only affects dislocation motion, in small-scale samples electric field might force all charged mobile dislocations to move out of the micro-pillar very quickly and annihilate at the sample surface, leading the sample into a state of dislocation lacking or free, similar to the phenomenon observed using *in situ* TEM [57]. In such circumstances, the flow strength of the micro-pillars would increase dramatically towards to its theoretical value.

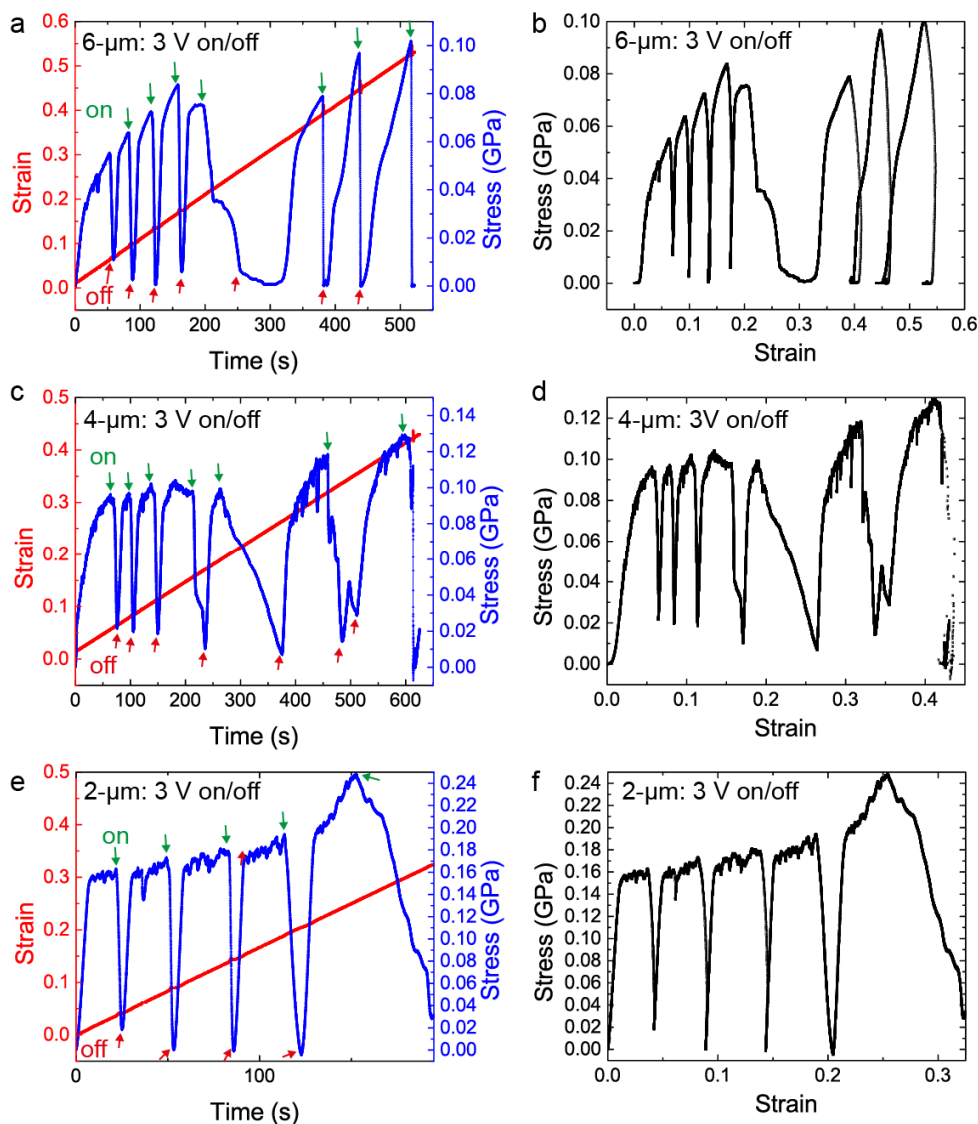


Fig. 3. Responses of plastic flow to potential jump (3V on/off) in a displacement control mode, strain and stress as a function of time for (a) 6 μm , (c) 4 μm and (e) 2 μm , respectively; stress-strain curves for the (b) 6 μm , (d) 4 μm and (f) 2 μm , respectively.

However, our observations in Figs. 3 and 4 do not show an increased flow stress, implying that the electric field might also influence the dislocation nucleation, which becomes strength controlling in small-scale samples. The effect of the electric field on dislocation nucleation is difficult to be observed in bulk materials due to a large number of dislocation sources. In addition, the relatively high surface area in small-scale samples (i.e. high surface area-to-volume ratio) might work as the dislocation source and fast track for dislocation motion, resulting in the considerable decrease of strength in micro-pillar samples. Up to now, how an electric field influences dislocation nucleation is still an open question to be answered.

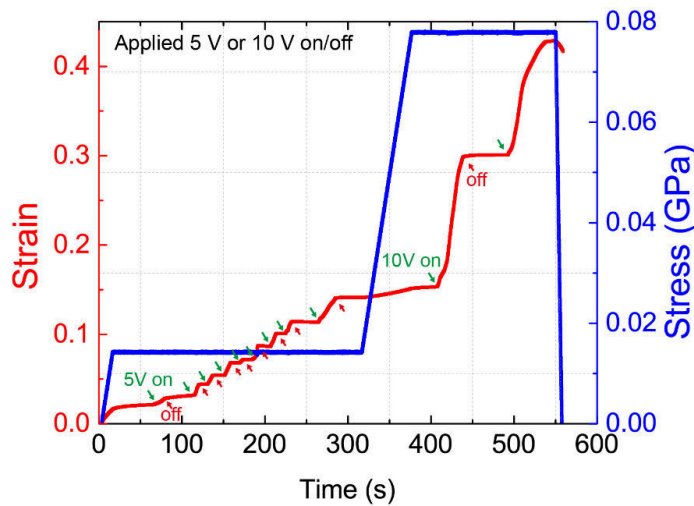


Fig. 4. Response of strain to potential jumps (5 V on/off and 10 V on/off) at a constant stress state in the elastic regime (below yield stress) for a 2- μm pillar.

The prospect of rock-salt ionic crystals at small scales is potentially technologically interesting. First, ionic crystals as actuator or sensor materials have a much larger strain range than other sophisticated smart materials. A large strain range from 0.01% to ~50% can be easily achieved using a single material. Second, the simple setup of the actuator makes it scalable to very small dimensions and can thus be employed in microelectronics and microsystems.

A final interesting point is that our experimental work on doped NaCl is simply an example of ionic crystals—a big family of solids; the above approach may be also applied to a number of different ionic crystals. For example, LiF and MgO

may be more appropriate candidates for actuator and sensor materials, due to their higher mechanical strength and chemical stability. Although much work remains for any proposed applications, the useful properties for rock-salt ionic crystals reported here may shed light on both fundamentally understanding the electro-plasticity phenomenon and their technological applications.

Challenges

The results are not always able to be repeated. The fabrication of the bottom electrode using FIB and how to avoid the electric field breakdown are very critical. The initial state of the samples (doping levels, dislocation density and annealing history) can also influence the results.

Outlook

A systematically experimental work following this report is urgently and strongly needed to give a better understanding the phenomena of electro-plasticity and plasto-electricity at small scales. The following questions should be answered in the future:

- What is the coupling between the traditional size effects on plasticity and an electric field?
- What are the minimum doping levels required to observe these phenomena at small scales? How about the baseline experiment with undoped NaCl?
- What is the critical electric field to generate plasticity without external stress?
- What are the limits of downscaling to observe the phenomena described above?
- Is the plasto-electric effect can be also detected at small scales? If so, as the electric current resulting from the plasto-electric effect requires a plastic strain gradient, which can be found in poorly aligned compression tests, bending geometries and torsion experiments, what is its sensitivity?

Acknowledgements

We thank ScopeM (ETHZ) for supplying electron microscopy facility and acknowledge the financial support through the Swiss National Science Foundation (SNF Grants: 200021_143633)

Supplementary Information

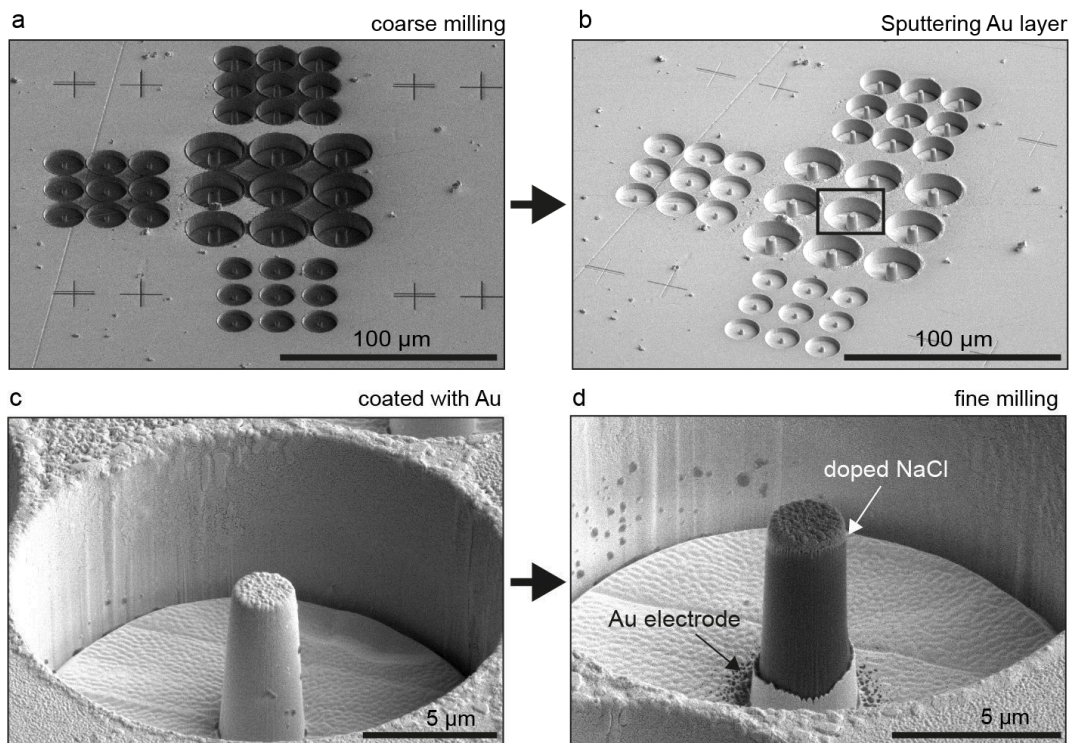


Fig. S1. Sample preparation for conductive micro-compression: (a) coarse milling of micro-pillars; (b) sputtering a 5-nm gold layer; (c) a 2 μm pillar, large magnification of the box area in (b); (d) the final fine milling to remove the gold layer on the pillar but retain the gold layer at the bottom.

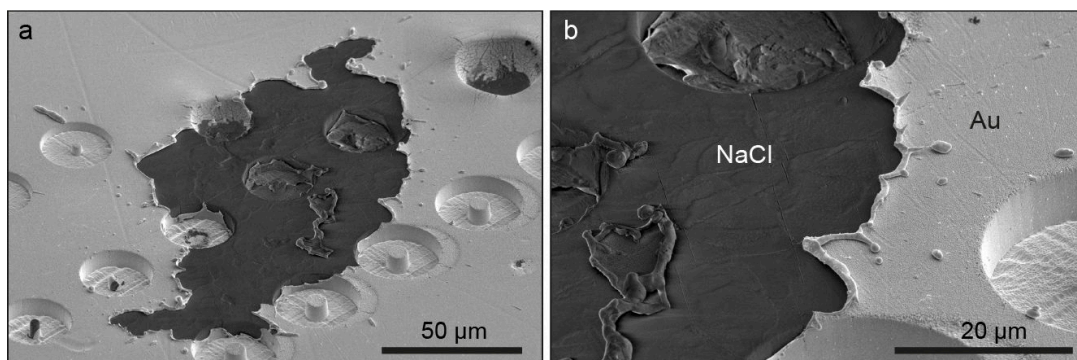


Fig. S2. SEM image of the sample surface after arcing under the applied voltage of 15 V: (a) the whole area and (b) a large magnification of the left area.

References

- [1] Uchic MD, Dimiduk DM, Florando JN, Nix WD. *Science* 2004;305:986.
- [2] Uchic MD, Shade PA, Dimiduk DM. *Annu Rev Mater Res* 2009;39:361.
- [3] Uchic MD, Dimiduk DM. *Materials Science and Engineering: A* 2005;400-401:268.
- [4] Volkert CA, Lilleodden ET. *Philos Mag* 2006;86:5567.
- [5] Greer JR, De Hosson JTM. *Progress in Materials Science* 2011;56:654.
- [6] Greer JR, Oliver WC, Nix WD. *Acta Mater* 2005;53:1821.
- [7] Ng KS, Ngan AHW. *Acta Mater* 2009;57:4902.
- [8] Kiener D, Motz C, Schoberl T, Jenko M, Dehm G. *Advanced Engineering Materials* 2006;8:1119.
- [9] Dou R, Derby B. *Scripta Materialia* 2009;61:524.
- [10] Schneider AS, Kaufmann D, Clark BG, Frick CP, Gruber PA, Monig R, Kraft O, Arzt E. *Phys Rev Lett* 2009;103.
- [11] Schneider AS, Frick CP, Clark BG, Gruber PA, Arzt E. *Mat Sci Eng a-Struct* 2011;528:1540.
- [12] Kim JY, Greer JR. *Acta Mater* 2009;57:5245.
- [13] Kim J-Y, Jang D, Greer JR. *Acta Mater* 2010;58:2355.
- [14] Nadgorny EM, Dimiduk DM, Uchic MD. *J Mater Res* 2008;23:2829.
- [15] Skrotzki W, Haasen P. *J Phys-Paris* 1981;42:3119.
- [16] Haasen P. *Mater Sci Tech-Lond* 1985;1:1013.
- [17] Korte S, Clegg WJ. *Philos Mag* 2011;91:1150.
- [18] Soler R, Molina-Aldareguia JM, Segurado J, Llorca J, Merino RI, Orera VM. *Int J Plasticity* 2012;36:50.
- [19] Rothwell WS, Greenler RG. *J Am Ceram Soc* 1964;47:585.
- [20] Spolenak R, Dietiker M, Buzzi S, Pigozzi G, Loffler JF. *Acta Mater* 2011;59:2180.
- [21] Loffler JF, Buzzi S, Dietiker M, Kunze K, Spolenak R. *Philos Mag* 2009;89:869.
- [22] Kiener D, Motz C, Dehm G. *Materials Science and Engineering: A* 2009;505:79.
- [23] Korte S, Ritter M, Jiao C, Midgley PA, Clegg WJ. *Acta Mater* 2011;59:7241.
- [24] Niederberger C, Mook WM, Maeder X, Michler J. *Materials Science and Engineering: A* 2010;527:4306.
- [25] Frederikse H, Lide D. CRC, Boca Raton 1996.
- [26] Hull DaDJB, editor *Introduction to Dislocations*: Elsevier Butterworth Heinemann: Oxford, 2001.
- [27] Radhakrishna S, Chowdari BVR. *Fortschritte der Physik* 1977;25:511.
- [28] Catlow CRA, Diller KM, Hobbs LW. *Philos Mag A* 1980;42:123.
- [29] Groves GW, Kelly A. *Philos Mag* 1963;8:1437.
- [30] Greer JR, Nix WD. *Phys Rev B* 2006;73.
- [31] Frick CP, Clark BG, Orso S, Schneider AS, Arzt E. *Materials Science and Engineering: A* 2008;489:319.

- [32] Kraft O. Size effects on deformation and fatigue of thin films and small structures. CAMTEC. Cambridge, UK, Presented, 2006.
- [33] Liu ZG, Skrotzki W. *Phys Status Solidi A* 1982;70:433.
- [34] Kraft O, Gruber PA, Monig R, Weygand D. *Annual Review of Materials Research*, Vol 40 2010;40:293.
- [35] Dimiduk DM, Uchic MD, Parthasarathy TA. *Acta Mater* 2005;53:4065.
- [36] Ng KS, Ngan AHW. *Acta Mater* 2008;56:1712.
- [37] Han SM, Bozorg-Grayeli T, Groves JR, Nix WD. *Scripta Materialia* 2010;63:1153.
- [38] D. Kaufmann RM, C.A. Volkert, O. Kraft,. *Int J Plasticity* 2011;27:470.
- [39] Ostlund F, Rzepiejewska-Malyska K, Leifer K, Hale LM, Tang YY, Ballarini R, Gerberich WW, Michler J. *Adv Funct Mater* 2009;19:2439.
- [40] Korte S, Barnard JS, Steam RJ, Clegg WJ. *Int J Plasticity* 2011;27:1853.
- [41] Rabier J, Montagne A, Wheeler JM, Demenet JL, Michler J, Ghisleni R. *physica status solidi (c)* 2013;10:11.
- [42] Ostlund F, Howie PR, Ghisleni R, Korte S, Leifer K, Clegg WJ, Michler J. *Philos Mag* 2011;91:1190.
- [43] Thilly L, Ghisleni R, Swistak C, Michler J. *Philos Mag* 2012;92:3315.
- [44] Parthasarathy TA, Rao SI, Dimiduk DM, Uchic MD, Trinkle DR. *Scripta Materialia* 2007;56:313.
- [45] Rao SI, Dimiduk DM, Tang M, Parthasarathy TA, Uchic MD, Woodward C. *Philos Mag* 2007;87:4777.
- [46] Oh SH, Legros M, Kiener D, Dehm G. *Nat Mater* 2009;8:95.
- [47] Kim JY, Jang DC, Greer JR. *Int J Plasticity* 2012;28:46.
- [48] Schneider AS, Frick CP, Arzt E, Clegg WJ, Korte S. *Philosophical Magazine Letters* 2013;93:1.
- [49] Schneider AS, Kiener D, Yakacki CM, Maier HJ, Gruber PA, Tamura N, Kunz M, Minor AM, Frick CP. *Materials Science and Engineering: A* 2013;559:147.
- [50] El-Awady JA, Uchic MD, Shade PA, Kim S-L, Rao SI, Dimiduk DM, Woodward C. *Scripta Materialia* 2013;68:207.
- [51] Foitzik A, Skrotzki W, Haasen P. *Mat Sci Eng a-Struct* 1989;113:399.
- [52] Zou Y, Spolenak R. *Philosophical Magazine Letters* 2013;93:431.
- [53] Lotfian S, Rodríguez M, Yazzie KE, Chawla N, Llorca J, Molina-Aldareguía JM. *Acta Mater* 2013;61:4439.
- [54] Schneider AS, Clark BG, Frick CP, Gruber PA, Arzt E. *Philosophical Magazine Letters* 2010;90:841.
- [55] Soler R, Molina-Aldareguia JM, Segurado J, Llorca J. *Advanced Engineering Materials* 2012;14:1004.
- [56] Johnston WG, Gilman JJ. *J Appl Phys* 1959;30:129.
- [57] Minor AM, Shan ZW, Mishra RK, Asif SAS, Warren OL. *Nat Mater* 2008;7:115.
- [58] Tinder RF, Trzil JP. *Acta Metallurgica* 1973;21:975.
- [59] Dimiduk DM, Woodward C, LeSar R, Uchic MD. *Science* 2006;312:1188.
- [60] Suzuki T, Skrotzki W, Haasen P. *physica status solidi (b)* 1981;103:763.
- [61] Tasker PW, Bullough TJ. *Philosophical Magazine A* 1981;43:313.

- [62] Weinberger CR, Cai W. Proceedings of the National Academy of Sciences 2008;105:14304.
- [63] Caillard D, Martin J-L. Thermally activated mechanisms in crystal plasticity: Elsevier, 2003.
- [64] Ng KS, Ngan AHW. Scripta Materialia 2008;59:796.
- [65] Norfleet DM, Dimiduk DM, Polasik SJ, Uchic MD, Mills MJ. Acta Mater 2008;56:2988.
- [66] Celli V, Thomson R, Kabler M, Ninomiya T. Phys Rev 1963;131:58.
- [67] Volkert C, Minor A. Mrs Bull 2007;32:389.
- [68] Crawley EF, De Luis J. AIAA journal 1987;25:1373.
- [69] Muralt P. J Micromech Microeng 2000;10:136.
- [70] Baz A, Imam K, McCoy J. Journal of Sound and Vibration 1990;140:437.
- [71] Cohen RE. Nature 1992;358:136.
- [72] Caffyn JE, Goodfellow TL. Nature 1955;176:878.
- [73] Fischbach DB, Nowick AS. Phys Rev 1955;99:1333.
- [74] Machlin ES. J Appl Phys 1959;30:1109.
- [75] Hull D, Bacon DJ. Introduction to dislocations: Elsevier, 2011.
- [76] Whitworth RW. Adv Phys 1975;24:203.
- [77] Li JCM. Materials Science and Engineering a-Structural Materials Properties Microstructure and Processing 1999;287:265.
- [78] Lai A, Du ZH, Gan CL, Schuh CA. Science 2013;341:1505.
- [79] Conrad H. Materials Science and Engineering A 2000;287:276.
- [80] Yamada T, Ozaki J, Kataoka T. Philos Mag A 1988;58:385.
- [81] Kataoka T, Colombo L, Li JCM. Philos Mag A 1984;49:395.

Chapter 3. Size Effect in High-entropy Alloys

3.1. Single crystalline micro-pillars made of a Nb₂₅Mo₂₅Ta₂₅W₂₅ refractory high-entropy alloy⁴

Abstract

High-entropy alloys (HEA) are evolving multi-component intermetallic systems, wherein multiple principal elements tend to form single solid-solution-like phases with strong tendency to solid solution strengthening. In this study, a Nb₂₅Mo₂₅Ta₂₅W₂₅ refractory HEA was synthesized by arc melting and well homogenized at 1800 °C. Single-crystalline HEA pillars in two orientations ([001] and [316]) and with diameters ranging from two microns to two hundred nanometers were produced by focused ion beam milling and compressed using a flat-punch tip in a nanoindenter. The HEA pillar samples can reach extraordinarily high strength levels of ~4-4.5 GPa, which is ~3-3.5 times higher than that of the bulk HEA (*Senkov et al. Intermetallics 2011*), meanwhile the ductility is significantly improved. Compared to pure Nb, Mo, Ta and W pillars (*Schneider et al. Phys. Rev. Lett. 2009* and *Kim et al. Acta Mater. 2010*), the HEA pillars exhibit higher strengths than any of them in both absolute and normalized values, and the HEA pillars also show relatively low compressive size effects, as evaluated by the log–log slope of strength vs. pillar diameter. The higher strength levels and lower size dependence for the HEA could be attributed to the increased lattice resistance caused by localized distortion at atomic length scales. The correlation between normalized strengths, length scales and temperatures for body-centered-cubic structured pillars is illustrated, and the relevance of a size-

⁴ Y. Zou, S. Maiti, W. Steurer, R. Spolenak, “Size-dependent plasticity in an Nb₂₅Mo₂₅Ta₂₅W₂₅ refractory high-entropy alloy” *Acta Materialia* 65 (2014) 85-97.

effect slope as well as the additivity of strengthening mechanisms is critically discussed.

Introduction

High-entropy alloys (HEA), conceptualized by Yeh and Chen *et al.* in 2004 [1], are usually made of five or more metallic elements with equimolar or near-equimolar ratios, where their configurational entropy, S_{conf} , increases with the number of elements n as $\Delta S_{conf} = R \ln(n)$, with R the universal gas constant. The high entropy stabilizes solid-solution phases at elevated temperatures and single-phase HEAs prevent the formation of possible intermetallics in these compositions [1-3]. HEAs may have interesting applications due to their simple average structure (body-centered cubic, bcc, or face-centered cubic, fcc), their distorted lattice and low diffusion rate in a multi-component system [1-5]. The main potential applications of HEAs are in the development of high-strength and high-temperature sustaining alloys [6, 7], wear-resistant materials [2] and diffusion barriers [8]. The conventional HEAs based on Al, Co, Cr, Cu, Fe and Ni have reached the strengths and workability comparable to those of steels [6, 7]. To achieve higher strengths in the high-temperature regime above 1100°C, the use of refractory metals in HEAs was implemented by Senkov *et al.* [9, 10], which is particularly relevant to aerospace industry, but their low room-temperature ductility might be a limitation for further processing steps. Furthermore, refractory metals or alloys have also been proposed to be employed for electrical resistors, medical implants, and micro- and nano-electromechanical systems (MEMS and NEMS) [11, 12]. So, it is also of great interest to apply refractory HEAs in the fabrication of micro- or nano- devices. However, to the authors' knowledge, so far all the investigations on refractory HEAs have been limited to bulk samples, and no study on the mechanical properties of refractory HEAs at submicron or nanometer scale has been reported.

Small-sized (extrinsic size rather than intrinsic size) metallic specimens, such as thin films, wires and pillars, exhibit size-related strengths in a range from several microns down to a few nanometers [13-15]. For the last several years, great advances have been made to understand the mechanical behavior of materials in micron and sub-micron regimes by applying the micro-compression technique to ion-milled pillars (see reviews [16, 17]). It has been widely found that the yield or flow strength (σ) of the pillar can be strongly increased when its dimension (D) is decreased, commonly expressed by a relationship of $\sigma \propto D^m$ [18, 19], where m is size-effect exponent. Fcc metals (e.g. Ni, Au, Al and Cu) exhibit a pronounced and constant size dependence of plasticity with m in the range between -0.6 and -0.9 [20-22]. Bcc metals (e.g. Nb, Mo, V, Ta and W) have a much more complex size-related behavior with various m values ranging from -0.2 to -0.9, reported by Schneider *et al.* [23, 24], Kim *et al.* [25, 26] and Han *et al.* [27]. Schneider and his co-workers [23] noticed that various m values in bcc metals could be correlated with different critical temperatures (T_c), above which flow stress becomes insensitive to test temperature, and equivalently residual Peierls potentials: the higher T_c , the lower size dependence. The popular interpretation of this correlation is that different non-planar dislocation cores in bcc metals play important roles in the mobility of screw dislocations, which influences the size dependence levels of bcc pillars [17, 24, 28, 29]. Both the simulation [30] and experiment [31] suggest that bcc and fcc metal pillars differ in the controlling mechanisms of the size effect. However, the exact mechanism which determines the size-dependent plasticity in bcc metals remains under debate.

HEAs are essentially solid solutions with a simple fcc or bcc structure. Now, two questions arise: what are the strength and ductility of single-crystalline HEAs at micron and submicron scales, compared with their bulk forms? And what is the size-dependent behavior of bcc refractory HEAs, compared with that of pure bcc metals? In this study, the mechanical properties of Nb₂₅Mo₂₅Ta₂₅W₂₅ HEA pillars with diameters ranging from approximately 2 μm to 200 nm were investigated using the micro-compression method. This work aims to answer the two

questions above and attempts to shed light on potential applications of HEAs in micro/nano device design.

Materials and methods

Compacted pellets of an approximately equimolar mixture of pure Nb, Mo, Ta and W powders were arc-melted in argon atmosphere. A Ti getter was used to consume any trace of oxygen in the argon atmosphere. The button-shaped cast was flipped upside down and re-melted four times. The cast alloy was then sealed inside a Ta ampoule and homogenized at 1800 °C (approximately 65% of the calculated melting temperature [9]) for 7 days. The phase purity of the homogenized HEA sample was determined by powder X-ray diffraction (XRD) (PANalytical X'Pert PRO diffraction system) using $\text{Cu-K}\alpha_1$ monochromatic radiation in a 2θ (diffraction angle) range from 20° to 120°. In order to determine the atomic displacement parameters (ADP), a piece of the HEA crystal smaller than 40 micron was extracted to collect a single-crystal XRD dataset. A single-crystal diffractometer with $\text{MoK}\alpha$ radiation source and a CCD detector (Oxford Diffraction, Xcalibur) was used for data collection. For microstructure and composition analysis, a SU-70 Hitachi scanning electron microscope (SEM) combined with energy-dispersive X-ray spectroscopy (EDX) (X-MAX, Oxford Instruments) was employed. A FEI Tecnai F30 high-resolution transmission electron microscope (HRTEM) was used to investigate the structures on sub-micron and nanometer levels. For the TEM investigation, the HEA sample was embedded inside a copper tube, cut into thin discs, fine polished with sand papers, dimple-polished on both sides with 3- μm diamond suspension and finally thinned by Ar jet milling.

The hardness of the HEA samples (as-cast and as-annealed for 2, 4 and 7 days) and the pure elemental bcc samples (Nb, Mo, Ta and W as-annealed for 7 days) was measured in 15 different positions using a Vickers micro-hardness indenter

with a load of 200 grams and dwell time of 10 seconds. The HEA sample which was homogenized for 7 days was used for the micro-compression tests. The orientations of the grains were determined by electron back-scatter diffraction (EBSD) using a FEI Quanta 200 FEG SEM. Before EBSD characterization, the HEA bulk sample was cross sectioned using an alumina cut-off wheel (Struers 50A13), polished using 3- μm diamond paste and finally polished using 60-nm SiO_2 particle suspension. After EBSD characterization, two orientations were selected to produce pillars using a focused ion beam (FIB) system (Helios Nanolab 600i, FEI): [316] orientation (tolerance angle $< 6^\circ$) with single-slip systems and [001] orientation (tolerance angle $< 4^\circ$) with multiple-slip systems, as circled in Fig. 1, respectively. The latter orientation can be used to make a direct comparison with the pure bcc pillars which have been reported in the literature [23, 26].

A two-step milling method was employed: 2.5 nA for coarse milling and 10-40 pA for fine milling. The FIB-milled pillars have diameters of approximately 2 μm , 1 μm , 500 nm and 250 nm and aspect ratios of 2.5-5. A taper of 2-3 $^\circ$ was generally observed in those pillars, and the top diameters were chosen to calculate engineering stresses. At least four pillars of each size and each orientation were compressed using a nanoindenter (Triboindenter, Hysitron Inc., USA) with a diamond flat-punch tip (5 μm in diameter, Synton-MDP, Switzerland) in the displacement control mode by feedback mechanism. A strain rate of $2 \times 10^{-3} \text{ s}^{-1}$ was used for all the compression tests. The displacement and loading time were changed according to the pillar height in order to keep the strain rate constant. The morphologies of the pillars were characterized using a high-resolution SEM (MAGELLAN, FEI) before and after the compressions.

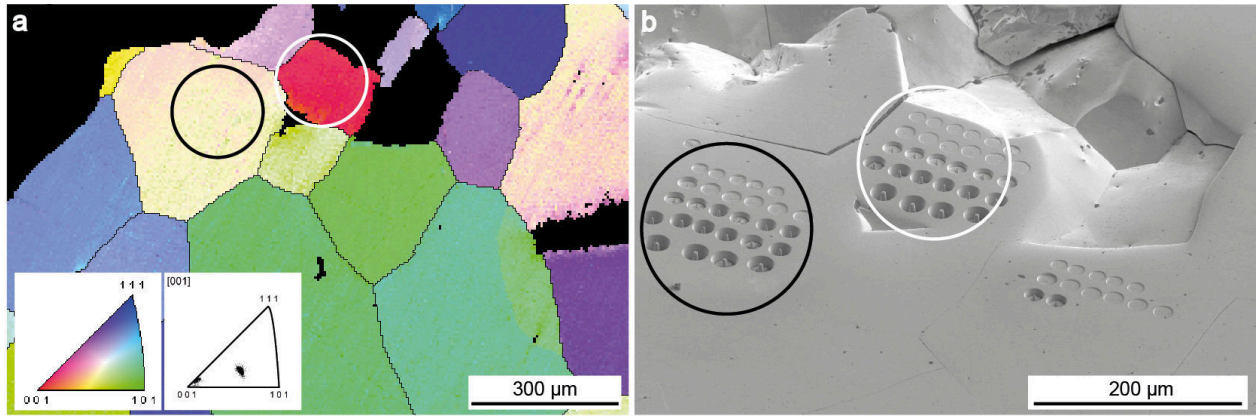


Fig. 1. (a) EBSD inverse pole figure map of the cross-section of the HEA bulk specimen before FIB milling. Two grains which were selected to mill pillars are indicated by circles: the left one is [316]-oriented (tolerance angle $< 6^\circ$) and the right one is [001]-oriented (tolerance angle $< 4^\circ$). The orientations of the two selected grains are also indicated in the inverse pole figure at the bottom. (b) A typical SEM image (SE mode) of the HEA specimen after FIB milling. The two selected grains are indicated by circles as well.

Results

Microstructure and phase analysis of bulk specimens

The powder XRD pattern of the homogenized HEA indicates a single-phase bcc structure with all the peaks indexed, as shown in Fig. 2. The experimental lattice parameter is $3.222 \pm 0.001 \text{ \AA}$, which is close to the predicted value of 3.229 \AA , according to Vegard's law [32]. After homogenization for 7 days, the grain size of the HEA is larger than 200 micron. The compositional homogeneity of the sample was measured by EDX with line scans inside a grain and across a grain boundary, respectively, as shown in Fig. 3. The back-scattered electron (BSE) images show no significant contrast either within a grain (Fig. 3a) or between two adjacent grains (Fig. 3c) and no trace of a dendritic segregation was found as that in the literature [9, 10]. The corresponding elemental analyses obtained by EDX are plotted in Figs. 3b and 3d. The elemental composition varies by 1-2% and the overall atomic compositions vary within 3%, compared to $\sim 10\%$ variation in the literature [9]. The average hardness value of the HEA is between 4.52 GPa and 4.85 GPa (Table 1), close to the value as reported in the literature (4.46 GPa) [10]. The standard deviations of the hardness decrease from 387 MPa to 58 MPa over

a homogenization time of 7 days. The HEA shows a much higher hardness than the pure bcc elements measured here, even ~1 GPa higher than pure W.

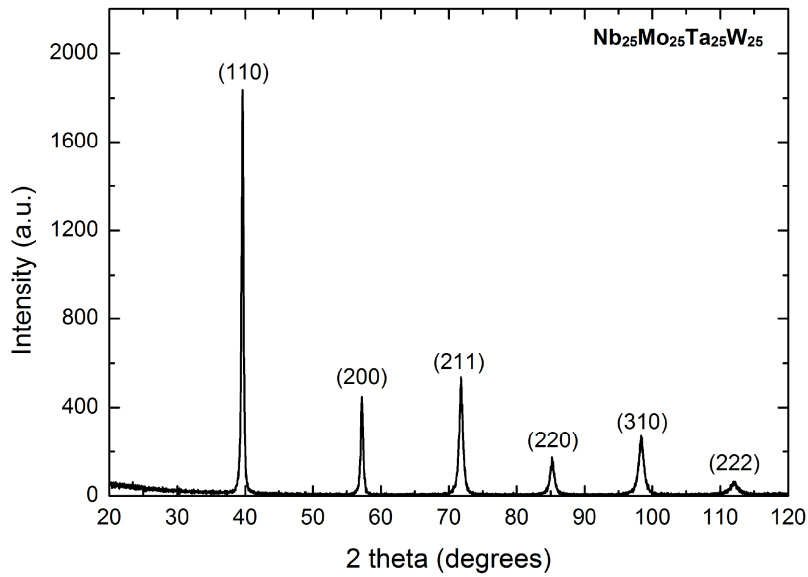


Fig. 2. X-ray diffraction pattern ($\text{CuK}\alpha_1$) of the Nb-Mo-Ta-W HEA annealed at 1800°C for 7 days. The pattern indicates a single-phase bcc structure.

The bright-field HRTEM image (Fig. 4a) was taken with the zone axis along the [100] direction. Fig. 4b shows a Fourier-filtered image of the lattice fringes in Fig. 4a. Two boxed regions in Fig. 4b are enlarged at the bottom and traced for their lattice fringes, as shown in Figs. 4c-f. The HRTEM images (Figs. 4a and 4b) show the (110) set of lattice planes and the fringes continue through the whole length of the sample. The Fourier-filtered image (Fig. 4b) shows that there are visible mismatches and local distortions in both the two sets of parallel lattice fringes. These local lattice distortions induce slight amount of kinks and bends in the lattice layers as also observed in bcc CoCrFeNiAl HEA [33].

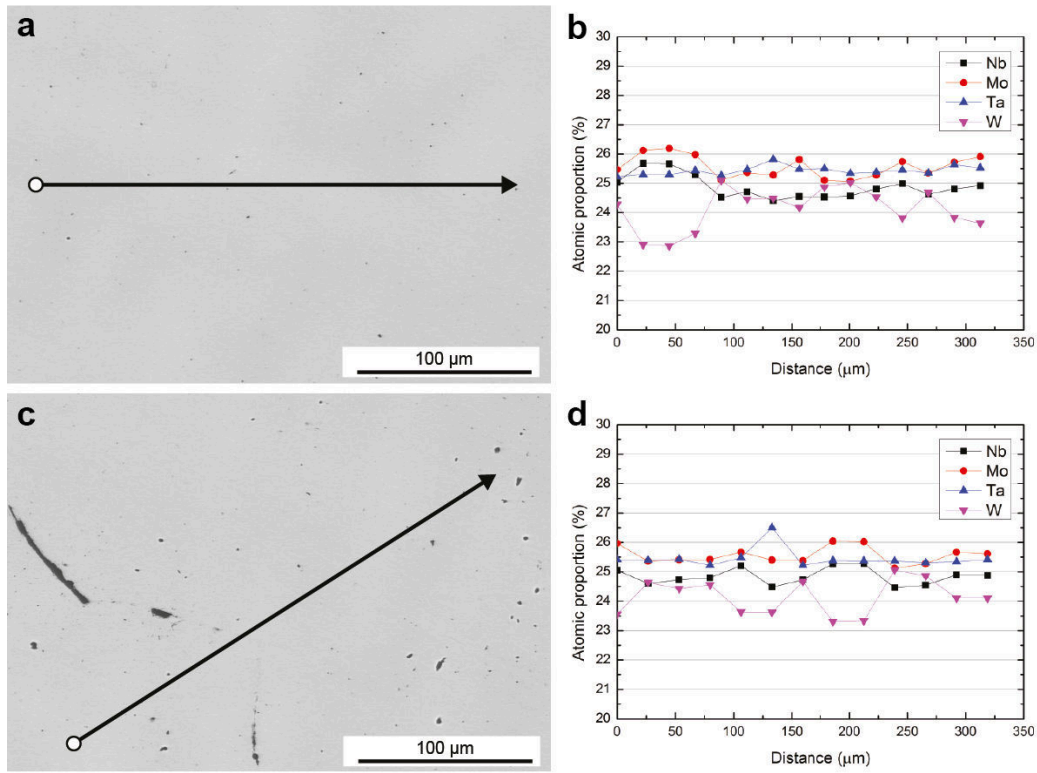


Fig. 3. SEM images (BSE mode) of the cross-sections of the Nb-Mo-Ta-W HEA annealed at 1800 °C for 7 days: (a) inside a grain and (c) including a grain boundary. The arrows indicate the line-scans for EDX analysis. (b) and (d) show the corresponding atomic proportions of the four elements along the lines in (a) and (c), respectively. The typical EDX resolution limit is about 1.0 at%.

Table 1. The average values and standard deviations (in MPa) of the Vickers microhardness of 15 random indents on the HEAs (as-cast and as-annealed at 1800 °C for 2, 4 and 7 days) and pure Nb, Mo, Ta and W (as-annealed at 1800 °C for 7 days).

Materials	Nb 7D	Mo 7D	Ta 7D	W 7D	HEA Cast	HEA 2D	HEA 4D	HEA 7D
Average	1086	1898	1488	3714	4853	4766	4803	4515
Std. Dev.	16	51	52	96	387	362	234	58

In order to obtain the ADP, the single-crystal diffraction dataset was refined by the program *SHELXL97* [34]. The average ADP value of the HEA was determined to 0.0091 Å². The average thermal component of the ADP, U_t , calculated from the Debye-Waller factors of the pure elements is 0.0037 Å² [35]. The static component of ADP, U_s , is calculated in a similar approach as in Ref. [40] and has the form:

$$U_s = \sum c_i (d_i - d_{al})^2 \quad (1)$$

where c_i is the mole fraction of the element i , d_i the lattice parameter of the pure element and d_{al} the lattice parameter of the HEA. The expected total ADP of the alloy, U_{al} , including the thermal and static components are calculated to be $U_t + U_s = 0.0037 + 0.0055 = 0.0092 \text{ \AA}^2$, which is close to the experimental value of 0.0091 \AA^2 .

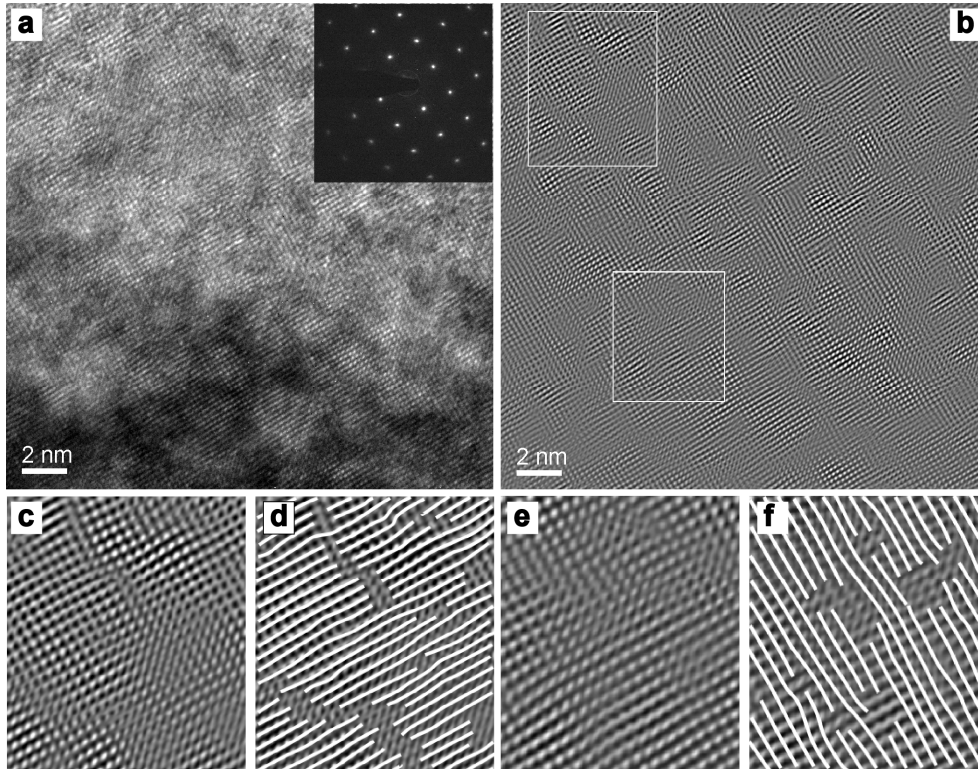


Fig. 4. High-resolution TEM images of the Nb-Mo-Ta-W HEA homogenized at 1800°C for 7 days: (a) a bright-field TEM image oriented in [100] zone axis and the corresponding electron-diffraction pattern; (b) an inverse fast Fourier transform image of the area (a); (c) and (e) are enlarged images of the indicated boxes in (b); (d) and (f) show lattice fringes which are traced for (c) and (e), respectively, to indicate the regions with lattice distortions.

Compression of pillar samples

As shown in the SEM images (Figs. 5a and 5b), single slips are observed in 2- μm and 1- μm [316]-oriented HEA pillars, which have slip bands traversing along the gauge length of the samples. The slip bands are oriented at approximately 40-70° off the loading axis. A second slip system could be also activated when the pillars were experienced large strains. Some localized shear offsets along slip planes are observed at the top part of the pillars (Fig. 5b). For smaller pillars (~500 nm and

~250 nm in diameter, Figs. 5c and 5d), multiple slips are usually observed. The multiple slips might be due to a slight misalignment between the pillar top and the flat punch or due to the influence of the tolerance angle. The multiple slips are expected to contribute to strain hardening. As shown in Fig. 5b, occasionally some degree of bending is observed. The data from bent pillars are not considered in the analysis. Compressed [001]-oriented HEA pillars are shown in Fig. 6. Wavy morphologies can be found in both large and small pillars. This wavy-slip feature may be attributed to the cross slip of screw dislocations along $\langle 111 \rangle$ directions, which is commonly observed in deformed bcc metals [36, 37]. This post-deformed morphology of the HEA pillars is similar to that of the W pillars as reported in [23, 26].

Figs. 7a and 7b show engineering stress-strain relationships for the representative [316]- and [100]-oriented HEA pillars, respectively. Although the crystal orientations are different, the two groups of pillars exhibit similar features of both stress magnitude and characters of curves: the small pillars have higher flow strengths than the big pillars and displacement bursts occurred in both big and small pillars, showing a similar phenomenon to that observed in fcc and bcc metal pillars [27, 36, 37]. The displacement bursts may be due to a relatively low feedback rate in displacement mode compared with the burst events, as explained in [38, 39]. In both orientations, the smaller pillars exhibit stronger displacement bursts in both magnitude and frequency meanwhile the smaller pillars show higher strain hardening rate than the big pillars, which might be due to more activated and interacting slip systems in the small dimension samples. To reduce the influence of the displacement bursts on analysis and make a direct comparison with pure bcc metal pillars in the references [23, 26], the highest flow stress values measured below 5% strain and 8% strain, which are defined as $\sigma_{0.05}$ and $\sigma_{0.08}$, respectively, are used to compare the strengths for different pillar dimensions.

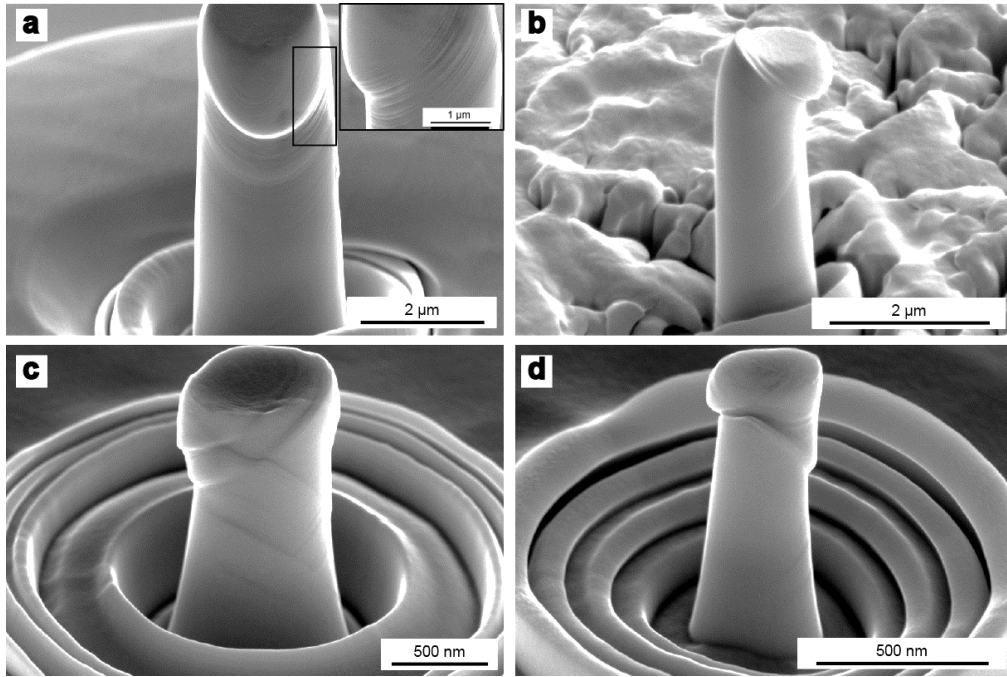


Fig. 5. SEM images (SE mode) of post-compressed [316]-oriented HEA pillars with approximate diameters of: (a) 2 μm , (b) 1 μm , (c) 500 nm and (d) 250 nm. An enlarged image which presents sharp slip bands is shown in the inset of (a).

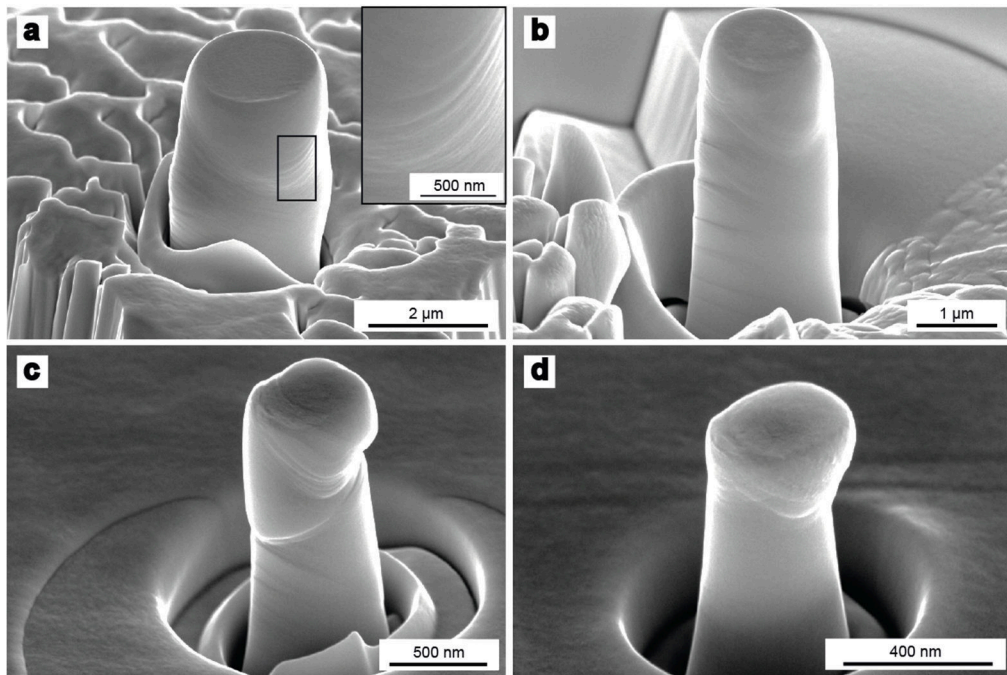


Fig. 6. SEM images (SE mode) of post-compressed [001]-oriented HEA pillars with approximate diameters of: (a) 2 μm , (b) 1 μm , (c) 500 nm and (d) 250 nm. An enlarge image which presents a wavy morphology is shown in the inset of (a).

The changes of $\sigma_{0.05}$ and $\sigma_{0.08}$ due to different pillar diameters for both [316] and [001] orientations are plotted in Fig. 8: for $\sigma_{0.05}$, [316] and [001]-orientated HEA pillars have size-effect exponents (m) of -0.30 ± 0.02 and -0.33 ± 0.02 ,

respectively; for $\sigma_{0.08}$, [316] and [001]-orientated HEA pillars have m values of -0.32 ± 0.02 and -0.36 ± 0.02 , respectively. The absolute strength levels for the pillars in two orientations are close to each other. [316]-oriented pillars have a slightly lower size dependence than [001]-oriented pillars.

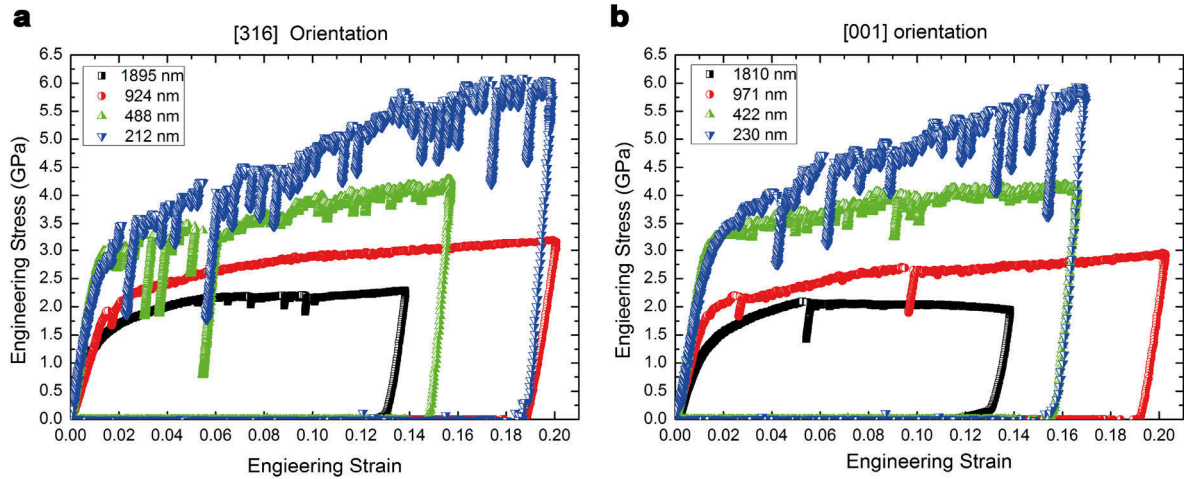


Fig. 7. Representative engineering stress-strain curves for (a) [316]-oriented and (b) [001]-oriented single crystalline HEA pillars with the diameters ranging from $\sim 2 \mu\text{m}$ to $\sim 200 \text{ nm}$.

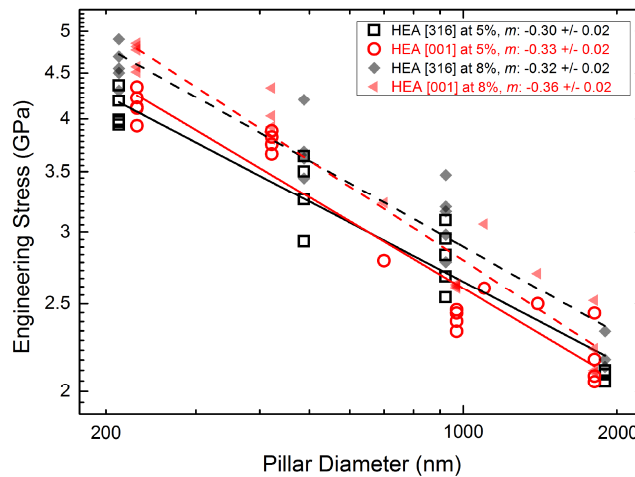


Fig. 8. The relationship between engineering stresses at 5% strain and 8% strain ($\sigma_{0.05}$ and $\sigma_{0.08}$) and pillar diameters for [316]- and [001]-oriented HEA pillars.

Discussion

Solid solution effect

Some physical properties of Nb, Mo, Ta, W and the HEA are listed in Table 2. The atomic sizes of Nb and Ta are about 5% larger than Mo and W. This atomic size misfit of the constituent elements in the HEA can cause a highly distorted

lattice (Fig. 4) with localized strains throughout the whole sample. The lattice distortion in the HEA specimen appears as splits in the atomic positions and localized shearing of several adjacent lattice fringes. The calculated ADP was approximately 2.5 times higher than the expected thermal ADP, also suggesting a local lattice distortion due to the difference in atomic sizes. The ADP values have been used as a measure of the local lattice distortion in a bcc ZrNbHf alloy [40], where it was observed that the average ADP of the alloy was many times higher than the expected thermal ADP. In addition, the thermal and static components of the modeled ADPs, if added up, match the experimental refined ADP of the HEA closely. This might validate the simple model of calculating static ADPs, and the average static displacement of the atoms could be around 0.074 Å. Moreover, the modulus misfit between the constituent elements has a large range: about 4% between W and Mo; around 70% between W and Nb. Compared with the pure bcc elements, the binding forces around different solute atoms in the HEA could vary depending on surrounding elements. This non-uniform bonding feature at atomic length level may lead to extremely inhomogeneous stress fields throughout the HEA specimen.

Table 2. Physical properties of pure Nb, Mo, Ta, W and the HEA.

Metal	a (Å)	ρ (g/cm ³)	τ_0^* (MPa)	G (GPa)	τ_0^*/G (10 ⁻³)	T_m (K)	T_c (K)	m for $\sigma_{0.05}$	m for $\sigma_{0.08}$
Nb	3.301	8.57	415	47.2 [41]	8.7	2750	350 [23], 290 [26]	-0.48 [23]	-0.93 [26]
Mo	3.147	10.28	730	158 [24]	4.6	2896	480 [23], 465 [26]	-0.38 [23]	-0.44 [26]
Ta	3.303	16.65	340	62.8 [41]	5.4	3290	450 [23], 440 [26]	-0.41 [23]	-0.43 [26]
W	3.165	19.25	280- 350	164 [42]	1.7- 2.1	3695	800 [23], 760 [26]	-0.21 [23]	-0.44 [26]
HEA Calc.	3.229	13.69	-	114	-	3158	520 [23], 489 [26]	-0.37	-0.56
HEA Exp.	3.222	-	-	-	-	-	~900-1200 [10]	-0.33	-0.36

The crystal lattice parameter, a , density, ρ , and melting temperature, T_m , of pure Nb, Mo, Ta and W are adapted from Table 2 of ref. [9]; Peierls stress, τ_0^* , is collected from ref. [42], the corresponding shear modulus, G , is chosen for the active slip systems of $\{112\} \langle 111 \rangle$ [24, 41, 42]; the values of critical temperature, T_c , and size-effect exponent, m , are chosen from refs. [23] and [26]. To give an estimation of T_c in the bulk HEA [10], an intersection point between the high-temperature linear part and the low-temperature linear part in the measured stress-temperature curve is chosen as the value of T_c . HEA Calc. is calculated due to the rule of mixtures. HEA Exp. is the value measured in this study.

In bcc metals, edge dislocations move much more easily than screw dislocations. Thus, the latter ones mainly control plastic flows, by a processes of kink nucleation and motion [43]. The effect of lattice distortion on plastic strength may be twofold [44, 45]: On one hand, the lattice distortion, by its stress field, may facilitate the nucleation of new kink pairs, leading to solid-solution softening; On the other hand, the propagation of screw dislocations is retarded by the stress fields of localized solute obstacles along the slip planes, resulting in solid-solution hardening. These two mechanisms compete in bcc solid solutions during plastic deformation. However, the phenomenon of solid-solution softening is mostly observed at intermediate low temperatures (~ 100 - 250 K) and low concentrations (less than ~ 5 at.%). In our study, due to the room-temperature measurement and high-concentration alloying, the solid-solution hardening effect should be dominant in the HEA.

HEA pillar vs. HEA bulk: ductility and strength

Ductility: Since the concept of HEA design was introduced [1], HEAs have been considered as potential high-performance structural materials. However, a big limitation to use refractory HEAs is their low ductility and toughness at room temperature. Senkov *et al.* [10] found that $\text{Nb}_{25}\text{Mo}_{25}\text{Ta}_{25}\text{W}_{25}$ and

$\text{Nb}_{20}\text{Mo}_{20}\text{Ta}_{20}\text{V}_{20}\text{W}_{20}$ HEAs fractured along grain boundaries at about 2% compressive strain at room temperature. In Fig. 9a, a fracture surface along the grain boundaries of the bulk HEA can be seen. Two HEA pillars with and without a grain boundary are compared, as shown in Figs. 9b and 9c. It is found that a crack that propagated along the grain boundary caused the failure of a 3- μm bicrystal pillar (Fig. 9b). The pillar top area and the corresponding force-displacement curve are shown in the insets. Fig. 9c exhibits a post-deformed [001]-oriented single-crystalline pillar, which can even bear large-strain bending ($\sim 75^\circ$) without any fracture or crack on the surface, corresponding to a tensile strain larger than 20% on one side of the pillar. This comparison suggests that the elimination of grain boundaries and decrease of sample size could significantly increase the ductility of HEAs.

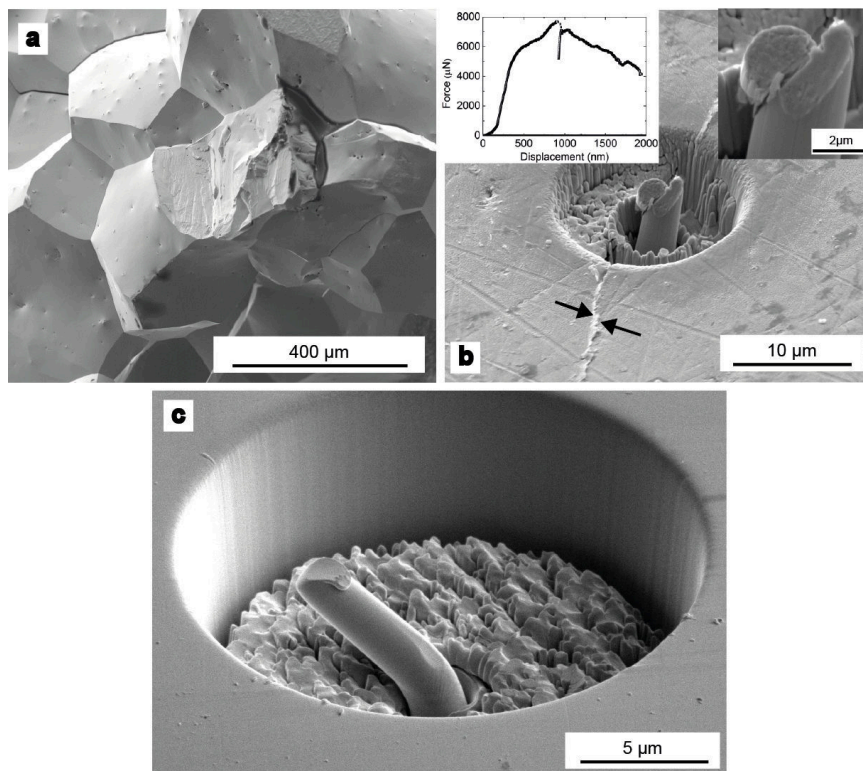


Fig. 9. Typical SEM images (SE mode) of: (a) a fracture surface in the HEA bulk sample, showing the fracture occurred along grain boundaries; (b) a post-deformed HEA pillar that contains a grain boundary (indicated by arrows), where the fracture occurred. The corresponding force-displacement curve and the enlarged area of the fracture region are shown in the insets; (c) a 2- μm [001]-oriented single-crystalline HEA pillar, which was severely bent without any fracture or crack after deformation.

Strength: Submicron-sized HEA pillars exhibit extraordinarily high strengths compared to the bulk HEA (~4-4.5 GPa vs. ~1 GPa [10]). The origin of the higher strength for the HEA pillars could be the same as the size-effect phenomena for the other metal pillars. It is generally believed that when the sample dimension is reduced into micron and submicron regimes, the strength is increased due to the decreased average size of dislocation sources. Weinberger and Cai [30] suggest, for bcc pillars, a single dislocation can also multiply itself repeatedly and forms dislocation segments and hard junctions, contributing to the increased strength.

HEA bcc pillar vs. pure elemental bcc pillars: size effects

Size-dependent strengths have been commonly and empirically characterized by a power-law relation, either in a non-normalized form, $\sigma=A(D)^m$, or in a normalized form, $\tau/G=A(D/b)^m$, where τ is the resolved shear stress on primary slip planes, A is a constant, D is the pillar diameter and b is the Burgers vector [16, 17, 19, 46, 47]. For the calculation of τ in this study, {112} slip planes are chosen [24, 41], and the Schmid factors for [316] and [001] orientations are 0.41 and 0.47, respectively. Here, we apply the power-law fits to the HEA pillars (this study) and to [001]-oriented Nb, Ta, Mo and W (literature data [23, 26]). In both non-normalized and normalized fitting lines (Figs. 10a-d), the HEA pillars exhibit higher strength levels than the pure bcc metal pillars. For example, the 200-nm HEA pillars have higher flow strengths than pure bcc metal pillars by a factor of ~2-4. In addition to higher strength levels, the HEA pillars also exhibit a reduced size effect (a smaller absolute value of m) compared to the pure bcc pillars here. The only exception to this trend is that the size dependence of the HEA is slightly larger than that of W by Schneider *et al.* [23], but it is smaller than that of W reported by Kim *et al.* [26] (compare Table 2).

Fig. 10e gives a schematic illustration of the normalized strength-diameter relationship of fcc and bcc pillars summarized from Refs. [17, 23, 26] and the

HEA pillars in this study. In the size range of a few microns, bcc pillars have higher normalized strength levels than fcc pillars, but in the submicron regime the strength levels of bcc pillars converge to those of fcc pillars. The HEA bcc pillars in this study shows extraordinarily high strength compared to the pure bcc elements. In order to understand the different size effects for pure bcc and HEA bcc pillars, we propose a simple analysis on the resolved flow stress of a pillar sample. The applied resolved shear stress, τ , is traditionally expected to be a sum of lattice friction, τ^* , elastic interactions between dislocations (i.e., Taylor hardening), τ_G , and source-controlled strength, τ_{source} , expressed as [47, 48]:

$$\tau = \tau^* + \tau_G + \tau_{source} \quad (2)$$

In Eq. (2), τ^* is the stress required to overcome the Peierls potential and arises as a consequence of the force-distance relation between individual atoms in a periodic lattice structure. τ^* is temperature-dependent and can be expressed as [49]:

$$\tau^* = \left(1 - \frac{T_t}{T_c}\right) \tau_0^* \quad (\text{with } T_t < T_c); \quad (3)$$

$$\tau^* \approx 0 \quad (\text{with } T_t \geq T_c), \quad (4)$$

where T_t is test temperature, usually room temperature, τ_0^* is the Peierls stress at 0 K. Above T_c , there is sufficient thermal energy to overcome the Peierls barriers by thermal activation. The second term in Eq. (2), τ_G , is an athermal component, which arises from the resistance to dislocation motion due to long-range elastic interactions, such as the interactions between dislocations. Here, τ_G may be simply approximated by using the Taylor-hardening relation as:

$$\tau_G = \alpha G b \sqrt{\rho_0 + \rho_\Delta}, \quad (5)$$

where α is a constant falling in the range 0.1 to 1.0, ρ_0 is the initial dislocation density before pillar compression, and ρ_Δ is the increased dislocation density due to the compression. For a small amount of strain, the dislocation density is in the order of 10^{12} - 10^{13} m⁻² for most of metals. Unlike in bulk metals, dislocation

storage in small-scale pillar specimens could be in a lower level, because new generated dislocations may move out of a pillar more easily due to a small confined dimension. Another contribution in Eq. (2), τ_{source} , is the minimal stress required to operate a dislocation source. In bulk samples dislocation segments in the length $\sim 10^4 b$ can act as Frank-Read source [49]. However, in pillar samples the average source length, $\bar{\lambda}$, is limited, and it is proportional to the pillar dimension. Single-ended sources could be dominant in the size range of $\sim 0.5\text{-}20 \mu\text{m}$ ($\sim 10^2\text{-}10^5 b$) [50]. The single-end source has also been seen in aluminum pillars using in-situ TEM [51]. The activation stress of a dislocation source in a pillar sample has been estimated by three-dimensional (3D) discrete dislocation dynamics (DDD) simulations [50] and could be expressed as:

$$\tau_{source} = KG \frac{\ln(\bar{\lambda}/b)}{\bar{\lambda}/b}, \quad (6)$$

where K is the source-strengthening constant in the order of 0.1. Although different controlling mechanisms could operate for bigger pillars ($>20 \mu\text{m}$ in diameter) and even smaller pillars ($<\sim 100 \text{ nm}$ in diameter), the single-end source model applies to the size range discussed in this study. Because T_t is smaller than T_c in most bcc metals, merging equations (3), (5) and (6) into (2), we obtain:

$$\frac{\tau}{G} = \left(1 - \frac{T_t}{T_c}\right) \frac{\tau_0^*}{G} + \alpha b \sqrt{\rho_0 + \rho_\Delta} + K \frac{\ln(\bar{\lambda}/b)}{\bar{\lambda}/b} \quad (7)$$

Pure elemental bcc pillars

In order to illustrate how the three mechanisms underlying the three terms in Eq. (7) influence the size dependence of the strength in bcc metals, the parameters for Mo, which have been most investigated for pillar compression, are chosen, as: $\alpha \approx 0.5$, $b \approx 2.728 \text{ \AA}$, $(\rho_0 + \rho_\Delta) \approx 5.0 \times 10^{12} \text{ m}^{-2}$, $K \approx 0.5$, and $\bar{\lambda} \approx D$ [47, 49, 50]. It should be noted that K is dependent on Poisson's ratio, dislocation type and

anisotropy of dislocation line tension, and $\bar{\lambda}$ is also influenced by dislocation densities and their distribution [50].

Here, we use the above values to give an estimation of pillar strengths. Fig. 11 shows a 3D graph of normalized strength (τ/G) vs. normalized length (D/b) and normalized temperature (T/T_c) for Mo pillars. The top surface with contour lines represents a sum of all the three mechanisms in Eq. (7). Each mechanism is also plotted in a single color below separately: τ^* (blue), τ_G (red) and τ_{source} (green).

The graph clearly shows how the local slope, m , increases in magnitude with an increase of normalized temperature. According to this graph, we could make the following predictions: at 0 K, if the sample size is smaller than $\sim 1000 b$, the strength is source-controlled, having strong a size dependence; if the size is larger than $\sim 1000 b$, the strength is controlled by the Peierls potential, showing nearly no size effect. However, when T_i equals T_c (~ 480 K for Mo), if the size is smaller than $\sim 20'000 b$, the strength is controlled by source action; but if the size is larger than $\sim 20'000 b$, dislocation interactions play an important role in reducing the size effect. At room temperature (i.e. T_i of 300 K), this calculated strength-size curve according to Eq. (7) is compared to the experimental data of [001]-Mo pillars [23, 26] and [111]-Mo pillars [52], as shown in Fig.12. The dashed lines present the individual contributions from the lattice friction (τ^* , blue), the Taylor hardening (τ_G , red) and the source strengthening (τ_{source} , green) to the overall strength (τ , black), respectively. In the case of Mo, the experimental data points are in a good agreement with the calculated strength curve at a reasonable scatter level, especially for the sample size larger than ~ 100 nm. Surface image stresses may have a large effect at the length smaller than ~ 100 nm. In the region in which two or three mechanisms are similar in magnitude, the normalized strength will change by up to a factor of three, compared to a scenario where only the strongest strengthening mechanism is relevant. This is the only scenario where an understanding, which strengthening mechanisms are additive and which are not, becomes important. If only one mechanism dominates the distinction is secondary.

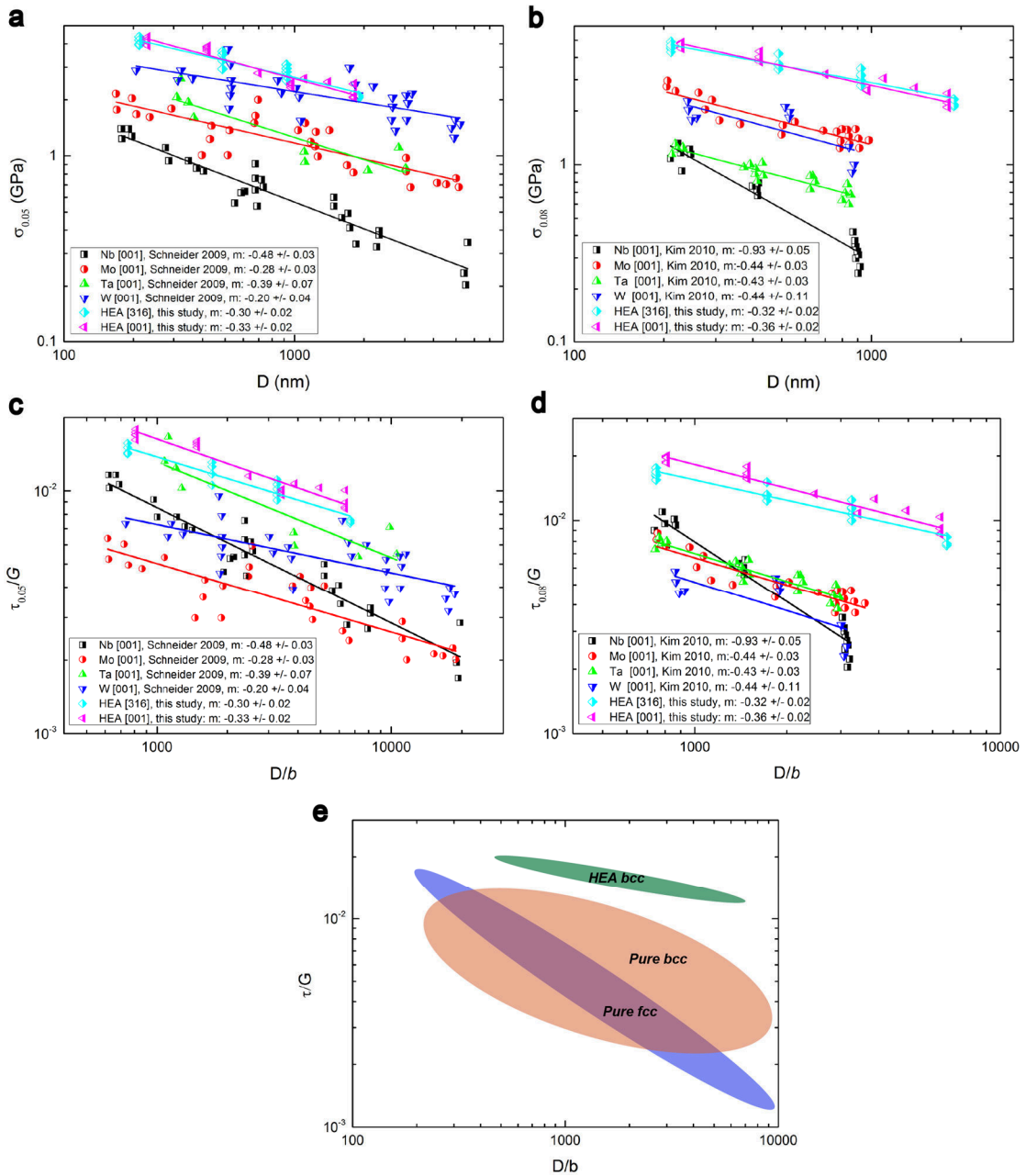


Fig. 10. Size-dependent strengths for the [316]- and [001]-oriented HEA pillars in this study and pure Nb, Mo, Ta and W as reported by Schneider *et al.* [23] and Kim *et al.* [26]. (a) and (b): $\sigma_{0.05}$ and $\sigma_{0.08}$ versus pillar diameters (D); (c) and (d): resolved flow strengths normalized by corresponding shear modulus (τ/G) versus pillar diameters normalized by Burgers vector (D/b). (e) Schematic illustration of size-dependent strengths for different metallic systems: FIB-milled pure fcc and bcc pillars (data summarized from [17, 23, 26]) and the HEA bcc pillars in this study, and the range of each group is indicated by a colored solid ellipse. The HEA bcc pillars exhibit both higher absolute and normalized strength levels than any other bcc metals but a relatively low size dependence of strengths.

HEA bcc pillar:

Here, we attempt to predict a strength-size curve for the HEA pillars using Eq. (7). Although there is no experimental data of the Peierls stress and shear modulus

for the HEA, the values of τ_0^*/G are available for Nb, Mo, Ta and W [42] (Table 2), which is between 10^{-3} and 10^{-2} . Wang [53] also calculates τ_0^*/G theoretically and estimates the values of τ_0^*/G are approximately 10^{-3} for bcc edge dislocations and about 10^{-2} for bcc screws. Here, the maximum τ_0^*/G value among the bcc metals, 8.7×10^{-3} , is chosen to give an estimation for the HEA pillars as well as b of 2.799 \AA , and T_c of 1050 K (Table 2).

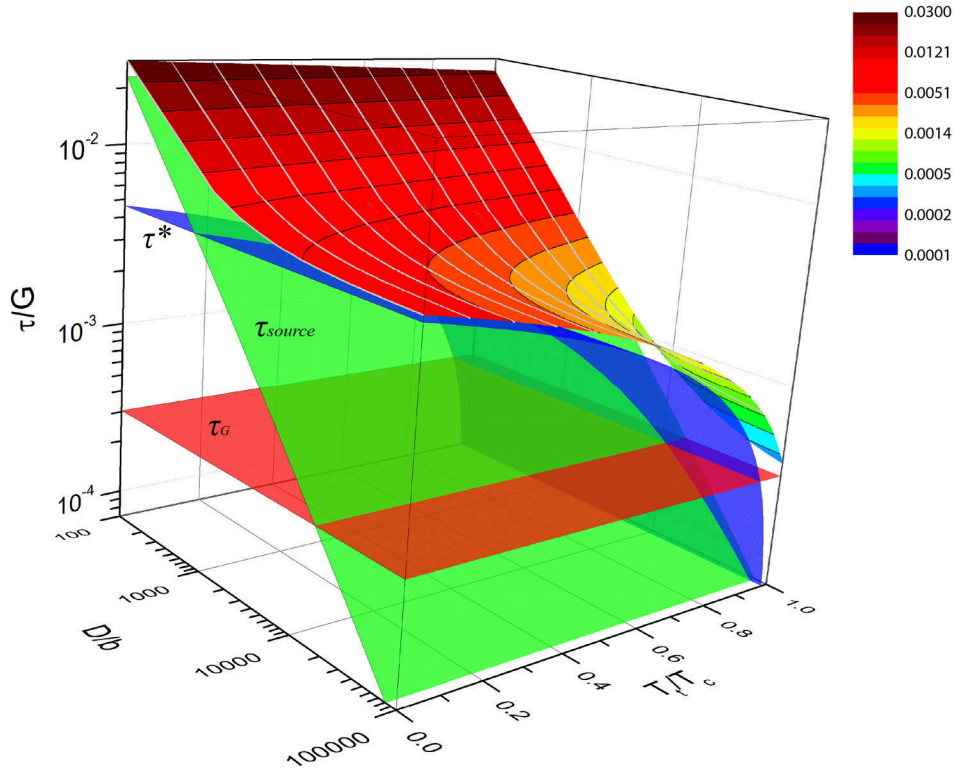


Fig. 11. A 3D illustration for the size and temperature dependence of the strengths in Mo pillars according to Eq. (7): normalized strength (τ/G) vs. (normalized length scale (D/b), normalized temperature (T/T_c)) in a size range of 10^2 - $10^5 b$ and a temperature range of 0 - T_c . In order to give the best estimation of the strength, the parameters are chosen as: $\alpha \approx 0.5$, $b \approx 2.728 \text{ \AA}$, $(\rho_0 + \rho_\Delta) \approx 5.0 \times 10^{12} \text{ m}^{-2}$, $K \approx 0.5$, and $\bar{\lambda} \approx D$, [47, 49, 50]. The top rainbow-colored surface with contours is a sum of all the strengthening mechanisms in Eq. (7). The contributions from the lattice resistance (τ^*), the Taylor hardening (τ_G) and the source strength (τ_{source}) are plotted in blue, red and green, respectively.

As can be seen in Fig. 12, the experimental data points are higher than the predicted curve by a factor of around two. The reason might be that unlike pure bcc elements the solute atoms in the HEA have different atomic dimensions which can induce significant localized lattice distortion (Fig. 4). While the rule of mixtures may be appropriate for determining the shear modulus, the severe lattice distortions in the HEA are expected to result in a significantly higher

Peierls potential than for each of the constituents. Moreover, the non-uniform stress fields throughout the HEA sample might cause an increased dynamic drag effect and the following phenomena might occur [45, 54, 55]: the emission of elastic waves during the deceleration and acceleration of dislocation sliding along a distorted lattice, the excitation of local vibrations of solute atoms, and the radiation of phonons by dislocation vibration like a string. Different from pure and lightly alloyed metals with a relative ideal lattice, the dynamic drag effect could be prominent in the HEA, and therefore the lattice friction could be significantly increased, leading to strong strengthening. However, to make a convincing conclusion, a precise experimental evaluation of T_c and τ_0^*/G as well as detailed microstructural analyses and atomic simulations of the non-planar dislocation core structure in HEAs will be a subject for future investigation.

As we have shown in Fig. 11, the apparent size effect exponent m depends not only on the superposition of strengthening mechanisms but also on the experimentally accessible size range. Nevertheless it is instructive to correlate m to the normalized temperature, if the analyzed size ranges and dislocation densities are comparable. Here, we adapted the method used in Schneider *et al.* [23] to correlate m and T_t/T_c for pure bcc and HEA bcc pillars. According to Eq. (7), the value of m can be expressed as:

$$m = \ln\left(\frac{b}{D}\right) \ln\left[B - \frac{\tau_0^*}{GA}\left(\frac{T_t}{T_c}\right)\right] \quad (8)$$

where B is a material-independent constant.

Because τ_0^*/G is nearly constant for most bcc metals and in the order of 10^{-3} to 10^{-2} , the m value could be mostly influenced by T_t/T_c . Using the values in Table 2, Fig. 13 indicates that the material that has higher T_t/T_c is expected to have a lower size effect. The HEA from this study is in reasonable agreement with this pattern.

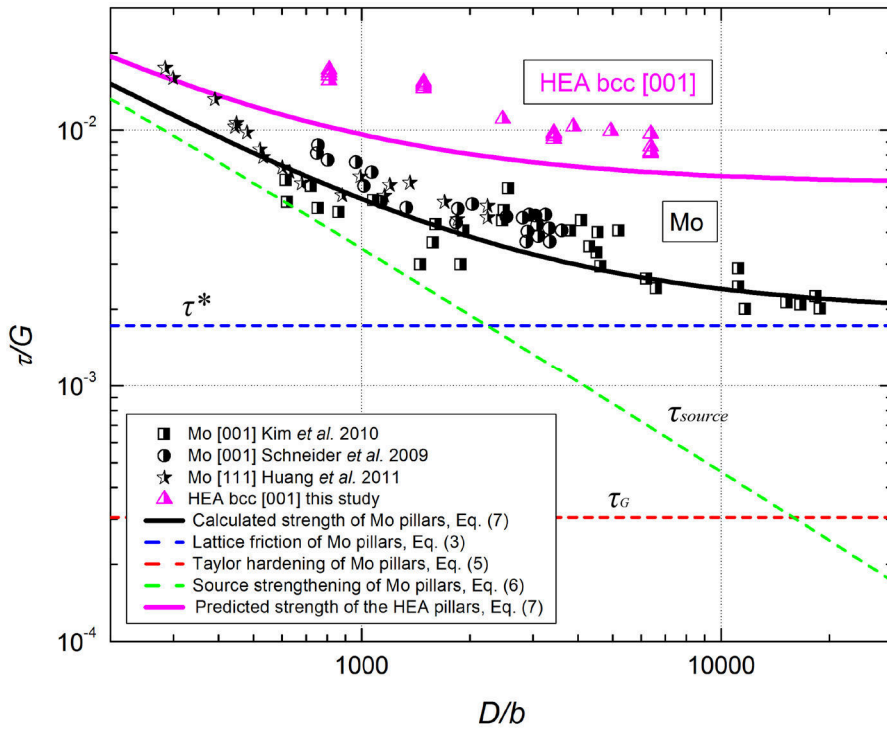


Fig. 12. The calculated normalized strength vs. normalized length for Mo pillars at room temperature (300 K) according to Eq. (7). The solid black line is a sum of all the mechanisms for Mo and the contribution of each mechanism is plotted separately in a dashed color line: τ^* (blue), τ_G (red) and τ_{source} (green). The black points are the experimental data of [001] Mo pillars [23, 26] and [111] Mo pillars [52]. The predicted curve for the HEA using Eq. (7) and the experimental data of [001] HEA in this study are also plotted. In order to calculate the strength levels of the HEA, the following parameters are chosen: $b \approx 2.799 \text{ \AA}$, $T_c \approx 1050 \text{ K}$ (Table 2) and the maximum τ_0^*/G value among the bcc metals, 8.7×10^{-3} .

Summary

In this work, a $\text{Nb}_{25}\text{Mo}_{25}\text{Ta}_{25}\text{W}_{25}$ refractory HEA was synthesized by arc melting and well homogenized at $1800 \text{ }^\circ\text{C}$ for 7 days. The HEA shows a simple bcc structure with the average lattice parameter of Nb, Mo, Ta and W, while localized lattice distortions at atomic length scales were observed using HRTEM. The mechanical properties of [316] and [001]-oriented HEA pillars have been measured using the micro-compression technique. Orientation change has minor influence on the size dependence of strengths. In both orientations, the HEA pillars exhibit higher strength levels than pure Nb, Mo, Ta and W pillars by a factor of $\sim 2\text{-}5$, as well as a relatively low size effect (log–log slope of strength vs.

pillar diameter about -0.3). Both the increased strength levels and reduced size dependence in the HEA could be attributed to a higher lattice friction in the HEA than that in pure bcc metals. In this paper, we also illustrate how the normalized strength correlates to the normalized length scale and the normalized temperature for bcc structures, and elucidates the contributions to the size-dependent strength from lattice resistance, dislocation interactions and source strength, respectively. Additionally, towards the application, both the strength and ductility of single-crystalline HEA pillar samples are significantly improved compared to polycrystalline bulk forms. These findings promise the refractory HEAs to be used as potential structural materials in micro/nano device design.

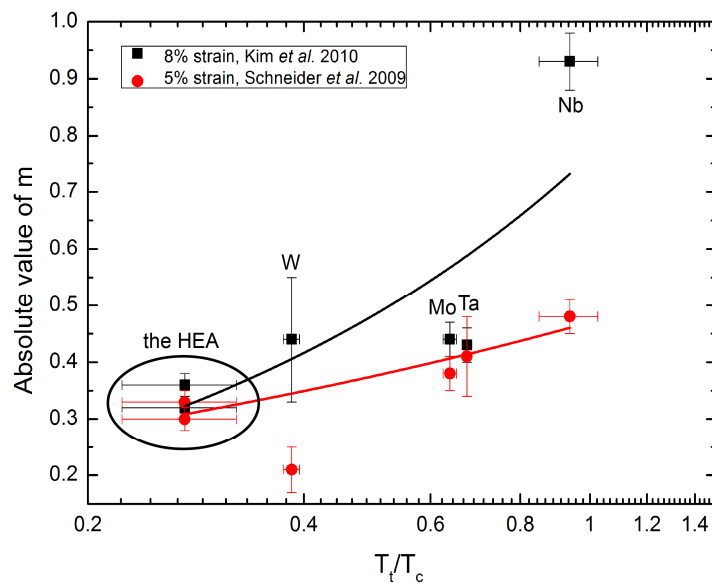


Fig. 13. The absolute values of m versus T_t/T_c : the correlation between the size effects and the critical temperatures of pure Nb, Mo, Ta and W pillars [23, 26] and the HEA pillars in this study.

Acknowledgements

The authors would like to thank P. Gasser, Dr. K. Kunze and Dr. Fabian Gramm (EMEZ, ETH Zurich) for their help in the sample preparation using FIB and HRTEM, Huan Ma, Matthias Schamel (LNM, ETH Zurich) for their help in SEM and EBSD characterization; Claudia Müller (LNM, ETH Zurich) for proof reading the manuscript. The authors also gratefully acknowledge financial support through SNF grants (200021_143633 and 200020_144430).

3.2. Fracture properties of the refractory high-entropy alloy: single crystals vs. bi-crystals⁵

Abstract

A majority of refractory high-entropy alloys suffer from brittleness and limited formability at ambient temperature, but studies of their fracture properties are scarce. Here, we have conducted *in-situ* micro-cantilever tests to investigate the fracture behavior of a typical refractory high-entropy alloy, Nb₂₅Mo₂₅Ta₂₅W₂₅. The results show that the fracture toughness and strength of bi-crystal specimens are one order lower than those of single-crystal ones, suggesting that brittle intergranular fracture is a major fracture mode and strengthening grain boundaries is critical.

Refractory high-entropy alloys (HEAs) are emerging metallic systems that consist of four or more refractory elements (e.g., Nb, Mo, Ta and W) with equimolar or near-equimolar ratios [9, 10, 56-60]. For the last four years, these alloys have attracted significant attention, because of their excellent properties at elevated temperatures above 1100 °C: extraordinary high strength/hardness [10, 61], outstanding structural stability [62] and good oxidation resistance [60, 63], even in excess of those of conventional nickel-based superalloys. However, most of them are brittle at room temperature, failing by cracking at low compressive strains, suffering from poor ductility and rendering them difficult to process [10, 59, 64, 65]. For example, two typical refractory HEAs, Nb₂₅Mo₂₅Ta₂₅W₂₅ and V₂₀Nb₂₀Mo₂₀Ta₂₀W₂₀, fracture by splitting at 2.1% and 1.7% compressive strains, respectively, and their good formability is only possible above 600 °C[64]. In a

⁵ Y. Zou, H. Yu, T. Sumigawa, T. Kitamura, S. Maiti, W. Steurer, R. Spolenak, "In-situ micro-cantilever studies of fracture properties of a refractory high-entropy alloy" (to be submitted to *Scripta Materialia*)

very recent study [59], we have employed micro-pillar compression on $\text{Nb}_{25}\text{Mo}_{25}\text{Ta}_{25}\text{W}_{25}$, and observed that a pillar containing a grain boundary (GB) fails easily due to crack propagation along the GB, while a single-crystal pillar shows much better ductility. This implies that the formability of the refractory HEAs is significantly reduced when intergranular fracture is involved in the process of crack advance, and thus the strength of GBs may determine the resistance against fracture in these alloys. Although a few face-centered cubic (fcc) HEAs, such as CrMnFeCoNi[66], have been reported to exhibit promising fracture resistance, the inadequate fracture-resistance property of body-centered cubic (bcc) refractory HEAs is in fact a bottleneck that limits their usage. So far, to the authors' knowledge, no study on the fracture properties (i.e., fracture toughness and fracture strength) has been reported.

In this work, we have applied the methodology of *in-situ* micro-cantilever fracture tests [67] to investigate the fracture behavior of single-crystal (SC) $\text{Nb}_{25}\text{Mo}_{25}\text{Ta}_{25}\text{W}_{25}$ and those containing a GB (i.e., bi-crystal, BC), in order to evaluate its intrinsic brittleness and the effect of GBs. Using this technique combining with finite element method (FEM) simulation, local fracture properties can be obtained and the behavior during fracture process can be recorded, which has been successfully applied in ceramics [68, 69], intermetallics [70, 71] and metals [72, 73].

A bulk $\text{Nb}_{25}\text{Mo}_{25}\text{Ta}_{25}\text{W}_{25}$ HEA was produced using the arc melting technique in an argon atmosphere, and then homogenized at 1800 °C for seven days (as described in [59]). The crystal orientations of the as-prepared HEA specimen were characterized using the electron back-scatter diffraction (EBSD) technique (Figure 1a). The specimen shows an equiaxed-grain structure with grain sizes of a few hundred microns. SC- and BC-cantilevers were fabricated from two adjacent $\langle 110 \rangle$ -oriented grains (misorientation angle $< 5^\circ$) using the focused ion beam (FIB) technique (Hitachi, FB-2200), as shown in Figure 1b and 1c, respectively. Both SC- and BC-cantilever beams have the length (L_0) of $\sim 6\text{-}8\ \mu\text{m}$

and the width (W) and thickness (B) of $\sim 1.5\text{-}2\ \mu\text{m}$, as schematically illustrated in Figure 1d. A notch with the depth of $\sim 0.3\text{-}0.5\ \mu\text{m}$ and the tip radius of $\sim 10\ \text{nm}$ was fabricated in each cantilever using a fine milling current (30 keV, 5 pA) and a milling time of a few seconds. In SC-cantilevers, the notches were close to the cantilever beam support and parallel to $\{100\}$ planes (the cleavage planes for most bcc metals). In BC-cantilevers, the notches were cut along the GBs.

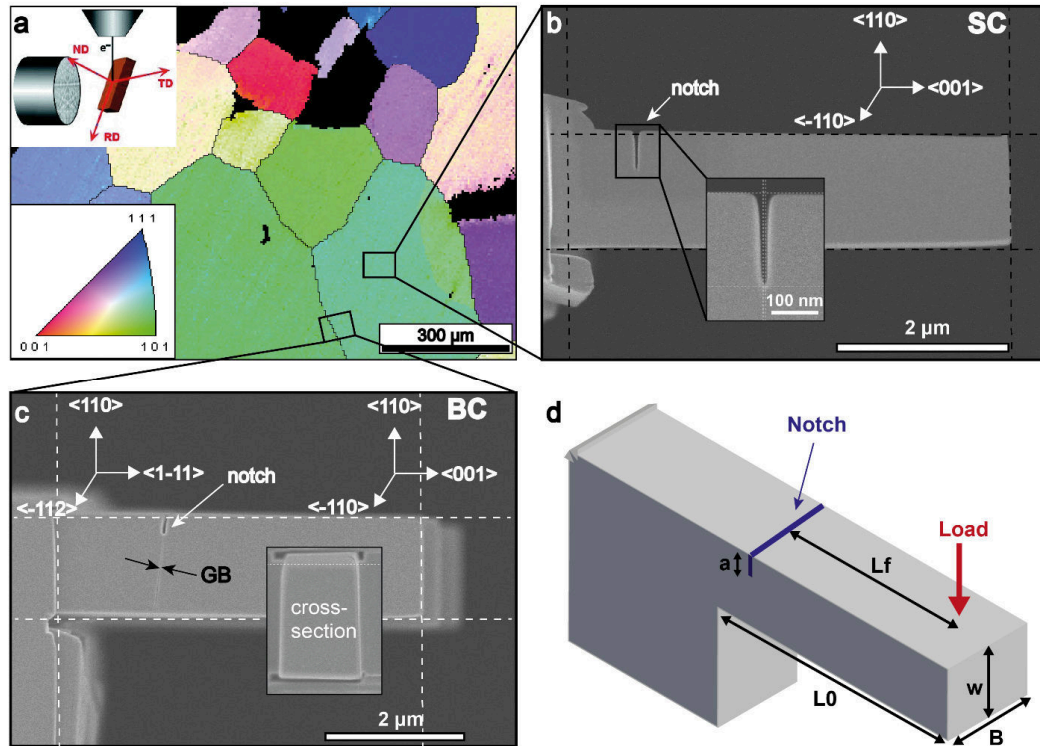


Figure 1. a. EBSD inverse pole figure map of the cross-section of the HEA bulk specimen. Two adjacent $\langle 110 \rangle$ -oriented grains were selected to fabricate micro-cantilevers, as indicated by boxes. b and c, typical SC- and BC-cantilevers fabricated by FIB, respectively. The notch, crystal orientation and grain orientation are indicated. d. schematic of the shape and dimension of the FIB-notched cantilevers with beam length, L_0 , width, W , thickness, B , loading length, L_f , and notch depth, a .

The micro-cantilever specimens were mounted in an indenter holder (Nanofactory Instruments AB, SA2000N), which was fitted to a transmission electron microscopy (TEM, JEOL JEM-2100). A sharp diamond tip was used to load at the beam close to the free end in a displacement control mode (2 nm/s) by feedback mechanism. Four specimens were measured for either SC- or BC-cantilevers.

Figures 2a-c and 2e-g present the snapshots of the movies of typical SC- and BC-cantilevers upon loading, respectively. Figures 2d and 2h show their corresponding load–displacement curves. The SC-cantilever exhibits a linear elastic behavior at the initial loading stage (between a and b), a slight yielding before reaching the maximum load (b) and a subsequent gradual force drop. In contrary to the SC-cantilevers, all the BC-cantilevers experienced a catastrophic event at the maximum load. They did not show any yielding before fracture, and the crack tips suddenly opened and advanced along the GBs (as shown in Fig. 2g), indicating that the BC-specimens are more brittle than the SC-ones.

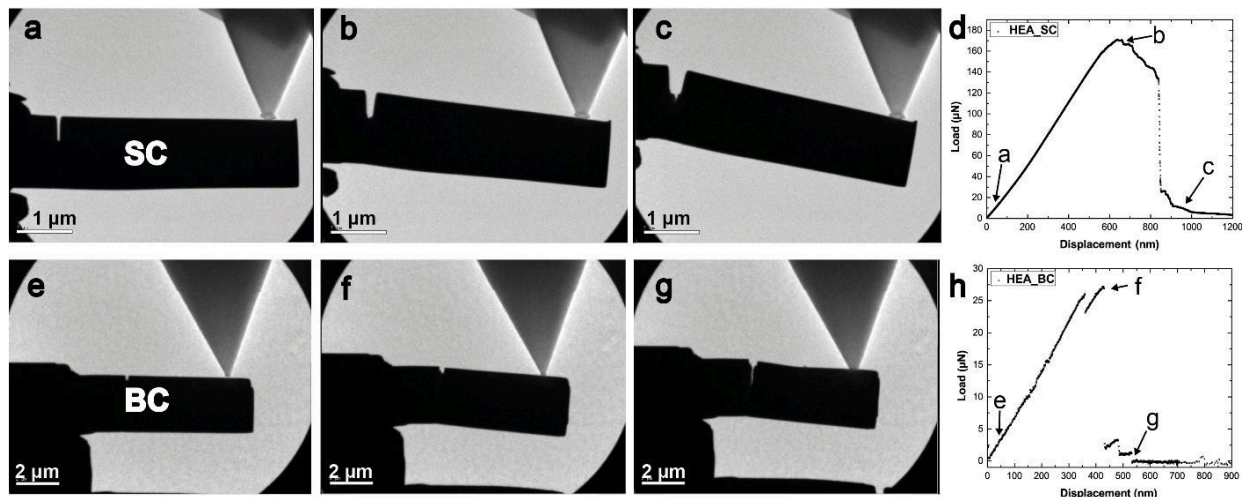


Figure 2. Representative *in-situ* TEM images of deflected SC- (a, b and c) and BC- (e, f, and g) cantilevers: a and e, initial contact; b and f, crack tip opening at the maximum load; c and g, fracture and load drop. d and h, the corresponding indenter load-displacement curves for the SC- and BC-cantilevers, respectively (the indenter displacement was evaluated using an image correction software).

After *in-situ* cantilever tests, fracture surfaces were characterized and compared. As shown in Figure 3, the two types of cantilevers revealed distinct appearance of surface morphology: the SC-specimen showed a quasi-cleavage feature with a faceted structure, suggesting that the cracks propagated preferentially along certain crystallographic planes; the BC-specimen showed an extremely flat and smooth surface along the grain boundary, which is a typical feature of brittle intergranular fracture.

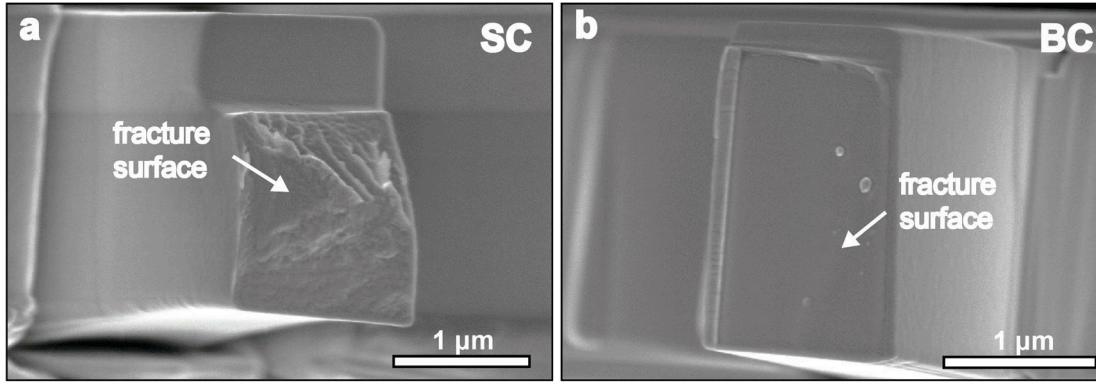


Figure. 3. Typical post-mortem SEM images of the fracture surfaces: the SC-cantilever specimen (a) shows a quasi-cleavage feature and the BC-cantilever specimen (b) exhibits a typical feature of brittle intergranular fracture.

Figures 2 and 3 suggest that both the SC- and BC-specimens show limited amount of crack tip plasticity before fracture, because a linear elastic behavior is present and no force-displacement plateau is observed. To calculate the plane strain fracture toughness, K_{Ic} , the following equation according to linear elastic fracture mechanics (LEFM) can be applied[75]:

$$K_{Ic} = \frac{F_{max}L_f}{BW^{\frac{3}{2}}} f\left(\frac{a}{W}\right) \quad (1)$$

where F_{max} is the maximum load before fracture (i.e., fracture force) and $f(a/W)$ is a geometry factor, which can be calculated using FEM simulations. In this study, two-dimensional extended FEM modeling was used to calculate the values of K_{Ic} for both SC- and BC-cantilevers using the J-integral method (the details of the method are explained in the supplementary data and in ref. [76]). Additionally, because the geometrical dimensions of the cantilevers in this study are comparable to the cantilevers in literature, the values of $f(a/W)$ can be also calculated using the formula given by Iqbal *et al.* [71], as:

$$f(a/W)=77.608(a/W)^3-48.422(a/W)^2+24.184(a/W)+1.52 \quad (2)$$

The K_{Ic} of SC- and BC-cantilevers obtained using the two means is illustrated in Figure 4a. The K_{Ic} of SC-cantilevers is 1.3-2.1 MPa·m^{1/2} with an average value of 1.6 MPa·m^{1/2}. This is nearly one order higher than that of the BC-cantilevers

($\sim 0.2 \text{ MPa}\cdot\text{m}^{1/2}$). It should be noted that in order to use the LEFM method, the size of plastic zone, ω , has to be significantly smaller than the specimen dimensions. It requires the specimen dimension to be above a critical thickness, ω_{th} , of $2.5 K_{Ic}^2/\sigma_y^2$, as elucidated in ASTM E399[75], where σ_y is the yield strength and can be obtained from the micro-compression tests [59] and K_{Ic} can be estimated using the values of single-crystalline tungsten [77]. Here, the obtained ω_{th} is approximately $1 \mu\text{m}$, which is slightly smaller than the specimen dimensions in this study. Thus, the plasticity of the crack tip might slightly affect K_{Ic} and the SC-specimens tested here may fracture in a mixed-mode condition, but it is mainly in a brittle cleavage mode. Nevertheless, the K_{Ic} shown in Figure 4a at least gives a lower limit for critical fracture toughness values. Furthermore, the fracture strength, σ_F , can be also estimated as [78]:

$$\sigma_F = K_{Ic}/(\pi a)^{1/2} \quad (3)$$

Figure 4b shows that σ_F of the SC-specimens is 950-1750 MPa, while the BC-ones exhibit a much lower σ_F of ~ 100 MPa. The BC-cantilevers are less fracture resistant than the SC-cantilevers, suggesting that the GBs in this HEA are weak and brittle intergranular fracture is its major failure mode rather than transgranular fracture. Figure 4d illustrates the fracture toughness as a function of yield strength for various materials tested using the micro-cantilever method. SC-Nb₂₅Mo₂₅Ta₂₅W₂₅ HEAs exhibit slightly higher fracture toughness than those of the ceramics, but lower than that of pure tungsten and close to those of intermetallics. Compared to the SC-HEAs, the BC-HEAs show both lower yield strength and fracture toughness.

In summary, the fracture toughness and fracture strength of a refractory HEA, Nb₂₅Mo₂₅Ta₂₅W₂₅, have been evaluated using the micro-cantilever fracture tests and FEM simulations. The single-crystal cantilevers fail by quasi-cleavage fracture with K_{Ic} of ~ 1.3 - $2.1 \text{ MPa}\cdot\text{m}^{1/2}$, while the bi-crystal cantilevers exhibit brittle intergranular fracture with much lower K_{Ic} ($\sim 0.2 \text{ MPa}\cdot\text{m}^{1/2}$). Therefore, the poor fracture resistance of this refractory HEA is mainly attributed to the

weakness of their GBs. For future studies, it would be interesting to investigate how the orientation and sample size influence their fracture properties. Towards applications, strengthening GBs in the refractory HEAs is a critical issue.

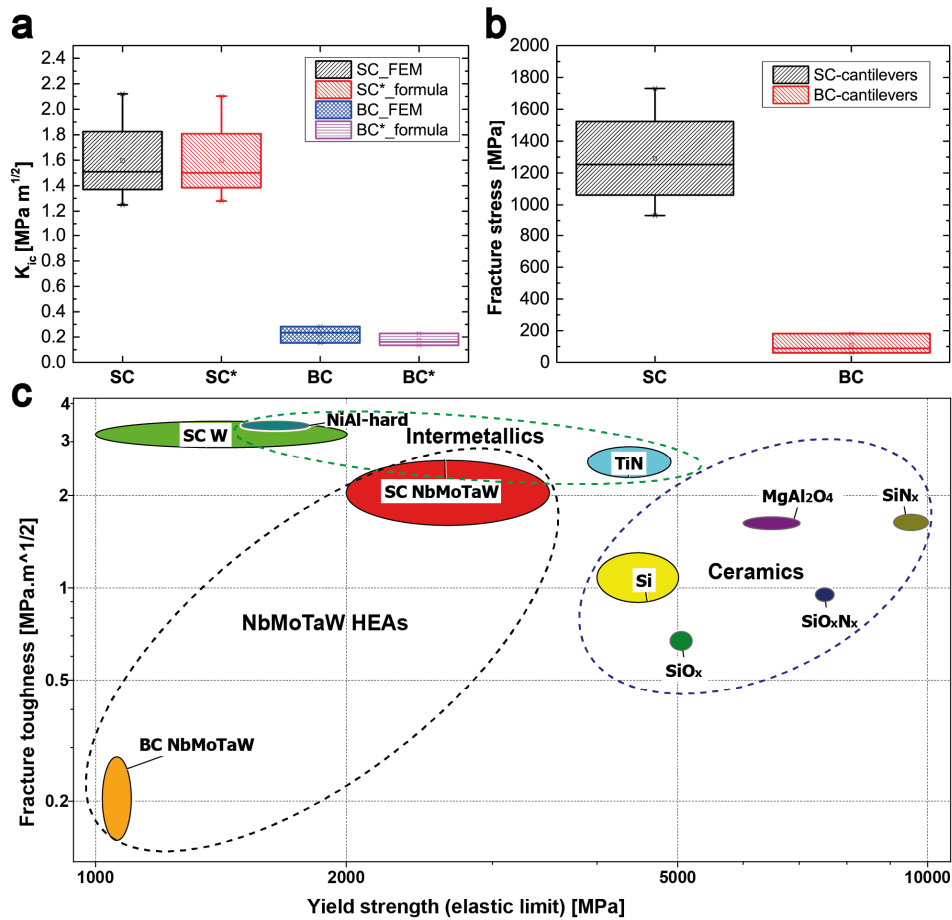


Figure. 4. a. Comparison of the fracture toughness between SC- and BC-cantilevers, using the extended FEM modeling and the formula obtained in literature[71]. b. Fracture strengths of SC-and BC-cantilevers. c. Ashby map showing fracture toughness as a function of yield strength for micro-cantilever HEAs in relation to the other materials [68, 70, 71, 73, 79] also tested using the micro-cantilever method (the yield strengths are obtained from micro-compression tests or estimated by nanoindentation hardness, K_{Ic} is calculated using the LEFM method and the values for Si are from pillar compression).

Acknowledgements

The authors thank H. Ma (ETH Zürich), E. Kawai and S. Ashida (Kyoto University) for their experimental help; Y.Z and S.M. acknowledge financial support through SNF Grants (200021_143633 and 200020_144430); Y.Z and H.Y. also acknowledge financial support through the JSPS program (GR14103 and P13055).

Supplementary Information

According to the shape features, the specimens can be modeled as a two-dimensional clamped plate in the plane strain condition, as show in Figs 2. First, the extended finite element method without the crack-tip enrichment functions [76] is employed to solve the crack tip elastic fields. Eight-node quadrilateral (Q8) elements are used over most of the mesh. Since the stress field has an inverse square root singularity in this problem, six-node quarter-point (T6qp) singular elements are employed to improve the accuracy. The mesh consists of 722 Q8 and 24 T6qp elements, with a total of 746 elements and 2330 nodes. Then, the fracture toughness is solved by using the J-integral which is defined as:

$$J = \int_C \left(\frac{1}{2} \sigma_{jk} \varepsilon_{jk} n_i - n_i \sigma_{ij} \frac{\partial u_j}{\partial x} \right) dC \quad (1)$$

where C is an arbitrary integral path surrounding the crack tip, originating from the lower crack face and ending at the upper crack face, and n_i is the unit outward normal vector to the contour C . Then, the fracture toughness can be solved according to the relation:

$$K_{IC} = \sqrt{\frac{E}{1-\nu^2}} J(F_c) \quad (2)$$

where $J(F_c)$ is the J-integral corresponding to the critical loading F_c .

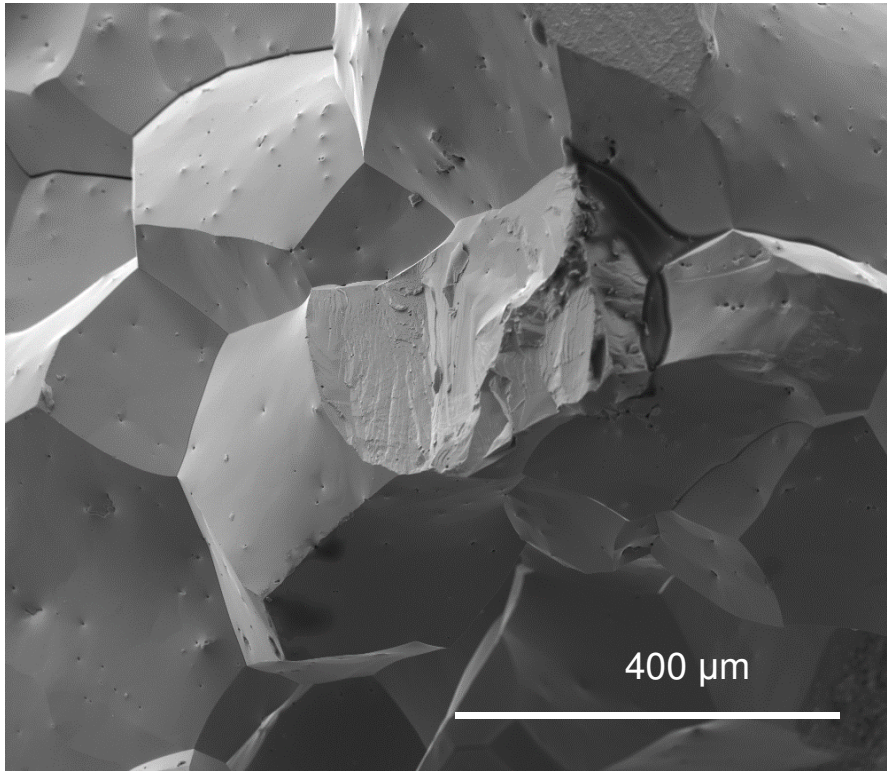


Fig. S1. A typical SEM image (SE mode) of fracture surfaces in the Nb₂₅Mo₂₅Ta₂₅W₂₅ HEA bulk sample, showing both intergranular and transgranular fracture.

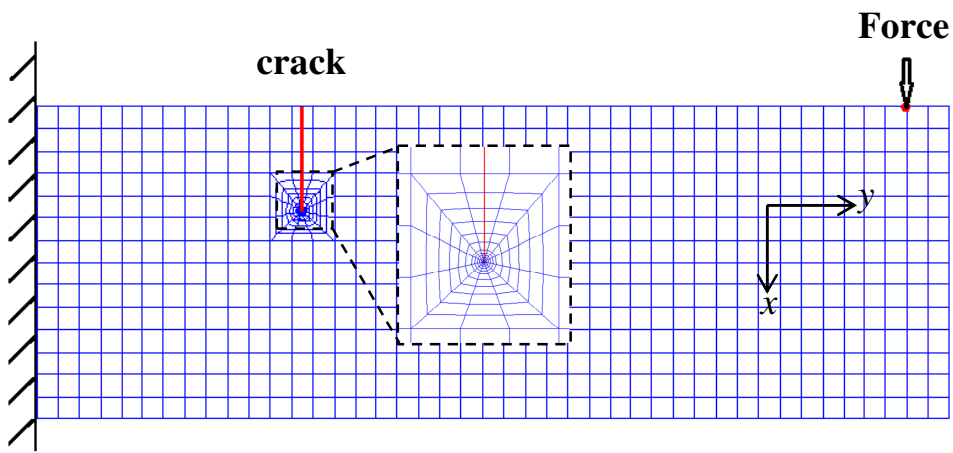


Fig. S2. Two-dimensional extended FEM modeling for the calculation of the fracture toughness using J-integral method.

3.3. Thin films and fine-scale pillars made of nanocrystalline high-entropy alloys⁶

Abstract

Refractory high-entropy alloys (HEAs) are a class of emerging multi-component alloys, showing superior mechanical properties at elevated temperatures and being technologically interesting. However, they are generally brittle at room temperature, fail by cracking at low compressive strains and suffer from limited formability. Here we report a strategy for the fabrication of refractory HEA thin films and small-sized pillars that consist of strongly textured, columnar and nanometer-sized grains. Such HEA pillars exhibit extraordinarily high yield strengths of approximately 10 GPa—among the highest reported strengths in micro-/nano-pillar compression and one order of magnitude higher than that of its bulk form—and their ductility is considerably improved (compressive plastic strains over 30%). Additionally, we demonstrate that such HEA films show substantially enhanced stability for high-temperature, long-duration conditions (at 1100°C for 3 days). Small-scale HEAs combining these properties represent a new class of materials in small-dimension devices potentially for high-stress and high-temperature applications.

Introduction

Developing high-strength, ductile and thermally stable materials is highly desirable for both scientific interests and critical applications [80-82]. Alloying has been explored as a means to strengthen metals since the Bronze Age. Conventionally, one principle element serves as the matrix material and solute atoms change local stress fields to impede dislocation motion and strengthen the

⁶ Y. Zou, H. Ma, R. Spolenak “*Ultrastrong, ductile and stable high-entropy alloys at small scales*” Nature Communications 6. doi:10.1038/ncomms8748

material, although it usually compromises ductility. Over the past few years, a new concept of alloys—HEAs, or equiatomic multi-component alloys, has attracted great attention [1, 83]. Such alloys usually consist of four or more elements with equimolar or near-equimolar ratios, form a simple single solid-solution-like phase and show a variety of interesting and unusual properties [66, 84]. Among them refractory HEAs are made of refractory elements and implemented for high-temperature applications. For example, a body-centered-cubic (bcc) structured NbMoTaW HEA subjected to uniaxial compression at 1600°C attain a yield strength of 400 MPa and high heat-softening resistance [9, 10]. However, all the refractory HEAs reported to date have been prepared using vacuum arc melting technique and a vast majority of them suffer from low ductility at room temperature [10, 59, 65]: rendering them very difficult to process and unsuitable for usage.

The ductility and strength of a material can be also controlled by scaling, that is sample and microstructural sizes [13, 17]. On the one hand, benefiting from higher surface-to-volume ratios and easier stress relaxation, cracking becomes more difficult in small-sized materials—the good deformability could be attained— even in conspicuous classes of brittle materials [79, 85, 86]. On the other hand, materials may attain significantly increased strengths by reducing their dimensions due to a limited scale of dislocation sources [20, 23, 26, 87, 88]. To achieve even higher strengths, a popular methodology is to include grain or interphase boundaries in micro- or nano-pillars, namely nanocrystalline (nc) or nanolaminate (nl) pillars, respectively. These nanostructured pillars can reach yield strengths of a few gigapascals [89-92], but their main drawback is that their microstructures are generally unstable: grains grow rapidly even at low temperatures, consequently their strengths decrease considerably. To stabilize nanocrystalline structures, a few effective means have been introduced to suppress grain growth, such as alloying [93, 94] and introducing texture [95].

So far promising HEAs have been mostly studied in their bulk forms, but small-dimension HEAs have received much less attention. As demands for micro- and nanoscale devices for high-temperature and harsh-environment applications increase, the fabrication and investigation currently popular HEAs at small sizes become more and more interesting. Now, the following question arises: what alloying and scaling conditions lead to the strongest both ductile and stable materials? Our strategy is to use the sample size and grain size as design parameters in a prototype refractory HEA, NbMoTaW alloy, to combine the benefits of alloying and scalings. Here, we show that fine-scale HEA films and pillars consisting of strongly textured, nanometer-sized and columnar grains exhibit ultrahigh strength, improved ductility and excellent thermal stability.

Results

Nanostructured HEA films and pillars. We used DC magnetron co-sputtering technique to deposit HEA films, as schematically illustrated in Figs 1a and 1b (also see the experimental setup in Supplementary Fig. 1). Ion beam assisted deposition (IBAD) method [96] was also applied to reduce deposition rate and decrease grain size. For simplicity, the method without using the ion gun is named as “Normal” as opposed to “IBAD”. Using the co-sputtering method, we produced 3- μm thick films that show good bonding with substrates and smooth surfaces (Fig. 1d). Electron backscatter diffraction (EBSD) orientation maps (inserts in Fig. 1d) show that the films consist of strongly (110)-textured columnar grains through the whole thickness of both IBAD and Normal deposited films. The films deposited under the IBAD condition exhibit smaller grain sizes than those produced under the Normal condition, with an average grain size of ~ 70 nm and ~ 150 nm, respectively. The energy-dispersive X-ray spectroscopy (EDX) analysis reveals the atomic composition varies by $\sim 5\%$ and the overall value varies within 10%, which is comparable to the previously reported bulk NbMoTaW HEAs [9, 59]. The X-ray diffraction (XRD) patterns indicates a

single-phase bcc structure in the as-deposited films, which also matches the bulk HEA in literature [9, 59]. The results in Fig. 1 confirm that the co-sputtered films are made of the same alloy as those bulk forms produced by arc melting.

Micro-mechanical testing of small-scale HEA pillars. Focused Ga ion beams (FIB) were used to mill fine-scale pillars out of the obtained HEA films and micro-compression tests were carried out using a nanoindenter. After compression a fraction of large pillars, above 1 μm in diameter, experience cracking at the top parts and cracks propagate along grain boundaries, showing intergranular fracture behavior, but it only occurs under strains larger than $\sim 20\%$ (Fig. 2a). The smaller pillars (Figs 2b-d) exhibit more uniform deformation without any cracking, even at above 30% compressive strain, suggesting that the compressive ductility is significantly improved. Furthermore, the columnar-structured HEA pillars exhibit very high yield and flow strengths. A 580-nm Normal HEA pillar shows a yield strength of ~ 5 GPa and a 580-nm IBAD HEA pillar exhibits a yield strength of ~ 6.5 GPa (Fig. 2e), which is almost twice of that of the single-crystal HEA pillar with the same diameter and orientation (Supplementary Fig. 4) and six times of that of the bulk HEA. Astonishingly, we find that the smallest IBAD HEA pillars (~ 70 -100 nm in diameter) exhibit remarkably high yield strengths of ~ 8 -10 GPa. To the best of our knowledge, such HEA pillars exhibit a strengthening figure of merit that is among the strongest pillars reported so far—for example, nc Ni-W pillar, ~ 1 GPa [91]; nc Zr pillar, ~ 4 GPa [97]; nl Cu/Nb, ~ 2 GPa [92]; Si, ~ 6 GPa [79]; GaN, ~ 8 GPa [98]; CrAlN/Si₃N₄, ~ 16 GPa [99] and Zn-based metallic glasses [85], ~ 2 GPa — and are in the same strength level of the defect-free Mo-alloy columns produced from etching NiAl–Mo eutectic compounds [100] and about half of that of pure W whiskers [101], still our HEA pillars exhibit much better ductility. Such HEA pillars also show a size-dependent strength, as presented by the relationship between the flow stress at 5% strain, $\sigma_{0.05}$, versus the pillar diameter, D (Fig. 2f). Our IBAD HEA pillars exhibit the highest strength levels, ~ 5 -7 times higher than

that of single-crystal W pillars, and the lowest size dependence, a log–log slope of -0.2.

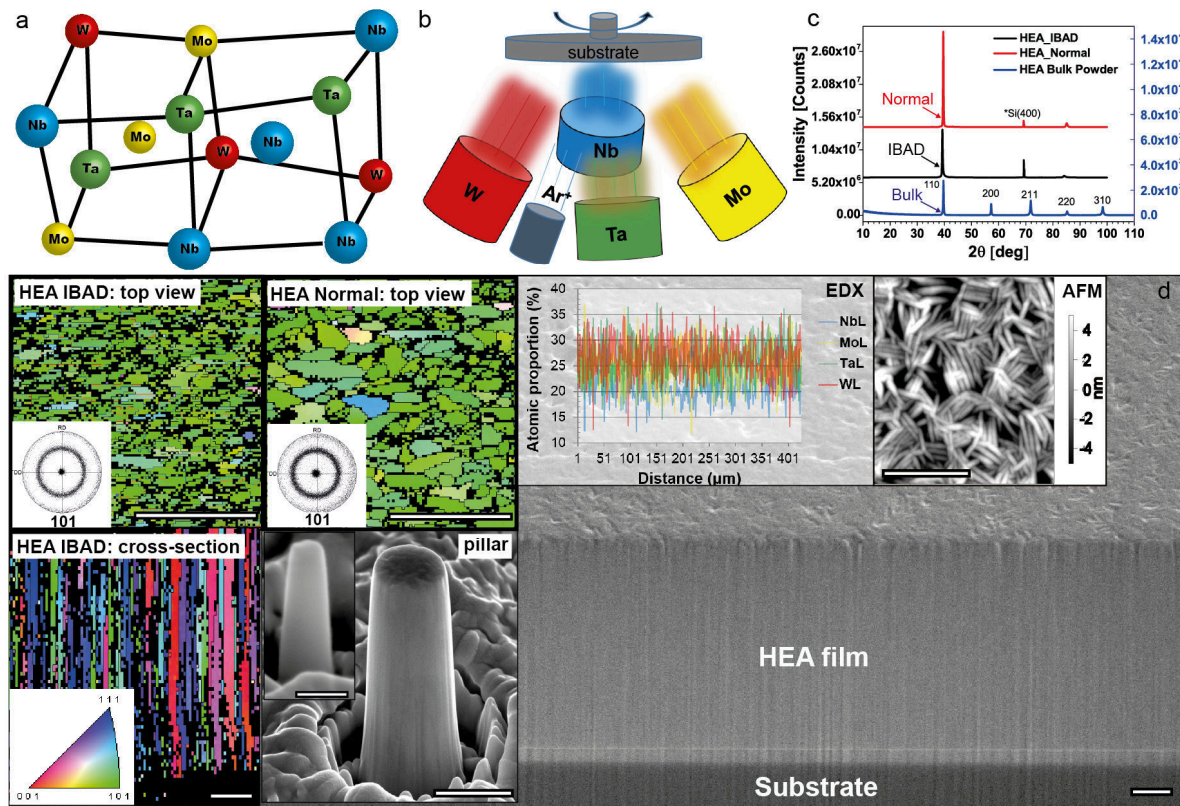


Figure 1. Fabrication and characterization of NbMoTaW HEA films and pillars. a, Schematic representation of an ideal lattice structure of a bcc NbMoTaW HEA. b, Schematic illustration of the DC magnetron co-sputtering system used to synthesize HEA thin films, in the conditions with and without Ar^+ ion beam assisted deposition: IBAD and Normal, respectively. c, Powder XRD patterns ($\text{Cu K}\alpha_1$) of the NbMoTaW HEA films, compared to that of its bulk powder[59], indicating a single bcc phase. d, A SEM image of the typical cross-section of as-deposited IBAD HEA films. The inserted EBSD maps show columnar grains through the whole thickness of the films with a (110) out-of-plane texture and an average grain size of ~ 70 nm and ~ 150 nm for the IBAD and Normal conditions, respectively. The EDX analysis indicates the four elements are homogeneously distributed in a large length scale. The roughness of the top surface measured by AFM is about 5 nm. Two representative FIB-milled pillars (diameters of ~ 500 nm and ~ 100 nm) are shown in the insert at the bottom. Scale bars, 500 nm, except the one for ~ 100 nm pillar is 100 nm.

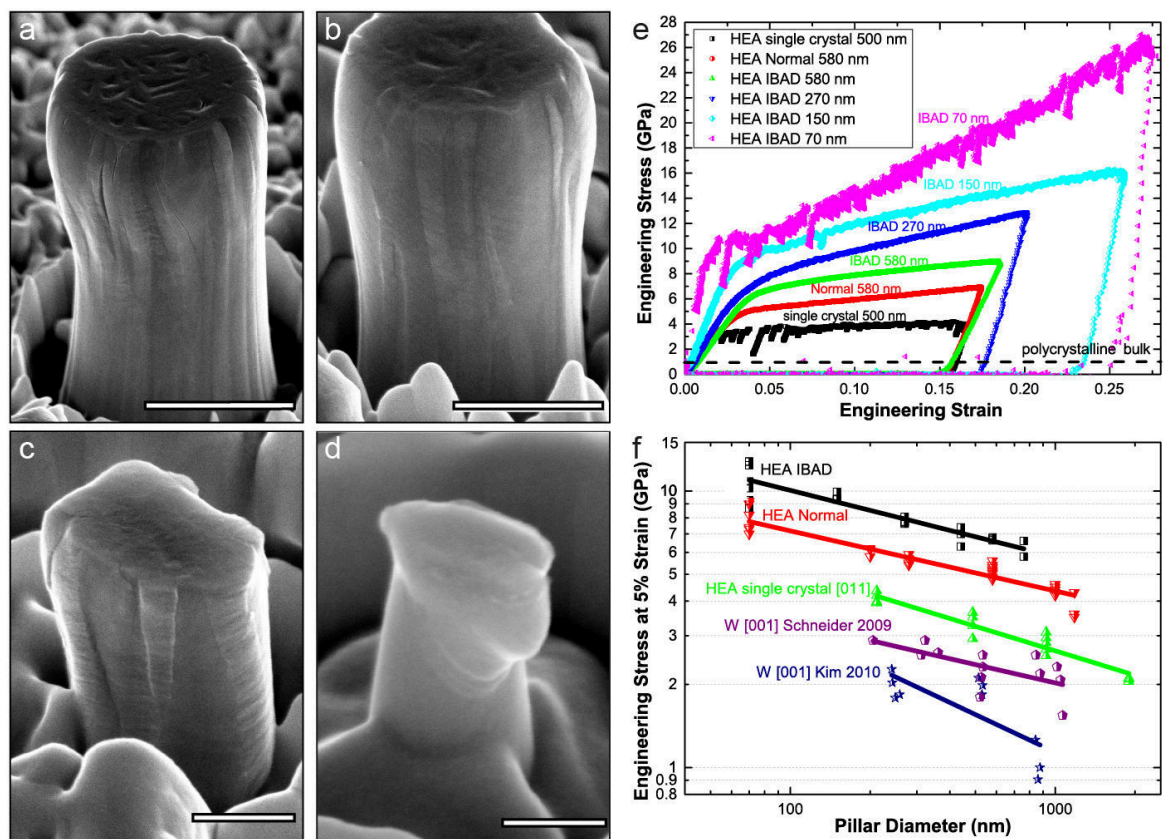


Figure 2. Compression results for the pillars prepared from the HEA films. a-d, SEM images of typical as-deformed HEA pillars (IBAD) with the diameter (D) ranging from approximately 1 μm to 100 nm. e, Representative stress-strain curves of the IBAD HEA pillars, showing a size-dependent strength. f, A comparison of the strength-size relationships for the columnar-structured HEA pillars, single-crystal HEA (using the bulk specimen[59]) and W pillars[23, 26]. The results for the Normal HEA pillars are similar to the IBAD HEA pillars (Supplementary Figs 2 and 3). Scale bars, 1 μm (a), 500 nm (b), 200 nm (c) and 100 nm (d).

Thermal stability of the HEA thin films. In addition to ultrahigh strength and improved ductility, we also demonstrate that such HEA films are substantially more stable after high-temperature, long-duration annealing compared to the pure W films which were prepared using the same experimental conditions. After three days' annealing at 1100°C in an argon atmosphere the pure W film shows obvious structural instability: the morphology of the top surface changes from needle-like shapes to equiaxed-crystal structures; a large quantity of micrometer-sized pores are formed through the whole thickness; the grain size is significantly increased from ~100-300 nm to a few micrometers, as shown in Fig. 3. In contrast to the W films, the post-annealed HEA film retains uniform needle-like morphology on the

top surface without obvious grain growth, and few pores have been found through the entire cross-section of the films. With regards to mechanical properties, the HEA pillars exhibit much higher strength and better ductility than the W pillars before and after annealing (see a deformed W pillar before annealing in Supplementary Fig. 5). The formation of micro-pores and the growth of grains may dramatically reduce the mechanical performance of the W films and pillars, while the post-annealed HEA pillar (diameter of $\sim 1 \mu\text{m}$) can still sustain a high yield strength of $\sim 5 \text{ GPa}$, which is nearly the same as that of the pre-annealed HEA pillar.

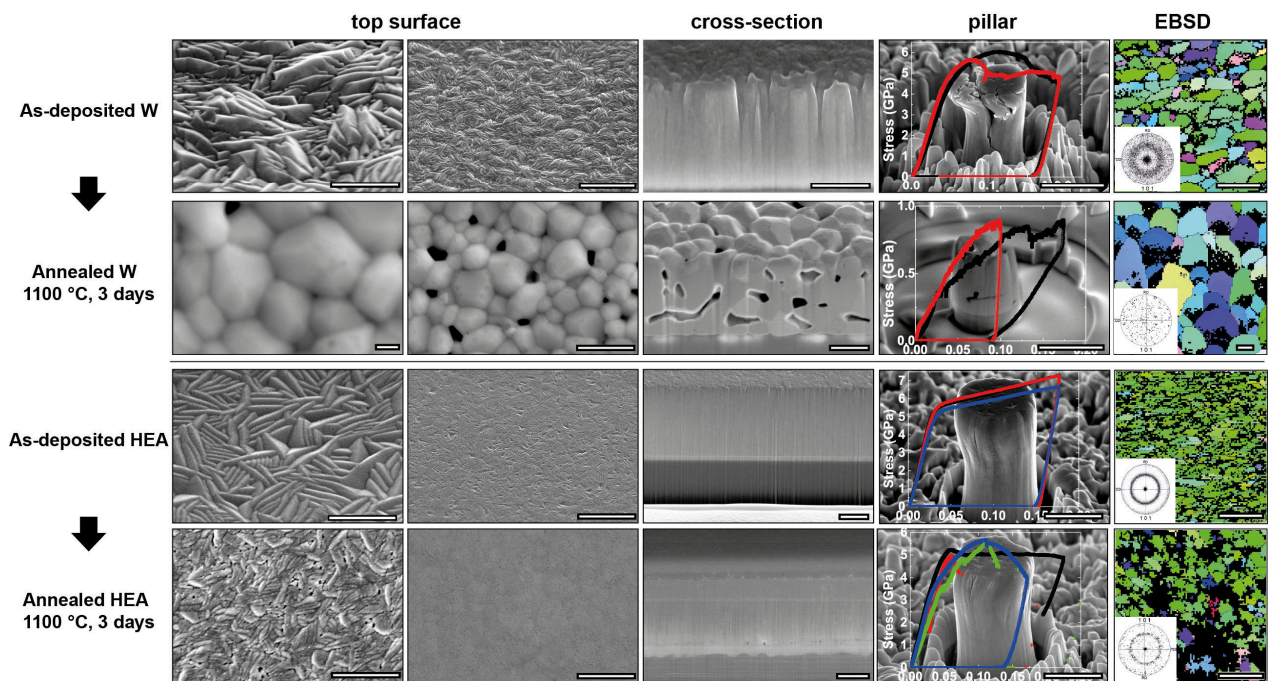


Figure 3. Pre- and post-annealing structures of the W and HEA films after three days at 1100°C . The top surfaces, cross-sections and grain structures indicate significant grain coarsening, pore formation and morphology change in tungsten films upon annealing, but the difference of microstructure and strengths of the HEA films before and after annealing is minor under the same deposition and annealing conditions. Scale bars, 200 nm (the first column, large magnifications of top surfaces); 300 nm (the last column, EBSD maps); $1 \mu\text{m}$ (the other images).

Discussion

In analogy to bundled bamboos, our column-structured HEA pillars actually consist of a set of strongly fiber textured nanometer-sized grains, schematically illustrated in Fig. 4a. As a comparison of the normalized strengths (resolved shear strength (τ) over corresponding shear modulus (G)), the IBAD HEA pillars

exhibit the highest values ($\sim 0.02-0.05$) among the typical single crystalline pillars and nanocrystalline pillars (Fig. 4b).

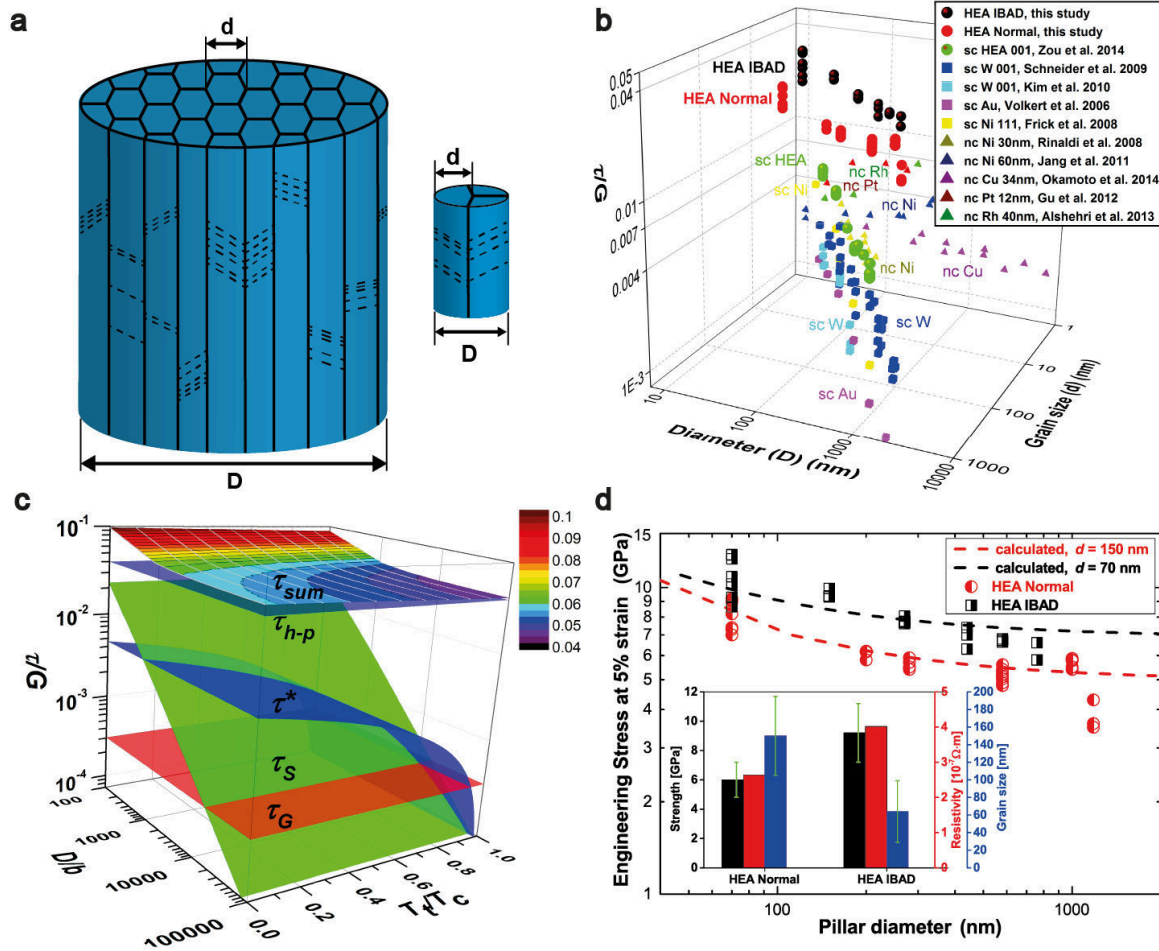


Figure 4. Size-dependent strength in column-structured pillars. **a**, Schematic illustrations of a big pillar and a small one, with D the pillar diameter and d the grain size. **b**, A 3-D graph shows the relation of normalized resolved shear strength (τ/G) vs. (D vs. d) for the HEA pillars in this study, single crystalline (sc) HEA[59], bcc W[23, 26], fcc Au[87], Ni[88] pillars, and nanocrystalline (nc) Cu[89], Ni[90], Ni-W[91], Pt[104] and Rh[105] pillars, with τ resolved shear strength and G the corresponding shear modulus. The Schmid factors of 0.417 and 0.5 are used for the bcc HEA pillar and the nc pillars in the available literature data, respectively. The sample sizes of sc pillars can be regarded as their grain sizes as well. **c**, A 3-D illustration of size- and temperature dependence of the strengths for the HEA pillars (τ/G) vs. (D/b) vs. (T/T_c)), as described in equation (1). **d**. A comparison between the calculated strengths using equation (1) and the experimental values for the HEA pillars. The insert compares pillar strengths, average grain sizes and resistivity of Normal and IBAD HEA films.

To understand the ultra-high strength of the HEA pillar, we propose a simple classical analysis on the resolved flow strength of the pillar (τ_{sum}), which is contributed by lattice friction (τ^*), Taylor hardening (τ_G) and source-controlled

strength (τ_s) and grain-boundary strengthening (τ_{h-p}), simply expressed as (adapted from Refs. [48, 59][47]:

$$\tau_{\text{sum}} = \sigma m = \tau^* + \tau_G + \tau_S + \tau_{h-p} = \left(1 - \frac{T_t}{T_c}\right) \tau_0^* + \alpha b G \sqrt{\rho} + K \frac{\ln(\bar{\lambda}/b)}{\bar{\lambda}/b} + m K_{h-p} G d^{-1/2} \quad (1)$$

Where σ flow stress, m Schmid factor, T_t test temperature, T_c critical temperature (above T_c flow stress becomes insensitive to test temperature), τ_0^* the Peierls stress, α a constant falling in the range 0.1 to 1.0, b the Burgers vector, G shear modulus, ρ dislocation density, K source-strengthening constant in the order of 0.1, $\bar{\lambda}$ average source length and K_{h-p} Hall–Petch constant. Fig. 4c presents a 3-D illustration of the additivity of different strengthening mechanisms in a size range of 10^2 – $10^5 b$ and a temperature range of 0 – T_c . To make a comparison with the experimental data, we choose the following parameters for the HEA pillars to give the best estimation: m 0.417 (the most probable slip systems $[111](\bar{2}11)$ with $[011]$ loading direction), T_t 300 K, T_c 1050 K[10], τ_0^* 446 MPa (the average value for Nb, Ta, Mo and W)[59], α 0.5, b 2.799 Å [59], ρ $5.0 \times 10^{12} \text{ m}^{-2}$, K 0.5, $\bar{\lambda}$ is proportional to the pillar dimension (as a function the sample volume [102]) which can be simply represented by D , K_{h-p} 1.7 GPa· $\mu\text{m}^{1/2}$ (for bulk Mo) [103]. The calculated values are in good agreement with the experimental data (Fig. 4d), implying that the four possible strengthening mechanisms could work simultaneously in the nanostructured HEA pillars. It should be also mentioned that the smallest pillars (~70-100 nm in diameter) show obviously higher scattering levels in strength compared to the larger pillars. This large scattering could attribute to the inhomogeneous distribution of grain boundaries in these small pillars. In addition, the higher strengths of the IBAD pillars than those of the Normal pillars could be mainly attributed to their finer grain sizes. The higher point defect density in the IBAD pillars (as measured by electrical resistivity shown in the insert of Fig. 4d) could influence the strength as well, but its contribution is deemed to be small.

It is also instructive to look at a thought experiment regarding strength and fracture. One could consider comparing this bundled-bamboo structure to a discrete array of single crystalline pillars of identical dimension as the grain size. With regards to strength these the single crystalline pillars would be close to theoretical strength provided they are defect-free. If some of them are not, the overall strength of the array would be slightly reduced and only decrease significantly if the overall number of defects were increased by increasing the number of pillars, i.e., increasing the diameter of the whole pillar. In the bundled-bamboo structure itself, yielding of a single grain will result in stress concentrations at the boundaries, activating dislocation sources in the adjacent grains [106] and, therefore, yielding in those as well leading to a reduced overall yield strength compared to the theoretical one. This is an alternative explanation of the size-dependent strength in the HEA pillars. With regards to fracture the single crystalline pillars, each columnar grain, would exhibit higher and higher aspect ratios with increasing diameter of the bundled-bamboo structure, assuming constant aspect ratio of the bamboo-like structure. Then the single crystalline pillars would fail more and more in a buckling mode. In this case of the bundled-bamboo structure, a larger cohesive strength of the grain boundaries is required for high aspect ratio grains to prevent buckling, which is intrinsically poor in HEAs [59]. If the deformation in each grain cannot be accommodated by its neighbors, it may lead to opening up voids and crack initiation along the boundaries [107]. This could explain why the large pillars eventually fail by intragranular fracture in contrast to the smaller ones where no fracture is observed.

The excellent thermal stability of the nanocrystalline HEA film could be attributed to their relatively low grain-boundary energy. Because grain interiors in the HEAs are highly disordered and far from a perfect crystal structure [59, 108], and the relative grain-boundary energy would be lowered than that of pure metals, such as pure W. Consequently, the driving force of grain boundary migration in the HEA would be lower compare to pure W, leading to reduced structural coarsening. Other mechanisms that could contribute to the high stability

of the HEA films are: at elevated temperatures the elements with higher diffusion rates may segregate to grain boundaries, decreasing grain boundary specific energy and stabilizing nanostructures against grain growth [93] ; similar as the recently reported nanolaminated nickel [95], the low-angle boundaries and high aspect ratios of grains in the columnar structure may reduce the mobility of grain boundaries as well as suppress recrystallization; the residual stresses in the HEA and W films in the annealing condition could also affect microstructural stability. Nonetheless, the refractory metals have very similar thermal expansion coefficients to the sapphire substrate at both room and high temperatures, so both the residual stresses of HEA and W would be significantly smaller than their yield strengths. Therefore, dislocation motion due to residual stress would not play a substantial role in grain growth compared to the other mechanisms.

Fig. 5 schematically illustrates how a strong, ductile and stable material is created by combining alloying effect and scaling laws. In contrast to the strength-ductility trade-off for a bulk coarse-grained W and HEA, both strength and ductility are significantly improved in nc HEA micro-pillars, compared to a bulk HEA, benefiting from reduced sample size and grain refinement (Fig. 5a). With regards to strength-stability synergy (Fig. 5b), the drawback of thermal instability in nc W can be overcome by alloying in nc HEAs which also results a higher strength level.

Technologically, the fabrication and properties of this new class of small-dimension refractory HEAs are interesting and attractive. Although co-sputtering technique has been suggested to produce HEA films in some earlier reports [109, 110], to our knowledge this work constitutes the first report of the formation of single-phase nanostructured refractory HEAs. Furthermore, the fabrication process for these thin films is fast and controllable: the alloy composition, film thickness and grain size can be tuned.

Towards application, although the HEA films and pillars contain heavy elements, they still offer the highest specific-yield-strength values (strength-to-weight

ratios) approaching 1 MJkg^{-1} and high Young's modulus (seen in Supplementary Fig. 6), and on this basis they surpass not only bulk metals and alloys but also other metallic pillars (Supplementary Fig. 7). The high specific strength of the small-scale HEAs combined with good ductility and high Young's modulus may permit access to high toughness, stiffness, hardness and wear resistance in a very high-stress environment, relative to other engineering materials. Last but not least, because the nanostructured HEAs are thermally stable at elevated temperatures and their bulk forms can even access large stresses above 1600°C , they may have a great opportunity to serve as high-temperature materials. Although mechanical tests for small-scale HEAs at high temperatures are still needed to prove this, our initial results of the HEA films under the high-temperature, long-duration conditions promise they are capable of heat resistance and may serve as diffusion barriers and electrical resistors.

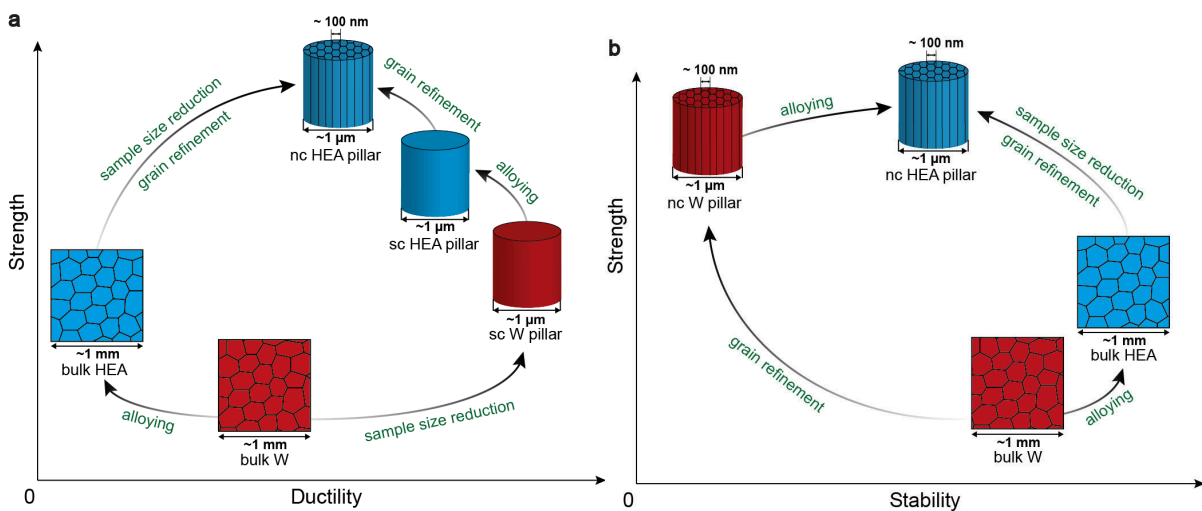


Figure 5. Schematic of strength-ductility and strength-stability synergies as comparing bulk coarse-grained W and HEA (NbMoTaW) to single crystalline (sc) or nanocrystalline (nc) W and HEA. a. The strength of a pure bulk W with coarse grains is increased by either alloying to a HEA at an expense of ductility (alloying effect) or by sample size reduction to a micrometer-sized single crystal with a benefit of being more ductile as well (sample size effect). The optimized strength-ductility combination can be achieved in a nc HEA micro-pillar with the benefits from sample size reduction, grain-boundary strengthening and solid-solution hardening. **b.** The strength of a pure bulk W can be either significantly increased by grain refinement to a nc W but at a dramatic expense of thermal stability or increased by alloying to a bulk HEA with an improvement of stability. In a nanostructured HEA both extraordinary strength and excellent thermal stability can be achieved.

Despite much work remains to optimize small-scale HEAs for applications, for example, the best alloying elements and optimized grain and specimen size combination, the extraordinary properties of small-scale HEAs reported here offer a strong motivation to pursue their development.

Methods

Sample preparation and characterization. Our NbMoTaW HEA films were deposited using DC magnetron co-sputtering technique on (100) silicon substrates (coated with 50-nm SiO₂ and 50-nm Si₃N₄ as diffusion barriers) or sapphire substrates (for annealing at 1100°C) at room temperature (Fig. 1b and Supplementary Fig. 1). The chamber base pressure was kept lower than 10⁻⁶ mbar. During co-sputtering, the powers of the magnetrons were adjusted to obtain the equal arriving ratio of Nb, Mo, Ta and W, and the substrate was rotating as 30 rotations per minute in to homogenize alloy composition and film thickness. The IBAD method was also applied using a broad ion beam source (KRI KDC 40, beam energy of 1.2 keV, current of 5 mA and incidence angle of 35°) to decrease grain sizes, as compared to the Normal sputtering condition without ion gun. The film thickness is 3 μm and no difference was observed between the films deposited on silicon and sapphire substrates, in terms of the microstructure and mechanical properties. As a control, we also produced pure W films using the same conditions and parameters. The crystal orientations and elemental compositions of the films were characterized by EBSD and EDX, respectively, in a FEI Quanta 200 FEG SEM. The grain size and phase were determined by XRD (Cu-Kα1 monochromatic radiation in a 2θ range from 10 to 100°).

From the obtained films, the pillar specimens were fabricated using a FIB system (Helios Nanolab 600i, FEI) with a coarse milling condition of 30 kV and 80 pA and a final polishing condition of 5 kV and 24 pA. The FIB-milled pillars have diameters of approximately 1 μm, 500 nm, 200 nm and 100 nm, and aspect ratios

of 2.5–5. The tapering angle is $\sim 2\text{--}4^\circ$ and the top diameters were chosen to calculate engineering stresses.

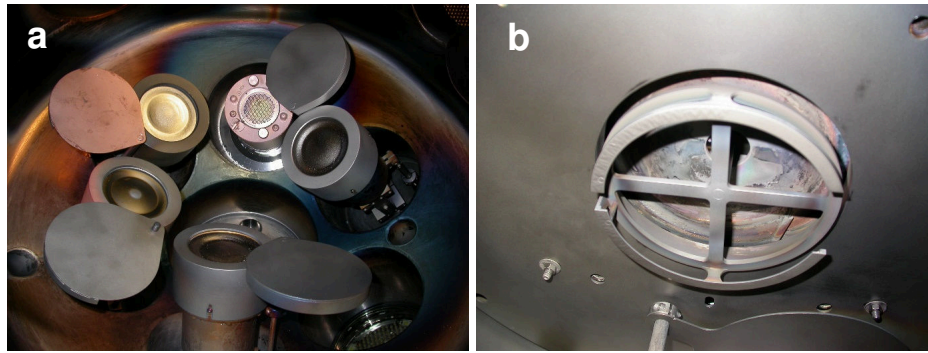
Mechanical testing. The micro-compression tests were carried out in a nanoindenter using a diamond flat-punch tip. To eliminate strain-rate effects, we compressed all the pillars with a strain rate of $2 \times 10^{-3} \text{ s}^{-1}$ in the displacement-control mode which was controlled by a feedback algorithm. It should be noted that a bigger tapering angle ($>5^\circ$), a higher aspect ratio (>5) and the misalignment between the pillar top and flat punch could lead to very localized plastic deformation, buckling and bending, respectively. All the pillars were examined using SEM before and after compression tests, and those showing the above phenomena were eliminated to minimize these influences. The yield stress of pillars were measured as offset flow stress at 0.2% of strain. However, a large stress–strain scatter was usually observed in initial stage of plastic flow during compression, so the flow stresses at 5% of strain were used to compare the size effects.

Heat treatment. To evaluate the thermal stability of the HEA and W films, we equilibrated the films with sapphire substrates at 1100°C in an argon atmosphere (the purity is $\geq 99,999$, PanGas AG, Switzerland) for three days (heating and cooling rates are 100°C per hour). Pre- and post-annealing films and pillar strengths were characterized, measured and compared.

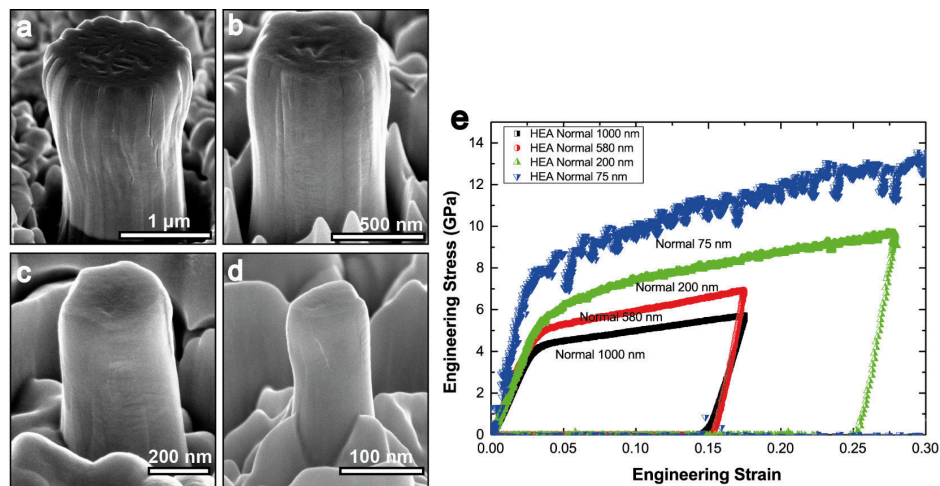
Acknowledgements

The authors would like to thank P. Gasser, K. Kunze (ScopeM, ETH Zurich) for their help with EBSD and FIB work, FIRST (ETH Zurich) for sputtering facility, S. Maiti and P. Kuczera (Crystallography, ETH Zurich) for supplying the bulk HEA sample and heat-treatment oven, C. Müller for proof-reading the manuscript. The authors also gratefully acknowledge financial support through the Swiss National Science Foundation (SNF Grants: 200021_143633 and 200021_140532).

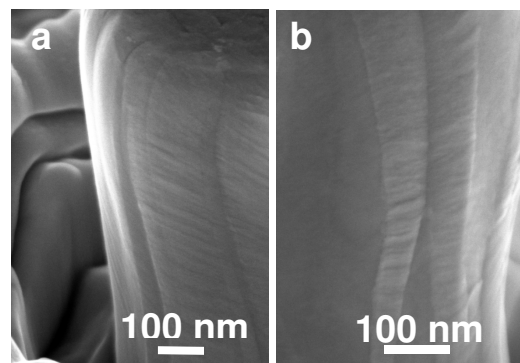
Supplementary Information



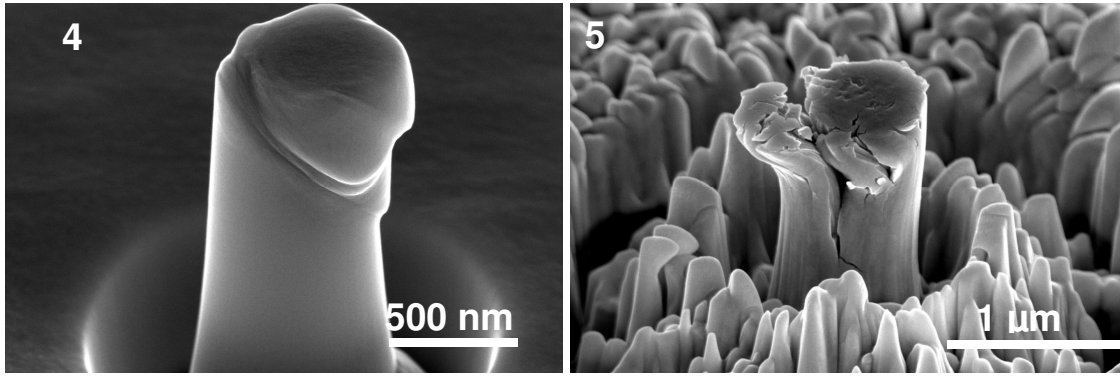
Supplementary Figure 1. The pictures of the magnetron co-sputtering system equipped with four targets arranged in a symmetry. This setup is used to synthesize the multi-component-alloy thin films: a, targets and the ion gun; b, the substrate holder.



Supplementary Figure 2. a-d, SEM images of typical as-deformed HEA pillars (Normal) with the diameter (D) ranging from approximately $1\ \mu\text{m}$ to $100\ \text{nm}$. e, Representative stress-strain curves of the HEA pillars, showing a size-dependent strength.

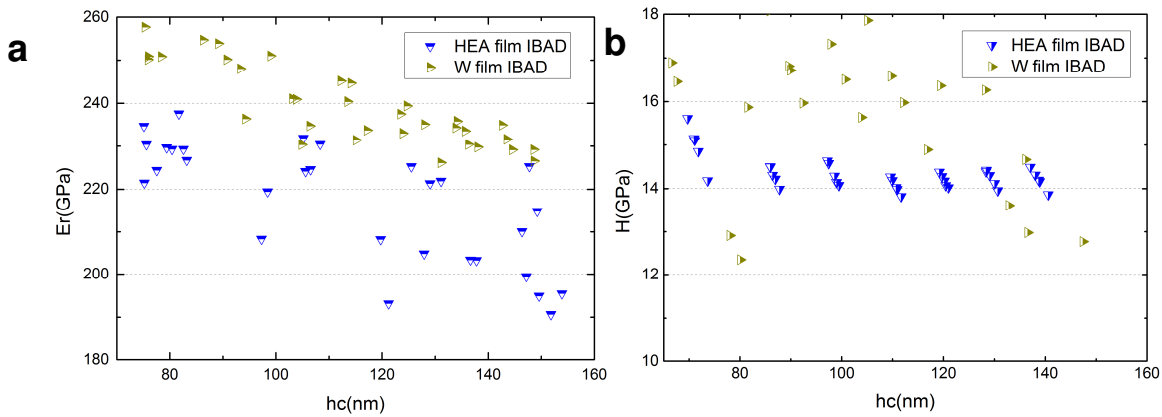


Supplementary Figure 3. High-resolution SEM images of typical as-deformed columnar-grain HEA pillar ($[011]$ orientation with the diameter of $\sim 500\ \text{nm}$)



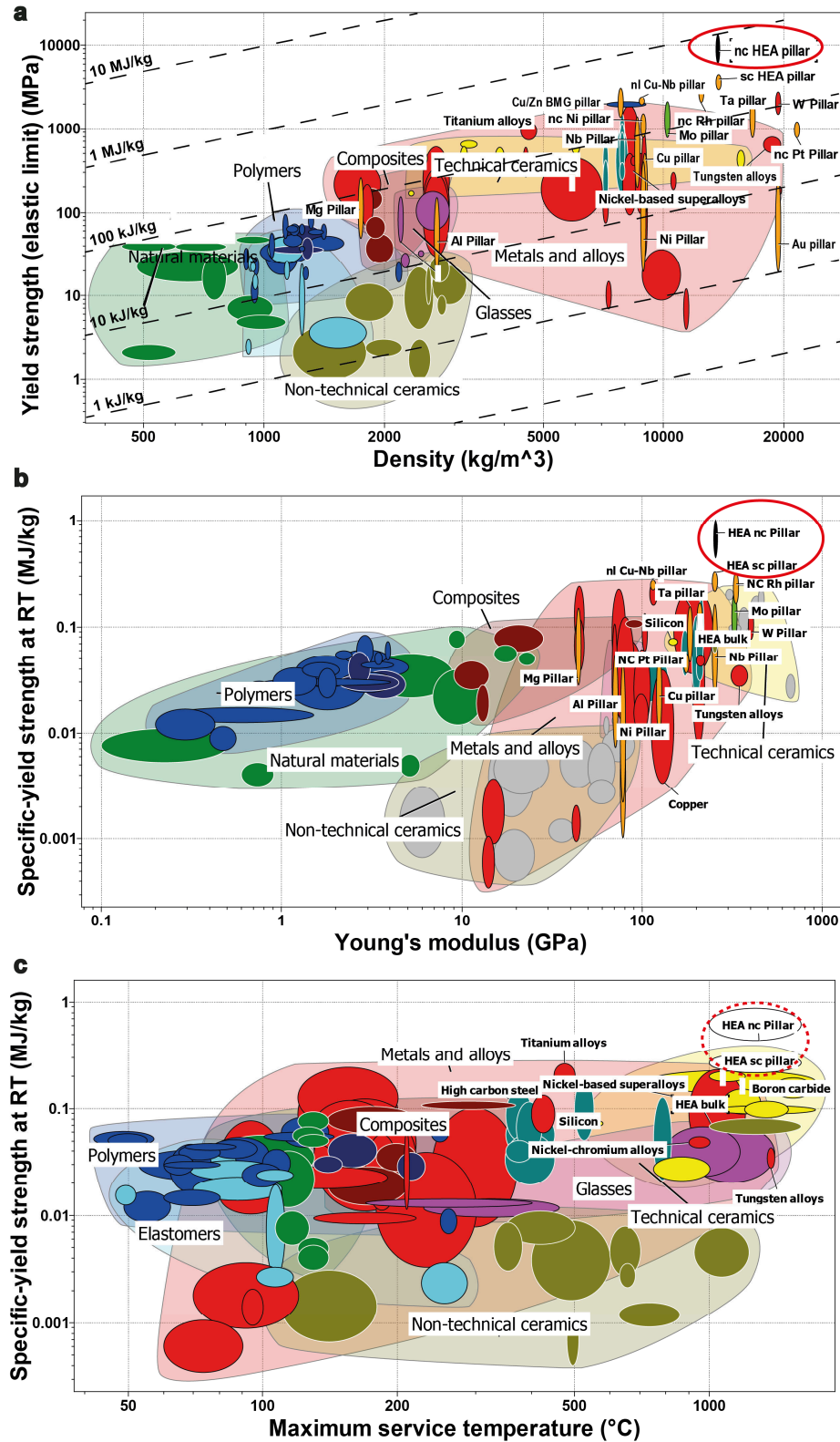
Supplementary Figure 4. SEM image of a typical as-deformed single-crystal HEA pillar ([011] orientation with the diameter of ~500 nm)

Supplementary Figure 5. SEM image of a typical as-deformed IBAD W pillar ([011] orientation with a diameter of ~700 nm), showing cracks propogage along the loading direction and indicating a brittle fracture behavior.



Supplementary Figure 6. Reduced modulus and hardness of the HEA and W films measured using nanoindenter with a Berkovich tip. The Young's modulus of the specimen can be calculated using the relation of

$\frac{1}{E_r} = \frac{1-\nu_i^2}{E_i} + \frac{1-\nu_s^2}{E_s}$. In our case, the specimen' modulus E_s is nearly the same as reduced modulus E_r . It should be note that W films have higher surface roughness than the HEA films and the roughness could also influence slightly on the measured modulus and hardness.



Supplementary Figure 7. Comparison of small-scale HEAs (single crystalline (sc) and nanostructured (nc) in this study) with various bulk materials and metallic pillars. Ashby maps of (a) yield strength vs. density, (b) specific-yield strength vs. Young's modulus and (c) specific-yield strength at room temperature vs. maximum service temperature (the service temperatures of the HEA pillars are assumed from the compression tests of the bulk specimen). The yield strengths for bulk specimens are based on tensile tests and those for the pillars are obtained from micro-compression tests (The data base for bulk materials is according to Granta Design Limited CES EduPack 2014)

References

- [1] Yeh JW, Chen SK, Lin SJ, Gan JY, Chin TS, Shun TT, Tsau CH, Chang SY. *Advanced Engineering Materials* 2004;6:299.
- [2] Huang PK, Yeh JW, Shun TT, Chen SK. *Advanced Engineering Materials* 2004;6:74.
- [3] Yeh JW, Chen YL, Lin SJ, Chen SK. *Materials Science Forum* 2007;560:1.
- [4] Senkov ON, Senkova SV, Woodward C, Miracle DB. *Acta Mater* 2013;61:1545.
- [5] Zhu C, Lu ZP, Nieh TG. *Acta Mater* 2013;61:2993.
- [6] C.J. Tong MRC, S.K. Chen, . *Metallurgical and Materials Transactions A* 2005;36A:1263.
- [7] Tsai CW, Tsai MH, Yeh JW, Yang CC. *J Alloy Compd* 2010;490:160.
- [8] Tsai MH, Yeh JW, Gan JY. *Thin Solid Films* 2008;516:5527.
- [9] Senkov ON, Wilks GB, Miracle DB, Chuang CP, Liaw PK. *Intermetallics* 2010;18:1758.
- [10] Senkov ON, Wilks GB, Scott JM, Miracle DB. *Intermetallics* 2011;19:698.
- [11] D. Kaufmann RM, C.A. Volkert, O. Kraft,. *Int J Plasticity* 2011;27:470.
- [12] Voyiadjis GZ, Almasri AH, Park T. *Mechanics Research Communications* 2010;37:307.
- [13] Arzt E. *Acta Mater* 1998;46:5611.
- [14] Kraft O, Gruber PA, Monig R, Weygand D. *Annual Review of Materials Research*, Vol 40 2010;40:293.
- [15] Dehm G. *Progress in Materials Science* 2009;54:664.
- [16] Uchic MD, Shade PA, Dimiduk DM. *Annu Rev Mater Res* 2009;39:361.
- [17] Greer JR, De Hosson JTM. *Progress in Materials Science* 2011;56:654.
- [18] Dimiduk DM, Uchic MD, Parthasarathy TA. *Acta Mater* 2005;53:4065.
- [19] Dou R, Derby B. *Scripta Materialia* 2009;61:524.
- [20] Uchic MD, Dimiduk DM, Florando JN, Nix WD. *Science* 2004;305:986.
- [21] Greer JR, Oliver WC, Nix WD. *Acta Mater* 2005;53:1821.
- [22] Ng KS, Ngan AHW. *Acta Mater* 2008;56:1712.
- [23] Schneider AS, Kaufmann D, Clark BG, Frick CP, Gruber PA, Monig R, Kraft O, Arzt E. *Phys Rev Lett* 2009;103.
- [24] Schneider AS, Frick CP, Clark BG, Gruber PA, Arzt E. *Mat Sci Eng a-Struct* 2011;528:1540.
- [25] Kim JY, Greer JR. *Acta Mater* 2009;57:5245.
- [26] Kim J-Y, Jang D, Greer JR. *Acta Mater* 2010;58:2355.
- [27] Han SM, Bozorg-Grayeli T, Groves JR, Nix WD. *Scripta Materialia* 2010;63:1153.
- [28] Malygin GA. *Phys. Solid State* 2012;54:1220.
- [29] Han SM, Feng G, Jung JY, Jung HJ, Groves JR, Nix WD, Cui Y. *Appl Phys Lett* 2013;102:041910.
- [30] Weinberger CR, Cai W. *Proceedings of the National Academy of Sciences* 2008;105:14304.
- [31] Greer JR, Weinberger CR, Cai W. *Mat Sci Eng a-Struct* 2008;493:21.

- [32] Denton AR, Ashcroft NW. *Phys Rev A* 1991;43:3161.
- [33] Zhou YJ, Zhang Y, Wang FJ, Chen GL. *Appl Phys Lett* 2008;92.
- [34] Sheldrick GM. *Acta Crystallogr A* 2008;64:112.
- [35] Peng LM, Ren G, Dudarev SL, Whelan MJ. *Acta Crystallogr A* 1996;52:456.
- [36] Spolenak R, Dietiker M, Buzzi S, Pigozzi G, Loffler JF. *Acta Mater* 2011;59:2180.
- [37] Loffler JF, Buzzi S, Dietiker M, Kunze K, Spolenak R. *Philos Mag* 2009;89:869.
- [38] Dimiduk DM, Woodward C, LeSar R, Uchic MD. *Science* 2006;312:1188.
- [39] Dimiduk DM, Nadgorny EM, Woodward C, Uchic MD, Shade PA. *Philos Mag* 2010;90:3621.
- [40] Guo W, Dmowski W, Noh JY, Rack P, Liaw PK, Egami T. *Metall Mater Trans A* 2013;44A:1994.
- [41] Duesbery MS, Vitek V. *Acta Mater* 1998;46:1481.
- [42] Suzuki T, Kamimura Y, Kirchner HOK. *Philos Mag A* 1999;79:1629.
- [43] Vitek V. *Progress in Materials Science* 1992;36:1.
- [44] Butt MZ, Feltham P. *J Mater Sci* 1993;28:2557.
- [45] Neuhäuser H, Schwink C. *Solid Solution Strengthening. Mater Sci Tech-Lond.* Wiley-VCH Verlag GmbH & Co. KGaA, 2006.
- [46] Korte S, Clegg WJ. *Philos Mag* 2011;91:1150.
- [47] Lee SW, Nix WD. *Philos Mag* 2012;92:1238.
- [48] Parthasarathy TA, Rao SI, Dimiduk DM, Uchic MD, Trinkle DR. *Scripta Materialia* 2007;56:313.
- [49] Hull DaDJB, editor *Introduction to Dislocations: Elsevier Butterworth Heinemann: Oxford, 2001.*
- [50] Rao SI, Dimiduk DM, Tang M, Parthasarathy TA, Uchic MD, Woodward C. *Philos Mag* 2007;87:4777.
- [51] Oh SH, Legros M, Kiener D, Dehm G. *Nat Mater* 2009;8:95.
- [52] Huang L, Li Q-J, Shan Z-W, Li J, Sun J, Ma E. *Nat Commun* 2011;2:547.
- [53] Wang JN. *Mat Sci Eng a-Struct* 1996;206:259.
- [54] Alshits V, Indenbom V. 1986.
- [55] Natsik VD, Chishko KA. *Crystal Research and Technology* 1984;19:763.
- [56] del Grosso MF, Bozzolo G, Mosca HO. *J Alloy Compd* 2012;534:25.
- [57] Lilensten L, Couzinié JP, Perrière L, Bourgon J, Emery N, Guillot I. *Mater Lett* 2014;132:123.
- [58] Widom M, Huhn WP, Maiti S, Steurer W. *Metallurgical and Materials Transactions A* 2014;45:196.
- [59] Zou Y, Maiti S, Steurer W, Spolenak R. *Acta Mater* 2014;65:85.
- [60] Gorr B, Azim M, Christ HJ, Mueller T, Schliephake D, Heilmaier M. *J Alloy Compd* 2015;624:270.
- [61] Senkov ON, Scott JM, Senkova SV, Meisenkothen F, Miracle DB, Woodward CF. *J Mater Sci* 2012;47:4062.
- [62] Wu YD, Cai YH, Wang T, Si JJ, Zhu J, Wang YD, Hui XD. *Mater Lett* 2014;130:277.
- [63] Liu CM, Wang HM, Zhang SQ, Tang HB, Zhang AL. *J Alloy Compd* 2014;583:162.

- [64] Senkov ON, Woodward CF. *Materials Science and Engineering: A* 2011;529:311.
- [65] Senkov ON, Senkova SV, Woodward C. *Acta Mater* 2014;68:214.
- [66] Gludovatz B, Hohenwarter A, Catoor D, Chang EH, George EP, Ritchie RO. *Science* 2014;345:1153.
- [67] Halford TP, Takashima K, Higo Y, Bowen P. *Fatigue Fract Eng M* 2005;28:695.
- [68] Matoy K, Schönherr H, Detzel T, Schöberl T, Pippan R, Motz C, Dehm G. *Thin Solid Films* 2009;518:247.
- [69] Cao W, Kundu A, Yu Z, Harmer MP, Vinci RP. *Scripta Materialia* 2013;69:81.
- [70] Massl S, Thomma W, Keckes J, Pippan R. *Acta Mater* 2009;57:1768.
- [71] Iqbal F, Ast J, Göken M, Durst K. *Acta Mater* 2012;60:1193.
- [72] Armstrong DEJ, Wilkinson AJ, Roberts SG. *Philosophical Magazine Letters* 2011;91:394.
- [73] Wurster S, Motz C, Pippan R. *Philos Mag* 2012;92:1803.
- [74] Sumigawa T, Shishido T, Murakami T, Kitamura T. *Materials Science and Engineering: A* 2010;527:4796.
- [75] International A. ASTM Standard E399-09. ASTM Standard E399-09. West Conshohocken, PA, , 2003.
- [76] Yu H, Wu L, Guo L, Du S, He Q. *International Journal of Solids and Structures* 2009;46:3710.
- [77] Giannattasio A, Roberts SG. *Philos Mag* 2007;87:2589.
- [78] Courtney TH. *Mechanical behavior of materials*: Waveland Press, 2005.
- [79] Ostlund F, Rzepiejewska-Malyska K, Leifer K, Hale LM, Tang YY, Ballarini R, Gerberich WW, Michler J. *Adv Funct Mater* 2009;19:2439.
- [80] Lu K, Lu L, Suresh S. *Science* 2009;324:349.
- [81] Chookajorn T, Murdoch HA, Schuh CA. *Science* 2012;337:951.
- [82] Ritchie RO. *Nat Mater* 2011;10:817.
- [83] Cantor B, Chang ITH, Knight P, Vincent AJB. *Materials Science and Engineering: A* 2004;375–377:213.
- [84] Zhang Y, Zuo TT, Tang Z, Gao MC, Dahmen KA, Liaw PK, Lu ZP. *Progress in Materials Science* 2014;61:1.
- [85] Jang DC, Greer JR. *Nat Mater* 2010;9:215.
- [86] Lai A, Du ZH, Gan CL, Schuh CA. *Science* 2013;341:1505.
- [87] Volkert CA, Lilleodden ET. *Philos Mag* 2006;86:5567.
- [88] Frick CP, Clark BG, Orso S, Schneider AS, Arzt E. *Materials Science and Engineering: A* 2008;489:319.
- [89] Okamoto NL, Kashioka D, Hirato T, Inui H. *Int J Plasticity* 2014;56:173.
- [90] Rinaldi A, Peralta P, Friesen C, Sieradzki K. *Acta Mater* 2008;56:511.
- [91] Jang D, Greer JR. *Scripta Materialia* 2011;64:77.
- [92] Mara NA, Bhattacharyya D, Dickerson P, Hoagland RG, Misra A. *Appl Phys Lett* 2008;92:231901.
- [93] Weissmüller J. *Nanostructured Materials* 1993;3:261.
- [94] Kirchheim R. *Acta Mater* 2002;50:413.

- [95] Liu XC, Zhang HW, Lu K. *Science* 2013;342:337.
- [96] Smidt F. *Int Mater Rev* 1990;35:61.
- [97] Zhang JY, Cui JC, Liu G, Sun J. *Scripta Materialia* 2013;68:639.
- [98] Wheeler J, Niederberger C, Tessarek C, Christiansen S, Michler J. *Int J Plasticity* 2013;40:140.
- [99] Liu S, Raghavan R, Zeng XT, Michler J, Clegg WJ. *Appl Phys Lett* 2014;104:081919.
- [100] Bei H, Shim S, George EP, Miller MK, Herbert EG, Pharr GM. *Scripta Materialia* 2007;57:397.
- [101] Starliper AG, Kenworthy H. *Electrodeposition and Surface Treatment* 1974;2:249.
- [102] Maaß R, Volkert CA, Derlet PM. *Scripta Materialia* 2015;102:27.
- [103] Johnson AA. *Philos Mag* 1959;4:194.
- [104] Gu XW, Loynachan CN, Wu ZX, Zhang YW, Srolovitz DJ, Greer JR. *Nano Lett* 2012;12:6385.
- [105] Alshehri O, Yavuz M, Tsui T. *Acta Mater* 2013;61:40.
- [106] Cottrell AH. *Trans. Met. Soc. AIME* 1958;212.
- [107] Hirth JP. *MT* 1972;3:3047.
- [108] Zhou YJ, Zhang Y, Wang FJ, Chen GL. *Appl Phys Lett* 2008;92:241917.
- [109] Chen TK, Shun TT, Yeh JW, Wong MS. *Surface and Coatings Technology* 2004;188–189:193.
- [110] Dolique V, Thomann AL, Brault P. *Plasma Science, IEEE Transactions on* 2011;39:2478.

Chapter 4. Size Effect in Quasicrystals

4.1. Icosahedral Al-Pd-Mn at room temperature⁷

The discovery of quasicrystals three decades ago unveiled a novel class of matter that exhibits long-range order but lacks translational periodicity [1]. Owing to their unique structures, quasicrystals possess many unusual and useful properties [2, 3]. However, a well-known bottleneck that impedes their widespread application is their intrinsic brittleness: plastic deformation has been found to be only possible at high temperatures or under hydrostatic pressures [4-7], and how they deform in the low-temperature regime is still unclear. Here, we report that a brittle quasicrystal exhibits an extraordinary ductility of over 50% compressive or tensile strains and a high strength of ~4.5 GPa at room temperature and submicrometer scales. Furthermore, in contrast to the generally accepted dominant deformation mechanism in quasicrystals— dislocation climb, our observation demonstrates that dislocation glide governs plasticity under high-stress and low-temperature conditions. The ability to plastically deform quasicrystals at room temperature should lead to an improved understanding of the underlying deformation mechanism and their application in small-scale devices.

In materials science, plasticity describes the non-reversible deformation of a solid in response to applied forces and determines the ability of a material to change its shape permanently without breaking. Regular crystalline materials, including most metals and ceramics, are generally plastically deformed through dislocation motion [8] or twinning [9]. The plasticity of amorphous solids, such as metallic

⁷ Y. Zou, P. Kuczera, A. Sologubenko, W. Steurer, R. Spolenak “*Superior room-temperature ductility of typically brittle quasicrystals at small sizes*”. (submitted to *Nature Communications*)

glasses, is based on the formation and propagation of shear bands [10]. In quasicrystals, despite their lack of periodicity, the plastic deformation can be also achieved by dislocation activities. In contrast to the situation in periodic crystals, every movement of a dislocation in a quasicrystal creates a cloud of for quasicrystals specific defects behind, which are called phasons [11]. As a consequence, the dislocation motion gets hindered and the material appears brittle. Although a great variety of quasicrystals has been synthesized [11, 12], and some have even been discovered in nature [13], only few of them have found applications so far, mainly due to their poor ductility and formability especially at room temperature. Hence, understanding and improving the room-temperature plasticity of quasicrystals are not only of academic interest but also essential for technological applications.

Early studies of the plastic deformation of quasicrystals focused on an easily to grow icosahedral quasicrystal, *i*-Al-Pd-Mn, in the high-temperature range above ~70% (~600°C) of its melting temperature. These studies demonstrated that the plastic deformation of *i*-Al-Pd-Mn was dominated by dislocation climb — with the Burgers vector perpendicular to the plane of dislocation motion, rather than dislocation glide — with the Burgers vector in the plane of dislocation motion [14]. It is generally believed that in quasicrystals dislocation climb is a much easier deformation mode than dislocation glide [15]. Although there are some hints that the glide motion may be possible in low-temperature conditions as suggested by numerical simulations [16], the required stress to activate the glide is extremely high, on the order of 1/10 of its shear modulus— a stress level leading to fracture without any plasticity. It has been a long-standing question concerning the deformation mechanism in quasicrystals at room temperature. Despite several investigators have sought to explore the plasticity of quasicrystals at or near room temperature using indentation or by confining gas/solid pressures, so far there is no common conclusion: the explanations include shear banding similar to metallic glasses [17], phase transformation [18], grain-boundary glide [6], pure dislocation climb [7], dislocation climb dominant [19] and

crystallization[20]. Therefore, one has to conclude that the plastic deformation of quasicrystals under a wide range of temperatures and pressures has been poorly explored — much in contrast to crystalline and amorphous solids. Two fundamental questions are still open: can steady-state plastic deformation be achieved at room temperature? If so, what is the underlying deformation mechanism?

Unveiling the room-temperature plasticity in quasicrystals hence relies on a new method to suppress fracture before plastic yielding in a simple load experiment. Our strategy is to increase the fracture strength over the yield strength in a quasicrystal by reducing a sample size. Although similar methods have been explored for other brittle materials such as ceramics [21] and metallic glasses [22], it has never been reported for quasicrystals — a rather large family of unusual solids with a lot of unknowns.

To predict at what size range a brittle quasicrystal may become ductile, we compare the different deformation mechanisms as a function of sample size: dislocation activities, crack propagation [23] and mass transport by diffusion [24]. We identify three deformation regimes: cracking-controlled, dislocation-controlled (dislocations or shear bands) and diffusion-controlled, as illustrated in Fig. 1. We find the critical size, r_p , for the brittle-to-ductile transition to be ~500 nm, and the size of the diffusion-controlled zone, r_d , should be smaller than 100 nm (see detailed analysis in Supplemental Information). Thus, our targeted sample size to attain steady-state plasticity falls in a size range from ~100 nm to ~500 nm.

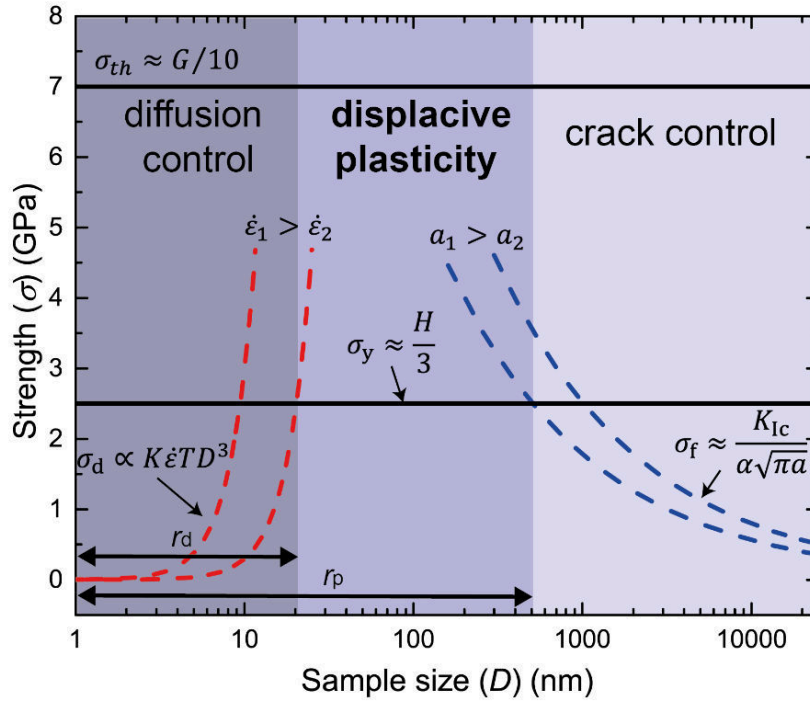


Fig. 1. Semi-quantitative representation of the deformation map for small-scale i-Al-Pd-Mn quasicrystals at room temperature. If the sample size, D , is larger than a critical size, r_p , defined as the intersection of the fracture strength, σ_f (the blue dash lines), and the yield strength, σ_y (the red dash lines), the material fails by cracking without notable plasticity, following Griffith's criterion [25], $\sigma_f = K_{Ic}/[\alpha(\pi a)^{-1/2}]$ with K_{Ic} the fracture toughness of the material, α a geometrical parameter on the order of unit and a the size of pre-existing cracks or flaws and showing a smaller-is-stronger phenomenon. If D is smaller than another critical size, r_d , the diffusion governs the strength, $\sigma_d \propto K\dot{\epsilon}TD^3$ with K , surface diffusivity, $\dot{\epsilon}$, strain rate, and T , temperature, and showing a smaller-is-weaker phenomenon. In between r_p and r_d , the curves of σ_f , σ_d and σ_y are crossed and distinguish a zone controlled by dislocations. The size range of this zone may vary by flaw sizes and strain rates, as illustrated.

In our experiments we compressed single-quasicrystalline i-Al-Pd-Mn pillars with diameters ranging from $\sim 2 \mu\text{m}$ to $\sim 150 \text{ nm}$. We observe a brittle-to-ductile transition with the critical pillar diameter between 510 nm and 350 nm (Fig. 2a): the 1.8- μm pillar exhibits a catastrophic failure at $\sim 3\%$ compressive strain; the 870-nm and 510-nm pillars show cracks about 45 degrees along the loading direction, failing at $\sim 6\%$ strain; when the pillar diameter is below 500 nm, the pillars present significantly improved ductility with compressive strains over 50% and without any cracking. The 400-nm and 200-nm pillars clearly show the deformation bands, while the 140-nm pillar reveals the deformation localized at the upper part of the pillar. All the corresponding stress-strain curves exhibit

displacement-burst phenomenon (Fig. 2a), which is generally observed in metals and metallic glasses. How the fracture strain or maximum plastic strain changes by decreasing the sample size demonstrates the brittle-to-ductile transition between 510 nm and 350 nm (Fig. 2b). When the pillar diameter is smaller than 350 nm no cracking is observed in our experiments. Regarding the size dependence of strength, the fracture strength increases from ~3.5 GPa to ~4.5 GPa with decreasing pillar diameters in the brittle regime, while the yield strength (the flow stress at the first displacement burst) is about 4.5 GPa in the ductile regime (Fig. 2c).

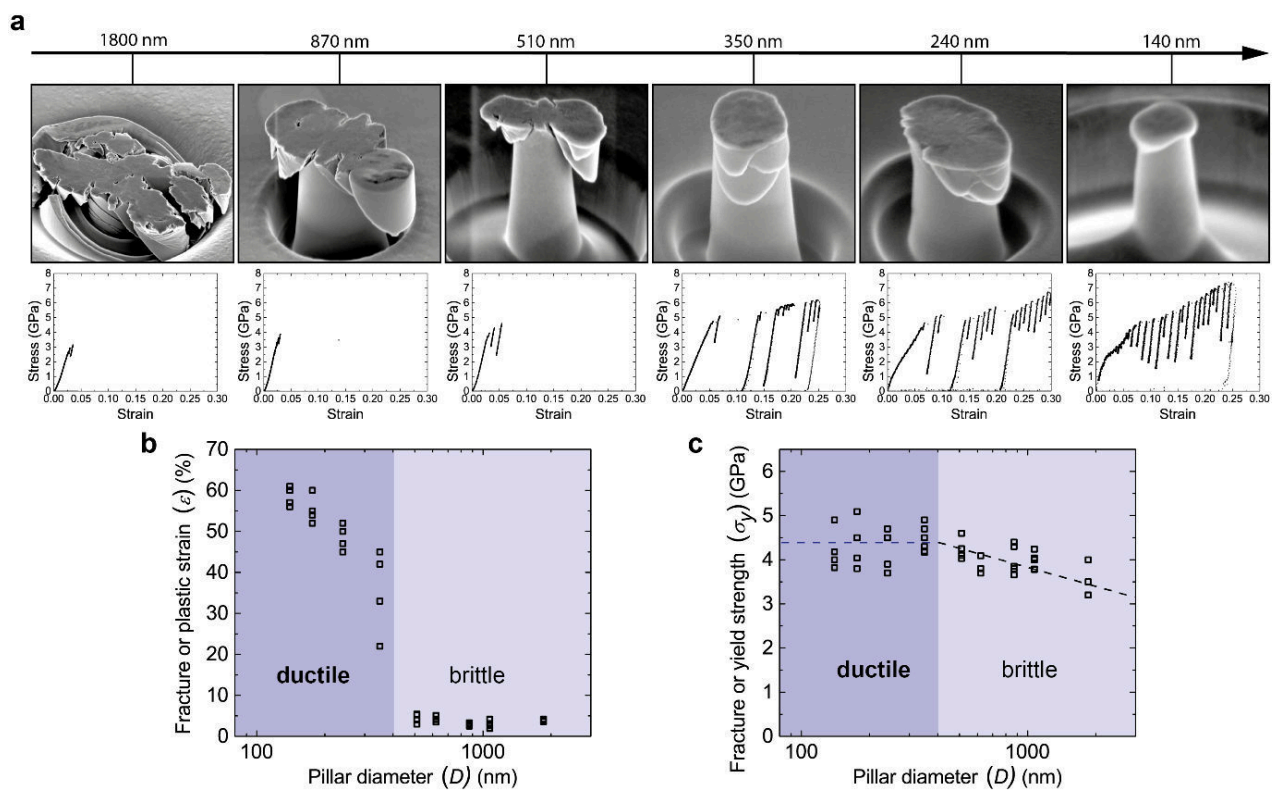


Fig. 2. Micro-compression for the single quasicrystalline i-Al-Pd-Mn pillars with the diameter ranging from ~2 μm to ~150 nm. (a) The typical SEM images of the post-deformed pillars, showing a brittle-to-ductile transition with the critical size between 510 nm to 350 nm. The corresponding engineering stress-strain curves are presented below. (b) The fracture strain or plastic strain as a function of the pillar diameter, indicating a brittle-to-ductile transition. (c) The fracture strength or yield strength as a function of the pillar diameter. In the brittle regime, the strength increases slightly with decreasing the pillar diameter; in the ductile regime, the strength is almost independent on the sample size.

Brittle materials usually show higher ductility in compression than tension. To examine the tensile ductility of the quasicrystal pillars, we employed micro-bending tests to induce an asymmetrical stress distribution. The *in-situ* SEM

bending of a 300-nm pillar shows that the deformation localizes near the pillar base by necking or thinning. We detect that the crack forms at the bending angle of $\sim 30^\circ$, and eventually fails in a catastrophic feature at the bending angle of $\sim 40^\circ$ (Fig. 3a). The *in-situ* TEM bending of a 110-nm pillar shows in a rather homogenous deformation without any cracking and fracture (Fig. 3b). The longitudinal tensile strain near the pillar center is estimated to be over 50%. The strain bands motion during the tests implies dislocation activities during the deformation (Fig. S3).

The results shown in Fig. 2 and Fig. 3 confirm that i-Al-Pd-Mn pillars are capable of both excellent ductility (compressive and tensile) and the high strength when the pillar diameter is below about 500 nm. As to our knowledge, this result was never been reported for quasicrystals before. The quasicrystal fine-scale pillars exhibit minor size dependence of strength and the deformation morphology with wavy feature (see high-resolution SEM images in Fig. S4), which is more similar to metallic glasses rather than metals.

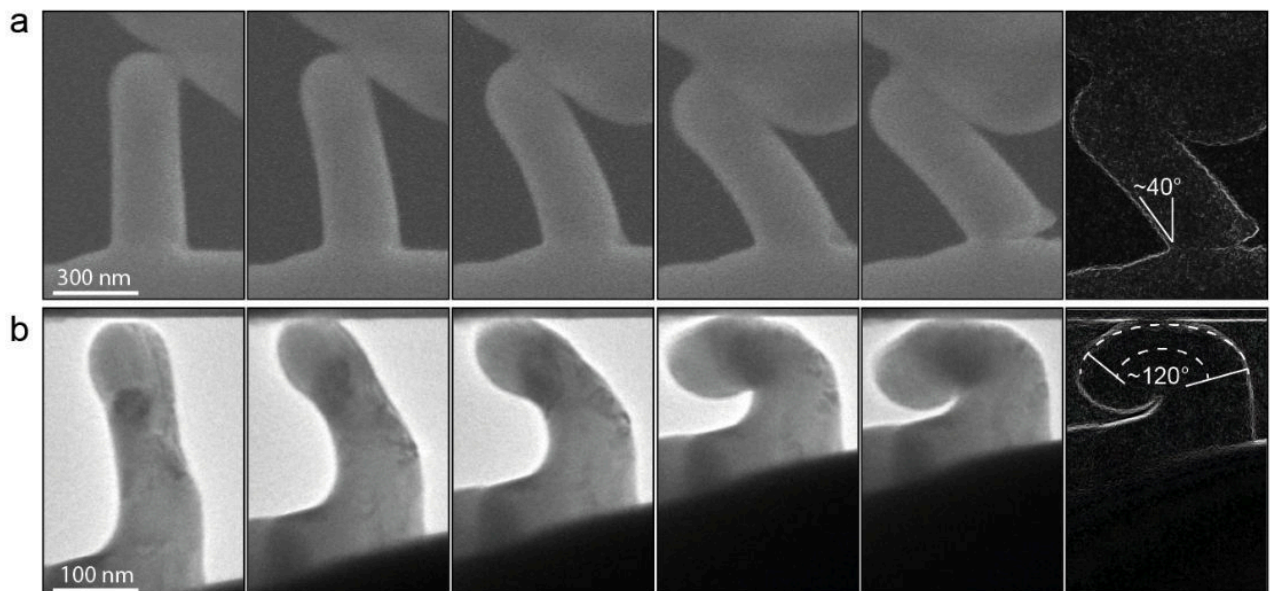


Fig. 3. *In-situ* SEM and TEM bending tests for the fine-scale i-Al-Pd-Mn pillars: (a) the SEM snapshots captured during the bending test of a pillar with the diameter of ~ 300 nm. Initial crack occurs near the pillar base at the bending angle of 30° and eventual fracture happens at the bending angle of 40° . (b) The TEM snapshots of the bending tests of a pillar in the diameter of ~ 110 nm, showing a homogenous deformation without any fracture, and the maximum tensile strain at the pillar middle is estimated to be over 50%.

A representative bright-field TEM image reveals the upper part of a deformed pillar along threefold axis (Fig. 4a). We find a slip line through the pillar and a step at the pillar edge. The loading direction is along a twofold axis and the slip plane contains another twofold axis. The high-resolution TEM image shows a very narrow band of $\sim 2\text{-}5$ nm in thickness. Along the band, there are strain-contrast modulations with a nearly equal distance of $\sim 2\text{-}5$ nm (Fig. 4b). Nevertheless, we do not observe any evidence of melting, crystallization (phase transformation) or cracking that were used to explain room-temperature deformation in quasicrystals. Using the inverse Fourier transformed images, we confirm the occurrence of dislocation arrays along the deformation band, as shown in Fig. 4c and 4d from the areas boxed in Fig. 4b. The inserted lattice fringes, as indicated by the arrows, suggest that there are dislocation components along the slip direction—the glide components. However, we do not find any dislocation component parallel the slip direction—the climb component.

Our atomic model of *i*-Al-Pd-Mn quasicrystal matches the orientation of the sample before and after deformation, respectively (Fig. 4e and 4f). The thin black lines indicate a chosen set of quasi-lattice planes. Along the slip line shown in Fig. 4f, we can identify the mismatch region generated by the dislocation glide due to the local shear between the quasi-lattice planes (Fig. 4g and 4h). Such discontinuous quasi-lattice planes could be interpreted as dislocations with Burger's vector along the slip direction, which compares to the lattice fringe patterns in Fig. 4c and 4d. The strain contrast shown in Fig. 4b could be attributed to strain fields of dislocations or related phason faults left behind. This is a strong indication that the plasticity of quasicrystals at room temperature is dominated by dislocation glide. Although climb motion leads to the removal or insertion of so-called "worms" without overlaps or open spaces, the process requires thermal activation. But at room temperature the diffusion in quasicrystals is believed to be inhibited. Under high-stress and low-temperature conditions, dislocation glide

may be active and even dominate, generating a high density of heavily distorted zones in the wake of the dislocation glide.

The approach of the reduction of the sample size to plastically deform typically brittle quasicrystals may pave way to fundamentally understand the deformation mechanism of quasicrystals at room temperature, possibly at even lower temperatures and for all the other types of quasicrystals. Towards technologically applications, small-scale quasicrystals are attractive not only due to their extraordinarily high strengths and ductility but also because they offer the highest specific-yield-strength values (strength-to-weight ratios, about 1 MJ/kg), surpassing reported metal and metallic glass pillars (Fig. S5). Small-scale quasicrystals having superior strength and ductility, together with their functional properties, may permit access to being structurally and functionally useful. Despite much work remains to optimize them for better properties, the observation of excellent room-temperature plasticity reported here offer a strong motivation to further explore our knowledge in quasicrystals and their engineering applications.

Methods

An initial compact of composition $\text{Al}_{70}\text{Pd}_{21.5}\text{Mn}_{8.5}$ was prepared from pure metals (Al 99.9999 %, Pd 99.9 %, Mn 99.95 %). The sample was pre-alloyed in an arc furnace. Afterwards it was placed in an Al_2O_3 crucible and sealed in a quartz glass ampoule under an Ar atmosphere. The heat treatment consisted of the following steps: heating to 1323 K (above its melting temperature), slow cooling to 1083 K at the rate of 30 K h^{-1} , annealing at 1083 K for 150 hours, and subsequent quenching in water. The composition of the resulting sample was confirmed using energy dispersive X-ray spectroscopy (EDX). The X-ray powder diffraction (XRD) pattern (in Fig. S1) indicates that the resulting sample is a single-phase icosahedral quasicrystal.

The prepared i-Al-Pd-Mn is thermodynamically stable with an average grain size about 300 μm and is also highly isotropic. We fabricated single quasicrystalline pillars, in cylindrical shapes, from a coarse grain in a well-polished i-Al-Pd-Mn sample using a FIB system (Helios Nanolab 600i, FEI): a coarse milling condition of 30 kV and 80 pA and a final milling condition of 5 kV and 7 pA. The diameters of the FIB-milled pillars are in the range of ~ 150 nm to ~ 2 μm and the aspect ratios are ~ 3.0 - 4.5 . A taper of 2 - 3° was generally observed and the top diameter of the pillar was chosen to calculate stress.

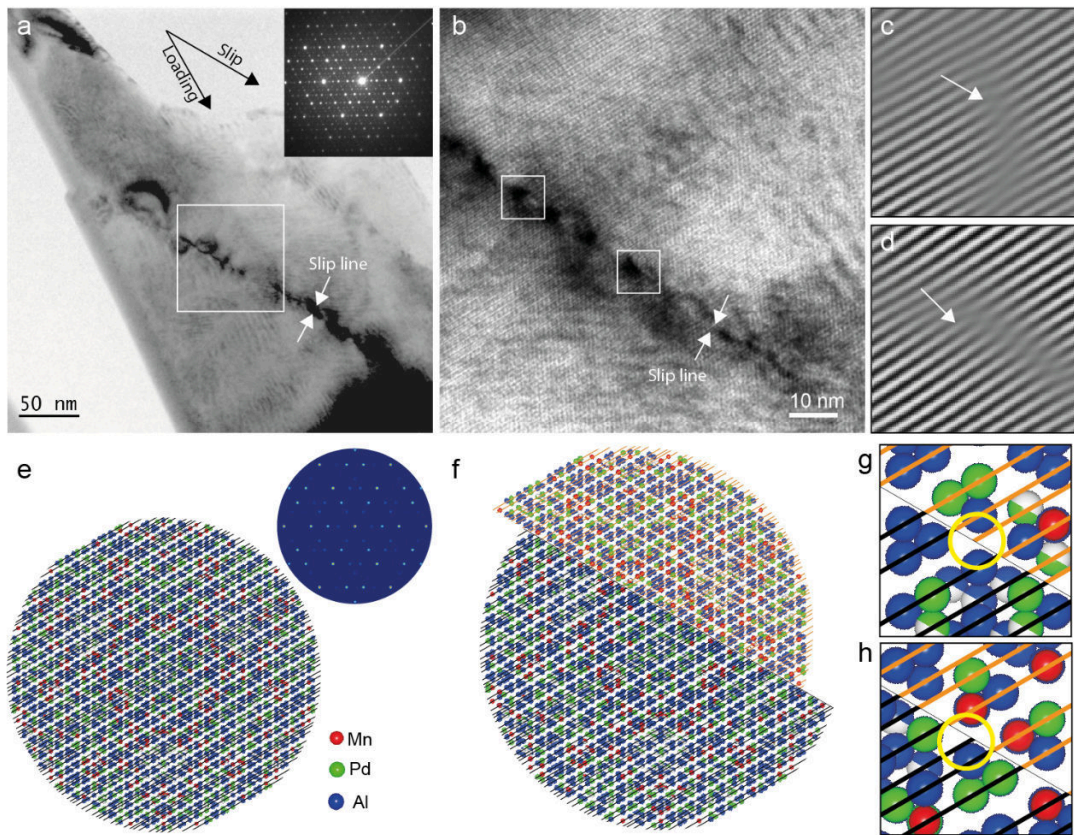


Fig. 4. TEM study of the locally deformed region in the i-Al-Pd-Mn pillar observed along a threefold axis. (a) A typical bright-field TEM image showing a narrow and straight band traversing the pillar and the corresponding electron diffraction pattern. The loading direction is along a twofold axis and the slip direction is along another twofold axis. (b) The high-resolution TEM image shows the deformation band with a thickness of ~ 2 - 5 nm and strain contrast modulations along the line. The rest area is nearly defect-free. (c) and (d) are the inverse Fourier transformation of the regions marked in (b), emphasizing the very localized and periodic lattice distortions along the deformation band. This indicates a dislocation array along the deformation band, implying the dislocation glide as a deformation mode. (e) The atomic model of i-Al-Pd-Mn projected along the threefold axis with its calculated the diffraction pattern to be compared with the experimental one in (a). (f) A schematic view in projection of the model after shear deformation, with the same loading and slip directions as shown in (b). (g) and (h) showing the local mismatches between the quasilattice planes, where the strain is concentrated.

We used the nanoindenter (Hysitron Inc., USA) with a diamond flat-punch tip (5 μm in diameter, Synton-MDP, Switzerland) to compress the pillars in a displacement control mode and the strain rate of $2 \times 10^{-3} \text{ s}^{-1}$ by feedback mechanism. At least four pillars for each size were compressed. The deformed pillars were imaged using a high resolution SEM (Magellan, FEI). For the post-mortem TEM characterization, the deformed pillars were thinned down to a lamella by ion milling, lift-out, thinning and polishing in the FIB system. Their cross-sections were then examined using a TEM (Tecnai F30, FEI, operated at 300 kV). *In-situ* SEM and TEM bending tests were carried out using a nano-manipulator (Kleindiek, Germany) fitted to a SEM (Hitachi SU 8200) and an indenter holder (Nanofactory Instruments AB, SA2000N) fitted to a TEM (JEOL JEM-2100), respectively, with a displacement rate of $\sim 5 \text{ nm s}^{-1}$.

For our deformation simulations, we used the QG atomic model ($\sim 70 \text{ \AA}$ in diameter) of icosahedral Al-Pd-Mn [26]. We oriented the model along the threefold axis and calculated the diffraction pattern to match the electron diffraction pattern. In this way, the orientation of our model matches the orientation of the sample in the figure.

Acknowledgements

We thank S. Takeuchi (Tokyo University of Science) and K. Edagawa (The University of Tokyo) for their helpful discussion, T. Yukishita and S. Ashida (Kyoto University) for their help in the bending tests and ScopeM (ETH Zurich) for supplying electron microscopy facility. Y.Z. acknowledges the financial supports through the Swiss National Science Foundation (SNF Grants: 200021_143633) and the JSPS strategic program (GR14103). T.S. and T. K. acknowledge the JSPS Grants (No. 25000012).

Supplementary Information

Prediction of brittle-to-ductile transition.

In a brittle material, the fracture strength, σ_f , follows Griffith's criterion [25], as $\sigma_f = K_{IC}/[\alpha(\pi a)^{1/2}]$ with K_{IC} the fracture toughness of the material, α a geometrical parameter on the order of unit and a the size of pre-existing cracks or flaws. Statistically, larger samples are more likely to contain larger flaws, or weaker links, and, consequently, smaller samples usually exhibit higher fracture strengths than the large ones—the size effect due to Weibull statistics [27]. Because the fracture strength, σ_f , cannot rise above the yield strength, σ_y , below a certain length scale plastic flow may determine the strength. The intersection between the curves for σ_f and σ_y provides a critical size, r_p , for a brittle-to-ductile transition, as illustrated in Fig. 1a. Assuming that the largest pre-existing cracks or flaws is one order of magnitude smaller than the sample dimension, we can obtain r_p approximately 500 nm for i-Al-Pd-Mn, using α , ~ 1 , K_{IC} , $\sim 1.25 \text{ MPa m}^{1/2}$ [28] and the hardness, H , $\sim 8.5 \text{ GPa}$ [28]. However, further reduction of the sample size down to the nanometer scale leads to a significant increase of the surface-to-volume, and surface diffusion may control the plastic flow, resulting in a reduced strength. In a relation similar to Coble creep [29], the diffusion strength, σ_d , reflects a ‘smaller is weaker’ phenomenon. The crossover between σ_d and σ_y defines a diffusion-controlled zone with the length scale of r_d (Fig. 1a). Although it is difficult to calculate the exact value of r_d due to the lack of available literature data, recent studies on $\text{Al}_{90}\text{Fe}_5\text{Ce}_5$ metallic glass [30] and pure Sn [31] demonstrate that diffusion controls plasticity below the sample sizes of 20 nm and 130 nm, respectively, at a strain rate of $\sim 10^{-3} \text{ s}^{-1}$ and room temperature. Hence, we estimate the r_d of i-Al-Pd-Mn as a few tens of nanometers (definitely smaller than 100 nm), under the similar experimental conditions. Based on this analysis, our targeted sample size to attain steady-state plasticity falls in a range approximately from $\sim 100 \text{ nm}$ to $\sim 500 \text{ nm}$.

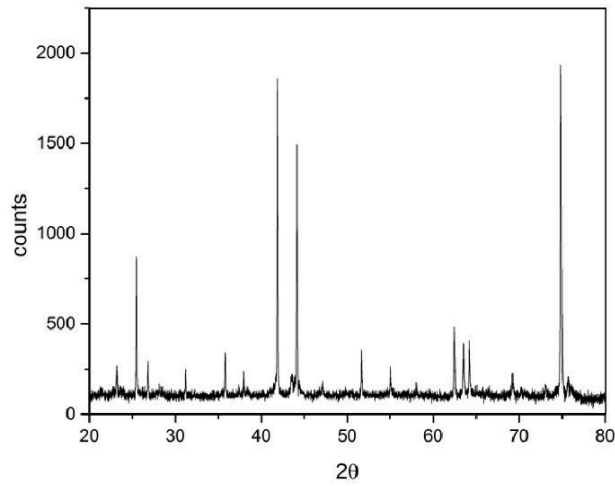


Fig. S1. Powder diffraction pattern of i-Al-Pd-Mn (Cu, $K_{\alpha 1}$), indicating an icosahedral phase which is comparable to the pattern in literature [32].

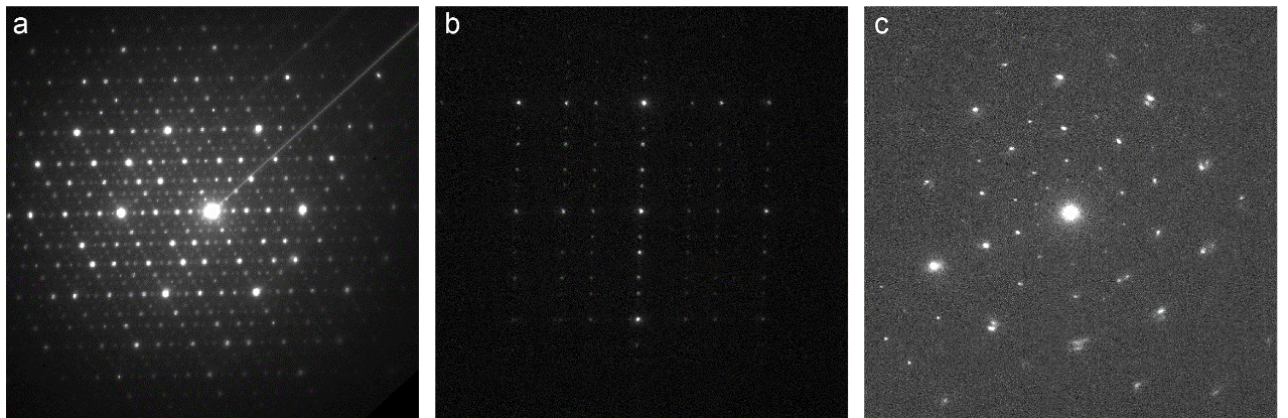


Fig. S2. Electron diffraction patterns of the i-Al-Pd-Mn pillar along (a) three-fold, (b) two-fold and (c) five-fold symmetry axis, indicating that the as prepared pillar is a single icosahedral quasicrystal.

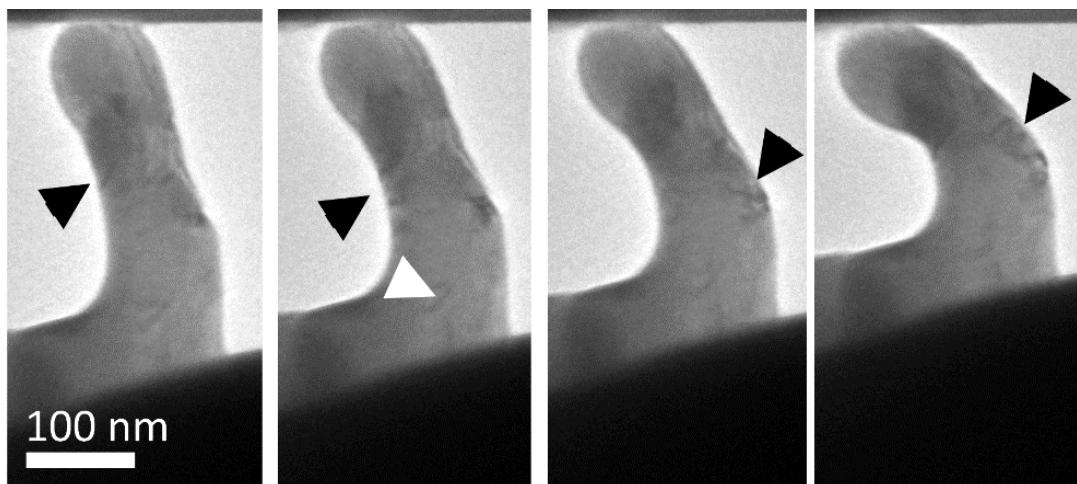


Fig. S3 The TEM snapshots of the bending tests. The arrows indicate the dislocation-like contrasts.

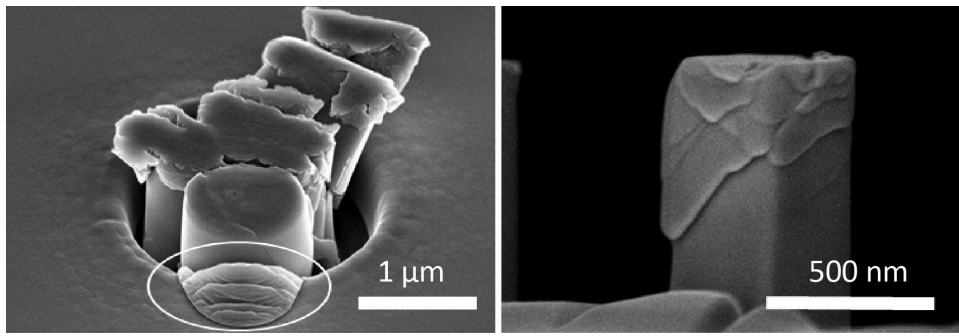


Fig. S4. Typical SEM images of the post-deformed pillars showing the deformation bands with wavy morphology.

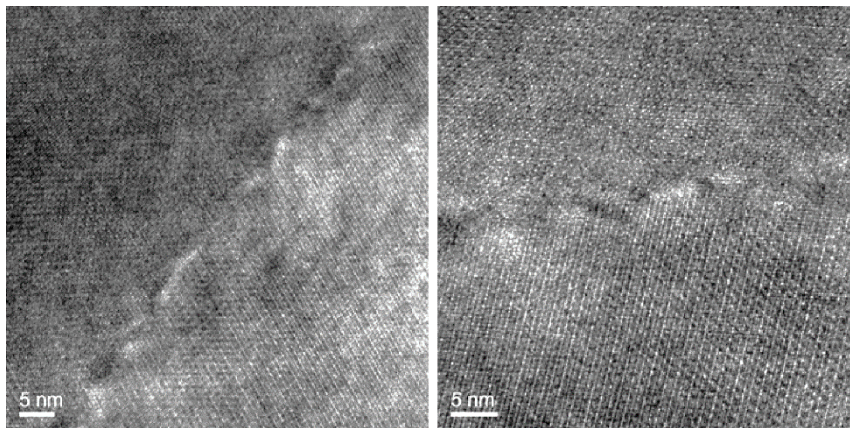


Fig. S5 High-resolution TEM image showing the deformation band with a thickness of ~2-5 nm and strain concentrations along the line. The rest area is nearly defect free.

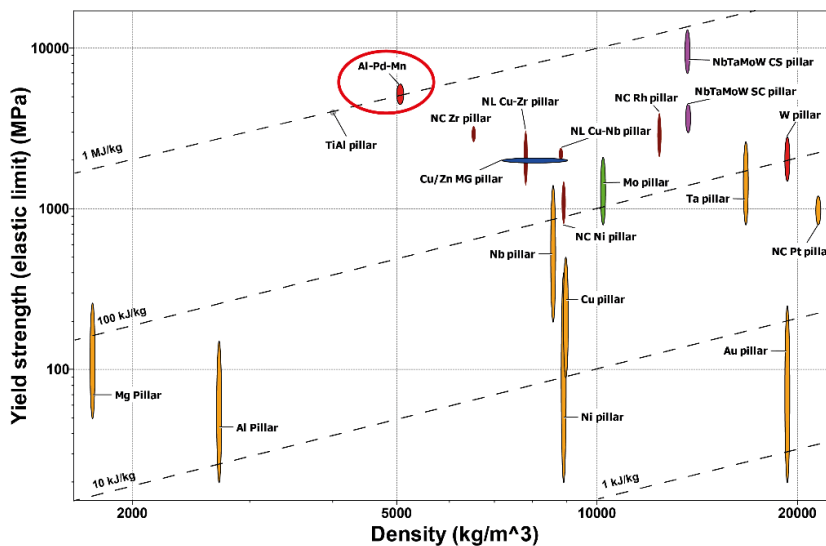


Figure S6. Comparison of the small-scale quasicrystal pillars with other metal and metallic-glass pillars. Ashby map (designed with CES EduPack 2014) of yield strength vs. density, indicating i-Al-Pd-Mn quasicrystal pillars exhibit the highest specific strength (the strength-weight ratio). (CS-single crystalline, NC-nanocrystalline, NL-nanolamellar and MG-metallic glass) Literature data for pillar strengths: pure metals Au [33] [34], Al [35], Ni [36] Cu [37], Nb, Ta, Mo and W [38] [39], and Mg [40], TiAl [41], nanocrystalline (nc) Cu [42], Ni [43], Ni-W [44], Pt [45] and Rh [46] pillars, NbTaMoW high-entropy alloys [47, 48], and metallic glasses (e.g. Cu- and Zn-based ones [49]).

4.2. Decagonal Al-Ni-Co at room temperature⁸

Abstract

Decagonal quasicrystals (DQCs), as a class of two-dimensional quasicrystals, are known to be highly anisotropic in most of their physical properties. Here we show that their plastic anisotropy can be considerably reduced, and even eliminated, when they are scaled down into sub-micrometer regime and deformed at room temperature. The reduced plastic anisotropy might be attributed to both size and temperature dependence of dislocation activities. This finding may shed light on the exploration of new deformation mechanisms for quasicrystals in a new scale and temperature regime.

Keywords: quasicrystals, plastic deformation, anisotropy, size effect, micro-compression

Introduction

Quasicrystals are a class of intermetallics that exhibit long-range order but miss translational symmetry [1, 50]. Among them, DQCs consist of quasiperiodic atomic layers with tenfold symmetry but stacked in a periodic order [51-53]. The distinct atomic arrangements along the tenfold axis (periodic) and the twofold axis (aperiodic) lead to their strongly direction-dependent properties [3, 54-56], for example, their significant plastic anisotropy [54]. In metals, plastic anisotropy is attributed to dissimilar dislocation mobilities on different slip systems or

⁸ Y. Zou, P. Kuczera, W. Steurer, R. Spolenak “*Disappearance of plastic anisotropy in decagonal quasicrystals at small scales and room temperature*”. (in press in *Extreme Mechanics Letters*)

preferred crystallographic orientations in polycrystals (i.e. texture), and high anisotropy will significantly reduce the ductility and formability of a material. For DQCs, the origin of plastic anisotropy is still an interesting topic to be explored in fundamental studies.

Early studies of Feuerbacher *et al.* [54, 57, 58] and Edagawa *et al.* [59, 60] unambiguously demonstrate that at high temperatures— above 75% of the melting temperatures— DQCs exhibit pronounced differences in yield strength and plastic behavior when they are compressed along different crystallographic directions. For example, in basic cobalt-rich $\text{Al}_{73}\text{Ni}_{10}\text{Co}_{17}$ [58], the yield strength for the loading direction perpendicular to the tenfold axis is about four times higher than for the one inclined 45° to the tenfold axis, while the one parallel to it is in between. It is believed that the plastic anisotropy in DQCs is associated with different dislocation characteristics along quasiperiodic and periodic directions [54]. A different question is whether the plastic anisotropy exists over a wide range of temperature and pressure. There are some hints that the deformation mechanism of quasicrystals would be significantly changed in a low-temperature regime [7, 19, 61]. Consequently the anisotropic behavior of DQCs may become different from that at high temperatures. To explore this question, one could plastically deform DQCs along different orientations at room temperature. This, however, is very difficult, because quasicrystals are extremely brittle at room temperature, failing in a catastrophic way before plastic yielding. Although several attempts have been made to study the room-temperature plasticity in quasicrystals through indentation [6] or under hydrostatic pressures [7], the complex load modes make it difficult to analyze the plastic behavior for each crystallographic direction. Thus, uniaxial compression of quasicrystals at room temperature would be still needed.

Our prior report [62] shows that an icosahedral quasicrystal, Al-Pd-Mn, exhibits an obvious “brittle-to-ductile” transition in uniaxial compression when the sample size is below around 500 nm, suggesting that micro-compression could

be an effective way to study the plastic behavior of DQCs at room temperature as well. Therefore, the current study focuses on the plastic deformation of a single-crystalline DQC, Al-Ni-Co, along three orientations (0° , 45° , 90° inclined with respect to the tenfold axis) and with a sample size ranging from $\sim 1 \mu\text{m}$ to $\sim 200 \text{ nm}$. We aim to explore the mechanical behavior of DQCs in a submicrometer-size and low-temperature regime.

Materials and methods

Single quasicrystals, Al-Ni-Co, were used for this study, because they are highly perfect, stable and intensively studied in bulk form. We prepared them from pure metals (Al 99.95 %, Ni 99.99 %, Co 99.99 %) with an initial composition of $\text{Al}_{77}\text{Ni}_{10.5}\text{Co}_{12.5}$ (Al-excess) and grew them using the self-flux method [63] in an Al_2O_3 crucible enclosed in a quartz ampoule under Ar atmosphere. The system was heated up to 1200°C and slowly cooled down to 1000°C at a rate of $1.2\text{-}5 \text{ Kh}^{-1}$, resulting in a growth of an agglomerate of several $\sim 0.5 \text{ cm} \times \sim 2\text{-}3 \text{ cm}$ decaprismatic crystals (the detailed procedure is described in [64]). The samples chosen for this study were additionally annealed at 1000°C for 48 hours and quenched in water. The powder diffraction pattern (Fig. S1) of the grown sample indicates a DQC phase, which is comparable to that in literature [51].

Three plate-like samples (2-3 mm thick) were cut using an alumina wheel (Struers 50A13) from the prepared single quasicrystal at angles of 0° , 45° , and 90° with respect to the tenfold axis, polished using $3\text{-}\mu\text{m}$ diamond paste and finally polished using a 60-nm SiO_2 particle suspension. The actual composition of the DQCs tested in this study is $\text{Al}_{74.4(0.2)}\text{Ni}_{9.3(0.2)}\text{Co}_{16.3(0.1)}$, measured by Energy-dispersive X-ray spectroscopy (EDX), indicating a basic cobalt-rich phase which is comparable to $\text{Al}_{73}\text{Ni}_{10}\text{Co}_{17}$ in literature [58].

Small-sized pillars were milled using a focused ion beam (FIB) system (Helios Nanolab 600i, FEI) in two steps: 2.5 nA for coarse milling and 10-40 pA for fine

milling. The orientations of the pillars were perpendicular, parallel and 45° to the tenfold axis, as indicated by A_\perp , A_\parallel , A_{45} , respectively (Fig. 1a and 1b) For convenience, we use the same symbols as those in literature [54], [58]. The diameters of the FIB-milled pillars are approximately 1 μm , 550 nm, 350 nm and 200 nm and their aspect ratios are 2.5-4. A taper of $2\text{-}3^\circ$ was generally observed in those pillars. The diameters of the pillar top were chosen to calculate engineering stresses and evaluated the yield strength at the pillar upper parts. At least four pillars of each size and each orientation were compressed using a nanoindenter (Triboindenter, Hysitron Inc., USA) with a diamond flat-punch tip (5 μm in diameter, Synton-MDP, Switzerland) in the displacement control mode by feedback mechanism. A strain rate of $2 \times 10^{-3} \text{ s}^{-1}$ was used for all the compression tests. The displacement and loading times were changed according to the pillar height in order to keep the strain rate constant (the detailed procedure is described in [65]). The morphologies of the pillars were characterized using a high-resolution scanning electron microscopy (SEM, FEI MAGELLAN) before and after compression.

Results

The SEM images show that the pillars in different orientations exhibit rather similar morphology after compression (Fig. 1c). All three orientations exhibit an obvious brittle-to-ductile transition when the pillar size is reduced: the 1- μm pillars fracture catastrophically without notable plasticity, the 500-nm pillars are plastically deformed with clear slip bands traversing along the samples and the 250-nm pillars show localized plastic deformation at their top parts. The brittle-to-ductile transition phenomena shown here is comparable to those observed for the icosahedral quasicrystal pillars [62]. Although it is hard to identify the exact slip systems based on the SEM images, the slip planes are tilted 30-60 degrees relative to the loading axis in all the orientations and multiple slip lines can be identified. Interestingly, the slip bands shown here are not as sharp as those

observed in typical metal pillars [66] or other crystalline solid pillars [21], but exhibit highly wavy, or zigzag, morphologies (see high-magnification SEM images in Fig. S2), which are very similar to those in metallic glass pillars [49] [67]. The localized deformation on the top of the smallest pillars could be due to the taper at the pillar top, which are also seen in metallic glass pillars [49] [67]. The wavy morphologies of the slip traces could be associated with the low mobility of dislocations due to their nonplanar core structure. The localized deformation at the pillar upper part might be attributed to the geometrical taper as well as a strain softening effect, which has been observed in bulk decagonal quasicrystals.

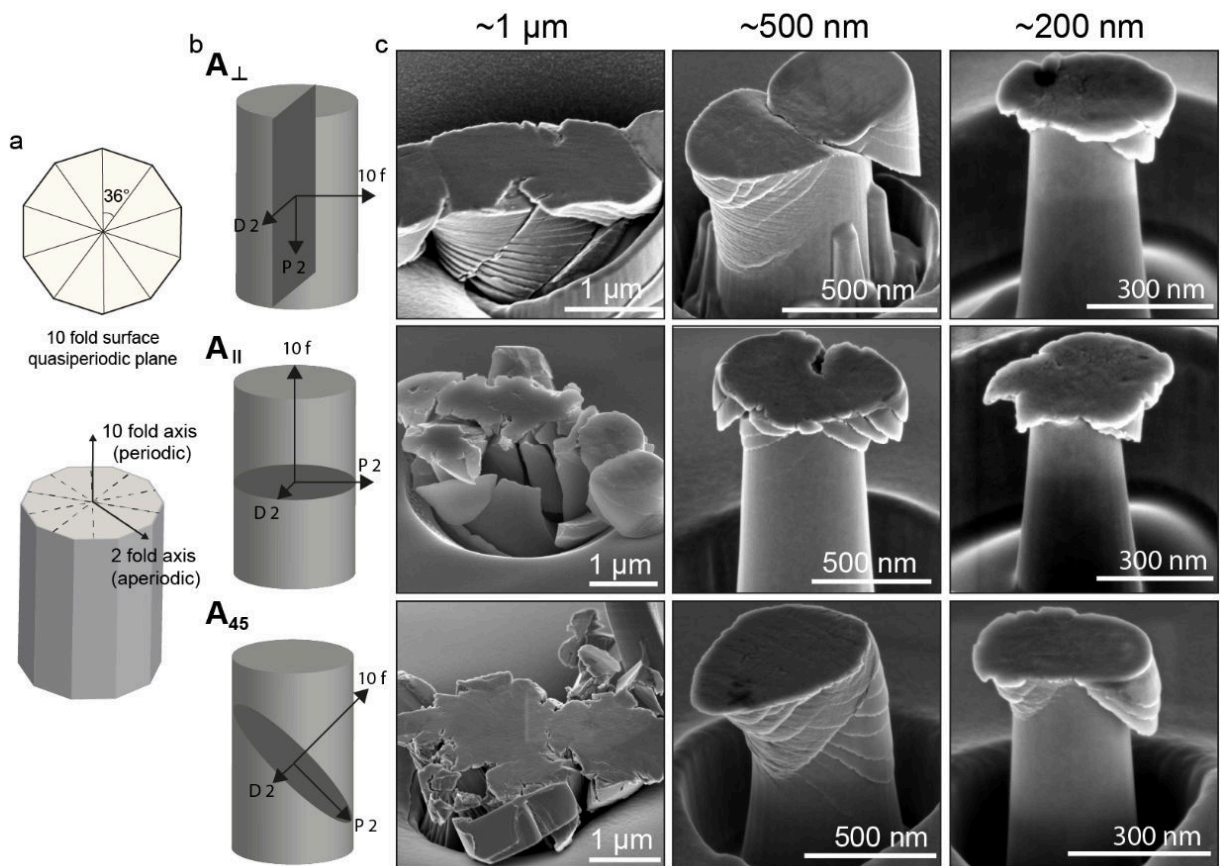


Fig. 1. Micro-compression of decagonal quasicrystal pillars: (a) schematic of a decagonal Al-Ni-Co quasicrystal showing quasiperiodic planes (tenfold surfaces) stacked along the periodic direction (tenfold axis). (b) Schematics of micro-pillars with three orientations: perpendicular to 10-fold axis (A_{\perp}), parallel to 10-fold axis (A_{\parallel}) and 45° to 10-fold axis (A_{45}). (c) Corresponding SEM images of compressed pillars with the diameters of approximate $1 \mu\text{m}$, 500 nm and 200 nm .

Figure 2 shows the stress–strain curves of these pillars during compression. We can further confirm that the large pillars ($\sim 1 \mu\text{m}$) have very limited ductility—fracture at $\sim 5\%$ strain, the 500-nm pillars present better ductility than the 1- μm pillars, failing at $\sim 10\%$ strain, while the small pillars ($\sim 200\text{-}300 \text{ nm}$) show remarkably ductility—over 30% strains without fracture. All the pillars exhibit a displacement-burst behavior, which has been commonly observed in both metal and metallic glass pillars [66] [49] [67]. The displacement bursts, or force drops, could be related to the intermittent nucleations and propagations of dislocations in a confined small volume. The first displacement burst can be attributed to the initiation of the dislocation motion on a specific plane— plastic yielding. Thus, the flow stress at the first displacement burst can be regarded as yield strength. We can observe a slightly increased yield strength as pillar size decreases in both A_{\perp} and A_{\parallel} orientations, but a significantly larger increase in A_{45} orientation.

If we assume that the slip bands are about 45° tilted relative to the loading direction, which means the Schmid factor is 0.5, we can obtain the critical resolved shear stress (CRSS) as a function of pillar diameter, as shown in Fig. 3. When the pillar size is large ($\sim 1 \mu\text{m}$), the A_{\perp} oriented pillars show the highest strength levels, the strength of A_{\parallel} oriented pillars is slightly lower than that of A_{\perp} , while the A_{45} oriented pillars show the lowest strength. It is interesting to note that this order of strength is the same to that reported in bulk compression: $A_{\perp} > A_{\parallel} > A_{45}$. As evaluated by the log–log slope, the A_{\perp} , A_{\parallel} and A_{45} pillars show size-effect exponents of -0.35 , -0.33 and -0.44 , respectively. At $\sim 200\text{-}300 \text{ nm}$, the CRSSs for all the three orientations converged to the same value of about 3 GPa—the plastic anisotropy has disappeared. The obtained CRSS of the DQCs in our experiments are very close to the simulated shear stress for the pure glide DQCs ($G/27$) in the tenfold plane [68] and approach the theoretical strength ($G/10$)[69], where G is shear modulus of about 80 GPa [70]. The observed scattering of strengths could be due to the statistical distribution of defects or dislocation sources in a sample, as demonstrated in pure metal pillars.

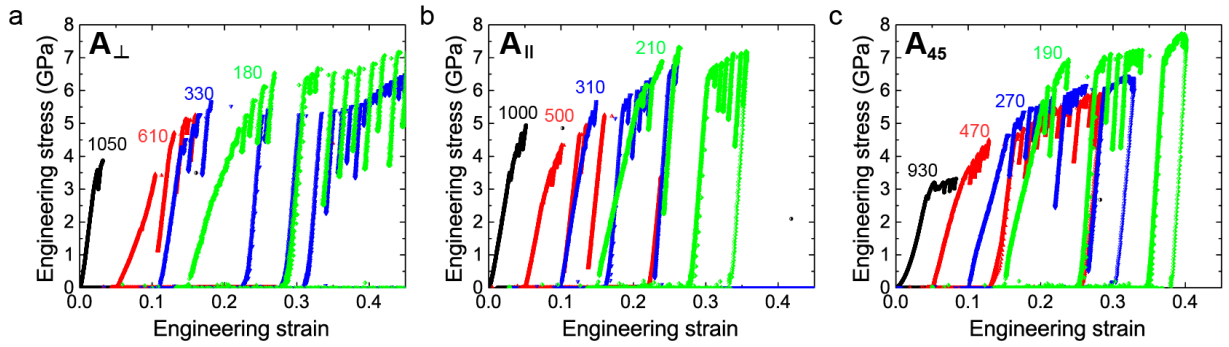


Fig. 2. Representative engineering stress-strain curves for (a) A_{\perp} , (b) A_{\parallel} and (c) A_{45} oriented pillars with the diameters ranging from $\sim 1 \mu\text{m}$ to $\sim 200 \text{ nm}$. (To identify each curve, the curves are shifted horizontally)

Plotting a 3-D graph of yield strength vs. sample size vs. temperature (Fig.4), we can compare the plastic anisotropy of bulk quasicrystals in literature [58] and our DQC pillars in a large temperature and size range. By reducing sample size and testing temperature, the DQCs change their behavior from plastic anisotropy (with a factor of 4) to plastic isotropy (a factor of ~ 1).

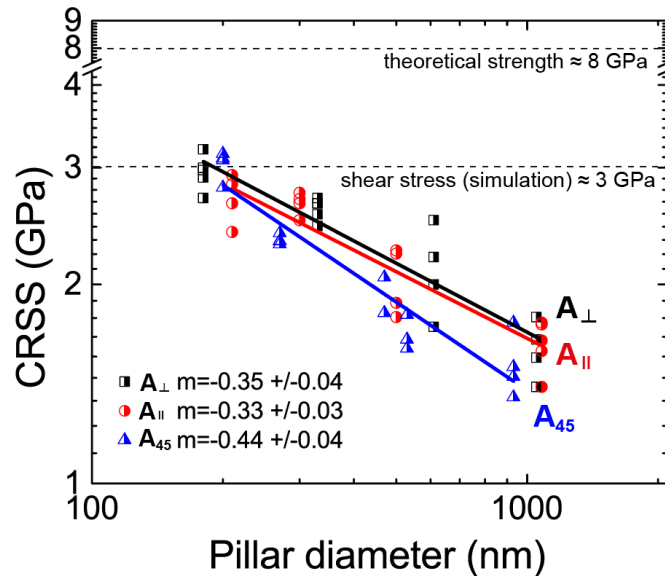


Fig. 3. The relation between critical resolved shear stress (CRSS) and pillar diameters for A_{\perp} , A_{\parallel} and A_{45} orientations. The size-effect exponents (m) for A_{\perp} , A_{\parallel} and A_{45} are -0.35 , -0.33 and -0.44 , respectively. The shear stress in tenfold planes is $G/27$ by simulation [68] and the theoretical strength is $G/10$, where G is shear modulus and about 80 GPa [70].

Discussion

Although decagonal Al-Ni-Co eight different ordering states, such as $\text{Al}_{70}\text{Ni}_{15}\text{Co}_{15}$ [57], $\text{Al}_{73}\text{Ni}_{10}\text{Co}_{17}$ [58] and $\text{Al}_{70}\text{Ni}_{21}\text{Co}_9$ [71], all of them show some

degrees of plastic anisotropy at high temperatures, as $A_{\perp} > A_{\parallel} > A_{45}$. Feuerbacher and Schall [54] summarized distinct dislocation characteristics and correlated with different deformation geometries: in A_{45} , periodic dislocations, i.e. Burgers vectors parallel to the periodic direction; in A_{\perp} , quasiperiodic dislocations, i.e. Burgers vectors within quasiperiodic planes and mixed dislocations i.e. Burgers vectors contain both periodic and quasiperiodic components; in A_{\parallel} , by both periodic and mixed dislocations. The bulk compression demonstrates that the lattice resistance, i.e., Peierls barrier, at high temperatures for periodic dislocations is lower than that for quasiperiodic dislocations. It is also well known that for metal micro-pillars, generally, $\tau_{CRSS} \sim \tau_0 + KGb/\lambda + Gb\sqrt{\rho}$ [74], where τ_0 lattice resistance, K source-strengthening constant in the order of 0.1, b the Burgers vector, λ the length of dislocation source and ρ dislocation density. Thus, both lattice friction and dislocation interactions can influence the size dependence of the strength in the same material system [75] [76].

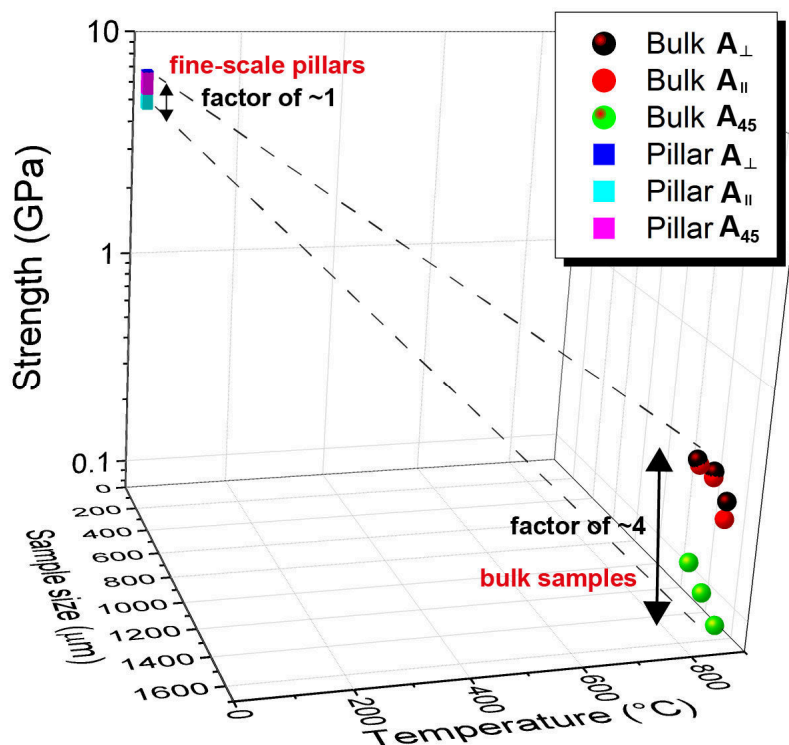


Fig. 4. A 3-D illustration showing the size and temperature dependence of yield strengths for the decagonal Al-Ni-Co bulk [58] and the pillars in this study. The strength anisotropy is reduced from a factor of ~4 in bulk forms (~1.5 mm) at ~800°C to identity at small scales (~200-300 nm) and room temperature.

The result in Fig. 3 indicates that the lattice resistance for A_{45} orientation is still lower than those for A_{\perp} and A_{\parallel} orientations, but their strengths are on the same levels when the sample size is scaled down to 200-300 nm. A few mechanisms could account for this reduced plastic anisotropy: first, as temperature decreases, the lattice resistances associated with the motions of periodic and quasiperiodic dislocations may both increase and approach to their extreme values at 0 K, which could be much less anisotropic; second, as the sample dimension is reduced, their strength becomes more nucleation-controlled rather than propagation-controlled, and the length of the dislocation source (e.g. kinks) can be related to columnar clusters [77], which become much less anisotropic in the nanometer-size regime. Third, the high stress and short dislocation lengths may activate alternative slip systems, leading to multiple slip and reduced anisotropy, which have been observed in submicrometer-sized magnesium [78] and high-entropy alloys [48].

Our results demonstrate that the pronounced plastic anisotropy in bulk DQCs in the system Al-Ni-Co, can be considerably reduced at small scales and room temperature. However, there is still much to be explored between the regime of high-temperature bulk deformation and that of room-temperature small-scale deformation, as seen in Fig. 4. For example, at what size and temperature one should observe a transition from bulk behavior to small pillar behavior is interesting for future studies. It should be noted that dislocation climb has been observed in plastic deformation of d-Al-Ni-Co at high temperatures and of i-Al-Pd-Mn under hydrostatic pressures. At low temperatures and under uniaxial compressions, diffusion is believed to be difficult. How the climb process might contribute to the plastic deformation of small-sized d-Al-Ni-Co at room temperature is still not clear so far and the detailed analysis of dislocation characteristics is still needed. Our studies also call for a detailed modeling of dislocation nucleation and propagation in quasicrystals in a large size and temperature regime. Our study suggests the possibility of using quasicrystals as strong-and-ductile materials. Together with their interesting physical properties,

small-sized quasicrystals may be potentially interesting for engineering applications in small-dimensional devices

Acknowledgements

We thank S. Takeuchi (Tokyo University of Science), K. Edagawa (The University of Tokyo) and A. Sologubenko (LNM, ETHZ) for their helpful discussions, ScopeM (ETHZ) for supplying electron microscopy facility. Y.Z and P.K. acknowledge the financial support through the Swiss National Science Foundation (SNF Grants: 200021_143633)

Supplementary Information

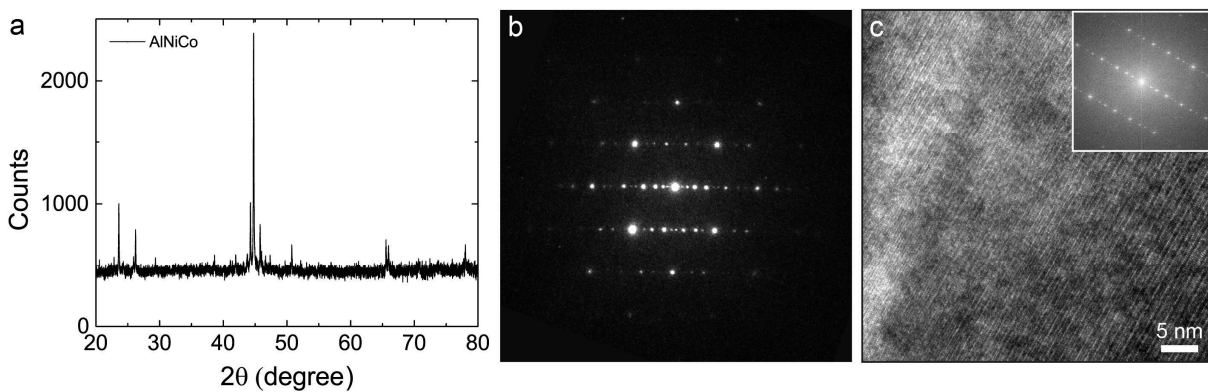


Fig. S1. (a) Powder diffraction (Cu, $K\alpha_1$), (b) TEM diffraction pattern, and (c) high-resolution TEM image with Fast Fourier Transform (FFT) for the as-prepared d-Al-Ni-Co before deformation, indicating a single decagonal quasicrystal phase.

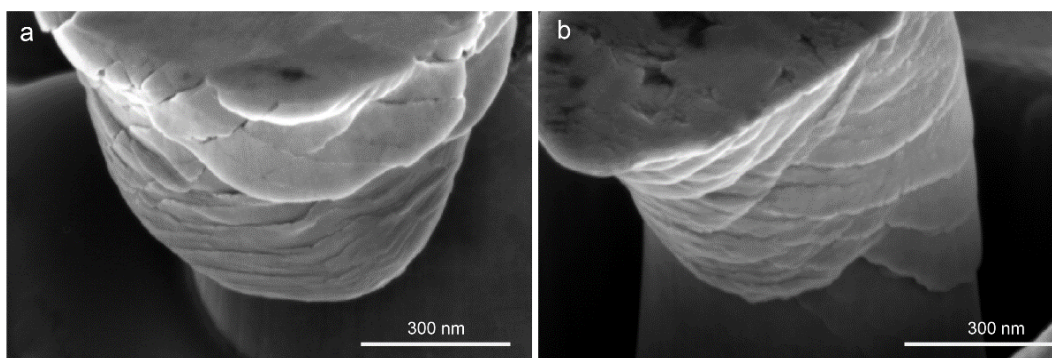


Fig. S2. High-magnification SEM images of the deformed pillars (a) A1 and (b) A45, showing wavy morphologies and multiple slips.

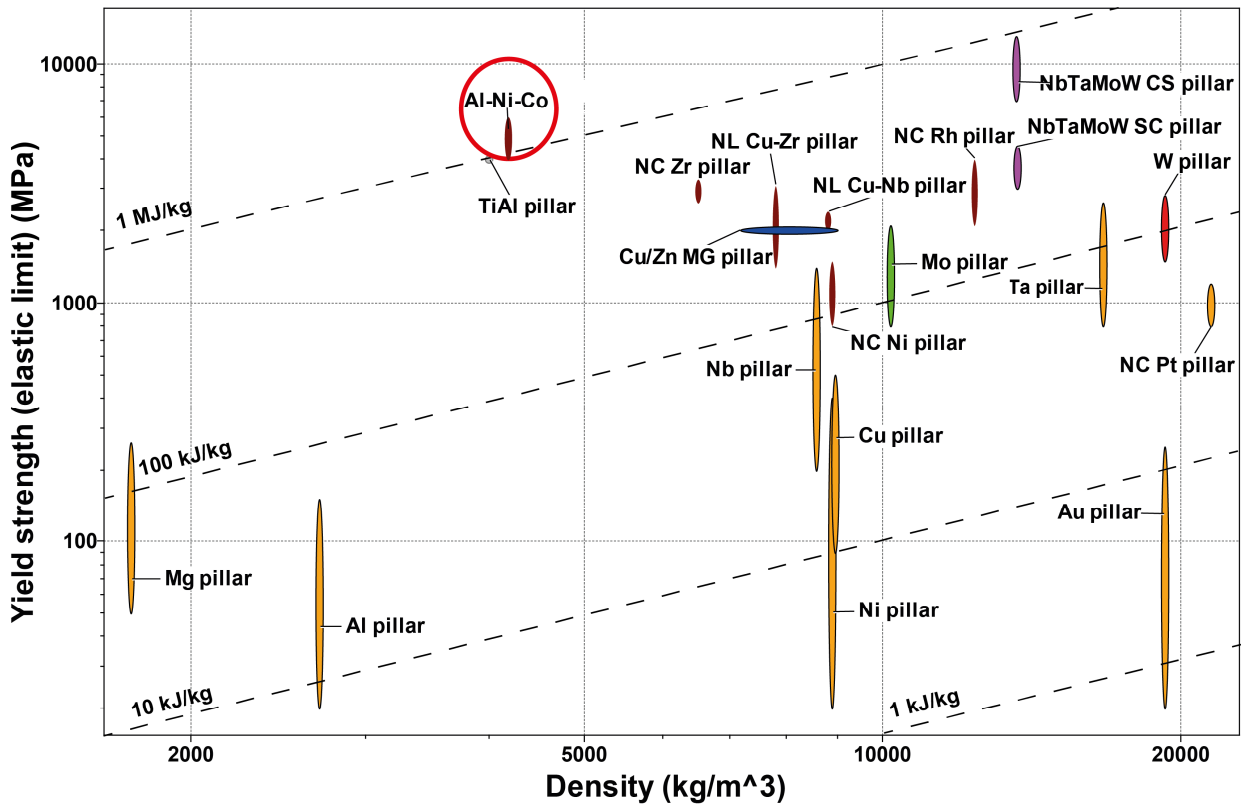


Figure S3. Comparison of the small-scale quasicrystal pillars with other metal and metallic-glass pillars. Ashby map (designed with CES EduPack 2014) of yield strength vs. density, indicating i-Al-Pd-Mn and d-Al-Ni-Co quasicrystal pillars exhibit the highest specific strength (the strength-density ratio). (Abbreviations: MG—metallic glass, NL—nanolaminate, NC—nanocrystalline, SC—single crystalline and CS—columnar structured.)

4.3. Decagonal Al-Ni-Co from room temperature to high temperatures⁹

Abstract

Ever since quasicrystals were first discovered about three decades ago, they have been found to be a host of many unusual and useful properties. However, a long-standing problem for these materials is that they are intrinsically brittle and suffer from low ductility and formability at room temperature, significantly impeding their practical usage. Moreover, the plastic deformation of quasicrystals at low and intermediate temperatures is rarely studied and the underlying mechanism is still poorly understood. Here, we employ in-situ micro-compression technique to deform decagonal Al-Ni-Co quasicrystal micro-pillars in the temperature range from room temperature to 500°C. We find three different regimes for quasicrystal plasticity: at room temperature, the plasticity is controlled by cracking; between 100-300°C, displacive plasticity shows serrated plastic flows with a constant flow stress; between 400-500°C, diffusion-enhanced plasticity exhibit homogenous deformation with flow stress decreased by increasing temperature. The quasicrystals at micron scales and 25-500°C exhibit extraordinarily high strengths of ~3.5 GPa, good ductility of over 15% compressive strains and low strain-rate sensitivity of 0.1. With these properties, our study may shed light towards the engineering applications of quasicrystals.

Keywords: quasicrystals, plasticity, micro-compression, size effect, brittle-to-ductile transition, serrations, diffusion

⁹ Y. Zou, J. Wheeler, A. Sologubenko, J. Michler, W. Steurer, R. Spolenak “*Bridging room-temperature and high-temperature plasticity in decagonal Al-Ni-Co quasicrystals by micro-thermomechanical testing*”. (submitted to *Acta Materialia*)

Introduction and background

Quasiperiodic crystals, or quasicrystals (QCs), are a novel class of materials that exhibit long-range order in atomic arrangement yet lack translational symmetry, in addition to crystalline and amorphous states of solids [1, 50, 79, 80]. The first experimental observation of QCs by Shechtman in the 1980s [1] demonstrated that a rapidly quenched Al-Mn alloy showed a five-fold symmetry, which was significantly forbidden according to the classical theorems of crystallography: two-, three-, four- and six-fold symmetries are allowed, but five-, seven- and all higher rotations are impossible. Owing to their special atomic arrangement, quasicrystals possess many unusual and useful properties—high thermal and electronic transport [2], mechanical reinforcement particles [81], light absorption [82], hydrogen storage [83], very low surface energies, and corrosion- and oxidation, wear-resistance with low friction coefficients [55, 84]. For the last three decades, hundreds of new quasicrystals have been synthesized in the laboratory [11, 85, 86], predicted by simulations [87] and even has been reported to be discovered in nature [13, 88]. However, despite of their interesting structures and useful properties, few of quasicrystals have been converted into practical products. A well-known drawback that hinders their applications is that they are extremely brittle: plastic deformation is only possible at high temperatures (above $\sim 75\%$ of their melting temperatures, T_m) [54, 89] [60] or under confining hydrostatic pressures (indentation [6, 20] or gas/solid hydrostatic pressures [7, 19]). Deformation at low and intermediate temperatures generally result in a catastrophic failure [90], rendering them very difficult to further process and often unsuitable for usage.

Although the studies of the plastic deformation of quasicrystals was as early as in 1985 [91], and experimentally studied [92] in 1987, only several years after the discovery of quasicrystals, the underlying deformation mechanism of QCs are still not completely explored, especially in the low- and intermediate-temperature regimes. Similar to regular crystals, quasicrystals can also be deformed via

dislocation activities, but their dislocations include specific components— phasons [93, 94], in addition to phonons, the components in the dislocation of regular crystals. In lieu of translational periodicity, quasicrystals exhibit another intriguing symmetry properties, namely self-similarity by scaling, for example, in icosahedra and decagonal quasicrystals the self-similarity is related to the scaling properties of the golden ratio τ , $(\sqrt{5}+1)/2$. The phasons are introduced by the violations of the matching rules due to the missing periodicity in quasicrystals. The motion of their dislocations have to overcome this mismatch by the rearrangement of phasons [70, 95]. As a consequence, dislocation motion is very difficult and the material is brittle.

Early studies of the plastic deformation of QCs were intensively focused on two perfect and stable QCs— i(icosahedral)-Al-Pd-Mn and d(ecagonal)-Al-Ni-Co— in their high-temperature ranges, usually between 600 °C and 1000 °C. Icosahedral quasicrystals (IQCs) have quasiperiodicity in three dimensions, while decagonal quasicrystals (DQCs) are two-dimensional QCs that consist of quasiperiodic atomic layers with tenfold symmetry but stacked in a periodic order. It is generally accepted that at high temperatures dislocation climb can be dominate for IQCs [14], while both dislocation climb and glide are possible in DQCs [54]. In the low temperature regime, numerical simulations [68] [16] suggest that plastic shear without thermal assistant might be possible, nevertheless the required stress is as high as $\sim 1/7$ of shear modulus, G , for IQCs and $\sim 1/27$ of G for DQCs, which typically lead to fracture of QCs without plastic yielding.

Numerous investigators attempted to understand the low-temperature plastic behavior of QCs through indentation or hydrostatic gas/solid pressure, they observed many interesting phenomena, such as grain-boundary glide rather than dislocation mechanism [6], pure dislocation climb [7], dominant climb with possible glide [19], phase transformations [20, 96], the nucleation and propagation of shear bands similar as metallic glasses [17, 61], but no agreed

conclusion has been reached yet. Still, the plasticity of quasicrystals under a wide range of temperature and pressure has been poorly explored—much in contrast to crystalline and amorphous solids. Unveiling the deformation mechanism of QCs in the low and intermediate temperature regimes hence relies on a novel mechanical characterization technique.

For the last decade, great advance has been made by applying the methodology of micro-compression [97] [98] [99] to study the mechanical behavior of a vast number and varieties of materials at small scales. Since then, over a thousand related studies have been reported, including regular metals [66], intermetallics [41], high-entropy alloys (HEA) [48], complex metallic alloys (CMA) [100], ionic crystals [65, 101], semiconductors [102], ceramics [103], metallic glasses [22, 49] and even polymers [104]— but no studies have been reported on QCs. In nanomechanical testing, many conspicuous class of brittle materials like semiconductors and metallic glasses present certain degrees of plasticity when the length scale of samples is reduced to submicron- or nanometer- sized regime. Our recent work demonstrate that i-Al-Pd-Mn [62] and d-Al-Ni-Co [105] show a size-induced brittle-to-ductile transition at room temperature when the length scale of samples is reduced to the sub-micrometer regime. Thus, micro-compression technique enable to study the plastic behavior of typically brittle quasicrystals by overcoming fracture before plastic yielding in a simply uniaxial load mode.

There is, however, still a gap between high-temperature plasticity for bulk QCs ($T > 600\text{ }^{\circ}\text{C}$ and $D > 1.5\text{ mm}$) and room-temperature plasticity for small-scale QCs ($T \approx 25\text{ }^{\circ}\text{C}$ and $D = 200\text{ nm-1 }\mu\text{m}$), where T is testing temperature and D is sample size. Thus, two fundamental questions arises: what mechanism controls the quasicrystal plasticity in the temperature range between room temperature to high temperatures? And at what size and temperature one should observe a transition from a bulk behavior to a small pillar behavior? Our exploration of the new deformation regime for QCs starts from d-Al-Ni-Co with the orientation 45° to

the tenfold axis (A_{45}), because its crystallographic orientation during deformation is well defined and the samples with A_{45} orientations exhibit higher ductility than the others[54]. This study focuses on the sample size ranging from about 1.5 μm to about 300 nm and the temperature ranging between room temperature to 500 $^{\circ}\text{C}$, a regime that has never been explored for quasicrystal plasticity.

Materials and experimental procedure

Single quasicrystals, d-Al-Ni-Co, were grown using the self-flux method [63]. The compact with an initial composition of $\text{Al}_{77}\text{Ni}_{10.5}\text{Co}_{12.5}$ (Al-excess) was prepared from pure metals (Al 99.95 %, Ni 99.99 %, Co 99.99 %) and pre-alloyed in an arc-furnace. The growth was carried out in Al_2O_3 crucible enclosed in a quartz ampoule under an Ar atmosphere. The sample was heated up to 1200 $^{\circ}\text{C}$ and slowly cooled down to 1100 $^{\circ}\text{C}$ at a rate of 5K h^{-1} . Between 1000 $^{\circ}\text{C}$ and 1100 $^{\circ}\text{C}$, the sample was cooled at the rate of 1.2 K/h with several 1-hour annealing steps. The liquid part was decanted at the temperature of 1000 $^{\circ}\text{C}$. This procedure resulted in a growth of an agglomerate of several $\sim 0.5\text{ cm} \times \sim 2\text{-}3\text{ cm}$ decaprismatic crystals [64]. The crystals chosen for further experiments were additionally annealed at 1000 $^{\circ}\text{C}$ for 48 h and quenched in water. A plate-like sample (2-3 mm thick) were prepared for micro-mechanical testing. It was cut from the bulk crystals at the angles of 45 $^{\circ}$ with respect to the tenfold axis. The measurement using energy-dispersive X-ray spectroscopy (EDX) showed that the inner parts of the decaprisms had slightly different composition than the outer parts (both within the compositional range of the decagonal phase). The inner part had a composition of $\text{Al}_{72.9(0.4)}\text{Ni}_{14.5(0.2)}\text{Co}_{12.6(0.3)}$, which at the temperature of 1000 $^{\circ}\text{C}$ indicates towards the so-called basic Ni rich phase. The outer parts had the composition of $\text{Al}_{74.4(0.2)}\text{Ni}_{9.3(0.2)}\text{Co}_{16.3(0.1)}$, which (1293 K) indicates towards the so-called basic Co rich phase. The mechanical experiments were performed on the outer parts of the samples. The X-ray powder diffraction pattern (Fig. 1a), transmission electron microscopy (TEM) diffraction pattern (Fig.1b) and high-

resolution TEM image with fast fourier transform (FFT) (Fig.1c) for the as-prepared d-Al-Ni-Co sample indicate a decagonal phase, which is comparable to that in the literature [51][58].

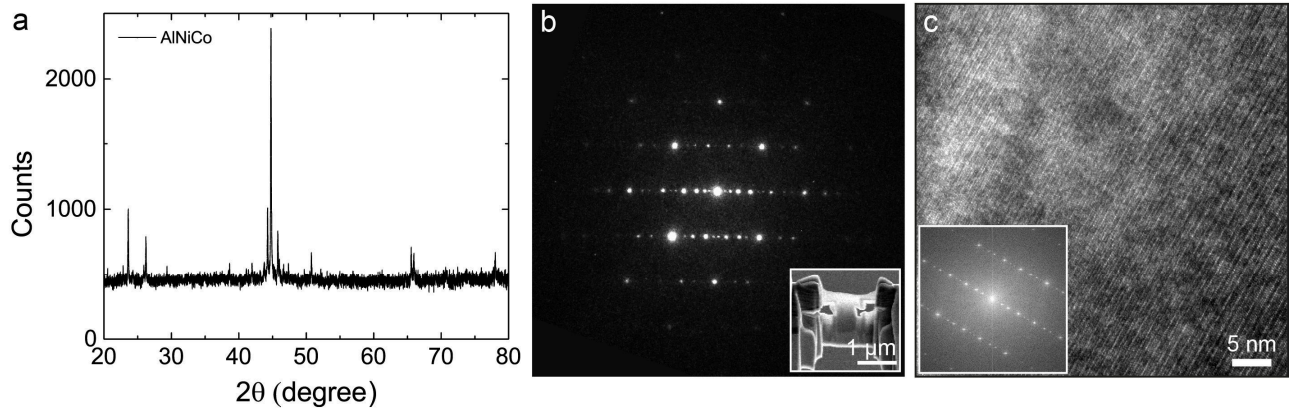


Fig. 1 (a) Powder diffraction (Cu, $K_{\alpha 1}$), (b) TEM diffraction pattern and (c) high-resolution TEM image with Fast Fourier Transform (FFT) for the as-prepared d-Al-Ni-Co before deformation, indicating a single decagonal quasicrystal phase.

Fine-scale pillars were milled using a focused ion beam (FIB) system (Helios Nanolab 600i, FEI) in two steps: 2.5 nA for coarse milling and 10-40 pA for fine milling. The orientation of the pillars was 45° to the tenfold axis, as indicated by A_{45} , (Fig. 2a and 2b). For the compression from room temperature to 500°C , the pillars have a diameter of $1.4\ \mu\text{m}$ and a height of $3.4\ \mu\text{m}$. For the compression at 500°C , we also fabricated smaller sized pillars with the diameters of 770 nm and 270 nm and aspect ratios of $\sim 3-4$. A taper of $2-3^\circ$ was generally observed in all the pillars, and the diameters in the pillar top were chosen to calculate engineering stresses. At least four pillars of each size and each orientation were compressed using an *in-situ* nanoindenter [106] (Alemnis, Switzerland), with a diamond flat-punch tip ($5\ \mu\text{m}$ in diameter, Synton-MDP, Switzerland), under displacement control. The strain rate of $1 \times 10^{-3}\ \text{s}^{-1}$ was used for all the compression tests. The indenter had been modified by incorporating a water-cooled frame and independent tip and sample heating, yielding typical thermal drift values of less than $0.02\ \text{nm}\ \text{s}^{-1}$ due to the thermally stable system frame and precise temperature matching of the sample and indenter temperatures. Testing was first carried out

at room temperature and then at 100 °C, 200 °C, 300 °C, 400 °C and 500 °C. The morphologies of the pillars were characterized using a high-resolution scanning electron microscopy (SEM, FEI MAGELLAN) before and after compression. Three pillars (deformed at 100 °C, 300 °C and 500 °C) were selected for the *post mortem* scanning transmission electron microscopy (STEM, Talos, FEI) characterization. The deformed pillars were thinned down to lamellas, lifted-out, further thinned down and polished in the FIB system.

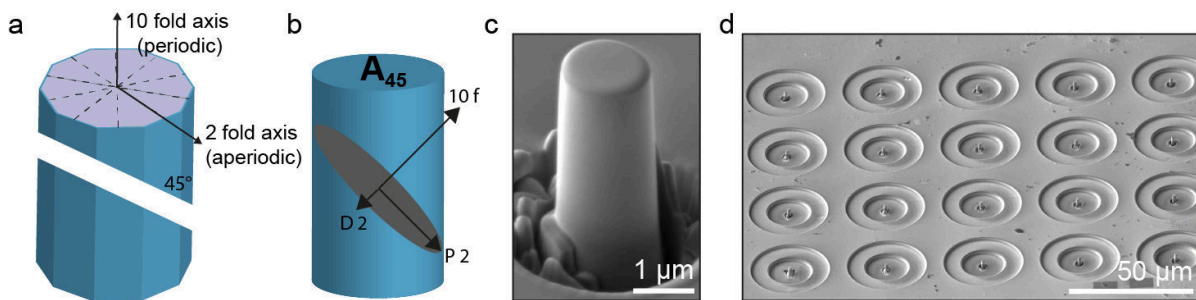


Fig. 2. Preparation of DQC Al-Ni-Co pillars: (a) schematic of a decagonal quasicrystal showing quasicrystalline planes (tenfold surfaces) stacked along the periodic direction (tenfold axis). (b) schematic of the micropillar with the orientation 45° to 10-fold axis, A₄₅. (c) SEM image of a typical FIB-milled pillar before compression (~1.5 μm in diameter). (d) matrix of FIB-milled pillars with the same size and geometry.

Nano-thermomechanical testing

The SEM micrographs of the deformed DQC pillars exhibit distinct morphologies after compression at 25-500 °C, as shown in Fig. 3. The pillar compressed at room temperature (Fig. 3a) shows a primary slip band, starting from the upper right corner and traversing along a plane about 45° from the compression direction. A close observation reveals that crack occurs along the shear direction, and a secondary slip band is also activated parallel to the primary one. The pillar deformed at 100 °C (Fig. 3b) shows a few more secondary slip bands which are also parallel the primary slip band, suggesting that only single slip is activated. The pillar deformed at 200°C (Fig. 3c) exhibits several primary slip bands with large steps and a couple of secondary slip bands as well, which intersect with the primary ones. The pillars deformed at 300°C (Fig. 3d) reveals more slip lines with small steps, suggesting that multiple slip systems are activated. For the pillar

deformed at 400 °C (Fig. 3e), the deformation is almost homogenous without any slip bands observed, but some wrinkle-like structures can be found at the pillar surface. The pillar compressed at 500 °C (Fig. 3f) also shows homogeneous deformation morphology without any slip bands, but some protrusions can be observed at the top part of the pillar. The in-situ SEM characterization can be seen in supplementary videos.

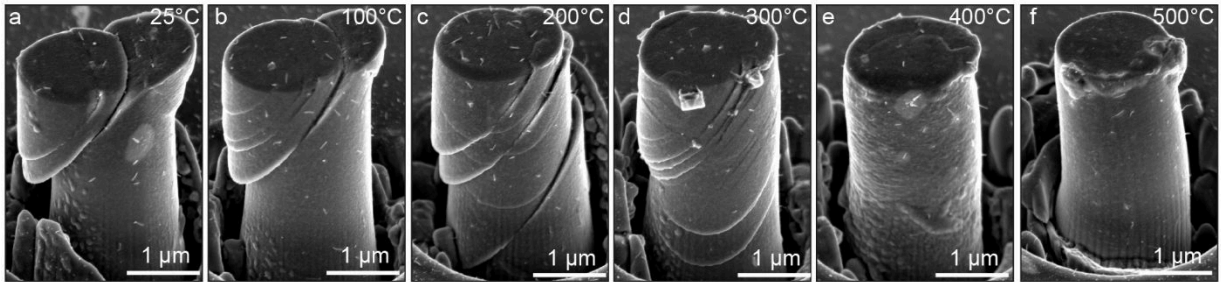


Fig. 3. Representative SEM micrographs of DQC Al-Ni-Co micropillars after compression at (a) 25°C, (b) 100 °C, (c) 200 °C, (d) 300 °C, (e) 400 °C and (f) 500 °C.

The engineering stress–strain curves (Fig. 4) characterize the dynamic behavior of the pillars deformed at each testing temperature. At room temperature (Fig. 4a), a linear elasticity can be observed below an engineering strain of ~2.5% with a peak engineering stress of ~3.5 GPa. As the pillar is continuously compressed, the engineering stress is significantly decreased, suggesting that the pillar top cannot hold such high force and cracking may occur. Between 100-300°C (Fig. 4b-d), the pillars exhibit stable plastic flows with the stress values of ~3.5 GPa. Interestingly, although the flow stresses for 100-300°C are nearly in the same level, the pillars show distinct serrated plastic flows (i.e. stress drops and rises with strains, or stick-slip behavior)—the magnitude of serrations increases, but the frequency decreases, by increasing temperature. At 400°C (Fig. 4e), the plastic flow shows homogenous plastic flows without serrations, but the strength levels are still about 3-3.5 GPa. The strain-rate jump tests indicate the pillars show a positive strain-rate sensitivity—flow stresses increase by increasing strain rate. At 500°C (Fig. 4f), the pillars also exhibit homogenous flow with positive strain-rate sensitivity, but the strength level is decreased to about 2.5 GPa.

At 500°C, the pillars with smaller sizes were also compressed. Fig. 5a and 5b show the deformed pillars with the diameter of 770 nm and 270 nm, respectively. Wrinkle-like structures can be observed in the 770-nm pillar and more obvious ones can be found in the 270-nm pillar. Fig. 5c and 5d show the stress-strain curves for the 770-nm and 270-nm pillars, respectively. Compared to that of the 1.5- μm pillar, the linear elastic regime of these small pillars are reduced, especially for the 270-nm pillars. The 770-nm pillars exhibit an elastic limit of ~ 2.5 GPa, while the 270-nm pillars show nearly viscous flows without obvious linear elasticity. The flow stress is slightly decreased by decreasing the pillar diameter, showing a “smaller is weaker” trend. The results in Fig. 5 imply that diffusion may affect the plasticity for this temperature and sample size.

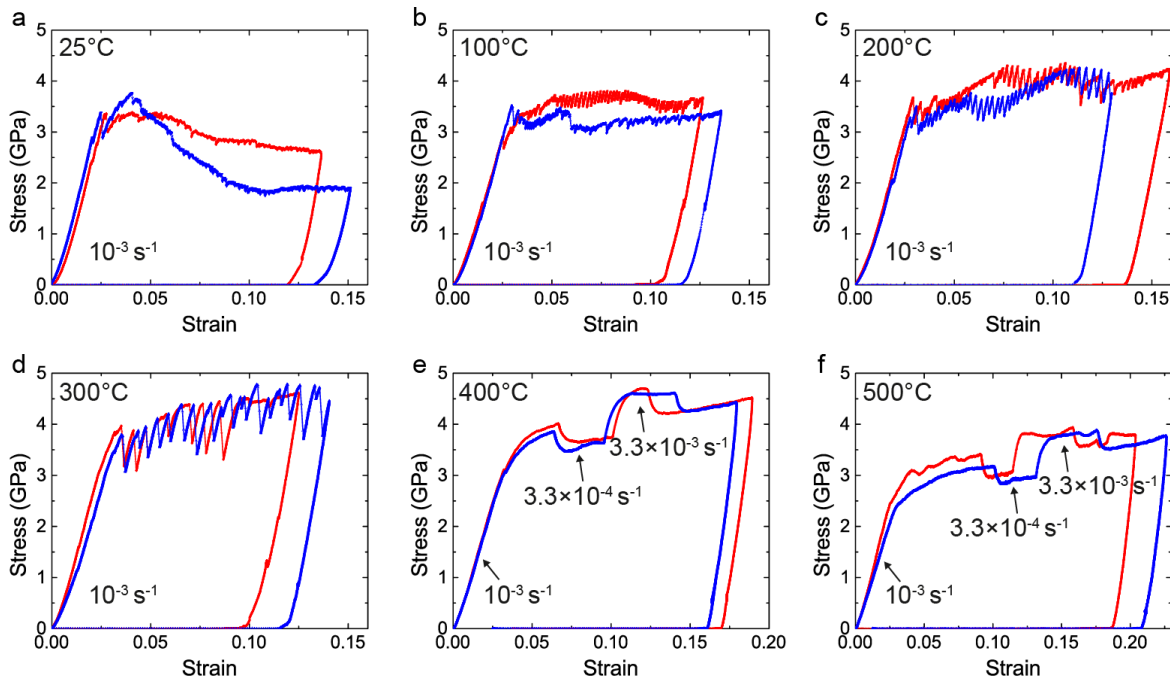


Fig. 4. Representative engineering stress–strain curves from micropillar compression at (a) 25°C, (b) 100°C, (c) 200°C, (d) 300°C, (e) 400°C and (f) 500°C. A constant strain rate of 10^{-3}s^{-1} was used from room temperature to 300°C, and strain rate jumps ($3.3 \times 10^{-4}\text{s}^{-1}$ and $3.3 \times 10^{-3}\text{s}^{-1}$) were employed for the compression at 400°C and 500°C

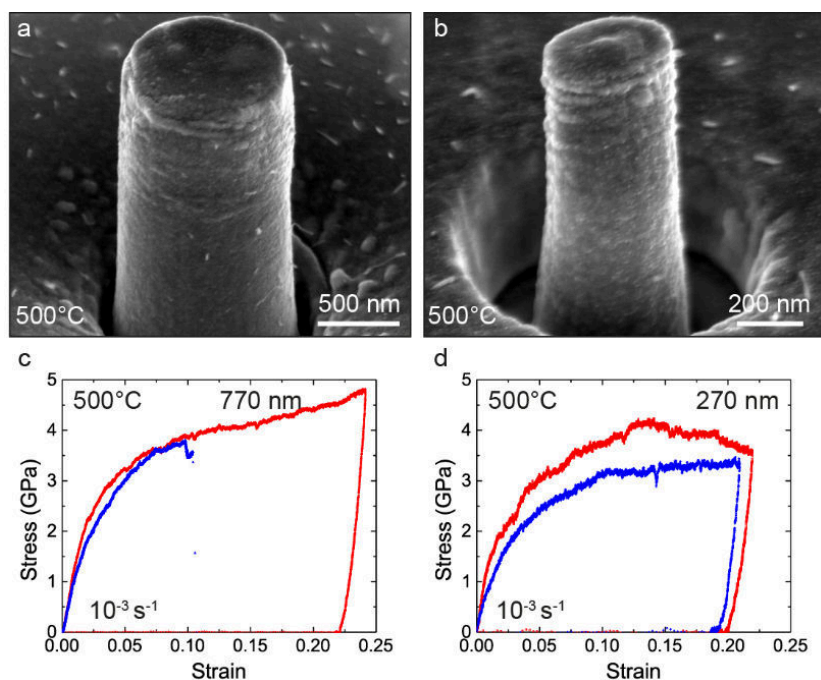


Fig. 5. (a, b) High temperature (500 °C) compression for sub-micrometer-sized pillars: representative post-deformation SEM images, (a) and (b), and (c, d) engineering stress–strain curves, (c) and (d), for pillars with 700 nm and 270 nm diameter pillars, respectively.

STEM characterization

The EDX maps and high-angle annular dark field (HAADF) images in the STEM mode for the pillars deformed at 100°C, 300°C and 500°C are shown in Figs. 6, 7 and 8, respectively. Both the pillars deformed at 100°C and 300°C show homogenous distribution of the three elements (Al, Ni and Co) with the initial composition (the dark region in the center of Fig. 6 is due to the FIB milling; the light dots distributed in Fig. 7 is due to contamination). Differently, the pillar deformed at 500°C exhibits a feature of recrystallization showing nano-scale grains at the upper right corner of the image (Fig. 8a). The EDX map of the pillar top (Fig. 8b) indicates that the small grains, which are corresponding to the protrusions in Fig. 3, are rich in Ni but poor in Co with a composition of $\text{Al}_{60.17}\text{Ni}_{35.26}\text{Co}_{4.58}$. This composition is out of the equilibrium decagonal quasicrystal phase, according to the Al-Ni-Co ternary phase diagram [107]. Interestingly, slip bands are also observed in the deformed pillar, as boxed (black) in Fig. 8a and enlarged in Fig. 9. As shown in the EDX map of the slip banding region (Fig. 9),

the slip bands are obviously rich in Ni by a factor of two comparing to the area without slip bands, but distribution of Al and Co are nearly homogenous. The results in Figs. 8 and 9 suggest that the plastic deformation at 500°C is not controlled by single mechanism but can be complex involving hybrid diffusive-displacive characters.

Discussion

To evaluate the temperature dependence of strength for the micro-pillars, the highest flow stress below 5% strain were compared. Fig. 10 shows the flow stress as a function of temperature for the 1.5- μm pillars. Below 400°C, the strengths are almost constant with increasing temperature, and above 400°C, the strengths are decreased and linearly approach the bulk strengths at 700-900°C. According on the stress-strain behavior (Fig.4) and deformation morphology (Fig.3), we define three different regimes for the plasticity of the DQC pillars: (I) below 100°C, crack nucleation and propagation, (II) 100-400°C, serrated plastic flows and constant flow stress and (III) above 400°C, homogenous plastic flow and flow stress starting to decrease. In the following part, we will analyze each deformation regime in detail.

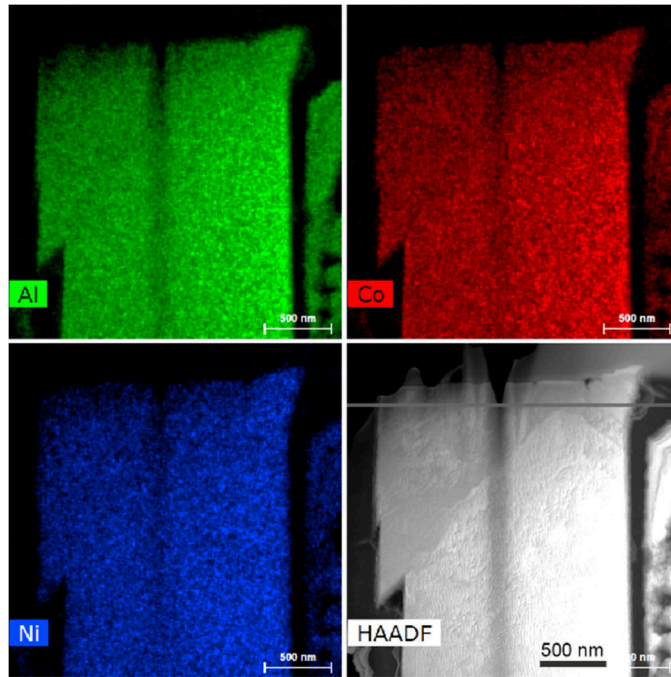


Fig. 6. HAADF STEM micrograph and EDX elemental maps of the pillar deformed at 100°C, indicating the homogeneous distribution of all the constituents. (Please note that the vertical dark band in the center of the micrographs is a FIB-milling artefact and is thinner than the adjacent regions of the pillar).

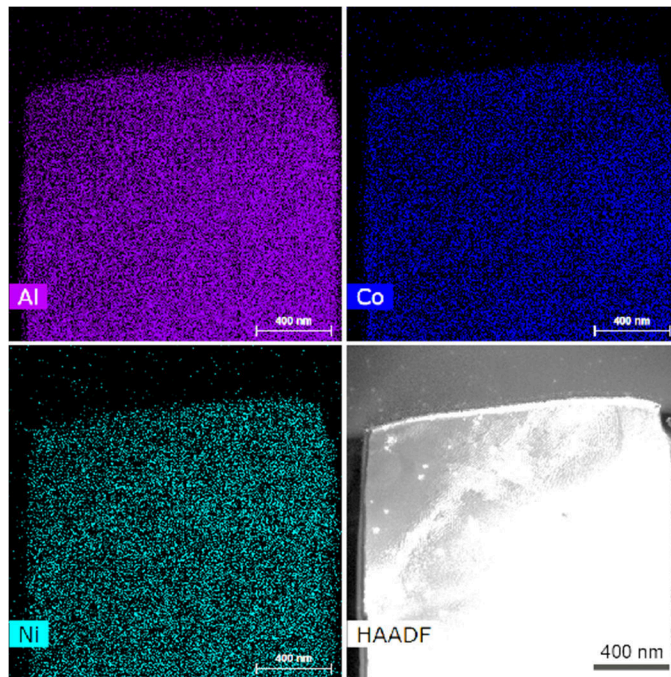


Fig. 7. HAADF STEM micrograph and EDX elemental maps of the pillar deformed at 300°C, showing the homogeneous elemental content of the pillar. (Please note that incidentally the star-like features homogeneously distributed upon the pillar and also the surrounding areas are the Pt-contamination. The Pt was used as a precursor to glue the pillar to the supporting TEM-half-grid.)

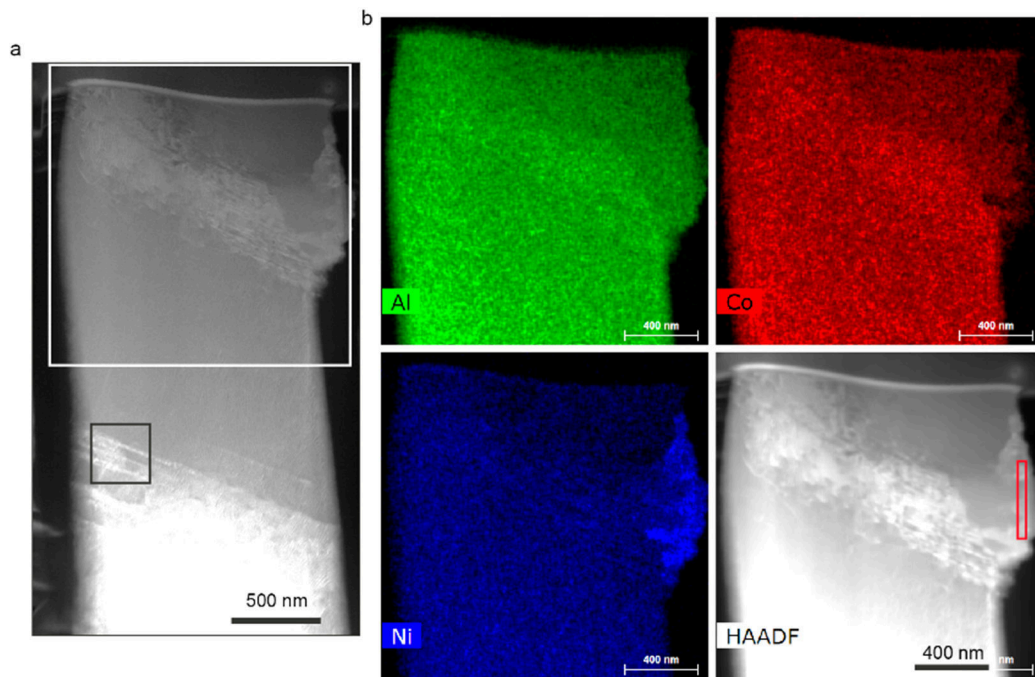


Fig. 8. (a) HAADF STEM micrograph (a) and (b) corresponding EDX elemental maps (b) of the pillar deformed at 500°C. The modulations in the Ni and Co signal at the right edge of the pillar indicate the occurrence of the phase separation. The brighter regions in (a) and the last image (HAADF) show the prominent channeling contrast.

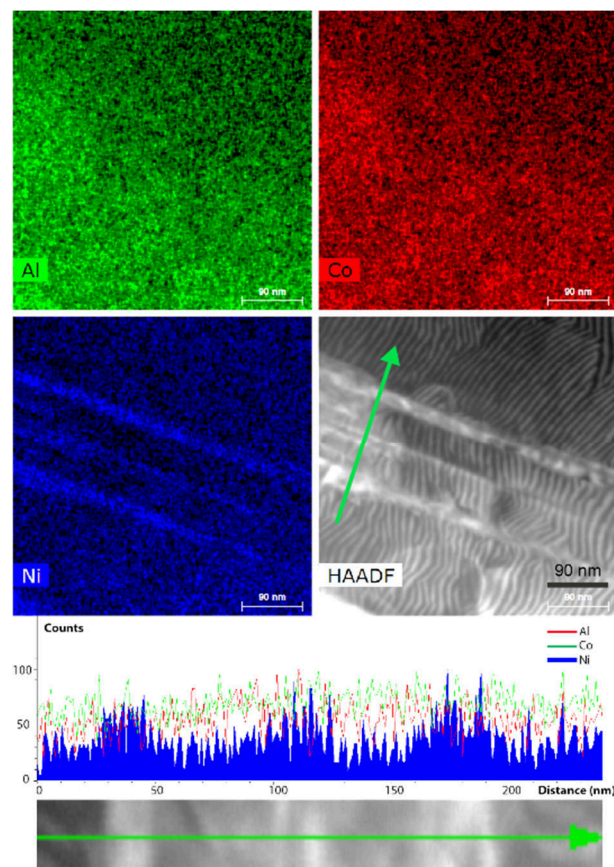


Fig. 9 . (a) HAADF STEM micrograph and (b) corresponding EDX maps of the shear band region of the 500°C compressed pillar. (c) The EDX line profile showing Ni enrichment of the slip bands.

Brittleness and cracking at room temperature

QCs are very hard and brittle at room temperature, and generally show brittle fracture behavior upon large deformation. To compare the brittleness of materials, the ratio between shear modulus, G , and bulk modulus, B , are commonly used—higher G/B usually more brittle [108] [70]. For example, the values of G/B for ductile Al, Ni and Co are about 0.26, while metallic glasses have a large range of G/B , from ~ 0.2 to ~ 0.5 . The *i*-Al-Pd-Mn and *d*-Al-Ni-Co have high values of G/B around 0.6 [70], indicating that they are relatively less intended to shear and more intended to open atomic bonds. Correlating G/B with the fracture energy [108], we can find that the QCs have the fracture energy below 0.01 kJ/m^2 , showing that they are even more brittle than most of the metallic glasses and fall in the same brittle regime with window glass and fused silica. This may explain why QC micro-pillars are even more brittle than metallic-glass ones at room temperature [22] [49]. But it is also interesting to note that the fracture modes in QC pillars are more similar to that in metallic glass pillars (shearing) [67] [10], rather than silicon and other semiconductors (splitting) [21]

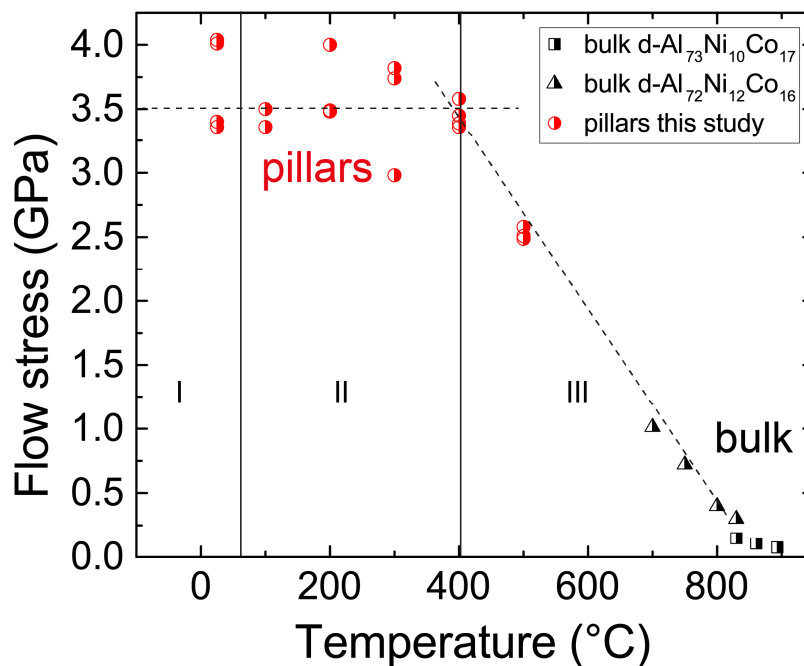


Fig. 10. Flow stress (the highest one below 5% strain) as a function of temperature for the micropillars in this study and bulk in literature. Three temperature regimes are identified: I. cracking-controlled plasticity, II serrated plastic flow and III diffusion-enhanced plasticity.

Brittle fracture and plastic flow can be two competing deformation modes in a large temperature and size range. Our previous reports demonstrated size-induced brittle-to-ductile transition with a critical size of about 500 nm. Fig. 3a and 4a indicate that the plastic flow for the DQC pillars at room temperature is not as steady as those deformed at higher temperatures, suggesting that cracking may occur. In literature, although the crack behavior has been studied using numerical simulations [68] [16] [109], detailed experiments on the fracture properties of QCs in the low temperature regime is still scarce. To understand the crack nucleation and propagation in our DQC pillars, we compressed a couple of pillars at small strains and stopped right before fracture occurs, as shown in Fig 11. The displacement bursts can be correlated to the slip lines shown at the pillar surface (Fig. 11a). The cracks propagate along the shear plane but open in a fracture model (I) [69], as shown in Fig. 11b. In general, the nucleation of dislocations can shield the forces acting on the crack tip and slow crack moving. However, dislocation mobility of quasicrystals is significantly reduced by phason walls, especially at low temperatures, and the cohesive strength of QCs is reduced along this walls. Consequently, the stress is concentrated at the crack tips, resulting cracks open. Our observation is in a good agreement with the earlier simulations [68] [110]. The simulation results also suggest that above 30% of T_m the crack does not remain atomically sharp but blunts spontaneously when the dislocations become more mobile, which can also explain why plastic flows are more stable at higher temperatures.

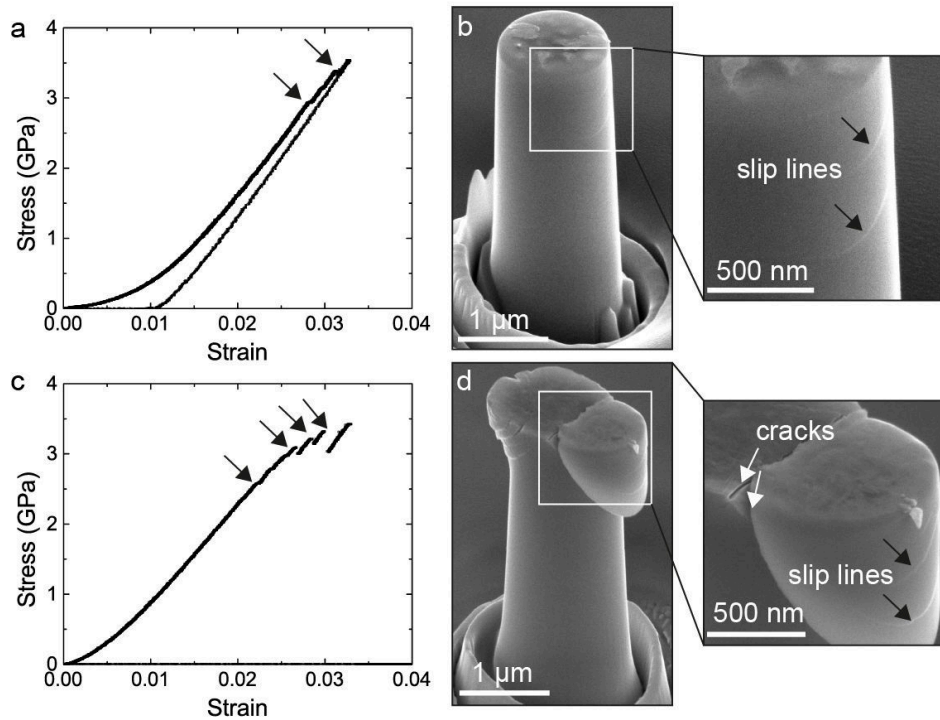


Fig. 11 Crack nucleation and propagation in micro-pillar compression at room temperature: (a) an engineering stress–strain curve and (b) its corresponding SEM image showing the onset of plasticity of a micro-pillar. Two slip lines revealed at the pillar surface correlate the two displacement bursts. (c,) and (d) showing a situation in which that cracks initiate from slip lines and propagate along crystallographic planes.

Plastic flows: serrations and strengths

The micro-compression results in Fig. 4 show intermittent flows for the pillars deformed in the temperature ranging from 100°C to 300°C: the magnitude of stress drops increases with increasing temperature, but the frequency of serrations decreases with increasing temperature, as highlighted in Fig. 12a. Interestingly, although the dynamic flow behavior varies by changing the testing temperature, the strength levels are nearly consistent from room temperature to 400°C. One may now ask what underlying mechanisms determine the serration behavior (i.e., magnitude and frequency) and the levels of strength for the DQC pillars, respectively.

Serrated stress-strain curves or jerky flows have been known for a long time since the first report in the plastic deformation of an aluminum alloy in the 1920s, as the Portevin–Le Chatelier effect (PLC) [111]. This effect is usually associated

with the competition between diffusing solutes pinning dislocations and dislocation breaking free of this stoppage [112] [113]. Serrated flows are also found in bulk metallic glasses (in the size of a few millimeters) [114], which is attributed to the process of shear-band aging, initiation and propagation [115] [116]. For the last decade, intermittent plastic flows have widely been observed in the compression of fine-scale metal pillars [66] [117] [118], which are believed to be associated with dislocation avalanche—dislocations nucleated from single, or very few, dislocation sources and suddenly move out of a pillar. Our results report the first observation of serrated flows in small-scale quasicrystals. It is also interesting to know that the similar transitions between smooth and serrated flow due to temperature are also observed in the micro-pillars of Zr-based metallic glass [67] and complex metallic alloy $\text{Al}_{13}\text{Co}_4$ [100]. Now, a different question to ask is whether the observed serrated flows in the DQC pillars are caused by pinning and unpinning process of grown-in dislocations, similar to those in the PLC effect, or by the nucleation and propagation processes, similar to those observed in metal and metallic glass pillars at small scales.

Mechanically, force drops (for displacement control mode) or displacement bursts (for force control mode) occurs in micro-compression is because the loading sensor or the feedback loop is not fast enough to follow the motion of the pillar top [97]. After stress relaxation, a flat punch needs a certain period of time to catch the movement of the pillar top. Under a fixed loading rate, a higher magnitude of stress drop, $\Delta\sigma$, or force drop, ΔF , should correspond to a faster plastic deformation, which means that $\Delta\sigma$ or ΔF is proportional to the velocity of dislocations, v_{dis} , or shear bands, as:

$$\Delta F \propto v_{dis} \quad (1)$$

Our DQC sample was annealed for long hours (48 h at 1000 °C) and the grown-in dislocation density should be low. During deformation the initial dislocations can move out of the pillar very quickly, leaving the pillar a state of dislocation lacking if few dislocations are nucleated. Nevertheless, in the experiment we can

still observe continuous serrated plastic flows during the whole loading period. This indicates that the intermittent flow observed in the DQC pillars is very unlikely due to, or dominated by, the PLC-like dislocation pinning effect but a response to a process of dislocation nucleation, propagation and annihilation.

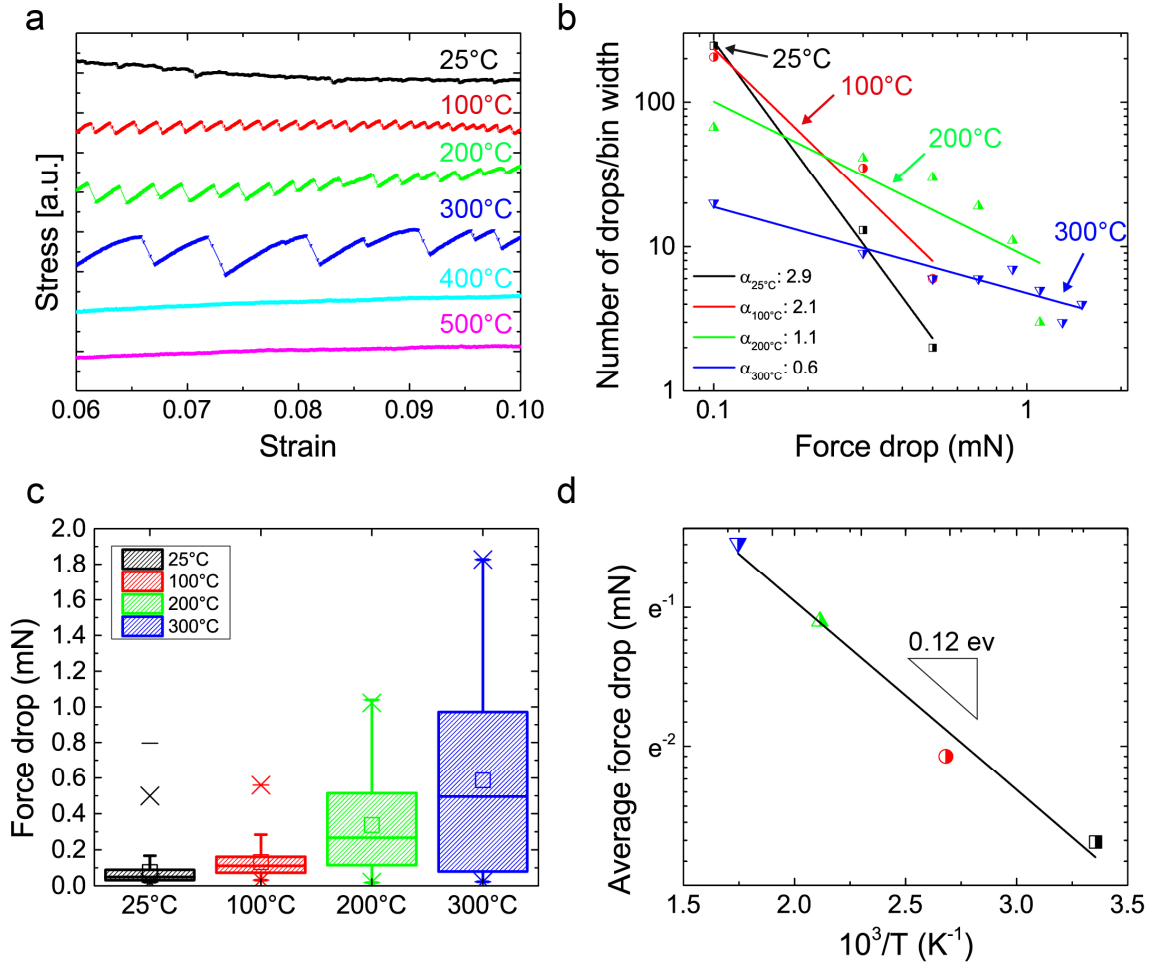


Fig. 12. Statistical analysis of serration behavior for the DQC micropillar compression: (a) illustration of the effect of temperature on the flow behavior, the segments of stress-strain curves are extracted from fig. 3 and to identify each curve the curves are shifted vertically. (b) Serration frequency distribution showing the number of force-drop events of a certain size versus event size, plotted on logarithmic scales. (c) Comparison of the magnitudes of force drops at different temperatures (-: max or min, ×: 99% or 1% and □: mean). (d) Average force drop level as a function of $1/T$.

For the scaling analysis, we plotted the number of force drops, $n(\Delta F)$, versus the force drop magnitude, ΔF , for the pillars tested between room temperature to 300°C (Fig. 12b). A noise threshold of $\sim 10 \mu\text{N}$ for detecting force drops is used and the magnitudes of the force drops exceeding the noise threshold are recorded

and sorted into bins for the pillars at each temperature. For each temperature, the probability of observing a force-drop event decreases as ΔF increases. The data collected from room temperature to 300°C demonstrate power-law scaling, fitting an expression of:

$$n(\Delta F) = C\Delta F^{-\alpha} \quad (2)$$

where α is a scaling exponent and C is a constant. The force drops for the pillars deformed at 400°C and 500°C are smaller than the noise threshold used. The values of α for the DQC pillars tested at 25 °C, 100 °C, 200 °C and 300°C are 0.6, 1.1, 2.1 and 2.9, respectively. The similar scaling analyses were used in single crystalline Ni [117] and LiF [119] micro-pillars, showing the values of α are 1.5 and 1.8–2.9, respectively. The observation of intermittent flow and power-law scaling (or scale-free behavior) is comparable to those observed in metal [117] and metallic glasses [116] pillars, suggesting that the plastic flow for DQC pillars are controlled by a nucleation and propagation process, at least in the tested size and temperature regime.

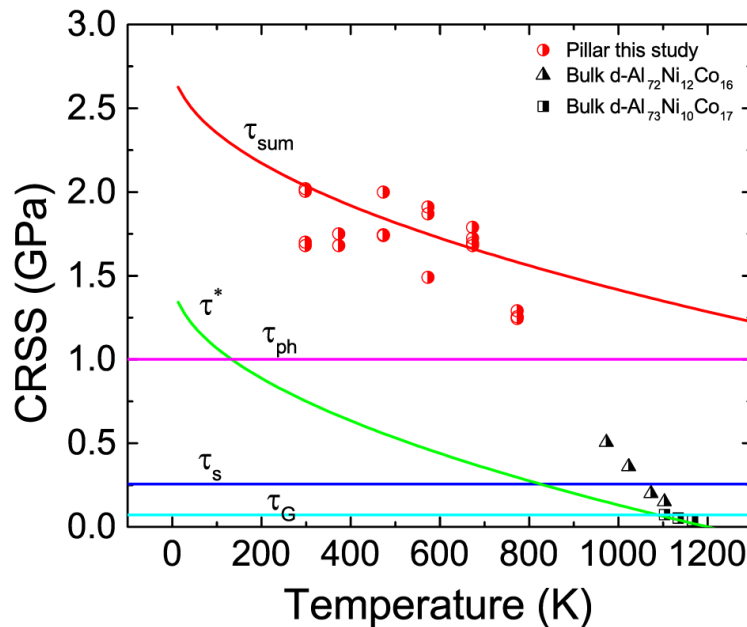


Fig. 13. The estimated CRSS as a function of absolute temperature for the DQC pillars. The red curve is a sum of all the mechanisms for DQC pillars. The contribution of each mechanism is plotted separately : τ^* (lattice friction), τ_{ph} (phason wall dragging), τ_s (source strengthening) τ_G (Taylor hardening). The experimental data for pillar compression and bulk compression are also plotted.

A close inspection of a single serration event suggests several stages: a new dislocation is nucleated from a source at the peak stress, the dislocation is activated and the stress is relaxed, the dislocation moves out of the pillar and the stress increases again preparing for the next nucleation. Because the average ΔF increases by increasing temperature (Fig. 12a), it suggests that the dislocation motion could be a thermally activated process, which generally follows an Arrhenius-type equation [120]:

$$v_{dis} = v_0 e^{\left(\frac{-Q(\tau)}{k_B T}\right)} \quad (3)$$

where v_0 is a constant, $Q(\tau)$ is the activation energy for dislocation motion at the shear stress of τ , k_B Boltzmann constant of 8.617×10^{-5} eV·K⁻¹ and T absolute temperature. With Eq. (1), a similar expression for the measured force drop ΔF can be obtained:

$$\Delta F = \Delta F_0 e^{\left(\frac{-Q(\tau)}{k_B T}\right)} \quad (4)$$

where ΔF_0 is a constant. The plot of the average ΔF as a function of $10^3/T$ (Fig. 12d) shows a well-fitted linear relation with the slope of -1358 K. Consequently, we can obtain that Q (1.8 GPa) is ~ about 0.12 eV, assuming a Schmid factor of 0.5. This activation energy is slightly lower than that for shear banding in metallic glasses, 0.32 eV [121], in the similar level to that for fcc metals, <0.2eV [122], much lower than that for dislocation motion silicon, ~1-2 eV [123]. Messerschmidt *et al.* [124] calculated the $Q(\tau)$ for the deformation of i-Al-Pd-Mn single quasicrystals in the high-temperature range (650-800°C) and showed that $Q(\tau)$ is decreased by increasing the stress level from 3 eV at 250 MPa to about 1 eV at 1.25 GPa.

It is also interesting to note that the dislocation velocity here is dependent of temperature rather than externally applied stress. Although the stress dependence of the dislocation velocity is well known, from the classical experiment of etching

LiF crystals [8], some early and recent mechanical testing indicate that the dislocation mobility could be primarily determined by the internal stress field landscape and its dynamics [76, 118, 125]. Our observation might be interpreted by that the actual dislocation velocity is controlled by the internal stress fields which is thermally activated.

The second question regarding to the plastic flows is what determines the flow stress for the DQC pillars. Classical analysis of the flow stress in regular crystals is contributed by both thermal and athermal components [122]— τ^* and τ_G , respectively. τ^* presents the thermal stress component which needs to overcome the lattice resistance or Peierls barrier, and τ_G is the athermal contribution of long-range dislocation interaction—Taylor hardening. For small-size pillars where dislocation source is limited, the source strength, τ_s , also contributes the flow stress. Additionally, particular to quasicrystals, the dislocation motion is accompanied with the rearrangement of the phason order (phason walls), generating an extra back stress, τ_{ph} [126]. Therefore, the total shear stress for the DQC pillars can be expressed as:

$$\tau_{ph} = \tau^* + \tau_G + \tau_{ph} + \tau_s \quad (5)$$

The friction mechanism of dislocation motion in quasicrystals is generally believed to be associated with kink pairs [70] [126]. Suzuki *et al.* [127] suggested that double-kink formation controls dislocation activity below T_c , and the relation between lattice friction and test temperature can be estimated as [128]:

$$\tau^* = \left[1 - \left(\frac{T_t}{T_c} \right)^{1/2} \right] \tau_p \text{ with } T_t < T_c \quad (6)$$

where τ_p is the Peierls stress. There is no literature value available for the Peierls stress along A_{45} orientation in d-Al-Ni-Co, but an early computer simulation suggests a theoretical estimation of the friction stress near 0 K of around 1.5 GPa for i-Al-Pd-Mn [129]. T_t is the test temperature and T_c is the critical temperature (the strain rate effect should be considered, which is calculated from bulk tests)

above which there is sufficient thermal energy to overcome the Peierls barriers by thermal activation and the stress is temperature independent. T_c can be estimated by the bulk compression at high temperatures, about 1200K [58]. The second term, τ_G , can be calculated using the Taylor hardening formula, as:

$$\tau_G = 0.5Gb\sqrt{\rho} \quad (7)$$

where G is the shear modulus, ~ 80 GPa for d-Al-Ni-Co [70], b is the Burger's vector for d-Al-Ni-Co along A_{45} orientation, 4\AA [54], ρ is the initial dislocation density, which is generally about 10^{12} - 10^{13} m^{-2} for annealed quasicrystals [54, 58]. There is still a question whether the third term, τ_{ph} , is a thermally activated component or not. Messerschmidt [126] suggests the formation of a phason wall has some similarity to the creation of a stacking fault, which is an athermal process. Simulations suggest the shear stress to trail the phason wall by glide is about 1 GPa for d-Al-Ni-Co [68, 126]. The source strengthening for a small-size pillar can be estimated using the following relation [130]:

$$\tau_s = KG \frac{\ln(\bar{\lambda}/b)}{\bar{\lambda}/b} \quad (8)$$

where K is a source-strengthening constant; $\bar{\lambda}$ is the statistical average length of the longest dislocation source, i.e., the weakest source. For a simple estimation, we assume $K \approx 1$ and $\bar{\lambda} \approx D$, pillar diameter. Therefore, with Eqs. (5), (6), (7) and (8), we obtain:

$$\tau_{sum} = \left[1 - \left(\frac{T_t}{T_c} \right)^{1/2} \right] \tau_p + 0.5Gb\sqrt{\rho} + \tau_{ph} + KG \frac{\ln(\bar{\lambda}/b)}{\bar{\lambda}/b} \quad (9)$$

Assuming a Schmid factor of 0.5, we plot the critical resolved shear stress (CRSS) as a function of the pillar diameter for both experimental data and calculated curves by Eqs. (6)-(9), as shown in Fig. 13. The calculated flow stress, τ_{sum} , is in a good agreement with the experimental measurement in the range from room temperature to about 400 °C, although the calculated τ_{sum} is a constant between 25°C and 400 °C. The constituted strength components, τ^* , τ_G , τ_{ph} and τ_s are also

shown in Fig. 13. Although τ^* is decreased by increasing temperature, τ_{sum} is dominated by τ_{ph} and τ_s , which contribute the temperature independence of CRSS. Even if the values of τ_{ph} and τ_p may vary slightly according to literature, the calculated curve can still show the general trend of the relationship between temperature and CRSS. Thus, the nearly constant CRSS between room temperature and 400 °C is mainly due to the very high athermal stresses. However, above 400 °C the calculated τ_{sum} does not fit the experimental data and the literature values for bulk compression at higher temperatures, suggesting a different mechanism dominate in this temperature regime.

Hybrid diffusive-displacive plasticity

The DQC pillars deformed at 400°C and 500°C exhibit very different post-deformation morphology (Fig. 3), dynamic behavior (Fig. 4), microstructure and chemical distribution (Figs. 8 and 9), compared to those deformed at lower temperatures (25-300°C). It suggests that diffusion may play an essential role in the plasticity at intermediate temperatures. The strain-rate jump experiments can be used to measure the strain-rate sensitivity of the stress, m , which is related to the apparent activation volume, V_a , as [120]:

$$V_a = \sqrt{3} \frac{K_B T}{m \sigma} \quad (10)$$

where m can be measured by the relation of flow stress, σ , as a function of strain rate, $\dot{\epsilon}$, by [120]:

$$m = \frac{\partial \ln \sigma}{\partial \ln \dot{\epsilon}} \quad (11)$$

The experimental measurement of V_a is important, because V_a is related to the area swept by the dislocation during the thermally activated event. In general, it is believed that a very small V_a ($\sim 0.1-1b^3$)—diffusion-controlled deformation, a small one ($\sim 10-100b^3$) can be related to Peierls mechanism, a large one ($100-1000b^3$)—dislocation solute interactions, and a very large one ($\sim 1000b^3$)—the forest mechanism [120, 126]. By evaluating the strain-rate jump results, we

obtained the average values of m for 400 °C and 500 °C of 0.113 and 0.097, respectively (Fig. 14a). Using Eq. (10), we derived the values of V_a for 400 and 500 °C to be around 0.04 nm³ and 0.05 nm³, respectively. Considering that the Burgers vector is 4 Å for A₄₅ d-Al-Ni-Co [54], the values of V_a for 400 °C and 500 °C are both about $1b^3$, which can be related to a diffusion-related mechanism, but is still higher than that for bulk diffusion ($0.1b^3$), suggesting that the plastic deformation could result from a combination of mixed displacive and diffusional modes, which matches our STEM observation (Fig. 9).

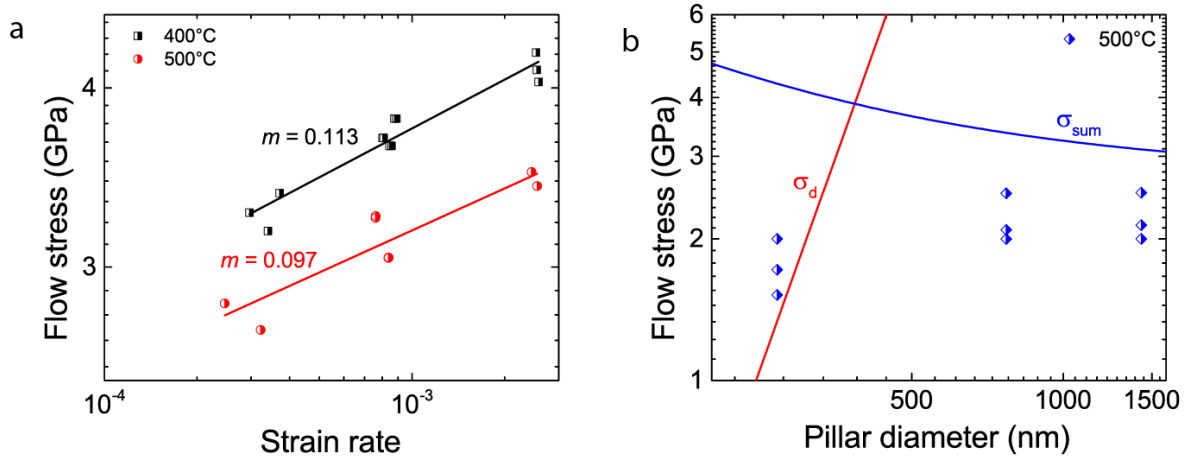


Fig. 14. Strain rate and size dependence of strength for the high temperature compressions. (a) The strain-rate sensitivity of flow stress for the pillars deformed at 400 °C and 500 °C. (b) Calculated flow stress based on Eq. (9) and surface-diffusion controlled strength based on Eq. (12) as a function of pillar diameter, comparing to the experimental data.

The activation volumes reported in the bulk compression of d-Al-Ni-Co at high temperatures (~800-900°C) are about $10b^3$ [54, 58]. It is interesting to see that although our d-Al-Ni-Co samples are deformed at a lower temperature, diffusion seems to play a more important role in our samples than those deformed at higher temperatures. In general, dislocation activity (i.e. displacive plasticity) plays a dominant role in the plastic deformation of crystalline solids at room temperature, while at elevated temperatures diffusive processes may result in plastic deformation via bulk diffusion (i.e. Nabarro-Herring creep [24]) or grain boundary diffusion (i.e. Coble creep [29]). Grain boundaries or free surfaces can be regarded as fast passes for atoms to diffuse, and the resulting the grain-

boundary diffusivity is about a few orders higher than bulk diffusivity. For example, the grain-boundary diffusivity and bulk diffusivity of Sn at room temperature are $1.45 \times 10^{-12} \text{ m}^2/\text{s}$ [131] and $2.86 \times 10^{-17} \text{ m}^2/\text{s}$ [132], respectively. In our micro-compression tests, by reducing sample dimension, its surface-to-volume ratio is increased accordingly. The surface diffusion process may play a significant role in plasticity instead of bulk diffusion. For example, high-temperature nanoindentation experiments [133], and small-contact-area indentations [134] on metal surfaces shows surface diffusion can be shown to be more important than bulk vacancy diffusion. Recently, *in situ* TEM tension of pure Sn [31] and Al-based metallic glasses [30] showed that surface diffusion could control the ductility even at room temperature for the sample sizes of $\sim 130 \text{ nm}$ and $\sim 20 \text{ nm}$, respectively. Using a model of small-scale ligament, Tian *et al.* [31] demonstrated that the surface-diffusion controlled strength has a similar relationship, and also the same order of diffusivity, with grain boundary diffusion, as:

$$\dot{\epsilon} = B \frac{\delta_s D_s \Omega}{D^3 K_B T} \sigma_d \quad (12)$$

where B is a dimensionless constant, δ_s is the nominal surface layer thickness, D_s is the surface diffusivity, Ω is the atomic volume, D is the sample size and σ_d is the diffusion-controlled stress. The bulk diffusion coefficients of Ni and Co in Al at $500 \text{ }^\circ\text{C}$ are about $1 \times 10^{-16} \text{ m}^2 \text{ s}^{-1}$ and $2.5 \times 10^{-16} \text{ m}^2 \text{ s}^{-1}$ [135] respectively. If we assume the surface diffusivity for Ni or Co in Al is also five orders of magnitude higher than its bulk diffusivity, similar to that for Sn, D_s for Ni and Co in Al should be in the order of $10^{-11} \text{ m}^2 \text{ s}^{-1}$ at 500°C . To give an simple estimation of σ_d , assuming $B \approx 1$, $\delta_s \approx 1 \text{ nm}$, $D_s \approx 10^{-11} \text{ m}^2 \text{ s}^{-1}$ and $\Omega \approx (2\text{\AA})^3$, and using $\dot{\epsilon} = 10^{-3}$, $T = 773 \text{ K}$ and $D = 1.4 \text{ }\mu\text{m}$ in the experiment, we obtain the σ_d as a function of D . As illustrated in Fig. 14b, σ_d decreases with decreasing sample size, showing a “smaller is weaker” trend, and the strength due to displacive plasticity, σ_{sum} , calculated using Eq.(9) increases with decreasing sample size, showing a “smaller is stronger” trend. These two curves cross over at sub-micrometer scales. Above

this critical size, the deformation is dominated by dislocation activities, and below this critical size, the deformation can be controlled by diffusion mechanisms, which may give an explanation why the strength of the smaller pillar is lower at 500°C.

However, the actual situation could become very complex. As shown in Figs. 8 and 9, diffusion and dislocation slip may couple and occur in tandem, comparable to dislocation creep which is operative at intermediate temperatures and high stresses [136]. It has been suggested that during dislocation creep the plastic strains are still mainly resulted from dislocation glides, but the creep rate is governed by the unlocking of dislocation locks and dislocation climb, controlled by bulk or dislocation core (pipe) diffusion [137]. This may explain why the flow stress at 400°C and 500°C are also kept at high levels in our experiment. Additionally, creep rate can be accelerated by dislocation glide, which has been observed in Ni₃Al single-crystal pillars [138]. Another question is why Ni is more diffusive than Co, despite Co having a slightly higher bulk diffusion coefficient than Ni in Al. At 500°C, intermetallic phase Ni₂Al₃ might become more stable than other intermetallic phases, and high stress at elevated temperature (i.e., high energy input) may enhance massive Ni diffusion, leading to phase transformation as well as dynamic recrystallization.

An interesting aspect towards engineering applications is that the small-scale QCs shows extraordinarily high strengths at very low density ($4.1 \times 10^3 \text{ kg m}^{-3}$). As pointed out by Zhu and Li [139] for the ultra-strength community, if the strain-rate sensitivity is small, the service life of a component can be long. In our QC pillars, $m \approx 0.1$ means a reduction of stress by half would cause a thousand-fold decrease in the strain rate. Consequently, assuming that our QC pillars fail in one day at 2 GPa, it would survive about three years at 1 GPa. Therefore, small-scale QCs may represent a new class of materials for structural usage.

Conclusion and outlook

We explored a new temperature–size regime for quasicrystal plasticity, specifically for d-Al-Ni-Co at the micrometer and sub-micrometer scales in the temperature range of 25-500°C, in addition to the traditional studies of bulk deformation of QCs at high temperatures. As summarized in a 3D plot (Fig.15), this size-temperature-strength deformation map includes:

(1) size-dependent strength at room temperature (black curve) [105]..

(2) temperature-dependent plastic behavior for 1.5- μm pillars (red curve): at room temperature, the plasticity is controlled by cracking; between 100-300°C, the pillars exhibit serrated plastic flows, which is controlled by dislocation motion in a thermal activated process, and constant strengths, which are determined by athermal processes of phason-induced stress and dislocation-nucleation strength; between 400-500°C, the diffusion coupled dislocation activities may become dominating in the plasticity.

(3) size-dependent plasticity at high temperatures (blue curve): the smaller pillars exhibit lower strength levels, which could be attributed to higher surface diffusion.

The new deformation-mechanism map for quasicrystals, after taking into account the size and temperature dependence, may pave way for engineering applications of quasicrystals, such as structural and functional components at small scales. For future studies, the borders of the deformation-mechanism maps may expand to a larger regime, and also include other materials, at extremely small scales and high stresses. For example, how the nanometer-scale DQCs deform at high temperatures, what are the deformation mechanisms for the DQCs with other orientations, IQCs CMAs at small scales and low temperatures are currently unknown and interesting to study.

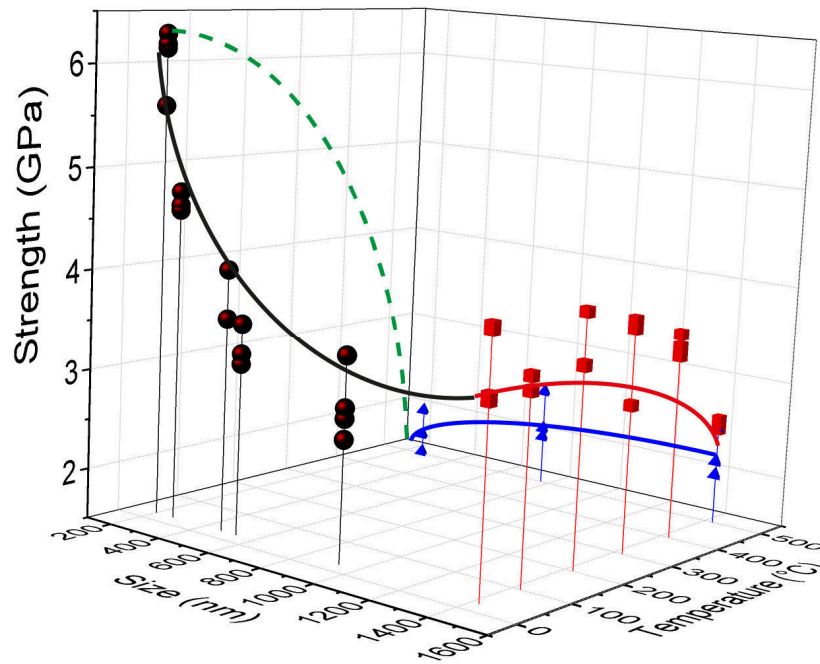


Fig. 15. 3D illustration of the size-temperature-stress deformation map for the DQC Al-Ni-Co pillars. Black curve: size dependence of strength at room temperature; red curve: temperature dependence of strength at micrometer scale; blue curve: size dependence of strength at high temperature (500°C); green curve: temperature dependence of strength at nanometer scale, the experimental data is still lacking and is of interest for future studies.

Acknowledgements

We thank P. Kuczera (ETH Zurich) for the preparation of the bulk quasicrystals. S. Takeuchi (Tokyo University of Science) and K. Edagawa (the University of Tokyo) for their helpful discussions, ScopeM (ETH Zurich) for supplying electron microscopy facilities. Y.Z. acknowledges the financial support through the Swiss National Science Foundation (SNF Grant: 200021_143633)

References

- [1] Shechtman D, Blech I, Gratias D, Cahn JW. *Phys Rev Lett* 1984;53:1951.
- [2] Dubois J-M. *Chemical Society Reviews* 2012;41:6760.
- [3] Dolinsek J. *Chemical Society Reviews* 2012;41:6730.
- [4] Feuerbacher M, Metzmacher C, Wollgarten M, Urban K, Baufeld B, Bartsch M, Messerschmidt U. *Materials Science and Engineering: A* 1997;233:103.
- [5] Kabutoya E, Edagawa K, Tamura R, Takeuchi S, Guo JQ, Tsai AP. *Philos Mag A* 2002;82:369.
- [6] Wollgarten M, Saka H, Inoue A. *Philosophical Magazine A* 1999;79:2195.
- [7] Momprou F, Caillard D. *Acta Mater* 2004;52:3613.
- [8] Johnston WG, Gilman JJ. *J Appl Phys* 1959;30:129.
- [9] Christian JW, Mahajan S. *Progress in materials science* 1995;39:1.
- [10] Greer AL, Cheng YQ, Ma E. *Materials Science and Engineering: R: Reports* 2013;74:71.
- [11] Takakura H, Gomez CP, Yamamoto A, De Boissieu M, Tsai AP. *Nat Mater* 2007;6:58.
- [12] Zeng X, Ungar G, Liu Y, Percec V, Dulcey AE, Hobbs JK. *Nature* 2004;428:157.
- [13] Bindi L, Steinhardt PJ, Yao N, Lu PJ. *Science* 2009;324:1306.
- [14] Caillard D, Momprou F, Bresson L, Gratias D. *Scripta Materialia* 2003;49:11.
- [15] Bonneville J, Caillard D, Guyot P. Chapter 85 - Dislocations and Plasticity of Icosahedral Quasicrystals. In: Hirth JP, editor. *Dislocations in Solids*, vol. Volume 14. Elsevier, 2008. p.251.
- [16] Dilger C, Mikulla R, Roth J, Trebin HR. *Philosophical Magazine A* 1997;75:425.
- [17] Azhazha V, Dub S, Khadzhay G, Merisov B, Malykhin S, Pugachov A. *Philos Mag* 2004;84:983.
- [18] Texier M, Prout A, Bonneville J, Rabier J. *Materials Science and Engineering: A* 2004;387–389:1023.
- [19] Texier M, Joulain A, Bonneville J, Thilly L, Rabier J. *Philos Mag* 2007;87:1497.
- [20] Reibold M, Belger A, Mukhopadhyay NK, Gille P, Paufler P. *physica status solidi (a)* 2005;202:2267.
- [21] Ostlund F, Rzepiejewska-Malyska K, Leifer K, Hale LM, Tang YY, Ballarini R, Gerberich WW, Michler J. *Adv Funct Mater* 2009;19:2439.
- [22] Volkert C, Donohue A, Spaepen F. *J Appl Phys* 2008;103:083539.
- [23] Lawn BR. *Fracture of brittle solids*: Cambridge university press, 1993.
- [24] Herring C. *J Appl Phys* 1950;21:437.
- [25] Griffith AA. *Philosophical transactions of the royal society of london. Series A, containing papers of a mathematical or physical character* 1921:163.
- [26] Quiquandon M, Gratias D. *Phys Rev B* 2006;74:214205.
- [27] Weibull W. *Journal of applied mechanics* 1951;103.
- [28] Deus C, Wolf B, Paufler P. *Philosophical Magazine A* 1997;75:1171.
- [29] Coble RL. *J Appl Phys* 1963;34:1679.
- [30] Luo J, Wu F, Huang J, Wang J, Mao S. *Phys Rev Lett* 2010;104:215503.

- [31] Tian L, Li J, Sun J, Ma E, Shan Z-W. *Scientific reports* 2013;3.
- [32] Tsai AP, Inoue A, Yokoyama Y, Masumoto T. *Mater T Jim* 1990;31:98.
- [33] Greer JR, Oliver WC, Nix WD. *Acta Mater* 2005;53:1821.
- [34] Volkert CA, Lilleodden ET. *Philos Mag* 2006;86:5567.
- [35] Kunz A, Pathak S, Greer JR. *Acta Mater* 2011;59:4416.
- [36] Frick CP, Clark BG, Orso S, Schneider AS, Arzt E. *Materials Science and Engineering: A* 2008;489:319.
- [37] Jennings AT, Burek MJ, Greer JR. *Phys Rev Lett* 2010;104:135503.
- [38] Schneider AS, Kaufmann D, Clark BG, Frick CP, Gruber PA, Monig R, Kraft O, Arzt E. *Phys Rev Lett* 2009;103.
- [39] Kim J-Y, Jang D, Greer JR. *Acta Mater* 2010;58:2355.
- [40] Lilleodden E. *Scripta Materialia* 2010;62:532.
- [41] Edalati K, Toh S, Iwaoka H, Watanabe M, Horita Z, Kashioka D, Kishida K, Inui H. *Scripta Materialia* 2012;67:814.
- [42] Okamoto NL, Kashioka D, Hirato T, Inui H. *Int J Plasticity* 2014;56:173.
- [43] Rinaldi A, Peralta P, Friesen C, Sieradzki K. *Acta Mater* 2008;56:511.
- [44] Jang D, Greer JR. *Scripta Materialia* 2011;64:77.
- [45] Gu XW, Loynachan CN, Wu ZX, Zhang YW, Srolovitz DJ, Greer JR. *Nano Lett* 2012;12:6385.
- [46] Alshehri O, Yavuz M, Tsui T. *Acta Mater* 2013;61:40.
- [47] Zou Y, Ma H, Spolenak R. *Nat Commun* 2015;6.
- [48] Zou Y, Maiti S, Steurer W, Spolenak R. *Acta Mater* 2014;65:85.
- [49] Chen CQ, Pei YT, De Hosson JTM. *Acta Mater* 2010;58:189.
- [50] Levine D, Steinhardt PJ. *Phys Rev Lett* 1984;53:2477.
- [51] Tsai AP, Inoue A, Masumoto T. *Mater T Jim* 1989;30:150.
- [52] Luck R, Scheffer M, Godecke T, Ritsch S, Beeli C. *Mater Res Soc Symp P* 1999;553:25.
- [53] Steurer W, Haibach T, Zhang B, Kek S, Lück R. *Acta Crystallographica Section B: Structural Science* 1993;49:661.
- [54] Feuerbacher M, Schall P. *Scripta Materialia* 2003;49:25.
- [55] Park JY, Ogletree DF, Salmeron M, Ribeiro RA, Canfield PC, Jenks CJ, Thiel PA. *Science* 2005;309:1354.
- [56] Freedman B, Lifshitz R, Fleischer JW, Segev M. *Nat Mater* 2007;6:776.
- [57] Feuerbacher M, Bartsch M, Grushko B, Messerschmidt U, Urban K. *Philosophical Magazine Letters* 1997;76:369.
- [58] Schall P, Feuerbacher M, Urban K. *Philos Mag* 2004;84:705.
- [59] Edagawa K, Arai Y, Hashimoto T, Takeuchi S. *Materials Transactions, JIM* 1998;39:863.
- [60] Edagawa K, Ohta S, Takeuchi S, Kabutoya E, Guo J, Tsai A-P. *Materials Science and Engineering: A* 2000;294:748.
- [61] Mukhopadhyay NK, Belger A, Paufler P, Gille P. *Philos Mag* 2006;86:999.
- [62] Zou Y, Kuczera P, Sologubenko A, Sumigawa T, Kitamura T, Steurer W, Spolenak R. *Probing room-temperature plasticity in quasicrystals by size effect*. 2015.

- [63] Canfield PC, Fisk Z. *Philos Mag B* 1992;65:1117.
- [64] Ortelli S. *Zuechtung Dekagonaler Quasikristalle*. Laboratory of Crystallography. Zurich: ETH Zurich, 2001.
- [65] Zou Y, Spolenak R. *Philosophical Magazine Letters* 2013;93:431.
- [66] Uchic MD, Dimiduk DM, Florando JN, Nix WD. *Science* 2004;305:986.
- [67] Wheeler JM, Raghavan R, Michler J. *Scripta Materialia* 2012;67:125.
- [68] Mikulla R, Roth J, Trebin H. *Philosophical Magazine B* 1995;71:981.
- [69] Courtney TH. *Mechanical behavior of materials*: Waveland Press, 2005.
- [70] Takeuchi S, Edagawa K. Chapter 8 Elastic and plastic properties of quasicrystals. In: Takeo F, Yasushi I, editors. *Handbook of Metal Physics*, vol. Volume 3. Elsevier, 2008. p.267.
- [71] Schall P, Feuerbacher M, Urban K. *Philosophical Magazine Letters* 2004;84:471.
- [72] Schall P, Feuerbacher M, Urban K. *Phys Rev B* 2004;69:134105.
- [73] Bartsch M, Schall P, Feuerbacher M, Messerschmidt U. *J Mater Res* 2005;20:1814.
- [74] Parthasarathy TA, Rao SI, Dimiduk DM, Uchic MD, Trinkle DR. *Scripta Materialia* 2007;56:313.
- [75] Korte S, Clegg WJ. *Philos Mag* 2011;91:1150.
- [76] Zou Y, Spolenak R. *Philos Mag* 2015:1.
- [77] Cervellino A, Haibach T, Steurer W. *Acta Crystallographica Section B: Structural Science* 2001;58:8.
- [78] Yu Q, Qi L, Mishra RK, Li J, Minor AM. *Proceedings of the National Academy of Sciences* 2013;110:13289.
- [79] Trebin H-R. *Quasicrystals: structure and physical properties*: John Wiley & Sons, 2006.
- [80] Steurer W. *Chemical Society Reviews* 2012;41:6717.
- [81] Dubois J, Kang S, Stebut JV. *Journal of Materials Science Letters* 1991;10:537.
- [82] Demange V, Milandri A, De Weerd M, Machizaud F, Jeandel G, Dubois J. *Phys Rev B* 2002;65:144205.
- [83] Stroud RM, Viano AM, Gibbons PC, Kelton KF, Misture ST. *Appl Phys Lett* 1996;69:2998.
- [84] Dubois JM, Kang SS, Massiani Y. *J Non-Cryst Solids* 1993;153-154:443.
- [85] Talapin DV, Shevchenko EV, Bodnarchuk MI, Ye X, Chen J, Murray CB. *Nature* 2009;461:964.
- [86] Hayashida K, Dotera T, Takano A, Matsushita Y. *Phys Rev Lett* 2007;98:195502.
- [87] Engel M, Damasceno PF, Phillips CL, Glotzer SC. *Nat Mater* 2015;14:109.
- [88] Bindi L, Yao N, Lin C, Hollister LS, Andronicos CL, Distler VV, Eddy MP, Kostin A, Kryachko V, MacPherson GJ, Steinhardt WM, Yudovskaya M, Steinhardt PJ. *Sci. Rep.* 2015;5.
- [89] Caillard D, Vanderschaeve G, Bresson L, Gratias D. *Philosophical Magazine A* 2000;80:237.
- [90] Yokoyama Y, Inoue A, Masumoto T. *Materials Transactions, JIM* 1993;34:135.
- [91] Levine D, Lubensky TC, Ostlund S, Ramaswamy S, Steinhardt PJ, Toner J. *Phys Rev Lett* 1985;54:1520.
- [92] Hiraga K, Hirabayashi M. *Jpn J Appl Phys* 1987;26:L155.

- [93] Socolar JES, Lubensky TC, Steinhardt PJ. *Phys Rev B* 1986;34:3345.
- [94] Feuerbacher M. *Chemical Society Reviews* 2012;41:6745.
- [95] Edagawa K. *Materials Science and Engineering: A* 2001;309–310:528.
- [96] Texier M, Thilly L, Bonneville J, Proult A, Rabier J. *Materials Science and Engineering: A* 2005;400–401:311.
- [97] Uchic MD, Shade PA, Dimiduk DM. *Annu Rev Mater Res* 2009;39:361.
- [98] Kraft O, Gruber PA, Monig R, Weygand D. *Annual Review of Materials Research*, Vol 40 2010;40:293.
- [99] Greer JR, De Hosson JTM. *Progress in Materials Science* 2011;56:654.
- [100] Walter C, Wheeler JM, Barnard JS, Raghavan R, Korte-Kerzel S, Gille P, Michler J, Clegg WJ. *Acta Mater* 2013;61:7189.
- [101] Nadgorny EM, Dimiduk DM, Uchic MD. *J Mater Res* 2008;23:2829.
- [102] Michler J, Wasmer K, Meier S, Ostlund F, Leifer K. *Appl Phys Lett* 2007;90.
- [103] Korte S, Clegg WJ. *Scripta Materialia* 2009;60:807.
- [104] Wang S, Yang Y, Zhou L, Mai Y-W. *J Mater Sci* 2012;47:6047.
- [105] Zou Y, Kuczera P, Steurer W, Spolenak R. Disappearance of plastic anisotropy in decagonal quasicrystals at small scales and room temperature. 2015.
- [106] Wheeler JM, Michler J. *Review of Scientific Instruments* 2013;84:045103.
- [107] Gödecke T, Scheffer M, Lück R, Ritsch S, Beeli C. *Z Metallkd* 1998;89:687.
- [108] Lewandowski * JJ, Wang WH, Greer AL. *Philosophical Magazine Letters* 2005;85:77.
- [109] Mikulla R, Stadler J, Krul F, Trebin HR, Gumbsch P. *Phys Rev Lett* 1998;81:3163.
- [110] Feuerbacher M, Urban K, Messerschmidt U, Bartsch M, Geyer B, Ledig L, Rudhart C, Gumbsch P, Trebin H-R, Paufler P, Wolf B, Weller M, Damson B, Sinning HR, Scarfone R, Golovin IS, Schurack F, Eckert J, Schultz L. *Mechanical Properties. Quasicrystals*. Wiley-VCH Verlag GmbH & Co. KGaA, 2006. p.431.
- [111] Portevin A, Le Chatelier F. *Comptes Rendus de l'Académie des Sciences Paris* 1923;176:507.
- [112] Cottrell AH. *The London, Edinburgh, and Dublin Philosophical Magazine and Journal of Science* 1953;44:829.
- [113] Lebyodkin MA, Estrin Y. *Acta Mater* 2005;53:3403.
- [114] Kimura H, Masumoto T. *Acta Metallurgica* 1983;31:231.
- [115] Klaumünzer D, Lazarev A, Maaß R, Dalla Torre FH, Vinogradov A, Löffler JF. *Phys Rev Lett* 2011;107:185502.
- [116] Maaß R, Löffler JF. *Adv Funct Mater* 2015:n/a.
- [117] Dimiduk DM, Woodward C, LeSar R, Uchic MD. *Science* 2006;312:1188.
- [118] Maass R, Derlet PM, Greer JR. *Scripta Materialia* 2013;69:586.
- [119] Dimiduk DM, Nadgorny EM, Woodward C, Uchic MD, Shade PA. *Philos Mag* 2010;90:3621.
- [120] Caillard D, Martin J-L. *Thermally activated mechanisms in crystal plasticity*: Elsevier, 2003.
- [121] Maaß R, Klaumünzer D, Löffler J. *Acta Mater* 2011;59:3205.

- [122] Hull DaDJB, editor Introduction to Dislocations: Elsevier Butterworth Heinemann: Oxford, 2001.
- [123] Alexander H, Kisielowski-Kemmerich C, Swalski A. *physica status solidi (a)* 1987;104:183.
- [124] Messerschmidt U, Haussler D, Bartsch M, Geyer B, Feuerbacher M, Urban K. *Mat Sci Eng a-Struct* 2000;294:757.
- [125] Gilbert M, Queyreau S, Marian J. *Phys Rev B* 2011;84:174103.
- [126] Messerschmidt U. *Dislocation Dynamics During Plastic Deformation.*, Springer Series in Materials Science, Volume 129. ISBN 978-3-642-03176-2. Springer-Verlag Berlin Heidelberg, 2010 2010;1.
- [127] Suzuki T, Skrotzki W, Haasen P. *physica status solidi (b)* 1981;103:763.
- [128] Celli V, Thomson R, Kabler M, Ninomiya T. *Phys Rev* 1963;131:58.
- [129] Messerschmidt U, Bartsch M, Feuerbacher M, Geyer B, Urban K. *Philosophical Magazine A* 1999;79:2123.
- [130] Rao SI, Dimiduk DM, Tang M, Parthasarathy TA, Uchic MD, Woodward C. *Philos Mag* 2007;87:4777.
- [131] Singh P, Ohring M. *J Appl Phys* 1984;56:899.
- [132] Sun P, Ohring M. *J Appl Phys* 1976;47:478.
- [133] Schuh C, Mason J, Lund A. *Nat Mater* 2005;4:617.
- [134] Cross GL, Schirmeisen A, Grütter P, Dürig UT. *Nat Mater* 2006;5:370.
- [135] Hirano K-i, Agarwala RP, Cohen M. *Acta Metallurgica* 1962;10:857.
- [136] Frost HJ, Ashby MF. 1982.
- [137] Love G. *Acta Metallurgica* 1964;12:731.
- [138] Ngan A, Wo P, Zuo L, Li H, Afrin N. *International Journal of Modern Physics B* 2006;20:3579.
- [139] Zhu T, Li J. *Progress in Materials Science* 2010;55:710.

Chapter 5. Discussion, Conclusions and Outlook

5.1. Discussion

The size effects for nearly all types of inorganic solids can be compared, including ionic crystals (e.g. NaCl, KCl, LiF [1] and MgO [2], soft and hard slips), pure metals (fcc Au [3, 4], Al [5], Ni [6] and Cu [7]; bcc Nb, Ta, Mo and W [8][9]; and hcp Ti [10] and Mg [11]), covalent crystals (e.g. Si [12], GaAs [13]), ordered intermetallics (e.g. TiAl [14]), disordered intermetallics (e.g. NbTaMoW high-entropy alloy), complex metallic alloys (e.g. Al₁₃Co₄ [15]), quasicrystals (e.g. decagonal Al-Ni-Co and icosahedral Al-Pd-Mn) and metallic glasses (e.g. Cu- and Zn-based ones [16]). As stated in Chapter 1 (Introduction), two questions have been asked throughout the thesis:

- What are the highest strength levels that can be obtained at micron- and sub-micrometer scales?
- What mechanism governs the size dependence of strength for all the tested materials?

Here, the highest strength of a material as a function of its shear modulus is plotted, as shown in Fig. 1. The critical resolved shear stress (CRSS) for all the materials fall in the strength range between $\sim G/30$ to $\sim G/100$. This is a strong indication that the CRSS at such length scale can be very close to their theoretical values. Covalent crystals (Si and GaAs), some ionic crystals (e.g. MgO (110)) and quasicrystals are almost on their theoretical strengths ($G/30$ - $G/10$) while metals are closer to the lower strength side ($G/100$). The difference might be due to lower grown-in dislocation density in covalent crystals than that in metals, in general, or the different damage levels caused by FIB milling.

Taking into account the size effect on material strengths, the traditional material-selection maps that were developed for bulk materials are not valid anymore, and the new maps, which include the size effect, have to be created. For example,

when a specific strength (strength-to-weight ratio) is the most critical factor to be considered, MgO, Si, TiAl and the QCs are good candidates while Au is a not a proper candidate (Fig. 2). The elastic energy density can be also compared using the plot in Fig. 2. Small-size silicon has the highest energy density around 1 MJ/kg, which is in the same level for Lithium batteries. MgO and intermetallic phases (TiAl, i-Al-Pd-Mn and d-Al-Ni-Co) shows slightly lower energy density, while Au has the lowest energy density in Fig. 2. This map can also suggest materials selection for energy applications using small-scale devices. However, in real engineering applications, many other important, sometimes even more dominating, factors should be considered such as fracture toughness, functional properties (e.g. thermal and electrical conductivities) and, of course, cost. Unfortunately, only few of these properties are completely known for such small scales.

The other question concerns how one can predict the “size effect” for a material according to its known characteristics. In general, it is found that hard and brittle materials exhibit a small or no size effect such as Si, metallic glasses and QCs, while soft and ductile materials show large size effect such as fcc metals, basal-slip hcp metals and ionic crystals deformed on soft slips. It is known that the brittleness, or softness, can be qualitatively correlated to the energy barrier or force that resists dislocation motion (or shear band propagation for metallic glasses), which can be described by Peierls stress, τ_p (or shear stress at 0 K for metallic glasses).

Fig. 3 illustrates the size-effect exponent, m , as a function of Peierls stress for different types of materials in a linear- logarithmic format. The value of m ranges from 0 to about 0.8, and τ_p ranges over nearly three orders of magnitude from ~ 0.001 GPa to ~ 1 GPa. A trend can be clearly revealed showing the higher Peierls stress the lower size effect: when $\tau_p < \sim 0.1$ GPa, $m \approx 0.6-0.8$; when ~ 0.1 GPa $< \tau_p < \sim 1$ GPa, $0 < m < \sim 0.6-0.8$, m decreasing with increasing τ_p ; when $\tau_p > \sim 1$ GPa, $m \approx 0$, no size effect. This correlation can be associated with the ratio of

dislocation-source strength to the dislocation-motion stress (shear bands for metallic glasses). For example, at ~ 100 nm, more than 95% of the flow stress is contributed by source strengthening in pure Ni, at the same size only less than 50% of the flow stress is from source strengthening in pure W, and only less than 5% of flow stress in quasicrystals are from source strengthening, figuratively speaking. Although the detailed underlying strengthening mechanism may vary among different materials, this general trend in Fig. 3 can be still technologically important, providing a common guide to predict material strengths at multi-scales.

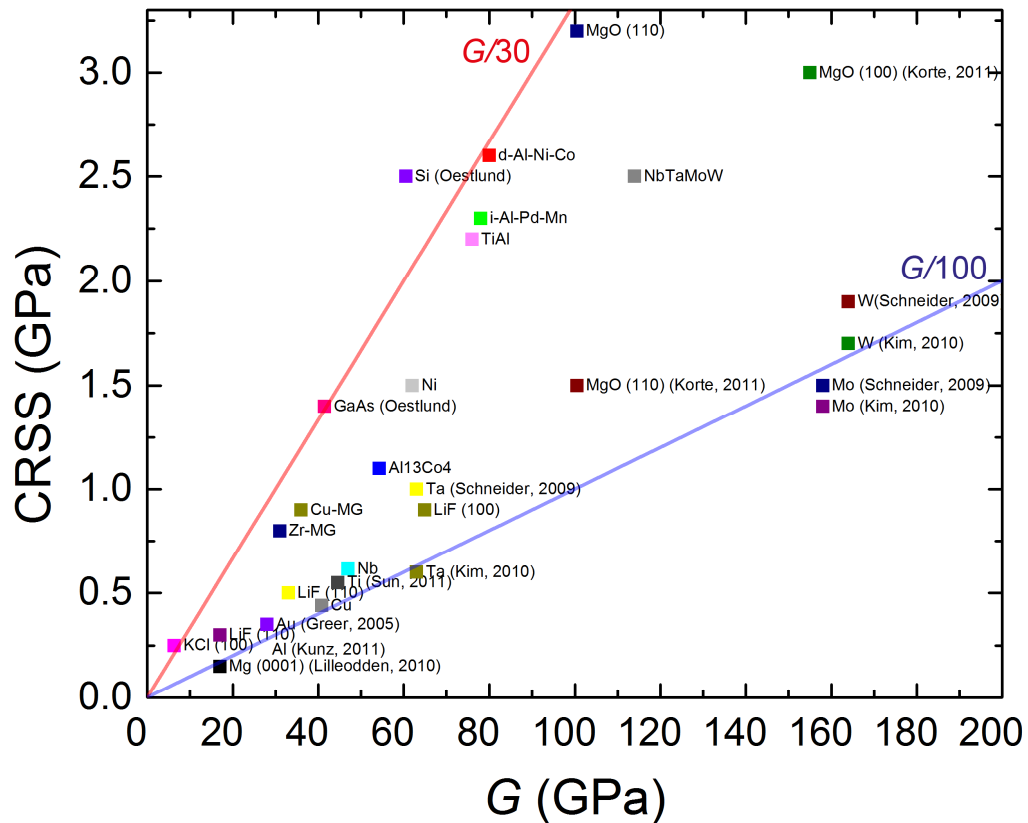


Fig. 1. CRSS as a function of shear modulus, G , for representative micro-pillars, (ionic crystals (e.g. NaCl, KCl, LiF [1] and MgO [2], soft and hard slips), pure metals (fcc Au [3, 4], Al [5], Ni [6] and Cu [7]; bcc Nb, Ta, Mo and W [8, 9]; and hcp Ti [10] and Mg [11]), covalent crystals (e.g. Si [12], GaAs [13]), ordered intermetallics (e.g. TiAl [14]), disordered intermetallics (e.g. NbTaMoW high-entropy alloy), complex metallic alloys (e.g. Al₁₃Co₄ [15]), quasicrystals (e.g. decagonal Al-Ni-Co and icosahedral Al-Pd-Mn) and metallic glasses (e.g. Cu- and Zn-based ones [16]). It indicates the strengths are in the range of $\sim G/30$ to $G/100$. Shear moduli are obtained from [17-20].

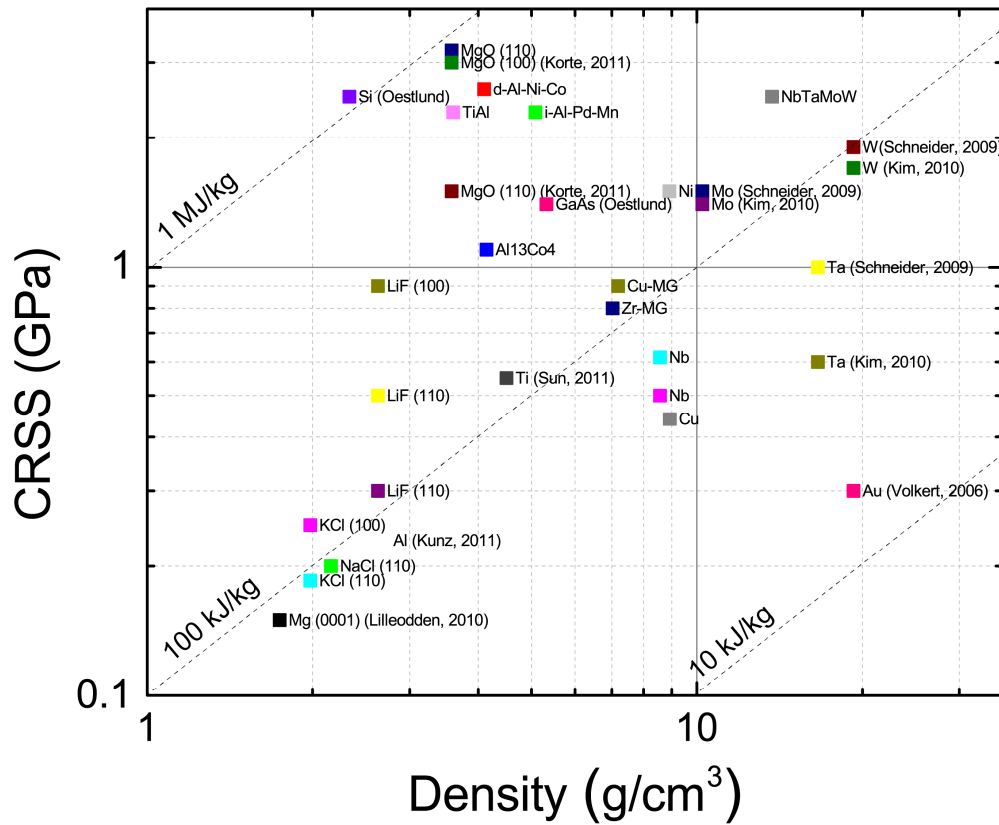


Fig. 2. CRSS as a function of density for representative micro-pillars, showing QC pillars are among the most high-strength and low-density pillars. Densities are calculated from their compositions.

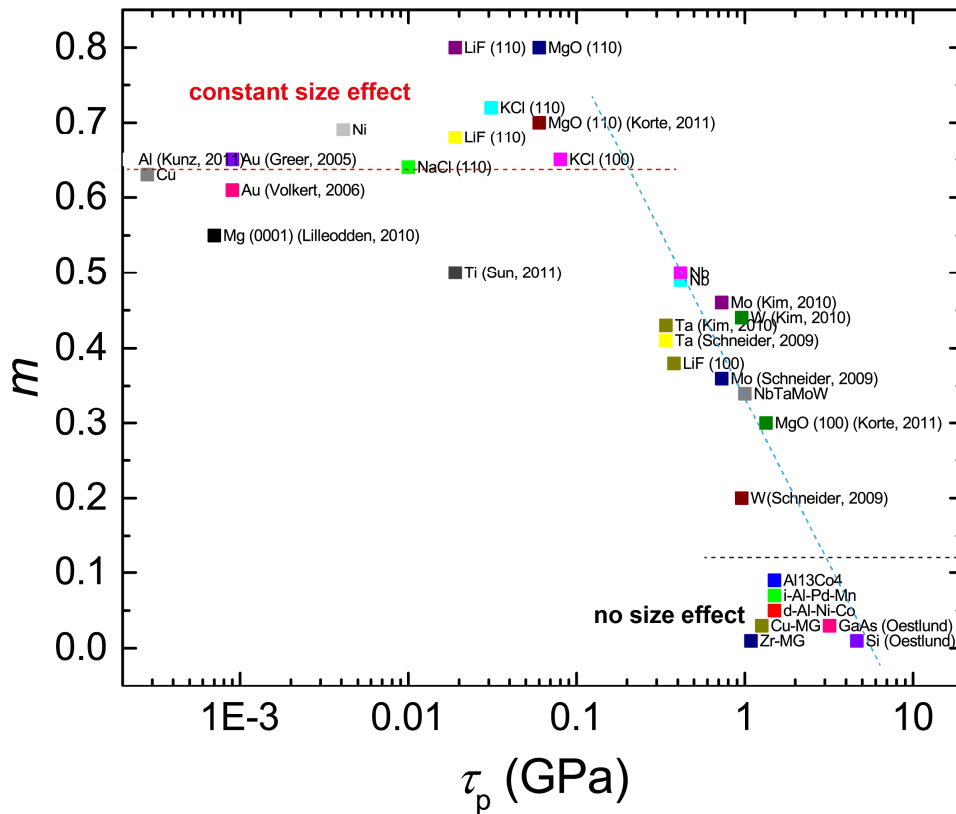


Fig. 3. Size-effect exponent, m , as a function of Peierls stress, τ_p , for representative micro-pillars, indicates that when $\tau_p < \sim 0.1$ GPa, $m \approx 0.6-0.8$; when ~ 0.1 GPa $< \tau_p < \sim 1$ GPa, $0 < m$

$< \sim 0.6-0.8$, m decreases with increasing τ_p ; when $\tau_p > \sim 1$ GPa, $m \approx 0$, no size effect; The values of τ_p (shear stress at 0 K for metallic glasses) are obtained from [17-21]. It should be noted that Si, GaAs, QCs and metallic glasses (MG) all have $m \approx 0$, the difference in m is for clarity shown in the graph.

5.2. Conclusions

The thesis focused on small-scale plastic behavior of ionic crystals, multi-component alloys and intermetallic quasicrystals, in addition to that of regular metals and metallic glasses which have been intensively studied. The general aim of the thesis is to offer some new insight into the currently popular small-scale mechanics and related size-effect phenomena and present a big picture that includes all types of inorganic solids. My studies show a general trend for the materials, regardless of chemical composition, lattice structure, atomic order and periodicity: they approach their theoretical strengths as in the range of $\sim G/30$ - $G/100$ at submicrometer scales and their size effects decrease when increasing the resistance for the propagation of plasticity mediums—dislocations or shear bands. However, each type of material shows some unique small-scale deformation behavior particular to its own class, which are summarized below:

Rock-salt structured ionic crystals

- The [001]-orientated NaCl, KCl, LiF and MgO single crystals deformed on the soft slip systems exhibit size-effect exponents of ~ 0.7 , which is similar to that of fcc metals.
- By studying the effects of crystal orientation, test temperature, pre-straining and doping levels on the size effects of KCl and LiF, it is found that those deformed on hard slip systems show similar size effects to bcc metals.
- The external electric field can enhance the motion of charged dislocations in ionic crystals at small scales, leading to decreased flow strength and increased ductility.

Bcc Nb₂₅Mo₂₅Ta₂₅W₂₅ refractory high-entropy alloys

- First, single crystalline HEA pillars exhibited higher strengths and lower size effect than those of pure Nb, Mo, Ta and W pillars, which could be attributed to a higher lattice friction in the HEA than that in pure bcc metals.
- Second, by measuring the fracture toughness of single-crystal and bi-crystal cantilevers, it is clear now that the poor fracture resistance of bulk HEAs is mainly due to the weakness of their grain boundaries, and, therefore, strengthening grain boundaries in the refractory HEAs is a critical issue.
- Third, a strategy for the fabrication of refractory HEA thin films and small-sized pillars has been proposed. By controlling the extrinsic and intrinsic sizes, such nanocrystalline HEAs exhibit extraordinarily high strengths and improved ductility.

Intermetallic quasicrystals

- First, a typically brittle quasicrystal i-Al-Pd-Mn exhibits an obvious brittle-to-ductile transition with a critical size of ~500 nm. Such small-scale quasicrystal pillars show an extraordinary ductility of over 50% compressive or tensile strains and a remarkably high yield strength of ~4.5 GPa at room temperature.
- Second, it was demonstrated that the pronounced plastic anisotropy in bulk d-Al-Ni-Co can be considerably reduced at small scales and room temperature.
- Third, the quasicrystal plasticity in a new temperature–size regime (~100-400 nm and 25-500°C) was studied. A size-temperature-strength deformation map for d-Al-Ni-Co has been created, involving three deformation mechanisms—cracking, dislocation activities and diffusion.

In addition to answering the questions proposed at the beginning of the thesis, several findings, sometimes by accident and curiosity, should be highlighted here, since they contribute a significant part of my PhD studies:

- Although the line fitting with the size-effect slope, m , has been commonly used to compare the size dependence in different materials, it might not be appropriate to describe size effects in a large experimental range of size and temperature, wherein the log-log size effect is not linear anymore.
- The electric and mechanical coupling in ionic crystals at small scales demonstrates that they may represent a new class of active materials as sensors and actuators.
- The nanostructured HEA pillars exhibit remarkably high yield strengths of ~ 10 GPa—a new record of strength among metallic micro-/nano-pillars, and excellent thermal stability comparing to typical refractory metals.
- Using TEM analysis, my co-workers and I suggest that dislocation glide may become dominant under high-stress and low-temperature conditions in contrast to the generally accepted deformation mechanism in quasicrystals—dislocation climb.
- The quasicrystal pillars are among the materials with the highest specific strengths (strength-to-weight ratio) to date.

5.3. Outlook

The following topics would be interesting for future studies:

First, although traditional deformation-mechanism and materials-selection maps have been well developed for coarse-grain bulk materials, the maps for materials at micrometer and nanometer scales are still lacking, and are urgently needed to provide a guide for micro- and nano-device design. It would be a good opportunity to study temperature-time-length scale effects on various material systems using emerging temperature and strain-rate controlled nano-mechanical

testing techniques, although the relevant facility is still rare and relatively unstable today.

Second, it would be interesting to couple mechanical properties with other functional properties at small scales. For example, some semiconductors such as ZnO and CdSe are well documented for their photo-plasticity—illumination increases or decreases their flow stresses, and deformation-induced luminescence—deformation produces continuous luminescence from the surface. So far, it is still unknown how these two phenomena behave at small scales, and it would be interesting for both scientific and technological studies. Another interesting aspect is “elastic strain engineering”: a large elastic strain, up to ~10%, can be achieved for small-scale materials and, consequently, the lattice parameters and elastic strain field can be changed. This methodology offers new opportunities for tuning many functional properties such as electronic, magnetic, optical, photonic and catalytic properties.

Last but not least, towards technological applications, it is critical to fabricate structural or functional small-scale devices using the knowledge obtained from nano-mechanical testing. However, there is still a gap between fundamental studies and manufacturing. Emerging nanofabrication techniques and additive manufacturing methods, also known as 3D printing, may supply many good opportunities to fabricate novel small-dimension materials, for example, functionally graded materials and architecture designed metamaterials.

References

- [1] Nadgorny EM, Dimiduk DM, Uchic MD. *J Mater Res* 2008;23:2829.
- [2] Korte S, Clegg WJ. *Philos Mag* 2011;91:1150.
- [3] Greer JR, Oliver WC, Nix WD. *Acta Mater* 2005;53:1821.
- [4] Volkert CA, Lilleodden ET. *Philos Mag* 2006;86:5567.
- [5] Kunz A, Pathak S, Greer JR. *Acta Mater* 2011;59:4416.
- [6] Frick CP, Clark BG, Orso S, Schneider AS, Arzt E. *Materials Science and Engineering: A* 2008;489:319.
- [7] Jennings AT, Burek MJ, Greer JR. *Phys Rev Lett* 2010;104:135503.
- [8] Schneider AS, Kaufmann D, Clark BG, Frick CP, Gruber PA, Monig R, Kraft O, Arzt E. *Phys Rev Lett* 2009;103.
- [9] Kim J-Y, Jang D, Greer JR. *Acta Mater* 2010;58:2355.
- [10] Sun Q, Guo Q, Yao X, Xiao L, Greer JR, Sun J. *Scripta Materialia* 2011;65:473.
- [11] Lilleodden E. *Scripta Materialia* 2010;62:532.
- [12] Ostlund F, Rzepiejewska-Malyska K, Leifer K, Hale LM, Tang YY, Ballarini R, Gerberich WW, Michler J. *Adv Funct Mater* 2009;19:2439.
- [13] Ostlund F, Howie PR, Ghisleni R, Korte S, Leifer K, Clegg WJ, Michler J. *Philos Mag* 2011;91:1190.
- [14] Edalati K, Toh S, Iwaoka H, Watanabe M, Horita Z, Kashioka D, Kishida K, Inui H. *Scripta Materialia* 2012;67:814.
- [15] Walter C, Wheeler JM, Barnard JS, Raghavan R, Korte-Kerzel S, Gille P, Michler J, Clegg WJ. *Acta Mater* 2013;61:7189.
- [16] Chen CQ, Pei YT, De Hosson JTM. *Acta Mater* 2010;58:189.
- [17] Haasen P. *Mater Sci Tech-Lond* 1985;1:1013.
- [18] Kamimura Y, Edagawa K, Takeuchi S. *Acta Mater* 2013;61:294.
- [19] Takeuchi S, Edagawa K. Chapter 8 Elastic and plastic properties of quasicrystals. In: Takeo F, Yasushi I, editors. *Handbook of Metal Physics*, vol. Volume 3. Elsevier, 2008. p.267.
- [20] Johnson W, Samwer K. *Phys Rev Lett* 2005;95:195501.
- [21] Wang JN. *Mat Sci Eng a-Struct* 1996;206:259.

Declaration

This PhD thesis and related publications do not represent the work of a single person, but the outcomes of stimulating collaborations both within the Laboratory for Nanometallurgy (LNM), ETH Zurich and with several research groups (Laboratory of Crystallography, ETH Zurich; Materials Science Group, Kyoto University; Laboratory for Mechanics of Materials and Nanostructures, Empa Thun). The people who contributed to this thesis are listed below in alphabetical order:

Pawel Kuczera was formerly a postdoctoral researcher in the Laboratory of Crystallography, ETH Zurich. He prepared bulk icosahedral and decagonal quasicrystals, did numerical simulations and contributed to the discussion in Chapter 4.

Takayuki Kitamura is the professor in Materials Science Group, Kyoto University. He contributed to the design and discussion of the micro-cantilever fracture tests in Chapter 3.2 and the experimental design of *in situ* SEM and TEM pillar bending tests in Chapter 4.3.

Huan Ma is a PhD student in LNM. He fabricated the HEA thin film, characterized the microstructure using XRD, EDX and EBSD, measured the electrical resistivity and contributed to the discussion in Chapter 3.3.

Johann Michler is the head of Laboratory for Mechanics of Materials and Nanostructures, Empa Thun. He contributed the discussion of high-temperature micro-compression in Chapter 4.3.

Soumyadipta Maiti is a PhD student in the Laboratory of Crystallography, ETH Zurich. He prepared the bulk refractory HEA, characterized the microstructure of the specimen using XRD, EDX, TEM, measured the micro-hardness and contributed the discussion in Chapter 3.1.

Alla Sologubenko is a senior scientist in LNM. She performed the TEM characterization of quasicrystals and contributed to analysing the TEM data and discussion in Chapter 4.1 and 4.3.

Ralph Spolenak is a professor at ETH Zurich and the head of LNM. He supervised the PhD thesis which is presented here.

Takashi Sumigawa is the associate professor in Materials Science Group, Kyoto University. He contributed to the design and discussion of the micro-cantilever fracture tests in Chapter 3.2 and the experimental design of *in situ* SEM and TEM pillar bending tests in Chapter 4.3.

Walter Steurer is a professor at ETH Zurich and the head of Laboratory of Crystallography. He contributed to the data analysis and discussion in both the HEAs and quasicrystals shown in Chapter 3 and 4, respectively.

Jeffrey Wheeler is a former research scientist in Laboratory for Mechanics of Materials and Nanostructures, Empa Thun and currently a senior scientist in LNM. He performed high-temperature compression for decagonal quasicrystal pillars and contributed the data analysis in Chapter 4.3.

Hongjun Yu was formerly a visiting professor in Materials Science Group, Kyoto University. He contributed the FEM simulation of the cantilever bending tests in Chapter 3.2.

Curriculum Vitae

Name Yu Zou
Date and Place of Birth March 18th, 1983 and Changchun, Jilin, China
Nationality Chinese

EDUCATION

November 2015 **Ph.D. Materials Science**
Swiss Federal Institute of Technology Zürich (ETH Zurich), Zurich, Switzerland.
Supervisor: Prof. Ralph Spolenak, Laboratory for Nanometallurgy

August 2014-
January 2015 **Visiting Ph.D. student**
Kyoto University, Kyoto, Japan
Host: Prof. Takayuki Kitamura, Materials Science Laboratory

June 2010 **M. Eng. Materials Engineering**
McGill University, Montreal, QC, Canada
Supervisors: Prof. Jerzy A. Szipnar, Laboratory for Texture and Microstructure; Prof. Stephen Yue, Laboratory for Hot Deformation

July 2007 **B. Eng. Materials Science and Engineering**
Beihang University (Beijing University of Aeronautics & Astronautics), Beijing, China
Advisor: Prof. Hua-Ming Wang, Laboratory for Laser Materials Manufacturing

TEACHING & ADVISORY EXPERIENCE

2011-2014 **Teaching assistant** Praktikum IV: mechanical testing, ETH Zurich
2011-2014 **Project advisor** Supervised two M.Sc. projects and one B.Sc. thesis

SCIENTIFIC PUBLICATIONS

Y. Zou, P. Kuczera, W. Steurer, R. Spolenak “*Disappearance of plastic anisotropy in decagonal quasicrystals at small scales and room temperature*” (in press in **Extreme Mechanics Letters**).

Y. Zou, H. Ma, R. Spolenak “*Ultrastrong, ductile and stable high-entropy alloys at small scales*” **Nature Communications** 6:7748 doi: 10.1038/ncomms8748 (2015), Highlighted in *ETH News; Pro-physik.de; Futurity; Labo; Analytik-news; ScientificAmerican (Asian)*.

Y. Zou, R. Spolenak, “*Size-dependent plasticity in KCl and LiF single crystals: influence of orientation, temperature, pre-straining and doping*”. **Philosophical Magazine** 95 (2015), 1795-1813.

H. Ma, **Y. Zou**, A. Sologubenko, R. Spolenak “*Copper thin films by ion beam assisted deposition: strong texture, superior thermal stability and enhanced hardness*” **Acta Materialia** 98 (2015) 17-28.

Y. Zou, S. Maiti, W. Steurer, R. Spolenak, “*Size-dependent plasticity in an Nb₂₅Mo₂₅Ta₂₅W₂₅ refractory high-entropy alloy*” **Acta Materialia** 65 (2014) 85-97.

Y. Zou, R. Spolenak, “*Size-dependent plasticity in micron- and submicron-sized ionic crystals*”. **Philosophical Magazine Letters**, 93 (2013) 431-438.

Y. Zou, D. Goldbaum, J. A. Szpunar, S. Yue “*Microstructure and nanohardness of cold-sprayed coatings: Electron backscattered diffraction and nanoindentation studies*” **Scripta Materialia**, 62 (2010) 395–398.

Y. Zou, W. Qin, E. Irissou, J. Legoux, S. Yue, J. A. Szpunar “*Dynamic recrystallization in the particle/particle interfacial region of cold-sprayed nickel coating: Electron backscatter diffraction characterization*” **Scripta Materialia** 61 (2009) 899-902.

Under review

Y. Zou, P. Kuczera, A. Sologubenko W. Steurer, R. Spolenak “*Superior room-temperature ductility of typically brittle quasicrystals at small sizes*” (under review in Nature Communications).

Y. Zou, J. Wheeler, A. Sologubenko, P. Kuczera, J. Michler, W. Steurer, R. Spolenak “*Bridging room-temperature and high-temperature plasticity in decagonal Al-Ni-Co quasicrystals by micro-thermomechanical testing*” (under review in Acta Materialia).

In preparation

Y. Zou, H. Yu, T. Sumigawa, T. Kitamura, S. Maiti, W. Steurer, R. Spolenak, “*In situ micro-cantilever studies of fracture properties of a refractory high-entropy alloy*” (to be submitted to Scripta Materialia).

Y. Zou and R. Spolenak “*Electric field controls nanoscale plasticity of ZnO*”.

Y. Zou and R. Spolenak “*Nanoscale sensor and actuator based on NaCl nanopillars*”.

SELECTED CONFERENCE PRESENTATIONS

Y. Zou, J. Wheeler, A. Sologubenko, P. Kuczera, J. Michler, W. Steurer, R. Spolenak “*Brittle-to-ductile transition of quasicrystals at small scales: size and temperature effects*” (oral presentation) MRS Fall 2015, Boston, USA.

Y. Zou, H. Yu, T. Sumigawa, T. Kitamura, S. Maiti, W. Steurer, R. Spolenak, “*In situ micro-cantilever studies of fracture properties of a refractory high-entropy alloy*” (oral presentation) MRS Fall 2015, Boston, USA.

Y. Zou, A. Sologubenko, J. Wheeler, J. Michler, P. Kuczera, W. Steure R. Spolenak “*Plasticity in small-scale quasicrystals: from room temperature to elevated temperature*” (oral presentation) EUROMAT 2015, Warsaw, Poland, September 2015.

Y. Zou, A. Sologubenko, P. Kuczera, W. Steure R. Spolenak “*Brittle-to-Ductile Transition of Small-scale Icosahedral Quasicrystals at Room Temperature*” (oral presentation) European Solid Mechanics Conference (ESMC), Madrid, Spain, July 2015.

Y. Zou, H. Ma, R. Spolenak, “*Ultrastrong and Thermally Stable Multi-component Alloys at Small Scales*” (oral presentation) 2015 TMS Annual Meeting & Exhibition, USA, March 2015.

Y. Zou, H. Ma, S. Maiti, W. Steurer, R. Spolenak, “*Ultrastrong Multi-component Alloys at Small Scales*” (poster presentation) Gordon Research Conference on Thin Film & Small Scale Mechanical Behavior, USA, July 2014.

Y. Zou, R. Spolenak, “*Size-dependent plasticity in KCl and LiF: Influence of orientation, temperature, pre-straining and doping*” (oral presentation) DPG conference in Dresden March 2014.

Y. Zou, S. Maiti, W. Steurer, R. Spolenak, “*Size-dependent plasticity in an Nb₂₅Mo₂₅Ta₂₅W₂₅ refractory high-entropy alloy*” (oral presentation) 2014 TMS Annual Meeting & Exhibition, USA, February, 2014.

Y. Zou, R. Spolenak, “*Size-dependent plasticity in KCl and LiF: Influence of orientation, temperature, pre-straining and doping*”. (poster presentation) ECI conference “Nano- and Micromechanical Testing in Materials Research and Development IV”, Portugal. October 2013.

Y. Zou, R. Spolenak, “*Micro- and Submicro-pillar Compression of Ionic Crystals: Size-dependent Plasticity*” (oral presentation) MRS Spring Meeting, USA, March 2013.

Y. Zou, R. Spolenak, “*Size-dependent plasticity in micron- and submicron-sized ionic crystals*” (poster presentation) Gordon Research Conference on Thin Film & Small Scale Mechanical Behavior (GRC), Maine, USA, July 2012.

HONORS & AWARDS

The Swiss National Science Foundation (SNSF) Early Postdoc. Mobility fellowship, 2015.

The Best Poster Prize in “Strength and Failure at the Micro- and Nanoscale”, MRS Fall, 2015.

Young researchers’ award in “Japanese-Swiss Science and Technology Program”, 2014.

The award in the 7th “Chunhui cup” innovation contest, Guangzhou, China, 2012.